Westbrook, G.K., Carson, B., Musgrave, R.J., et al., 1994
Proceedings of the Ocean Drilling Program, Initial Reports, Vol. 146 (Part 1)

5. SITES 889 AND 890[1]

Shipboard Scientific Party[2]

HOLE 889A

Date occupied: 5 October 1992

Date departed: 9 October 1992

Time on hole: 2 days, 16 hr, 48 min

Position: 48°41.958′N, 126°52.098′W

Bottom felt (rig floor; m; drill-pipe measurement): 1322.0

Distance between rig floor and sea level (m): 10.8

Water depth (drill-pipe measurement from sea level; m): 1311.2

Total depth (rig floor; m): 1667.8

Penetration (m): 345.8

Number of cores (including cores with no recovery): 44

Total length of cored section (m): 325.8

Total core recovered (m): 223.14

Core recovery (%): 68

Oldest sediment cored:
Depth (mbsf): 346.0
Nature: glauconitic clayey silt
Earliest age: late Pliocene

HOLE 889B

Date occupied: 10 October 1992

Date departed: 12 October 1992

Time on hole: 1 day, 1 hr, 36 min

Position: 48°41.850′N, 126°52.392′W

Bottom felt (rig floor; m; drill-pipe measurement): 1327.0

Distance between rig floor and sea level (m): 10.8

Water depth (drill-pipe measurement from sea level; m): 1316.2

Total depth (rig floor; m): 1713.5

Penetration (m): 386.5

Number of cores (including cores with no recovery): 21

Total length of cored section (m): 189.5

Total core recovered (m): 48.15

Core recovery (%): 25

Oldest sediment cored:
Depth (mbsf): 386.5
Nature: clayey silt
Earliest age: late Pliocene

HOLE 889C

Date occupied: 15 October 1992

Date departed: 17 October 1992

Date reoccupied: 18 October 1992

Date departed: 22 October 1992

Time on hole: 6 days, 2 hr, 45 min

Position: 48°49.908′N, 126°52.230′W

Bottom felt (rig floor; m; drill-pipe measurement): 1326.0

Distance between rig floor and sea level (m): 10.9

Water depth (drill-pipe measurement from sea level; m): 1315.1

Total depth (rig floor, m): 1710.5

Penetration (m): 384.5

Number of cores (including cores with no recovery): 0

HOLE 889D

Date occupied: 17 October 1992

Date departed: 18 October 1992

Time on hole: 1 day, 7 hr, 12 min

Position: 48°41.982′N, 126°52.128′W

Bottom felt (rig floor; m; drill-pipe measurement): 1322.0

Distance between rig floor and sea level (m): 10.9

Water depth (drill-pipe measurement from sea level; m): 1311.1

Total depth (rig floor, m): 1476.0

Penetration (m): 154.0

Number of cores (including cores with no recovery): 4

Total length of cored section (m): 58.5

Total core recovered (m): 22.86

Core recovery (%): 39

Oldest sediment cored:
Depth (mbsf): 154.0
Nature: clayey silt
Earliest age: Pleistocene

HOLE 890A

Date occupied: 9 October 1992

Date departed: 9 October 1992

Time on hole: 5 hr

Position: 48°39.750′N, 126°52.890′W

Bottom felt (rig floor; m; drill-pipe measurement): 1337.2

Distance between rig floor and sea level (m): 10.9

Water depth (drill-pipe measurement from sea level; m): 1326.3

Total depth (rig floor, m): 1342.5

---

[1] Westbrook, G.K., Carson, B., Musgrave, R.J., et al., 1994. *Proc. ODP, Init. Repts.,* 146 (Pt. 1): College Station, TX (Ocean Drilling Program).

[2] Shipboard Scientific Party is as given in the list of participants preceding the contents.

Penetration (m): 5.3

Number of cores (including cores with no recovery): 1

Total length of cored section (m): 5.3

Total core recovered (m): 3.71

Core recovery (%): 70

Oldest sediment cored:
Depth (mbsf): 9.50
Nature: clay
Earliest age: Pleistocene

HOLE 890B

Date occupied: 10 October 1992

Date departed: 10 October 1992

Time on hole: 4 hr

Position: 48°39.750′N, 126°52.890′W

Bottom felt (rig floor; m; drill-pipe measurement): 1337.2

Distance between rig floor and sea level (m): 10.9

Water depth (drill-pipe measurement from sea level; m): 1326.3

Total depth (rig floor, m): 1385.0

Penetration (m): 47.8

Number of cores (including cores with no recovery): 5

Total length of cored section (m): 45.3

Total core recovered (m): 37.76

Core recovery (%): 83

Oldest sediment cored:
Depth (mbsf): 47.8
Nature: silty clay to clayey silt
Earliest age: Pleistocene

Principal results: Sites 889 and 890 (prospectus Site VI-5) are located on a 15- to 20-km-wide region of gently undulating topography in the mid-continental slope off Vancouver Island, in water depths of 1315 and 1326 m below sea level (mbsl), respectively. Coring began in bedded, slope-basin sediment, and at Site 889 extended into the underlying, deformed sediments of the accretionary wedge. Site 890 was cored to only about 50 m below seafloor (mbsf) to sample the near-surface sediments. A major objective at this site was the investigation of a well-developed bottom-simulating reflector (BSR) at 225 mbsf. Holes 889A, 889B, and 889C penetrated that reflector. A borehole seal (CORK) was emplaced in Hole 889C to provide for long-term observation of the thermal, chemical, and hydrogeological conditions associated with the gas hydrate zone that is inferred to overlie the BSR and with dewatering of the accretionary wedge.

Sediments at Sites 889 and 890 range in age from late Quaternary to late Pliocene. A hiatus in the record occurs at 87 mbsf, separating late Quaternary from early Pleistocene deposits.

Three lithostratigraphic units were recognized at Sites 889 and 890. Unit I includes clayey silts, fine sands, and diagenetic carbonates; it extends from the surface to a depth of 128.0 mbsf in Hole 889A. Unit I comprises slope and slope basin sediments that are hemipelagites, turbidites, and mass-flow deposits. Unit II is similar in composition to the lower portion of Unit I, but it is noticeably more consolidated than the overlying unit and is highly fractured. Diagenetic carbonates were observed throughout the section. Unit II is thought to consist of abyssal plain silts and clays that were postdepositionally fractured during accretion. Unit II extends to 301.5 mbsf, beneath which the glauconite content increases sharply, at the top of Unit III. The sediments in Unit III appear to be abyssal plain deposits like those in Unit II above, but the abundant authigenic glauconite suggests deposition under suboxic conditions.

Three structural domains were established. Domain I (0–104 mbsf; Hole 889A) is dominated by subhorizontal bedding, with little apparent deformation of the slope basin sediments. In Domain II (104–127 mbsf; Hole 889A) the less common sand/silt beds dip 40°–70° to the west and show evidence of slump folding. At the top of Domain III at 127 mbsf (Hole 889A) small-scale fractures are evident and increase in density to 150 mbsf. Below 150 mbsf, fractures are pervasive and produce well-developed angular fragments that commonly exhibit an interlocked geometry. Some of the fragment surfaces are polished and marked with slickenlines. The dominant fracture fabric dips 45°–60°. Because fractures are ubiquitous in Domain III, and no clear indicators of fault zones were recovered, we infer that tectonic stress in the accretionary wedge sediments sampled at this site is accommodated largely by distributed strain.

The downhole variation in consolidation is clearly shown in the distribution of bulk density and porosity. Unit I is characterized by normally consolidated deposits in which porosity declines regularly with increasing depth. Between 128 and 160 mbsf (upper Unit II) the porosity decreases rapidly and the sediments become overconsolidated to the base of Unit II. There are distinct excursions from the general porosity decrease with depth that correlate with variations in diagenetic carbonate cementation and organic geochemistry (organic carbon content, methane, N, and S concentrations). The position of the BSR falls within one of these excursions, but it is not unique. Lithostratigraphic Unit III exhibits an apparently anomalous increase in porosity with increasing depth.

The inorganic chemistry of the pore waters defines two zones. Within lithostratigraphic Unit I, sulfate declines to 0 at 10 mbsf, accompanied by an increase in the alkalinity. The loss of sulfate removes inhibition to carbonate deposition, and as a result Ca^{2+} and Mg^{2+} concentrations decrease rapidly from 0 to 60 mbsf. Chloride concentration declines from 550 mM at the sediment/water interface to 363 mM at the base of chemical Zone 1 (130 mbsf). The linear change in Cl^- is diagnostic of a diffusion gradient.

Zone 2 (130–386.5 mbsf) shows a nearly constant Cl^- concentration of 370 mM. The concentrations of Na^+, Mg^{2+}, and phosphate are also nearly constant, indicating that the low Cl^- concentration is a dilution effect. Low-chloride fluids might be derived by lateral advection from land, by dehydration of hydrated mineral species at depths greater than 1–2 km within the accretionary wedge, or perhaps by clay membrane filtration. A probable source, however, is the dissociation of gas hydrate, either upon sampling or in situ, following a change in temperature that is sufficiently recent (a few thousand years) for the low chlorinity not to have been dispersed by diffusion or by fluid advection. The degree of dilution suggests that less than 40% of the pore volume was filled with hydrate. Below 300 mbsf, increases in the gradients of concentration of calcium and silica, and a decrease in potassium, indicate diffusion or mixing with a deeper seated fluid.

Lithostratigraphic Unit I (0–128.0 mbsf) yielded elevated methane concentrations (60×10^3 to 80×10^3 ppmv) below the sulfate-reduction zone. Methane declines to $<30 \times 10^3$ ppmv at the base of Unit I. Over this same interval, ethane and propane were essentially absent, and the C_1/C_2 ratio was $>10^3$, indicating that the methane is biogenic. A small spike (33 ppmv) in the ethane concentration at 129 mbsf (associated with the Cl^- minimum) suggests a deeper source for fluids at this level.

Gas compositions change markedly in the interval 130–247 mbsf. Headspace (HS) samples contain 30×10^3 to 77×10^3 ppmv methane, 5–35 ppmv ethane, and 0.5–3.4 ppmv propane. The large concentrations of methane found in this interval could be indicative of saturation of the pore water with methane, but the calculations of the degree of methane saturation have yet to be made. If the methane is at concentrations at or above saturation in the pore fluid in cores recovered from the hydrate stability zone, then it has probably been released from hydrate that dissociated before being recovered on the ship.

Below 250 mbsf, the methane concentrations become highly variable. Ethane increases markedly below 300 mbsf, and propane increases rapidly below 360 mbsf. Within this interval, the C_1/C_2 ratio declines from values of about 2000 to <100, indicating a mixture of thermogenic and bacterially derived gas.

Both Holes 889A and 889B were logged with the geophysical and Formation MicroScanner (FMS) tool strings; a vertical seismic profile (VSP) was run in Hole 889B. The base of lithostratigraphic Unit I exhibits particularly high porosity in the logs. This high-porosity zone is associated with geochemical anomalies (Cl^-, Ca^{2+}, Mg^{2+}, S, N, methane, and ethane), which implies that it collects fluids evolved from greater depths. Within lithostratigraphic Unit II, high velocity and resistivity values correlate with low neutron porosity and indicate the presence of carbonate cementation.

Six in-situ temperature determinations were made with the water-sampling temperature probe (WSTP) and ADARA tools. Temperature increases linearly with depth, with a gradient of 54°C/km. The data imply conductive heat loss rather than advection, although upward movement of fluid at rates of around 1 mm/yr or less cannot be excluded, and predict the base of the hydrate stability field for methane and pure water (17°C) at 260 mbsf.

The BSR at Sites 889 and 890 is situated 276 ms below the seafloor in the migrated seismic section. Time-depth curves derived from the sonic log and VSP indicate that the BSR is located at 225 mbsf (Hole 889B). There is no evidence in either the logs or the cores for the accumulation of hydrate in massive form, but the temperature of –1.4°C measured in a core at 220 mbsf (about 10°C lower than the usual core temperature from this depth) could have been produced by the dissociation of hydrate filling 8% or more of the pore space.

Although the sonic log does not exhibit a substantial decrease in velocity across the BSR, the VSP data define a rise in velocity just above the BSR with a distinct low-velocity zone beneath it. Velocities are lower than in seawater, and are typical of the presence of small amounts of free gas. The disparity between the sonic-log and VSP results may be attributed to drilling disturbance, which could deplete the gas phase in the immediate vicinity of the borehole. Also, the sonic log will not record velocities lower than that of the seawater filling the drill hole.

The geophysical and geochemical data, taken together, are most satisfactorily explained by the presence of hydrate in the sediment above the BSR at 225 mbsf and by the presence of a small amount of free gas (no more than 5%) in the 25-m interval beneath the BSR. If this interpretation of the data is correct, then the stability field for hydrate formed from a mixture of pure water and pure methane is not appropriate for the natural system investigated at Site 889. The estimated stability field for methane and seawater gives a closer prediction of the depth of the BSR.

The low chlorinity throughout much the interval beneath the BSR may have its origin, at least in part, in dissociation of hydrate accompanying the upward migration of the base of the hydrate stability field as the upper few hundred meters of the section warmed after the last glacial period, during which time the temperature at the seafloor may have been below 0°C.

The pattern of variation in the organic and inorganic geochemistry of the pore fluids and in the physical properties does not show some of the large discontinuities that are seen at Sites 891 and 892 in association with major faults. With the exception of a narrow interval at about 130 mbsf, there is little evidence of significant fluid flow that is confined to conduits or fluid pathways provided by permeable beds or faults. Lithostratigraphic Units II and III are pervasively fractured, and it seems probable that flow through the section would be quite dispersed through this fractured rock. An in-situ measurement of pore-fluid pressure made with the lateral stress tool (LAST-II) at a depth of 140 mbsf in Hole 889D yielded a value close to hydrostatic, indicating small excess-pressure gradients (further processing is required to remove the effect of heave from the data). No direct evidence for large-scale fluid flow through the section was discovered at Site 889, and the linearity of the increase of temperature with depth implies that any flow that is occurring must be at velocities of less than a few millimeters per year.

The purpose of the CORK borehole seal deployed at Hole 889C is to provide data on the distribution of temperature and pressure in the hole, after the effects of drilling have equilibrated. From these data, it should be possible to determine the temperature profile through the hydrate stability zone in more detail, and post-cruise hydrogeological tests at the CORK should define rates of fluid advection from this portion of the accretionary wedge through the BSR.

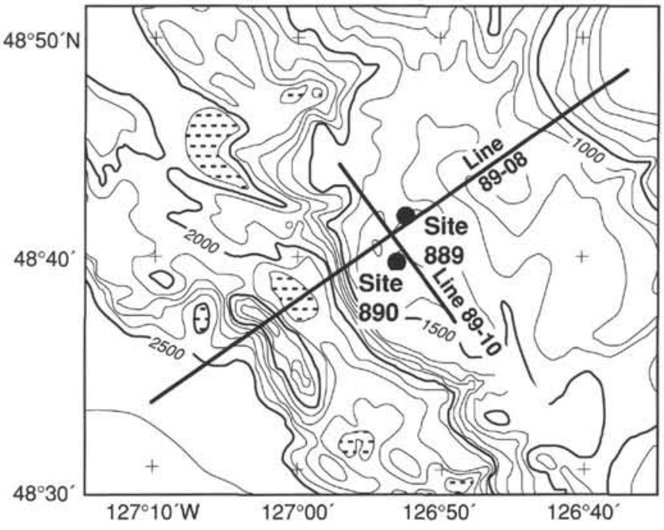

Figure 1. Positions of Sites 889 and 890, associated seismic reflection lines 89-08 and 89-10, and bathymetry of the Vancouver Island continental margin. Bathymetric contours are shown at 100-m intervals. Enclosed bathymetric lows are indicated by the dashed pattern.

BACKGROUND AND OBJECTIVES

Ocean Drilling Program (ODP) Site 889 lies on the continental slope off Vancouver Island, at a depth of 1315 meters below sea level (mbsl) (Fig. 1). The site is positioned on a 15- to 20-km-wide, gently undulating portion of the mid-slope. To the west, a steep escarpment separates this region from the lower slope (water depth 2300–2500 m). The variation in the character of the topography between the two regions is a manifestation of contrasting subsurface structure apparent in seismic-reflection lines (Fig. 2). Beneath Site 889 the accretionary wedge is characterized by reflectors that are laterally incoherent. The faults inferred to cut the deformed sediments forming the wedge are poorly imaged (Davis and Hyndman, 1989; Spence, Hyndman, et al., 1991). Pervasive faulting and folding is characteristic of accretionary wedge material in this structural position, which probably accounts for the poor coherence of reflectors. In contrast, the accreted sediments of the lower slope are well stratified and are elevated above Cascadia Basin along a series of distinct, landward-dipping thrust faults and perhaps by thickening associated with distributed deformation that does not degrade the seismic character significantly (K. Wang and R.D. Hyndman (unpubl. data).

Site 890 lies just 4 km south-southwest of Site 889, at a depth of 1326 mbsl (Fig. 1). The structural setting for the two sites is identical, with the exception that Site 890 lies to the south of a saddle between two small, north-trending hills. Site 889 is situated to the north of these topographic highs.

A veneer of stratified slope deposits covers the accretionary wedge material at Sites 889 and 890. These sediments appear to consist dominantly of turbidites and hemipelagic deposits, but given the position of the sites on the margin, they may include mass-flow deposits as well. As the accreted sediment is inferred to be of Pliocene-Pleistocene age, the slope cover deposits are thought to be Pleistocene to Holocene in age. Across Sites 889 and 890 this near-surface sediment thickens to the southwest.

Within the incoherent, accretionary sediment section a strong, seismically continuous bottom-simulating reflector (BSR) occurs at about 270 ms two-way traveltime (TWT) (Fig. 2). The BSR is inferred to mark the base of the stability field of methane hydrate (Hyndman and Spence, 1992). Bottom-simulating reflectors are common in accretionary settings (Kvenvolden and Barnard, 1983), and it has been suggested (Davis et al., 1990) that the BSR on this margin is supported by the diffuse, upward advection of methane-bearing pore fluids, which encounter pressure and temperature conditions appropriate to formation of clathrate at this depth.

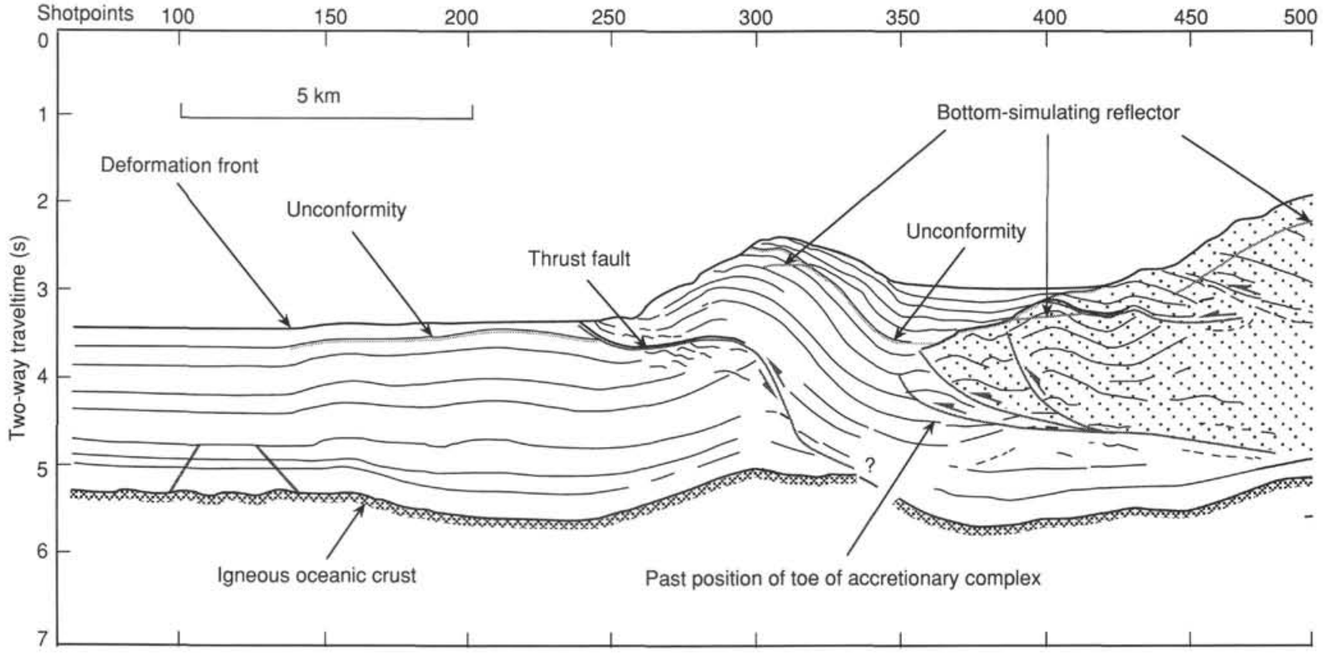

Figure 2. Line drawing of seismic-reflection line 89-08, showing the position of Site 889 in the migrated time section from accreted sediments and overlying bedded sediments of the mid-slope, the thrust sheets of the lower slope, and undeformed Cascadia Basin deposits to the west. Most of the reflectors within the accretionary wedge are short and commonly nonlinear. The seismic character of most of the wedge is reflective, but incoherent.

Drilling at Sites 889 and 890 was undertaken primarily to measure the geochemical, thermal, physical properties, and hydrologic conditions that support formation of the BSR. Coordinated sampling, logging, and downhole experiments (in-situ temperature, packer test, LAST and geoprops tools, and CORK borehole seal) were planned to sample and analyze fluids and the associated hydrates, and to determine the fluid flow and thermal regime in an area thought to be dominated by diffuse fluid discharge.

Three holes were drilled at Site 889. Holes 889A and 889B were cored and logged. Hole 889C was cased and fitted with a borehole seal.

Operations at Site 889 were complicated by the fact that the drilling site lay within 10 nmi of the center of a munitions dumping area. Concern about contamination resulted in a Canadian government directive to survey the bottom with the drill-string TV camera (to avoid any manufactured objects), and to wash down through the upper 20 m of sediment (where canisters may be buried) in this zone. Site 890 was occupied to core the upper 20 m section of the sediment column that could not be drilled at Site 889. Site 890 was drilled to a depth of 51 mbsf, to provide sufficient overlap for correlation with Site 889.

SEISMIC STRATIGRAPHY

Sites 889 and 890 lie on a small plateau on the accretionary wedge off Vancouver Island. To the west, a steeply sloping part of the surface of the accretionary wedge leads down to a lower slope basin, which in turn lies to the east of a prominent anticlinal ridge at the toe of the wedge (Figs. 1–2). Site 889 lies on multichannel seismic-reflection line 89-08, from the survey run by Digicon Geophysical Corp. for the Geological Survey of Canada in 1989 (Spence, Hyndman, Davis, et al., 1991). Line 89-08 is crossed orthogonally in the center of the plateau by line 89-10, from the same survey. Site 890 lies 1.3 km southwest of line 89-10.

In the plateau on which the sites lie, what are interpreted to be accreted sediments locally crop out at small culminations, but they are generally covered by a layer of bedded sediments that thickens into basins formed in synclines or on the footwall side of thrusts. Reflectors in the accreted sediments are typically discontinuous and irregular in form and are rarely longer than a kilometer in length. The few reflectors of greater length are mostly eastward-dipping and probably delineate thrust zones. At the base of the slope west of the plateau, the reflectors are far more coherent in the broader structures developed near the toe of the accretionary wedge. The much smaller structures represented by the incoherent reflectors beneath the region of Sites 889 and 890 are presumably a product of more intense deformation than is seen at the toe of the wedge. It also appears likely, however, that in addition to this intense deformation, the sediments in the part of the wedge beneath the sites were initially accreted as a thinner layer and so started their deformation in shorter wavelength structures than are seen at the present toe of the wedge.

East of the sites, a broad slope basin has developed, filled by up to 0.5 s TWT of sediment that may include turbidites, as indicated by small local unconformities and onlap, as well as hemipelagic drape (Fig. 3). The basin is divided into four sub-basins by ridges of deformed accreted sediment. Uplift of the ridges, relative to the sub-basins, to the present time has produced thinned and locally deformed sequences over the ridges between thicker, less deformed sedimentary sequences in the axes of the basins. The onlap of the basin sequences against the western flanks of the ridges indicates clockwise rotation of the ridges, as shown in the view of the section from the southeast. One explanation of this pattern would be that the western flanks of the ridges lie at the tops of westward-dipping listric normal faults, which implies that this upper part of wedge has been undergoing extension. A westward-dipping reflector in the accreted sediments beneath Shotpoint 900 may be interpreted as a fault (Fig. 2). An alternative explanation for this pattern of basin development is that the ridges are brought up along many small thrust faults that lie within them and dip predominantly westward, with some antithetic eastward-dipping faults also present. The sense of rotation of the features would be the same, but overall the basin would be in compression. The part of the basin that lies immediately to the northeast of Site 889 illustrates this situation well (Fig. 3). The southwestern margin of the basin lies at a small eastward-facing scarp of the outcrop of a fault near Shotpoint 640, which appears, from the asymmetry of the deformation of the basin sediments and the uplift of the ridge, to be westward-dipping. The fault plane is not imaged in the seismic section. A single fault, however, would not produce the observed

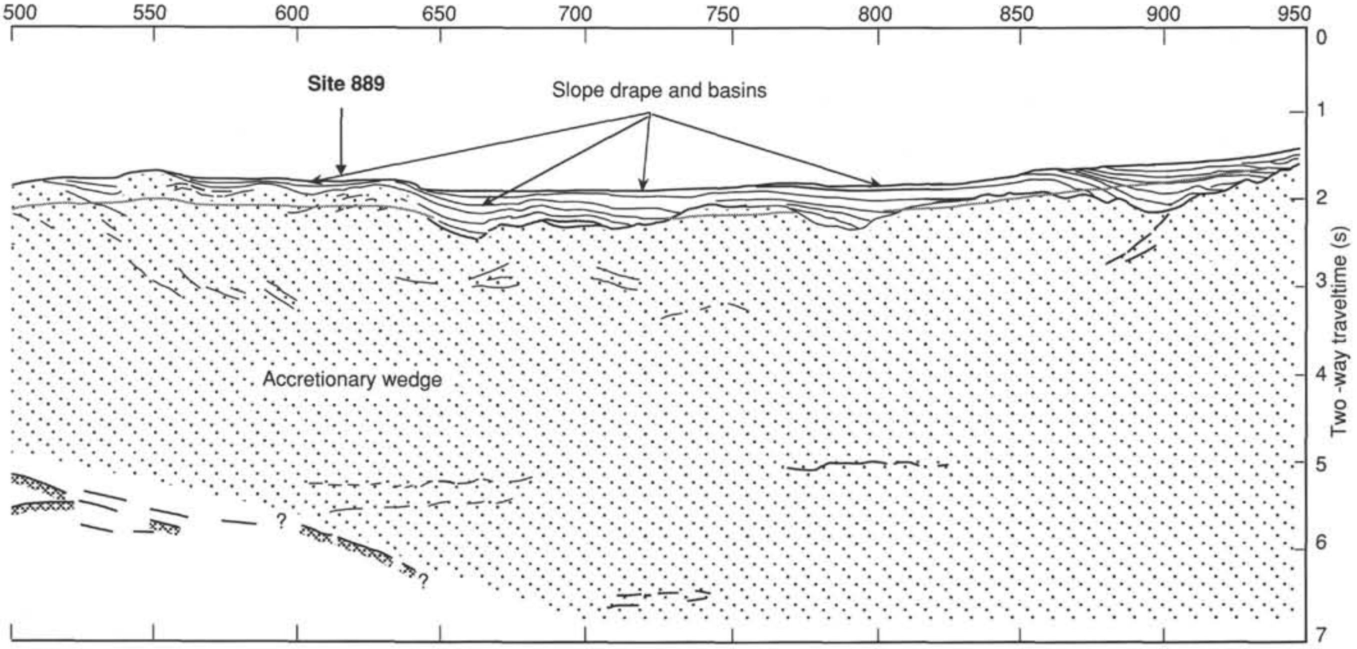

Figure 2 (continued).

pattern of westward thinning of the sediments in the basin. In fact, the reverse would be expected, as the footwall would subside progressively with continued movement on the fault. The movement that has prodced the relative uplift of the southwest margin of the basin must be distributed over a number of small faults.

Running across the section (Figs. 2–3) from Shotpoints 450 to 940, with little interruption, is a BSR that lies at 400 ms TWT beneath the seafloor at Shotpoint 450 and shallows to 200 ms TWT at Shotpoint 940. The reflector has negative polarity.

The detail of the seismic section in the immediate vicinity of Site 889 is displayed in Figure 4, and the position of the holes in relation to the shotpoints of line 89-08 is shown in Figure 5. Care must be taken in the interpretation of the lower and less coherent part of the seismic section (Fig. 4), because noise in the migration of the section has produced "events" that dip at about 30° in both directions across the section and particularly as the line appears to run obliquely to the local strike of structure at this location. The uppermost 100 ms TWT of the section drilled at Site 889 comprises nearly horizontal sedimentary layers that onlap against upwarped, layered strata at about Shotpoint 600 and are themselves upwarped from Shotpoint 620 eastward to crop out at the seafloor. The coherent layered sequence of the upper part of the section is at a maximum time-thickness of about 200 ms TWT near Shotpoint 603. The lower layers onlap against the deformed section beneath, to the northeast, and rise unconformably above a ridge of deformed sediments to the southeast that formed subsequent to their deposition. These lower layers appear to have undergone some local deformation, including the development of a thrust fault near Shotpoint 608. A detailed interpretation of the deformed section would have little meaning, given the problems of distinguishing processing artifacts from primary reflectors, but that said, it can be stated that the section is cut by many faults, some of which cut the overlying cover sequence, as shown in the interpretation of seismic line 89-08 (Fig. 4). The interpretation of the seismic section shows that the area of Site 889 was undergoing deformation throughout the period that the cover sequence was deposited and that there has been local inversion of the topographic relief.

Running across the section at about 2030 ms TWT (275 ms TWT below seafloor, at Site 889) is a prominent BSR with a clearly negative polarity. Although there are local interference effects between the BSR and the crosscutting reflections, there is no evidence that the BSR is offset across any of the faults crossing it, except, perhaps, at the intersection with a fault near Shotpoint 603. This apparent offset is not clear cut and could be explained as the result of interference.

A detailed interpretation of seismic-reflection section 89-08 in relation to the results of logging and a vertical seismic profile (VSP) is given in the "Downhole Logging" section of this chapter.

OPERATIONS

Site 889

Site 889 (prospectus Site VI-5) is located about 33 nmi north northwest of Site 888. Only 3.75 hr were required for the short transit. An additional 0.75 hr was spent lowering the thrusters and hydrophones, and a positioning beacon was dropped to commence operations at 1730 hr Universal Time Coordinated (UTC) on 5 October 1992.

Because the drill site is less than 10 nmi from the center of an old munitions dumping ground, where mustard gas canisters had been disposed following World War II, certain safety precautions were required by the Canadian government. They included a requirement to conduct a video survey in the drilling area to ascertain that the seafloor was clear of hazardous objects and a prohibition on coring the uppermost 20 mbsf. No manufactured objects were detected during the video survey.

Before spudding the first hole, a jet-in test was performed to determine the depth to which 16-in. conductor casing could be set for the planned reentry cone installation.

Hole 889A

The seafloor tag at 1311 mbsl was confirmed by observation with the camera. An advanced piston corer/extended core barrel (APC/XCB) bottom-hole assembly (BHA) was spudded at 0805 UTC, 6 October, and the bit washed down to 20 mbsf as required. Coring with the APC then began (Table 1): no evidence of mustard gas was seen in the recovered cores.

The Tensor and Eastman-Whipstock multishot tools were run to orient the APC cores. The ADARA temperature shoes were run on Cores 146-889A-1H, -3H, -5H, -7H, -9H, and -13H. A water-sampler temperature probe (WSTP) run was made at 104 mbsf after Core 146-889A-9H. Hydrocarbon-gas expansion caused the disruption of all

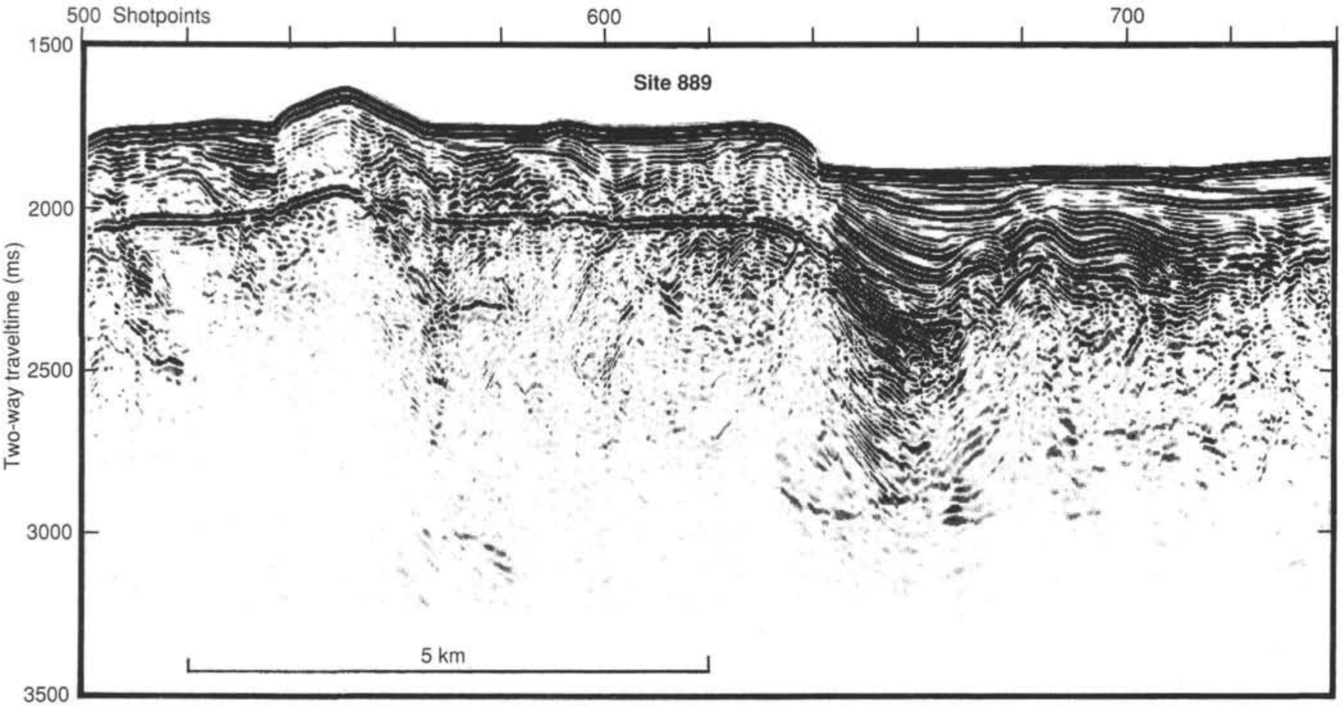

Figure 3. Part of a migrated time section from seismic line 89-08, between shotpoints 500 and 740, showing well-developed slope basins in the eastern part of the section and the location of Site 889 in a small slope basin on an upraised part of the accretionary wedge. A prominent BSR is present below Site 889 at 275 ms TWT below the seafloor.

cores. Plastic liners failed on three cores. Incomplete stroke of the APC began with Core 146-889A-6H and coring proceeded by the advance-by-recovery method through Core 146-889A-16H at 129 mbsf, where penetration had decreased to nil. A pressure core sampler (PCS) core at 128 mbsf recovered sediment and gas at hydrostatic pressure.

Continuous XCB coring proceeded below 129 mbsf, with additional WSTP deployments at 140 and 168 mbsf. Five additional PCS runs were made over the interval to 266 mbsf. Two runs recovered water under pressure, but no sediment was captured.

Hole conditions were good until the bit passed 300 mbsf, and they deteriorated quickly beyond that depth. After recovery of Core 146-889A-44X, hole fill had increased to 14 m and serious trouble with the hole was imminent. Coring was therefore terminated at 345.8 mbsf. Despite sweeping the hole with extra-high-viscosity mud and two wiper trips, 50 m of fill accumulated in the hole.

The bit was pulled to logging depth at 73 mbsf. The logging program consisted of runs of the geophysical and Formation MicroScanner (FMS) tool strings beginning at 260 and 255 mbsf, respectively. Log quality was adversely affected by the washed-out and irregular borehole walls.

Upon completion of the logging operations, the hole was displaced with drilling mud and plugged with cement.

Site 890

To core the upper 20 m of the sequence and to provide samples for a microbiological study, the ship was repositioned to drill an additional site outside of the 10-nmi safety radius around the munitions dumping site. The drill ship was moved in dynamic positioning (DP) mode. A beacon was launched to commence operations at Site 890 at 1900 UTC, 9 October.

Hole 890A

An APC core found the mud line at about 1326 mbsl, but failure of the core liner left the core in poor condition, with some core apparently lost and other portions disturbed in the process of removal from the core barrel. A second, less disturbed, core of the interval was requested, so the bit was repositioned to 1324 mbsl for a respud.

Hole 890B

On the second attempt, an undisturbed seafloor core was recovered and the seafloor depth was established at 1326.3 mbsl. Four more APC cores were taken, with ADARA temperature shoes on Cores 146-890B-2H and -4H. A liner failure resulted in no recovery in Core 146-890B-4H. Following the retrieval of this core, the first deployment of the lateral stress tool (LAST-II) was made. The tool appeared to function as designed. Because of the failure of Core 146-889B-4H, an additional core was requested to complete the overlap in section with Site 889. The APC was fitted with the ADARA shoe, the 2.5 m of hole disturbed by the LAST probe was drilled out, and Core 146-890B-5H was taken from 38.3 to 47.8 mbsf.

The drill string then was recovered, ending Site 890, and the two positioning beacons were recalled.

Return to Site 889

During the pipe trip for a rotary core barrel (RCB) BHA, the vessel was offset in DP mode to the proposed location of Hole 889B and a new positioning beacon was placed. A video survey for manufactured objects was again conducted, and again was negative. Seafloor depth was determined to be 1316.1 mbsl by using the TV to observe bit contact.

Hole 889B

The hole was drilled without difficulty to 197 mbsf, where a mud sweep was circulated and the "wash barrel" was retrieved. The WSTP was run to record sediment temperature before coring began. Core 146-889B-1R had no recovery, which was initially attributed to an excessive circulation rate during the coring operation. The next core barrel contained only a small carbonate concretion in the core catcher. The

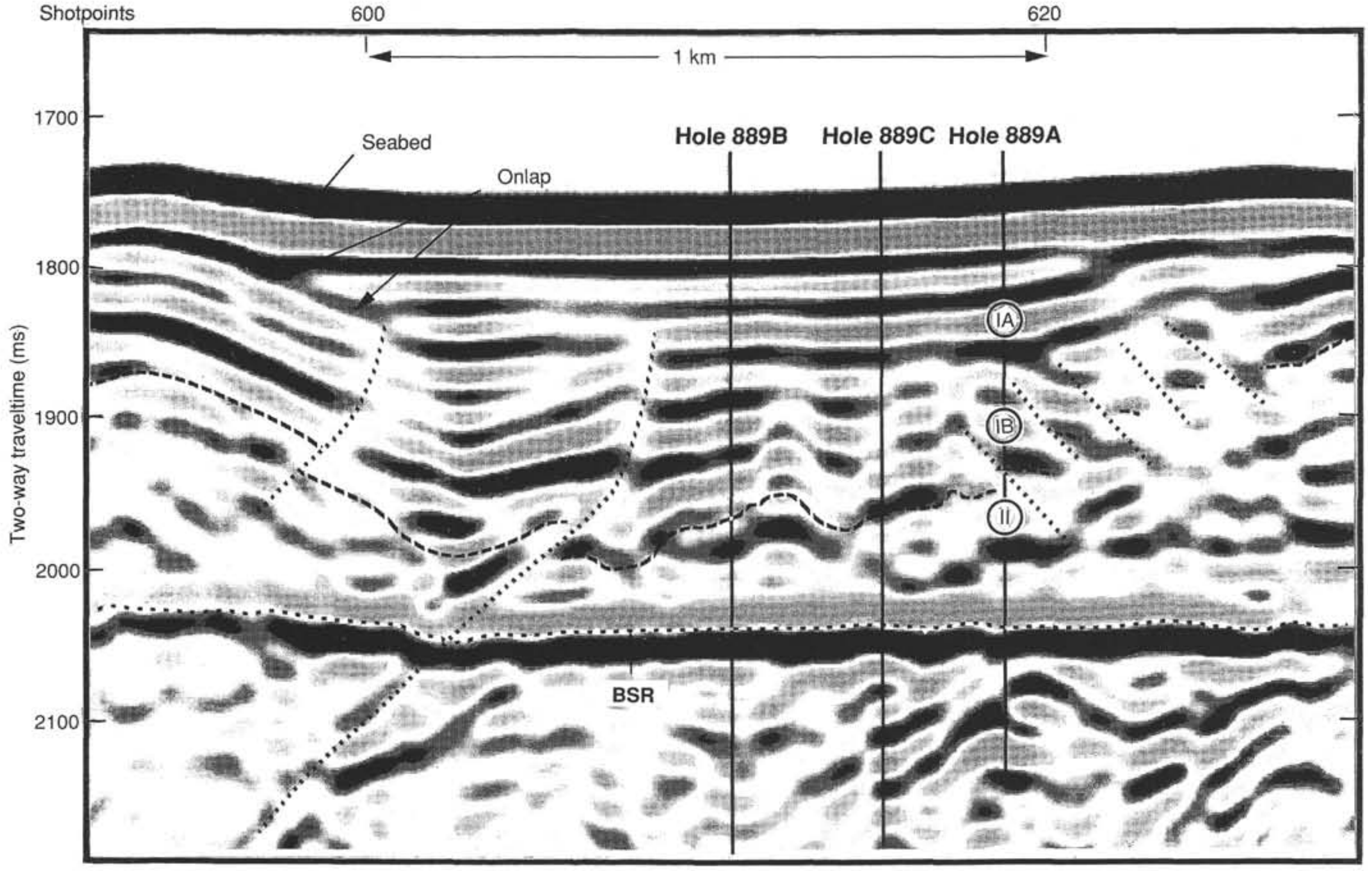

Figure 4. Detail of migrated time section from seismic line 89-08, in the immediate vicinity of Site 889. The polarity conventions are as follows: black is positive, gray is negative, and white is low amplitude. Layered sediments of up to 200 ms time-thickness fill a small slope basin above deformed accreted sediment. A prominent BSR of negative polarity crosses the section at about 275 ms TWT below the seabed. Subunits IA and IB and Unit II are indicated.

bit deplugger was pumped to the bit and then recovered before coring continued. Core 146-889B-3R recovered 2.3 m of sediment; however, 4 m of fill had accumulated when the pipe connection was made.

Inadequate hole cleaning persisted, with 1–6 m of fill despite mud sweeps of various volumes on every core. A WSTP run after Core 146-889B-5H was unsuccessful because the fill could not be cleaned completely from the hole. Carbonate concretions interfered with core recovery. Below about 330 mbsf, core recovery decreased and hole conditions began to deteriorate progressively. Torque and circulating pressure began to build during Cores 146-889B-20R and -21R and did not respond to mud sweeps. When 14 m of fill accumulated during the retrieval of Core 146-889B-21R, coring operations were terminated at 386.5 mbsf.

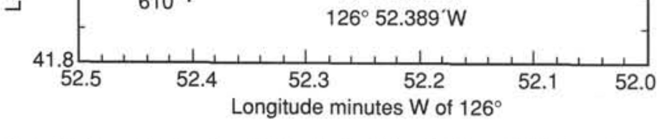

Figure 5. Map of the location of Holes 889A, 889B, 889C, and 889D, in relation to the shotpoints of seismic line 89-08.

To prepare the hole for logging, a 30-bbl sweep of extra-high-viscosity prehydrated bentonite mud was circulated and a wiper trip was made to 71 mbsf. When the bit was run back, fill was found at 305 mbsf. After 3.5 hr and three mud sweeps, the hole had been cleaned only to 338.5 mbsf. The mechanical bit release (MBR) was actuated by wireline to release the bit at 331 mbsf. The pipe was then pulled to 89 mbsf for logging.

The first logging attempt with the geophysical tool string could not pass an obstruction at 238 mbsf. A log was recorded up to 61 mbsf by raising the drill string one stand in the derrick. An attempt was made to clean the hole deeper with the drill string in case the obstruction was only a bridge, but the open-ended BHA was stopped by "tight hole" at 297 mbsf. In order to log across the BSR the side-entry sub (SES) was rigged, and a geophysical log was obtained from 259 mbsf. With the hole opened by the recent passage of the pipe, an FMS log was recorded from 251 mbsf without assistance from the drill string.

The second phase of the logging program was a vertical seismic profile (VSP) using the Schlumberger well seismic tool (WST). The SES was used to place the WST at 243 mbsf and the pipe was pulled up the hole to 107 mbsf (to minimize noise). The VSP was conducted with a 300-in.^{3} air gun and a 400-in.^{3} water gun as separate sources and an additional hydrophone at 200 mbsl to monitor the source signature. Winds of up to 40 kt had produced 5-m seas, a highly unfavorable environment for a seismic survey. The operation was interrupted twice, and was complicated by handling problems when the

Table 1. Coring summary, Sites 889 and 890.

Core no.	Date (1992)	Time (UTC)	Depth (mbsf)	Cored (m)	Recovered (m)	Recovery (%)
146-889A-						
1H	Oct. 6	0920	20.0–29.5	9.5	10.16	106.9
2H	Oct. 6	1010	29.5–39.0	9.5	10.36	109.0
3H	Oct. 6	1100	39.0–48.5	9.5	11.00	115.8
4H	Oct. 6	1140	48.5–58.0	9.5	10.91	114.8
5H	Oct. 6	1235	58.0–67.5	9.5	10.23	107.7
6H	Oct. 6	1310	67.5–77.0	9.5	10.85	114.2
7H	Oct. 6	1415	77.0–86.5	9.5	9.42	99.1
8H	Oct. 6	1500	86.5–94.5	8.0	8.05	100.0
9H	Oct. 6	1630	94.5–104.0	9.5	10.28	108.2
10H	Oct. 6	1835	104.0–113.5	9.5	10.06	105.9
11H	Oct. 6	1930	113.5–119.0	5.5	5.29	96.2
12H	Oct. 6	2015	119.0–127.0	8.0	8.49	106.0
13H	Oct. 6	2115	127.0–128.0	1.0	0.57	57.0
14H	Oct. 6	2150	128.0–129.0	1.0	1.22	122.0
15P	Oct. 6	2310	129.0–130.0	1.0	0.45	45.0
16H	Oct. 6	2345	130.0–130.1	0.1	0.03	30.0
17X	Oct. 7	0050	130.1–139.6	9.5	1.89	19.9
18X	Oct. 7	0350	139.6–149.1	9.5	7.67	80.7
19X	Oct. 7	0525	149.1–158.6	9.5	6.16	64.8
20X	Oct. 7	0715	158.6–168.0	9.4	7.37	78.4
21X	Oct. 7	0930	168.0–177.5	9.5	0.00	0.0
22X	Oct. 7	1025	177.5–186.8	9.3	8.62	92.7
23P	Oct. 7	1115	186.8–187.8	1.0	0.00	0.0
24X	Oct. 7	1215	187.8–197.3	9.5	9.93	104.0
25X	Oct. 7	1415	197.3–206.8	9.5	3.42	36.0
26X	Oct. 7	1515	206.8–216.3	9.5	8.58	90.3
27P	Oct. 7	1600	216.3–217.3	1.0	0.00	0.0
28X	Oct. 7	1700	217.3–226.8	9.5	6.81	71.7
29P	Oct. 7	1755	226.8–227.8	1.0	0.00	0.0
30X	Oct. 7	1855	227.8–237.2	9.4	7.26	77.2
31X	Oct. 7	1945	237.2–246.7	9.5	9.58	101.0
32X	Oct. 7	2100	246.7–256.2	9.5	4.13	43.5
33P	Oct. 7	2145	256.2–257.2	1.0	0.00	0.0
34X	Oct. 7	2300	257.2–265.7	8.5	4.46	52.5
35P	Oct. 8	0015	265.7–266.7	1.0	0.00	0.0
36X	Oct. 8	0145	266.7–275.2	8.5	1.39	16.3
37X	Oct. 8	0320	275.2–284.1	8.9	0.20	2.3
38X	Oct. 8	0505	284.1–292.8	8.7	0.07	0.8
39X	Oct. 8	0720	292.8–301.5	8.7	1.15	13.2
40X	Oct. 8	0915	301.5–310.5	9.0	7.18	79.8
41X	Oct. 8	1140	310.5–319.5	9.0	5.85	65.0
42X	Oct. 8	1400	319.5–328.4	8.9	0.74	8.3
43X	Oct. 8	1555	328.4–337.2	8.8	1.79	20.3
44X	Oct. 8	1725	337.2–345.8	8.6	1.52	17.7
Coring totals				325.8	223.14	68.50
146-889B-						
1R	Oct. 11	0455	197.0–206.4	9.4	0.00	0.0
2R	Oct. 11	0620	206.4–215.9	9.5	0.05	0.5
3R	Oct. 11	0825	215.9–225.3	9.4	2.27	24.1
4R	Oct. 11	0930	225.3–234.8	9.5	2.87	30.2
5R	Oct. 11	1050	234.8–244.3	9.5	0.42	4.4
6R	Oct. 11	1320	244.3–253.9	9.6	3.87	40.3
7R	Oct. 11	1440	253.9–262.7	8.8	6.63	75.3
8R	Oct. 11	1555	262.7–271.6	8.9	6.76	75.9
9R	Oct. 11	1650	271.6–280.4	8.8	2.27	25.8
10R	Oct. 11	1750	280.4–289.3	8.9	3.97	44.6
11R	Oct. 11	1850	289.3–298.2	8.9	0.00	0.0
12R	Oct. 11	2020	298.2–307.1	8.9	6.02	67.6
13R	Oct. 11	2155	307.1–315.8	8.7	4.46	51.2
14R	Oct. 11	2325	315.8–324.6	8.8	2.03	23.0
15R	Oct. 12	0045	324.6–333.3	8.7	2.31	26.5
16R	Oct. 12	0205	333.3–342.1	8.8	0.03	0.3
17R	Oct. 12	0345	342.1–351.0	8.9	1.61	18.1
18R	Oct. 12	0525	351.0–359.9	8.9	1.04	11.7
19R	Oct. 12	0700	359.9–368.7	8.8	0.30	3.4
20R	Oct. 12	0840	368.7–377.6	8.9	0.21	2.4
21R	Oct. 12	1145	377.6–386.5	8.9	0.95	10.7
Coring totals				189.5	48.07	25.4
146-889D-						
1H	Oct. 18	0110	80.0–89.5	9.5	9.73	102.0
2W	Oct. 18	0700	105.0–140.0	35.0	9.57	(wash core)
3X	Oct. 18	1015	140.0–149.5	9.5	1.16	12.2
4N	Oct. 18	1155	149.5–154.0	4.5	2.40	53.3
Coring totals				23.5	13.29	56.6
Washing totals				35.0	9.57	
Combined totals				58.5	22.86	
146-890A-						
1H	Oct. 9	2245	0.0–5.3	5.3	3.71	70.0
Coring totals				5.3	3.71	70.0
146-890B-						
1H	Oct. 9	2330	0.0–7.3	7.3	7.30	100.0
2H	Oct. 10	0035	7.3–16.8	9.5	10.16	106.9
3H	Oct. 10	0110	16.8–26.3	9.5	9.78	103.0
4H	Oct. 10	0235	26.3–35.8	9.5	0.00	0.0
5H	Oct. 10	0520	38.3–47.8	9.5	10.52	110.7
Coring totals				45.3	37.76	83.4

Table 1 (continued).

guns had to be recovered in bad weather conditions for repairs to a broken hose and a flooded solenoid valve in the water gun.

Upon completion of the VSP the hole was filled with mud and plugged with cement. The drill string then was tripped for emplacement of the reentry cone at Hole 889C.

Hole 889C

Hole 889C was spudded at 1315 mbsl at 0800 UTC on 15 October. Four joints of 16-in. conductor casing hanging from a reentry cone were jetted-in with some difficulty through sticky clays, placing the casing shoe at 51 mbsf.

A 14¾-in. hole then was drilled to 300 mbsf with mud sweeps at 150, 200, 250, and 300 mbsf. No drilling problems occurred and the hole seemed absolutely clean at total depth (TD). The hole was swept with 50 bbl of prehydrated bentonite mud before the pipe was tripped for the surface casing string. An 11¾-in. casing string was made up, reentered, and run in to 259 mbsf. The surface string was then cemented into place.

Hole 889D

About 36 hr was required for the cement to cure before the shoe could be drilled out at Hole 889C. The time was used by drilling a dedicated hole for downhole measurements, including the ADARA temperature shoe and the LAST-II and geoprops instruments. Hole 889D was spudded at 2130 UTC on 17 October close to Hole 889A, and was drilled to 80 mbsf for the first planned APC core. However, upon recovery of the core barrel, the shearpins were found to have failed prematurely before the APC was landed, so no core was recovered. No temperature data were collected owing to an instrument failure. After a second drilled interval to 105 mbsf, another APC attempt was made. This was also unsuccessful, because of the failure of the APC seals to seat correctly. The ADARA shoe functioned normally, but no data of value were collected because no sediment penetration occurred.

The bit was drilled ahead to 140 mbsf. The LAST-II was then deployed and pressure data were recovered (though the probe was slightly bent). After an XCB core to 149.5 mbsf and two mud sweeps, the motor-driven core barrel (MDCB) was used to cut a core and provide a 4.5-m "rathole" for the geoprops probe. Unfortunately, the probe entered the hole only by about 1 m (apparently because of hole fill) and the packer elements were not inflated. Temperature measurement and other tool functions were tested, however.

During the LAST II and Geoprops tests in Hole 889D, the weather and vessel-motion conditions deteriorated. A wind gust of 68 kt was recorded while the hole was being filled with mud. The weather improved through the morning as the pipe trip was made and the vessel was offset back to Hole 889C.

Return to Hole 889C

Hole 889C was reentered with a drilling BHA and tri-cone bit, and the cement plug and shoe drilled out. Drilling continued to a TD of

384.5 mbsf. An assembly of four joints of perforated and two joints of unperforated 5-in. line pipe was made up and run in the hole. The perforated casing extends from 270 to 322.5 mbsf. Weather conditions were again deteriorating with wind gusts to 50 kt with heavy seas at right angles to a 5.5-m swell. We lost 7 hr waiting on weather (WOW).

Under improved weather conditions, the BHA was made up with the TAM straddle packer with two elements installed, reentered, and run to 203 mbsf. When the go-devil landed, the pump was stopped at about 300-psi internal pipe pressure. The pressure was noted to bleed off fairly rapidly, and this loss of pressure recurred after each of several attempts to inflate the packer elements. Efforts to inflate the packer were abandoned and the drill string was recovered. The uppermost drill collar was found to have a major sublongitudinal crack that appeared to be the origin of the loss of pressure.

The BHA then was reconfigured for deployment of the instrumented borehole seal (CORK). Three 7-in. drill collars were used as a "stinger" below the CORK. Above the CORK were a 3-ft-long drill-collar pup joint (for handling) and two stands of drill collars. Reentry was routine. The thermistor string was run into the pipe with Teflon sampling tubing attached to the sensor string. The sensor string began to "hang up" as the data logger passed through the BHA. The sensor string was retrieved to the rig floor, and the Teflon sampling tube was found to be broken off at its connection to the data logger. The Kevlar coating of the thermistor string was severely abraded. An electrical check showed that continuity had been lost to two of the 10 thermistors. The damaged upper 15 m of the sampling tube was cut out and a new section was spliced in.

A second attempt to land the sensor string was then made, but the data logger again came to a stop inside the BHA. Obstruction of the 5-in. liner was suspected. The entire sensor string was recovered and the sampling tube was cut off. Sinker bars lowered to sound the hole met resistance at 253 mbsf—10 m into the 5-in. liner and 6 m above the 11¾-in. casing shoe. Traces of sediment were found on the sinker bars. It appears that the liner had filled with sediment that flowed in through the perforations or it had failed near the casing shoe during the rough-weather setting operation. Evidence supporting the former possibility was the observation of cloudy water in the reentry cone during reentries with the liner and with the packer BHA, but clear water before the casing shoe had been drilled out and for the CORK reentry.

In deteriorating weather, the sensor string (shortened to 240 m) was run back into the pipe without the fluid-sampling tube. On the third attempt, it was landed successfully, latched down, and released by shearing the overshot pin. The coring line was retrieved as wind gusts peaked at 46 kt. The CORK was then set by landing it in the 11¾-in. casing hanger; the latch-in was tested with 35,000-lb overpull (Fig. 6).

Before the running tool was unjayed from the CORK, the remotely operated vehicle (ROV) landing platform was assembled around the drill pipe and dropped to the top of the reentry cone. The drill string and beacons were recovered, and *JOIDES Resolution* departed Site 889 at 1815 UTC, 22 October, in moderating weather.

LITHOSTRATIGRAPHY

Lithostratigraphy at Site 889

At Site 889, cores were recovered from Holes 889A, 889B, and 889D. In Hole 889A coring began at 20 mbsf and continued to 345.8 mbsf (APC and XCB). At Hole 889B, coring began at 197 mbsf and continued to 386.5 mbsf (RCB). At Hole 889D, only four cores were taken, the deepest of which (Core 146-889D-4N, 149.5–154.0 mbsf) was collected with the motor-driven core barrel (MDCB). The recovery was highly variable and apparently did not depend on the coring method. Drilling disturbance was strongest in the XCB and RCB cores.

On the basis of visual core descriptions, analyses of smear slides and thin sections, X-ray diffractometry (XRD), and grain-size analyses, three lithostratigraphic units were distinguished (see Fig. 104).

Lithostratigraphic Unit I is divided into two subunits. Subunit IA (0–91.5 mbsf) consists of clayey silt to silty clay interbedded with silt and fine sand layers of turbiditic origin. Sediments show variable dark gray colors and subhorizontal bedding. Grain size decreases downhole, and Subunit IB (91.5–128.0 mbsf) is dominated by silty clay with rare millimeter-thick silt horizons. Sedimentary structures (e.g., homogenization of sediment) indicate reworking of the material in Subunit IB above Core 146-889A-11H (113.5 mbsf), and in the lower part of the subunit tilted sedimentary beds with steep inclinations (from 45° to 72°) occur. All cores in Unit I show horizontal fractures, which are characteristic of gas expansion upon recovery.

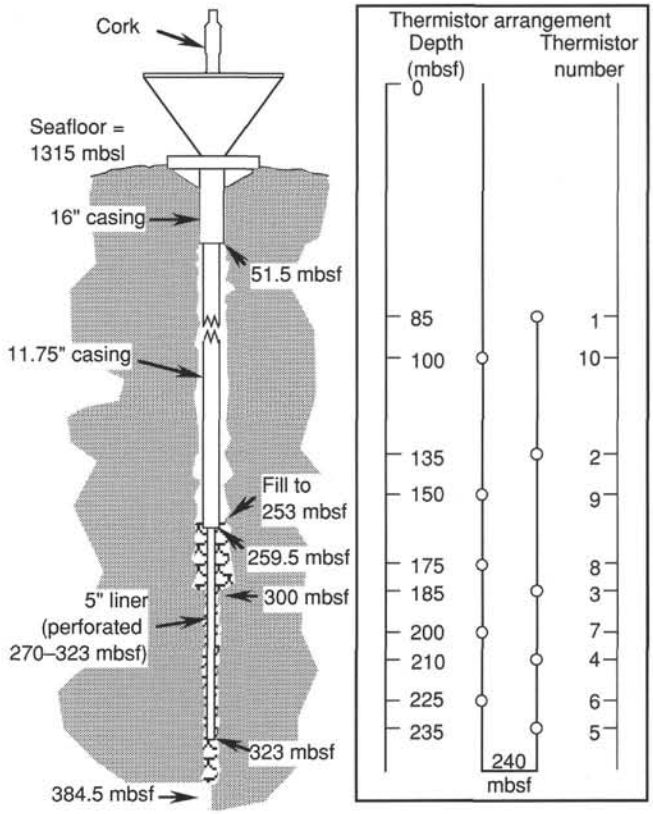

Figure 6. Schematic illustration of borehole seal deployment at Hole 889C.

The boundary between Unit I and Unit II is placed at 128 mbsf and corresponds to increasing lithification of the sediment, which induces a more brittle response to drilling disturbance. Unit II comprises mainly firm, graded silt of a very dark gray color. Indurated sediments are fractured into subangular pieces supported by a drilling-produced clayey, firm to soupy matrix. Carbonate concretions of dolomitic composition are present.

At 301 mbsf in Hole 889A and at 307 mbsf in Hole 889B, the lower boundary of Unit II is indicated by a sharp increase in the amount of glaucony. Unit III consists of firm clayey silt with significant amounts of glaucony. Because of the deformation of the weakly lithified clayey silt, the Unit III deposits are fractured into subangular fragments (see "Structural Geology" section, this chapter).

Lithostratigraphic Units

Unit I

Intervals: Hole 889A, Cores 146-889A-1H to -13H; Hole 889D, Cores 146-889D-1H to -2W
Depth: Hole 889A, 0–128.0 mbsf; Hole 889D, 80.0–140.0 mbsf
Age: early Pleistocene to Holocene

The sediments recovered in lithostratigraphic Unit I were divided into two subunits according to their grain-size distribution and their sedimentary structures. However, the most marked lithologic change is a downhole decrease in the incidence and the thickness of sand layers. Compared with Subunit IB, the sediments of Subunit IA show a higher abundance of sand, both in the frequency of the layers and in their thickness. Below Unit I (128.0 mbsf), sand occurs as sporadic beds of millimeter thickness.

All cores from Unit I are heavily disturbed by horizontal to subhorizontal fractures produced by gas expansion.

Subunit IA

Intervals: Hole 889A, Core 146-889A-1H to Section 146-889A-8H-4, 50 cm; Hole 889D, Core 146-889D-1H
Depth: Hole 889A, 0–91.5 mbsf; Hole 889D, 80.0–89.5 mbsf
Age: early Pleistocene to Holocene

Lithostratigraphic Subunit IA consists of silty clay and clayey silt interbedded with very fine sand layers (<1 to 8 cm thick). Both lithologies are very dark gray to dark olive gray, or dark greenish gray. The silty clay and clayey silt are mostly structureless, but faint parallel lamination was observed in some cases (Sections 146-889A-4H-2, -5H-5 to -7, and -6H-1). Fine sand is interlayered with the finer sediments. Sand abundance decreases downhole (Figs. 7–9). The beds are normally graded, and show sharp bottom contacts, some with basal scours (Section 146-889A-7H-3). The thickness of the sand layers usually is less than 10 cm; sporadic layers in excess of 50 cm are present. The grains are well sorted and dominantly of subrounded shape. Cores 146-889A-7H and -8H (77.0–94.5 mbsf) contain abundant mud clasts and soft pebbles supported by a coarse sandy matrix. The layers containing mud clasts are mottled dark greenish gray and are normally graded (Fig. 10). No other sedimentary structures are preserved in these sediments.

The composition of the siliciclastic silt and sand is described under the subheading "Petrography" in this section. A biogenic fraction (foraminifers, diatoms, sponge spicules, and mollusk shell fragments) of up to 5% was commonly observed. Black sulfide-rich patches or thin layers occur commonly throughout the interval from Cores 146-889A-1H to -6H. Mud clasts are present either as isolated clasts (at Sections 146-889A-3H-2, -5H-1, and -5H-7) or as a sequence displaying an upward decrease in clast frequency (Section 146-889A-4H-2 and Core 146-889D-1H). Shell fragments are scattered through Cores 146-889A-3H, -4H, -7H, and -8H. Wood fragments are dispersed in the sediments of Core 146-889A-1H.

Gas expansion fractures seem to be common only in the silt and sand layers and are particularly frequent at the interfaces between sands and fine sediment.

Subunit IB

Intervals: Hole 889A, Section 146-889A-8H-4, 50 cm, to Core 146-889A-13H; Hole 889D, Core 146-889D-2W
Depth: Hole 889A, 91.5–128.0 mbsf; Hole 889D, 105.0–140.0 mbsf (89.5–105.0 mbsf not cored)
Age: early Pleistocene

Subunit IB is composed of very dark gray to dark olive gray silty clay with rare layers and patches of fine sand. This subunit is distinguished from Subunit IA on the basis of a significant decrease in average grain size and the occurrence of tilted beds, which define a transitional boundary (cf. Figs. 7–9). Porosity (see "Physical Properties" section, this chapter) significantly increases at the top of Subunit IB (Section 146-889A-8H-4, 50 cm; 91.5 mbsf) and fluctuates widely down to Core 146-889A-11H (115 mbsf).

Sands occur rhythmically within Subunit IB, but less commonly than in Subunit IA. Bed thickness varies from 0.5 to 6 cm. Sand layers with sharp basal contacts are common in Sections 146-889A-8H-4 to -9H-CC (Fig. 7). The frequency of the sand layers gradually decreases downhole. This trend is mirrored by a relative decrease in the proportion of the coarse-grained components (e.g., lithic grains and volcanic glass) in the smear slides (Fig. 11). The sediment is partly homogenized (thought to result from both natural deformation and drilling disturbance), but bedding planes and normal gradation still are visible.

Mud clasts are present throughout Subunit IB. In places they are concentrated into poorly defined layers. Characteristic components of these matrix-supported, poorly sorted sediments are subangular pebbles and firm mud clasts (less than 1 cm in diameter), sulfide concretions, and mollusk shell fragments. A single grain-supported layer, consisting of firm clasts (up to 5 cm across) of indurated mud, occurs in Sections 146-889A-11H-3 and -11H-4 (117.5–118.5 mbsf; Fig. 12). Inclined bedding planes with dips between 20° and 65° (Fig. 13) are present (see "Structural Geology" section, this chapter).

Major and minor components of the sediments of Subunit IB are described under the subheading "Petrography" in this section. In several intervals the silts are diatomaceous (e.g., Core 146-889A-12H, where up to 30% diatoms were observed).

It is not possible to correlate precisely the sediment recovered from wash coring in Hole 889D (Core 146-889D-2W) with the lithostratigraphic units defined in the other holes. In an interval of 35 m of sediments, only 9.55 m was recovered. The exact location of the wash-core material within the sediment column is unknown.

Cracks resulting from gas expulsion are present in the cores throughout Subunit IB.

Unit II

Intervals: Hole 889A, Cores 146-889A-14H to -39X; Hole 889B, Cores 146-889B-1R to -12R; Hole 889D, Cores 146-889D-3X to -4N
Depth: Hole 889A, 128.0–301.5 mbsf; Hole 889B, 197.0–307.1 mbsf; Hole 889D, 140.0–154.0 mbsf
Age: late Pliocene to early Pleistocene

Lithostratigraphic Unit II consists of firm clayey silt of dark gray to dark olive gray or dark greenish gray color. The silts contain varying amounts of biogenic components (up to 10%, except for the diatom-rich clayey silt in Core 146-889A-14H). Significant changes in mineralogical composition were not observed (see the subheading "Petrography" in this section) between Units I and II. Unit II differs from Unit I by its lower abundance of sand and the reduced thickness of the sand layers. As a consequence, Unit II is on average more fine grained than Unit I.

The sediments of Unit II are also more indurated: both firmer through compaction and slightly cemented. Cementation is indicated by an increase in the amount of carbonate (mainly dolomite) in the smear slides of Unit II. The change in induration is transitional over several tens of meters (Cores 146-889A-14H to -24X). Indurated clayey silt is systematically fragmented into subangular pieces, 5 to 60 mm in diameter, which are supported by a clayey matrix (Fig. 14).

Sedimentary structures that can be recognized are generally limited to sharp interlayer boundaries in the moderately disturbed sediment (Fig. 15) or to normal grading in fine sand layers (Core 146-889A-18X). Use of the MDCB in Hole 889D (Core 146-889D-4N; 149.5–154.0 mbsf) resulted in better preservation of the original sedimentary fabrics: these were largely destroyed over the same interval in cores recovered from the other holes. In this core clayey silt is interbedded with fine sand of very dark gray color. Layers are normally graded, showing sharp bases and transitional upper contacts. Thickness varies up to 8 cm, and composition is similar to the sands of Unit I (see the subheading "Petrography" in this section). Because of the better sediment preservation in Core 146-889D-4N, turbiditic sand layers and clayey silt with fracture fabric were clearly identified (Fig. 16; see also "Structural Geology" section, this chapter).

The clayey to silty matrix of the indurated sediment of Unit II is either firm or soupy. Several intervals of soupy sediment occur throughout this unit (Fig. 17) varying in thickness from about 5 cm to more than 50 cm (Cores 146-889A-5H, -7H, -21X, -41X, -45X, and 146-889B-1R). In the case of Core 146-889A-47X, all of the recovered sediment was soupy.

Carbonate concretions, largely of dolomitic composition, are common in Unit II, and they are present especially in Hole 889B (Figs. 18–20). Carbonate concretions consist mainly of micritic dolomite, with broken foraminifers, clay minerals, sulfides, and small amounts (less than 1%) of quartz and feldspar. One massive carbonate layer 29 cm thick is observed at Section 146-889B-7R-4, 62–91 cm (258.0–258.3 mbsf). The most lithified material (clayey siltstone) was found at a depth coincident with the highest incidence of carbonate concretions (Core 146-889A-32X), but these sediments display little microscopic evidence of carbonate cement. Below 256 mbsf, the sediment again becomes less indurated and shows characteristic drilling biscuits.

One 60-cm-thick layer, consisting of firm silt clasts and carbonate concretions of gravel size in a soupy clay matrix, is present in Section 146-889A-18X-1. Patches and thin layers of black, sulfide-rich silt were observed in Sections 146-889A-32X-1 and 146-889B-8R-4. Shell fragments are dispersed through the whole unit, but occur most abundantly in Cores 146-889A-20X and -24X and 146-889B-7R and -9R.

Unit III

Intervals: Hole 889A, Cores 146-889A-40X to -44X; Hole 889B, Cores 146-889B-13R to -21R
Depth: Hole 889A, 301.5–345.8 mbsf; Hole 889B, 307.1–386.5 mbsf
Age: late Pliocene

Lithostratigraphic Unit III is distinguished from Unit II on the basis of a significant increase in "glaucony" (cf. Odin and Matter, 1981, and subheadings "Petrography" and "Results of X-ray Diffractrometry" of this section). The marked increase in the amount of glaucony is demonstrated by the sediment composition as determined by smear slide analyses (Figs. 21–24).

No other compositional or structural differences were observed between Units II and III. Firm silty clay to clayey silt of dark gray to dark olive gray color dominates the lithology. Indurated sediments are fragmented into subangular pieces (usually 2–15 mm, rarely up to 5 cm across), supported by a firm to soupy matrix. Shell fragments and semiplastic mud pebbles occur sporadically.

Characteristic features, chiefly observed in Hole 889B, are carbonate concretions. Like those of Unit II, these carbonates were found to be largely of micritic dolomitic composition (Figs. 18–19). They are more concentrated at the top of the unit and at the base of the recovered interval (i.e., Cores 146-889B-14R and -15R and 146-889B-19R, -20R, and -21R).

Petrography

Visual estimates were made of the grain composition of more than one hundred smear slides prepared from representative lithologies of the three units. The full results of this preliminary petrographic analysis are presented in the smear slide description table in the Appendices. In general, there is little variation in the grain composition with depth, averaged on a core-by-core basis. Similarly, apart from an increased incidence of one component (glaucony, as discussed subsequently) in Unit III, the composition of the sediments does not show any marked changes at the postulated unit boundaries. The changes observed between units are, in general, gradual.

Unit I

The petrography of the fine silts and clays of Unit I mirrors the composition of the coarser silts and sands for the most part. The relative abundance of the various detectable minerals is similar. The clays have mostly a brownish or greenish gray body color and show some birefringence. They are rather plastic, show swelling within the core, and may be partly smectitic. There is commonly 1%–2% biogenic silica in the silts and clays, consisting mostly of diatoms, some of which are unusually large (Fig. 25). The main compositional characteristics of Unit I are shown in the sands and coarse silts, which occur abundantly in this interval.

Major Components. Feldspars were largely plagioclase of intermediate composition (determined on the basis of their low to moderate twin-extinction angles), with a little altered potassium feldspar and rare microcline and perthite.

Quartz was largely monocrystalline and unstrained, but this group included some polycrystalline and strained grains. The quartz commonly has inclusions of magnetite, apatite, and rutile, although one variety is characterized by numerous fluid inclusions.

The lithic fragments were largely basic to intermediate volcanic rocks and plutonic igneous rocks, with some chert of various colors. Rarely, micaceous schist occurs. As was commonly found in the clastic sequences, the lithic fragments become progressively more abundant in coarser grain sizes. This has an effect on the distribution of rock fragments in the smear slides with depth (Fig. 11), as the grain size decreases downsection.

Minor Components. The most common variety of the amphiboles is hornblende, which has a distinctive pleochroic scheme from yellowish green to apple green to bluish green. This hornblende, which is subhedral in shape, accounts for more than 90% of the amphiboles, and it forms up to 10% of some sands in Unit I (e.g., Sample 146-889A-4H, 4 cm). A proportion of 2%–5% is typical. Actinolitic varieties, with more subdued pleochroism and a more bladed habit, occur in small amounts, and sodic amphibole (probably glaucophane) occurs as a trace component (e.g., Sample 146-889A-9H-9, 63 cm).

Three varieties of micas could be distinguished, the most common of which is brown biotite, with a subordinate amount of co-occurring green mica and a rare white mica. Together, micas are estimated to comprise up to 12% of some sediments in Sections 146-889A-1H-6 to -7. More commonly, 3%–5% mica occurs in the sands and fine silts of Unit I. The occurrence of the mica-group mineral glauconite is discussed subsequently.

Both orthopyroxene and clinopyroxene are present in sands from Unit I. Pyroxene makes up 10% of Sample 146-889A-1H-6, 75 cm. Usually, pyroxenes are recorded only in trace amounts, in part because the grains are altered and difficult to identify positively.

In the opaque minerals category are included sulfides, magnetite, ilmenite, and manganese minerals, which are thought to be the main opaque phases in the sands of Unit I. About 5% opaque grains is typical of the sands in the unit. From the grain morphology, most of the grains are thought to be pyrite (cubes and framboids), with sporadic, smaller grains of magnetite and ilmenite recognizable.

In the smear slides, it was difficult in all cases to distinguish volcanic glass from the basal sections of micas because of the similarity in color and relief and the coincidence of brown, green, and colorless grain body colors in both constituents. Usually, the distinction could be made on the basis of turbidity and inclusions in the glass or on a more ragged grain shape for the mica. We estimated that volcanic glass usually forms 5%–10% of the sands and coarse silts of Unit I. In Sections 146-889A-1H-6 and -1H-7, three intervals with major proportions of volcanic glass (between 15% and 20%) were found.

For biogenic silica, we found a low, but consistent, incidence of siliceous fossil material in the sands of Unit I, with up to 1% typical. This material consists mostly of diatoms, which are concentrated in the silt fraction, with some sponge spicules and sporadic radiolarian tests. Preservation is good.

Various accessory minerals were found in the sands and coarse silts of Unit I. Epidote and the epidote group minerals zoisite and clinozoisite occur most abundantly (up to 1%) and are ubiquitous. Apatite, garnet (colorless, probably grossularite), zircon, and rutile occur in trace amounts. Few other heavy minerals were found in the unit.

Petrographic Distinction Between Subunits IA and IB. The petrographic changes between the two subunits are subtle. The average

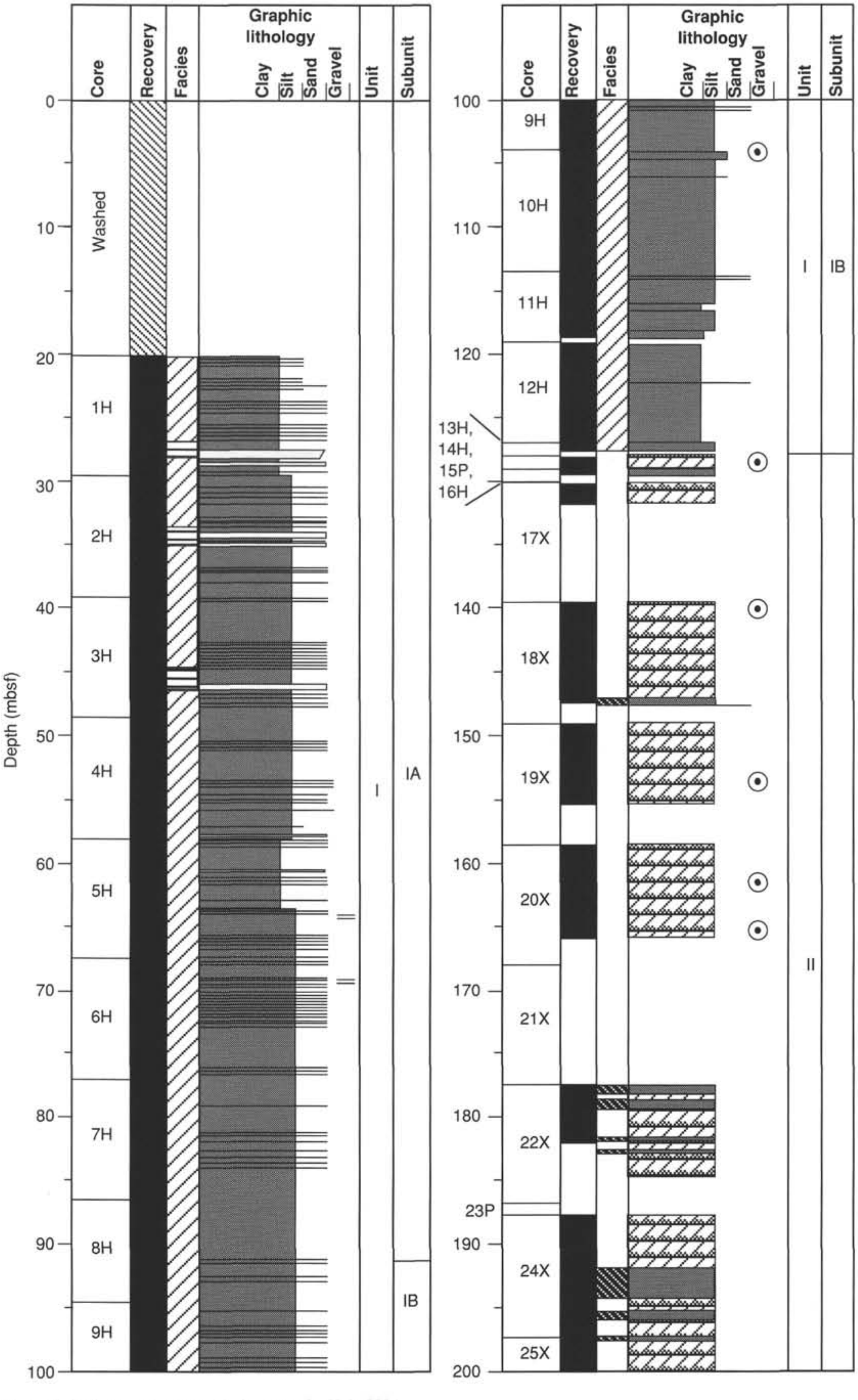

Figure 7. Sediment column and facies types for Hole 889A.

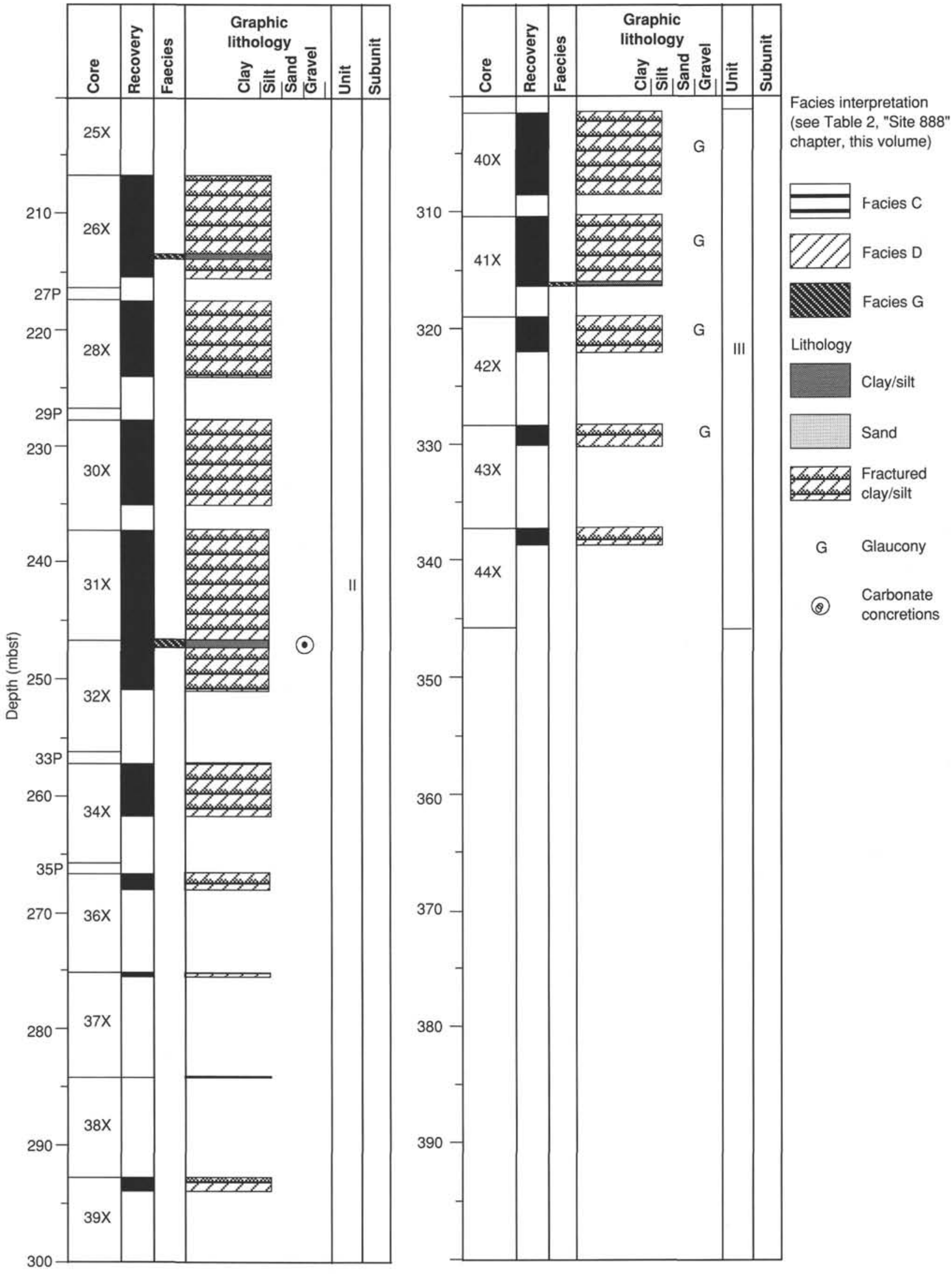

Figure 7 (continued).

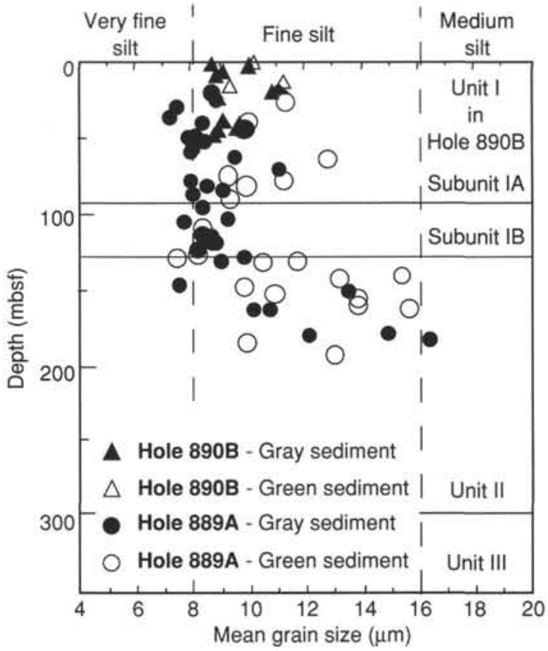

Figure 8. Results of grain-size analyses on fine-grained sediments from Holes 889A and 890B. The results are meaningful only for Unit I. The scattered values of Unit II are caused by incipient lithification of the sediment, which prevented proper dispersion of the grains. Note that green sediments appear to be coarser than gray sediments. This could reflect a different size of the clay minerals (green sediments are richer in smectite; see "Results of X-ray Diffractrometry" discussion in the text).

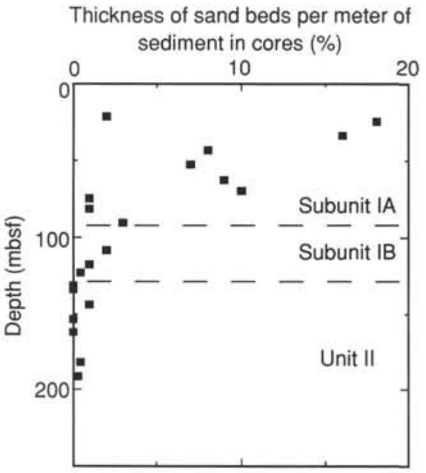

Figure 9. Proportion of sand in sediments vs. depth at Hole 889A, estimated by measurements of layer thickness.

grain size of Subunit IB is lower than that of Subunit IA, which in itself skews the modal composition away from certain components (e.g., lithic fragments; Fig. 11). There is possibly a slight increase in the abundance of feldspar relative to quartz, and a reduction in the amount of mica and hornblende in Subunit IB. More skeletal biogenic silica was observed in Subunit IB, but the most marked change in this component occurs at about 80 mbsf, near the base of Subunit IA.

A number of layers that consist of matrix-supported concentrations of varicolored clay and siltstone clasts are present in Subunit IB.

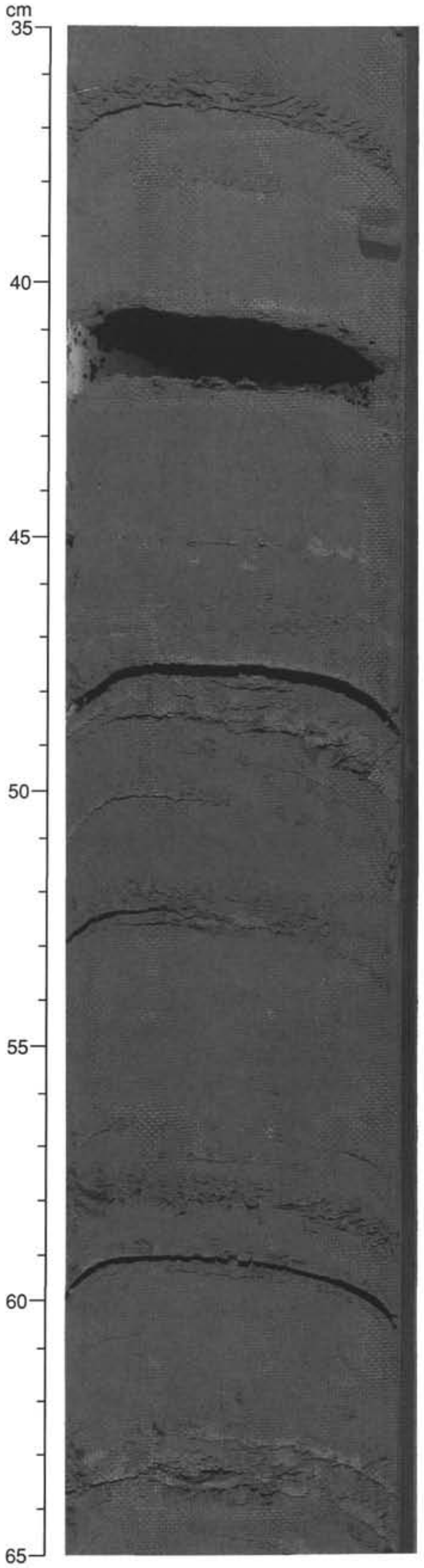

Figure 10. Graded bedding of fine sand layers in clayey silt from Subunit IA (Section 146-889A-6H-2, 35–65 cm).

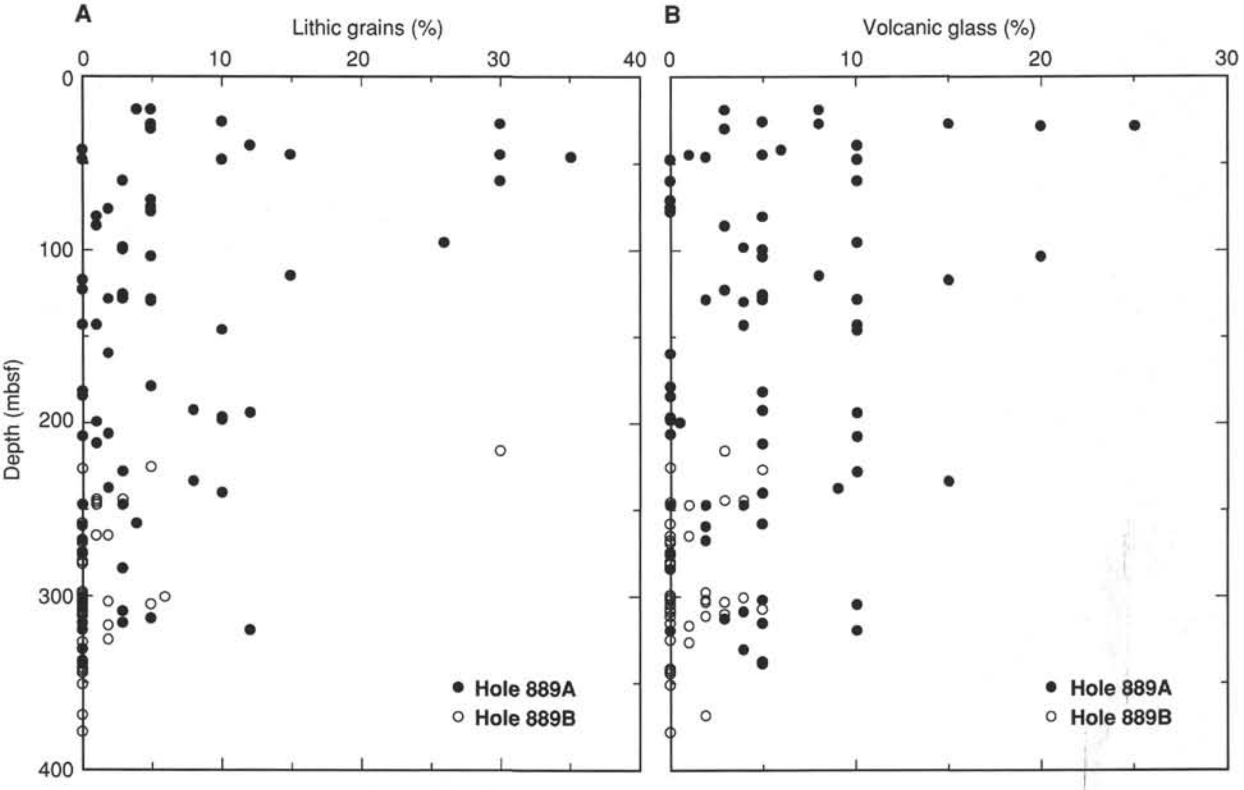

Figure 11. Abundance of (**A**) lithic grains (rock fragments) and (**B**) volcanic glass vs. depth, from smear slide description of Holes 889A and 889B.

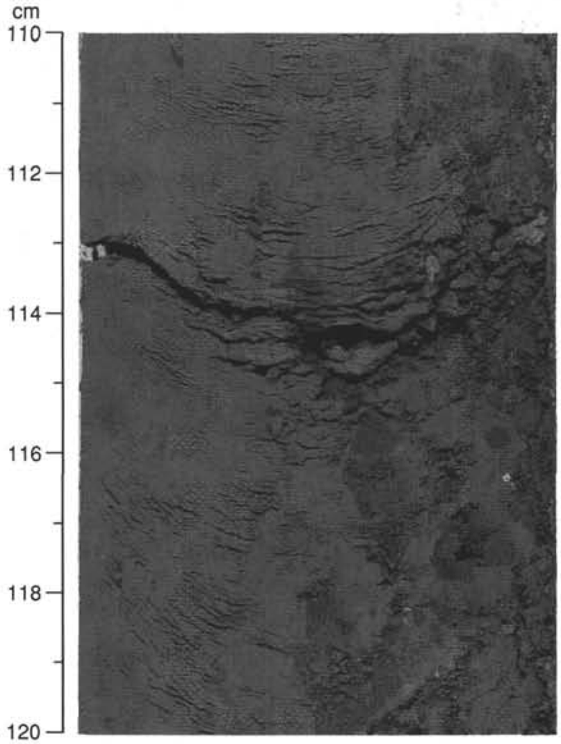

Figure 12. Subrounded mud clast in partly grain-supported deposits (Section 146-889A-11H-3, 110–120 cm).

Although different colors and textures of mud fragments were observed in these layers, they were not found to be petrographically distinct in the smear slides.

Unit II

Unit II is generally more fine grained than Unit I, and this is reflected in the composition of the sediment observed in smear slides. The gradual change from Units I to II is typified by the increase in the number of carbonate concretions recorded. No other compositional differences between Units I and II can be identified on the basis of the petrographic data analyzed to date.

Unit III

The distinction between Units II and III is based primarily on the occurrence of abundant glaucony in the latter. Glaucony is present in quantities between 5 and 55 modal% in Unit III below 300 mbsf. Above this level, in Units I and II, its occurrence is sporadic, typically only in trace amounts, if at all (Fig. 24). The general distribution of "green minerals" at Sites 889 and 890 is discussed subsequently in this section.

Other than this distinct change, the background sedimentation appears to be essentially the same in Units II and III. In the rare sands and coarse silts, the major minerals are the same as in Unit II. Rock fragments and volcanic glass are relatively rare (Fig. 11). It is thought that these changes result from a combination of the grain-size effect (that is a decrease in the amount of rock fragments with a decrease in grain size), changes in provenance, and, possibly, an increase in the diagenetic degradation of both components with depth. Generally, less biogenic silica is present in Unit III than in Unit II. The reduction in metastable forms of silica may represent either a change in the depositional environment or a diagenetic effect, as described subsequently.

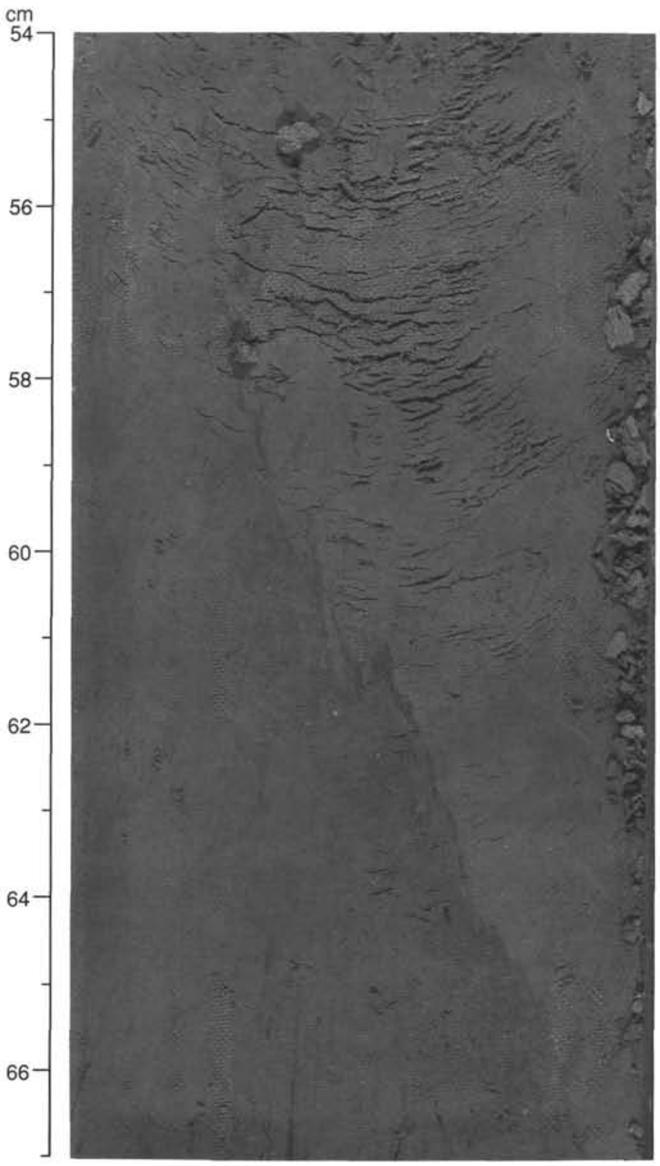

Figure 13. Inclined bed of tilted sediments of Subunit IB (Section 146-889A-11H-1, 54–67 cm).

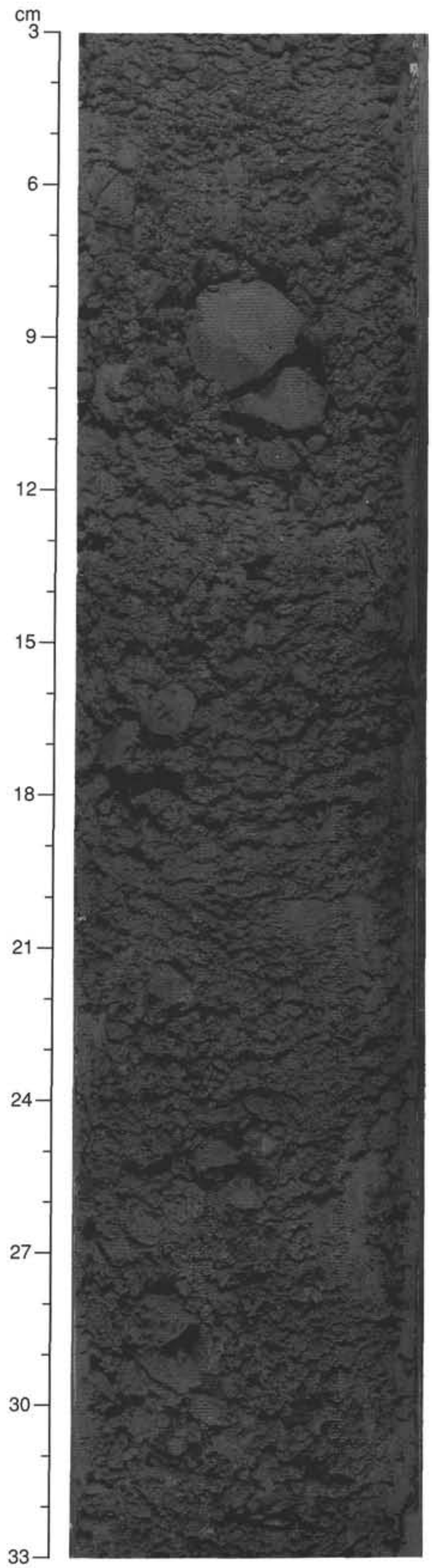

Figure 14. Example of the indurated clayey silt of Unit II, fragmented and brecciated by drilling (Section 146-889A-17X-3, 3–33 cm).

Carbonate grains are more abundant and larger in Unit III than in Unit II, and their frequency of occurrence continues to increase with depth to the base of the cored interval (Fig. 18). Dispersed carbonate is also present in both the fine- and coarser grained sediments of Unit III. Dolomite occurs as small euhedral rhombs and is accompanied by finer grained carbonate, for which the mineral species has not been positively identified. In addition, small quantities of shell debris, and intact and broken foraminiferal tests, are present in many of the smear slides. Together these carbonate components make up to 5% of the sediment, although these visual estimates are probably accurate only to ±2%. Chemical and X-ray determinations are necessary to constrain the amount and mineralogy of the carbonate component more closely.

Lithostratigraphy at Site 890

Site 890 was drilled close to Site 889 so as to obtain additional information on the uppermost sedimentary section and complete the upper part of the sediment column not cored at Site 889 (see Master

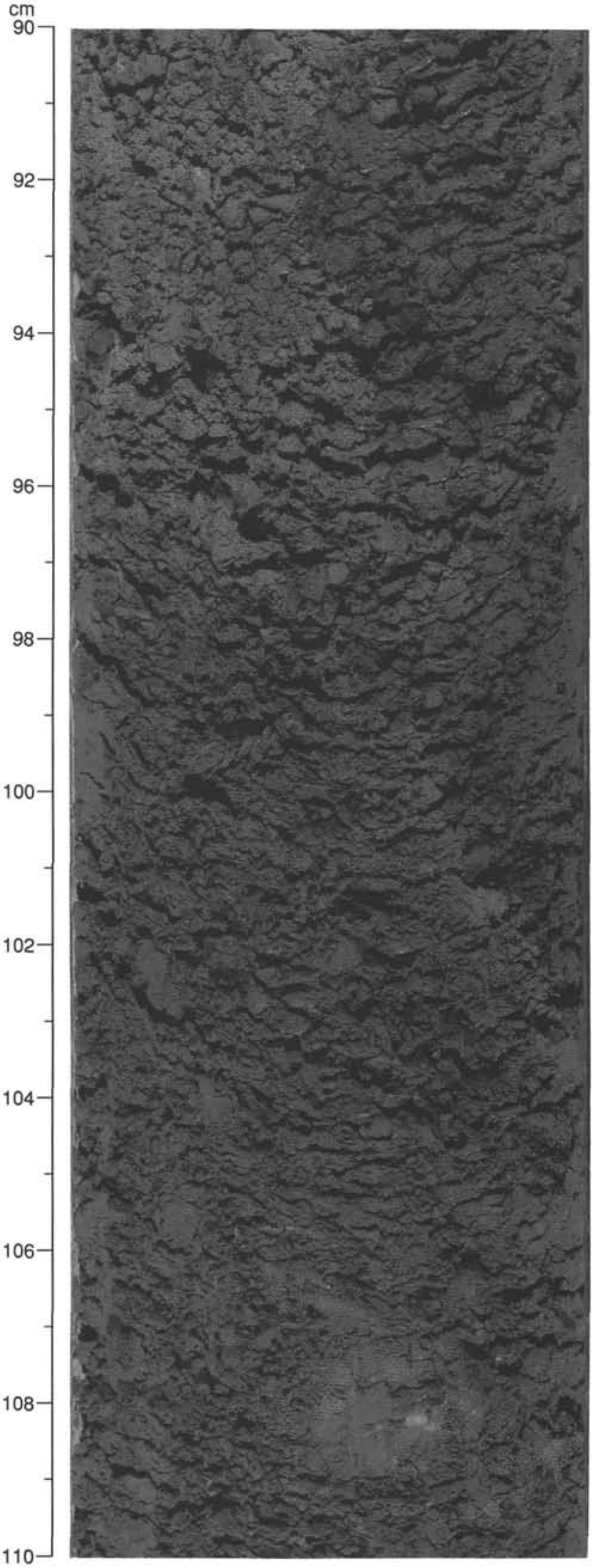

Figure 15. Sharp boundary between dark greenish gray and olive black firm clayey silt of Unit II (Section 146-889A-20X-3, 90–110 cm).

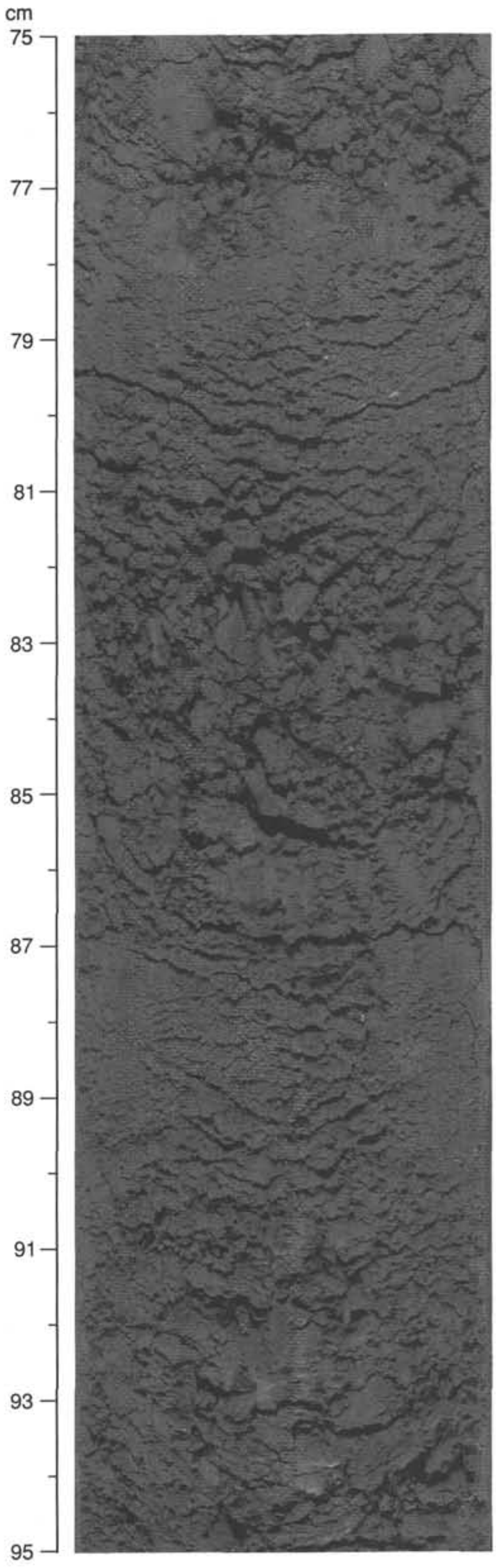

Figure 16. Turbidites interbedded with firm clayey silt of Unit II (Section 146-889D-4N-1, 75–95 cm). Fining upward-gradation can be observed in the turbiditic sands. The scaly fabrics were preserved in the firm clayey silt as a result of the use of the MDCB.

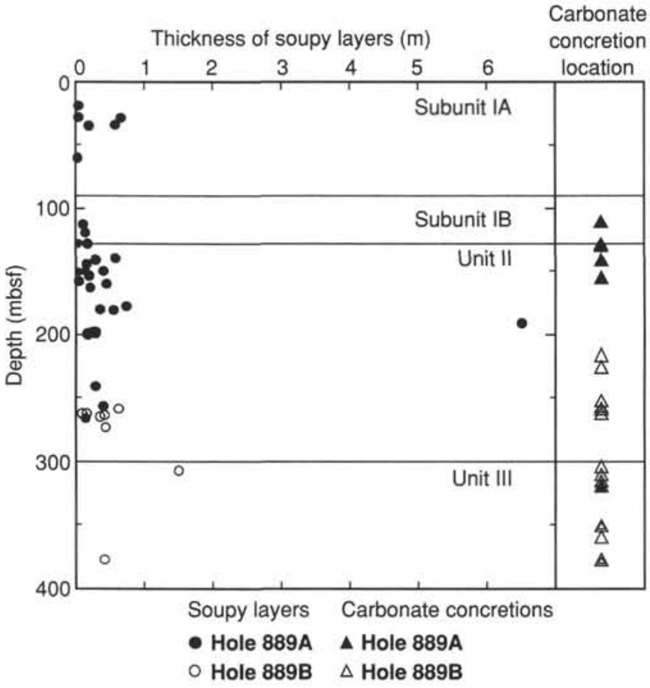

Figure 17. Distribution and thickness of soupy layers (left) and distribution of carbonate concretions (right) vs. depth, based on visual core description in Holes 889A and 889B.

Chart, Fig. 104). The one lithostratigraphic unit identified at Site 890 differs from Subunit IA of Site 889, and consequently is described separately here. Dominant lithologies are clay, silty clay, and clayey silt, with the sporadic occurrence of very fine sand layers in Core 146-890B-5H (Fig. 26). Average grain size coarsens significantly downhole, but the amount of sand never exceeds 10% of the sediment. Sediment identification was based on visual core description, smear slide, and grain-size analysis (see "Explanatory Notes" chapter, this volume). The XRD analyses, although performed on samples of mixed grain size, were taken into consideration.

Lithostratigraphic Units and Petrography

Unit I

Intervals: Hole 890A, Core 146-890A-1H; Hole 890B, Cores 146-880B-1H to -5H
Depth: Hole 890A, 0–5.3 mbsf; Hole 890B, 0–47.8 mbsf
Age: Pleistocene to Holocene

Lithostratigraphic Unit I of Site 890, which includes all cored sediments of both holes at this site, is characterized by an alternation of mainly clay to silty clay or clayey silt. Color varies from dark gray to olive gray and very dark greenish gray. The upper part of both Holes 890A and 890B consists of pure clay with rare millimeter-thick layers of fine silt. Fine parallel lamination (Fig. 27) of interbedded layers of greenish (rich in chlorite and glauconite) or black (disseminated sulfide) color on a millimeter scale is preserved. Slight bioturbation occurs in the upper interval of Hole 890B (Core 146-890B-1H).

Grain size and the abundance of silt and sand beds gradually increase with depth in Cores 146-890B-2H to -5H. Layers are less than 10 mm thick and usually show sharp bottom and gradational upper boundaries. No preserved sedimentary structures can be identified except for an upward fining of grain size in each thin layer of silt or fine sand.

Sands consist mainly of angular to subrounded quartz, feldspar (plagioclase of albitic to intermediate composition), lithic fragments (largely basaltic volcanics), amphibole, and opaque minerals (sulfide/pyrite, ilmenite, and manganese minerals). Minor components are orthopyroxene, clinopyroxene, volcanic glass, biogenic silica, and accessory minerals (apatite, epidote, garnet, and zircon).

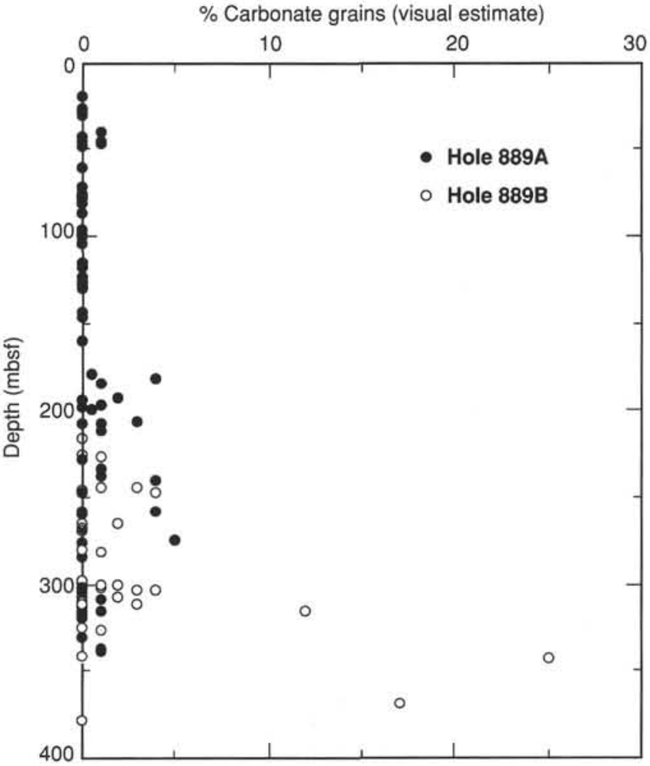

Figure 18. Abundance of carbonate vs. depth, determined from smear slide description of Holes 889A and 889B.

Clays are composed of various clay minerals of brownish, greenish, or gray body color. Clay minerals usually are present as flocculated aggregates. The composition of the fine silt fraction is similar to that of the silty to fine sands. Major components are angular to subangular grains or shards of feldspar (largely plagioclase with polysynthetic twinning), quartz (monocrystalline grains), opaque minerals (sulfide, manganese minerals, magnetite, and ilmenite), and amphibole (pleochroic green hornblende is common). Accessory minerals (pyroxenes, epidote, apatite, and zircon), small rock fragments, and a consistent, low amount of biogenic silica (diatoms and sponge spicules) were found. At the top of the cored interval, close to the sediment/water interface, glaucony pellets occur in amounts up to 20%.

Shell fragments, mud clasts, and rare carbonate concretions were observed in the clayey silt.

All cored sediment is commonly horizontally fractured as a result of gas expansion (Fig. 28). The occurrence of these fractures seems to be restricted to the coarser grained intervals.

Occurrence of Biogenic Silica at Sites 889 and 890

One of the most notable compositional changes in the cored section of Site 889 is in the quantity of biogenic silica. This change is not correlated with the unit boundaries. In the coarse silts recovered from Hole 889A more than 10% diatoms (with a corresponding though small increase in radiolarians) was found persistently in Cores 146-889-7H though to -34X (Fig. 29). This increased incidence ranges from the lower part of Subunit IA, at 77 mbsf, through to the middle part of Unit II, at 260 mbsf. In Core 146-889A-6H, 1%–3% diatoms were found. This amount is typical of the sediment between this depth and the surface. Sample 146-889A-7H-4, 50 cm, contains

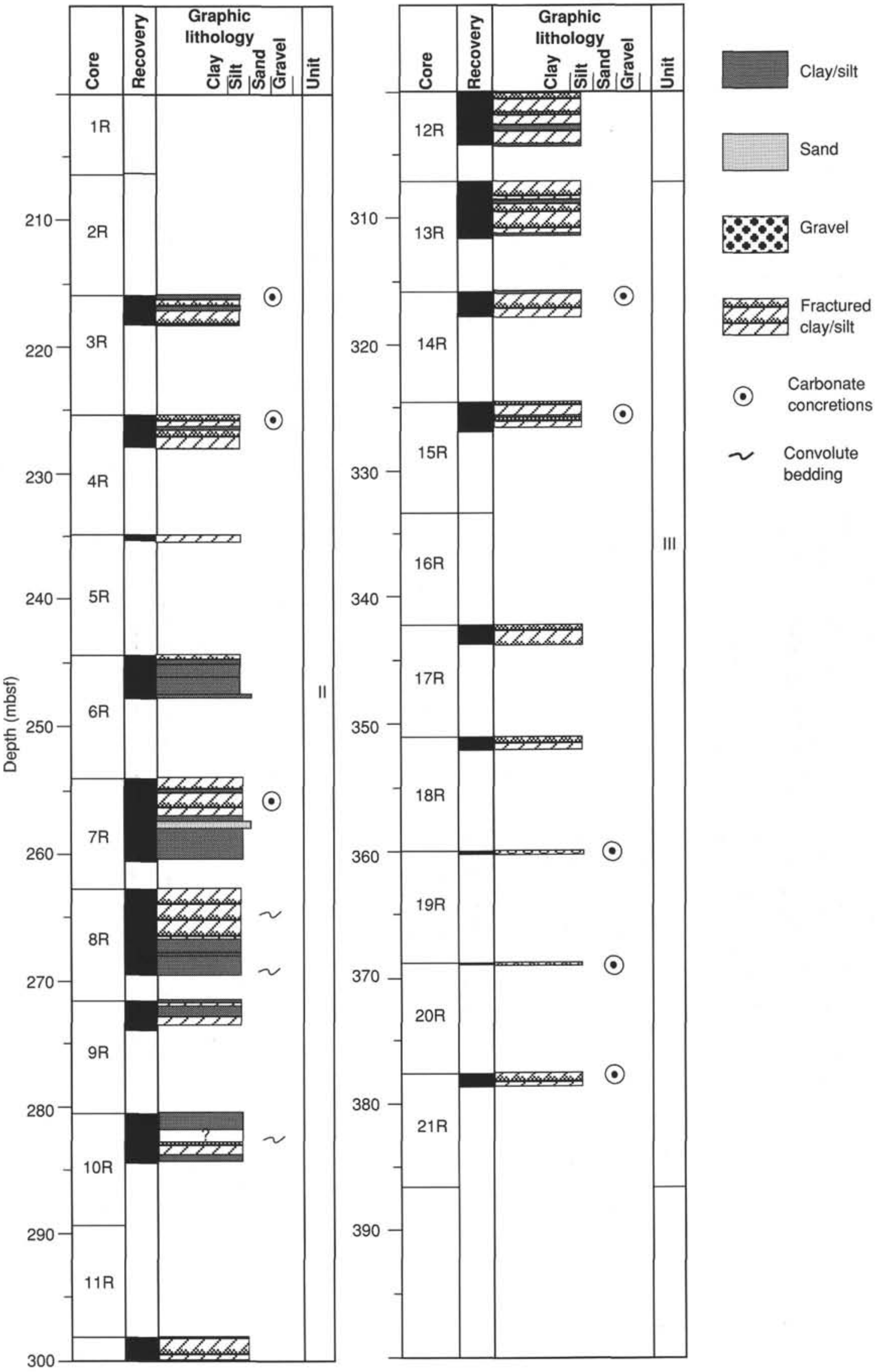

Figure 19. Graphic lithology for Hole 889B, below 200 mbsf.

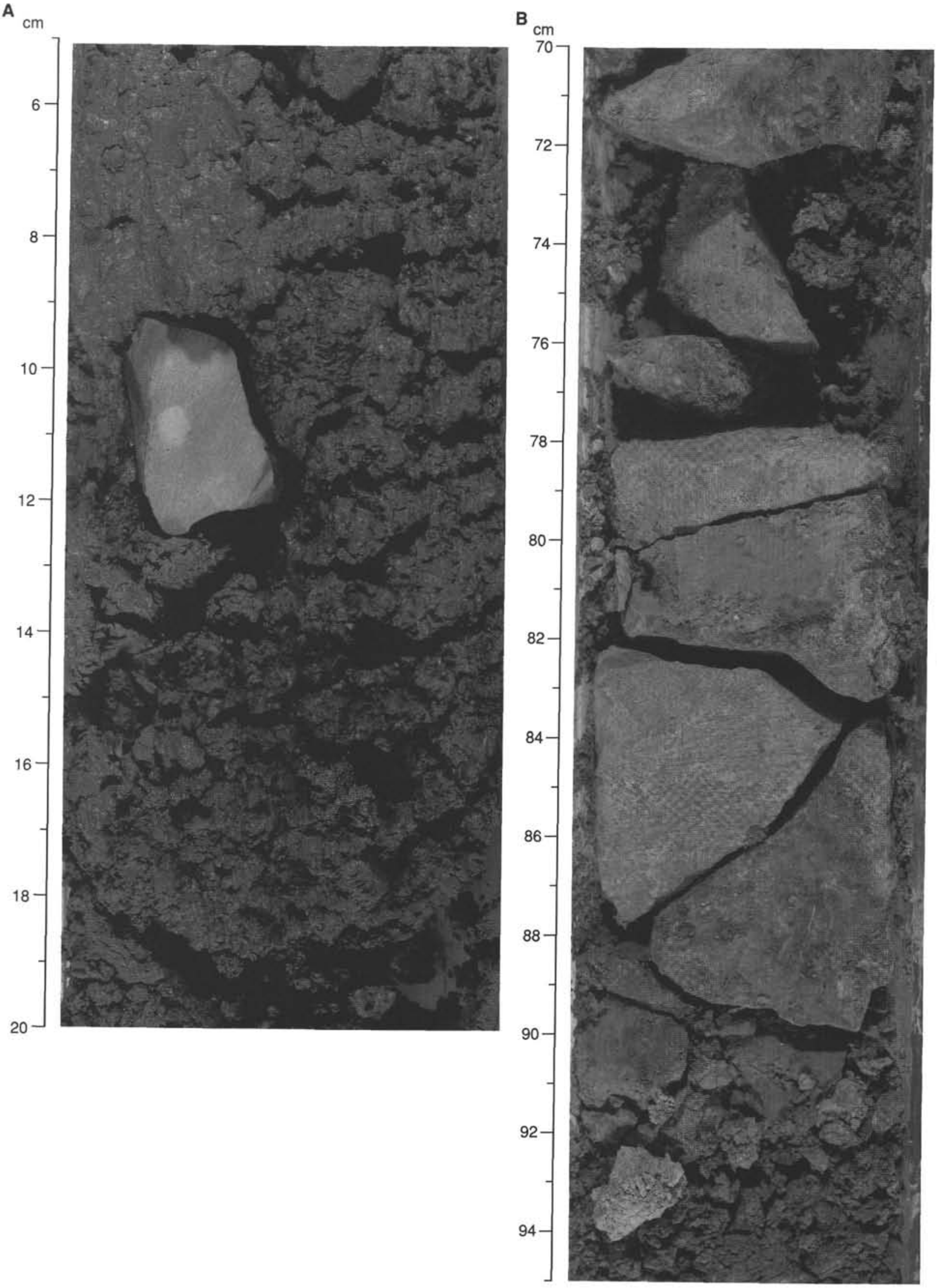

Figure 20. **A.** An isolated carbonate concretion of Unit II (Section 146-889A-14H-2, 5–20 cm). **B.** Massive carbonate layer in Unit II (Section 146-889B-7R-4, 70–95 cm).

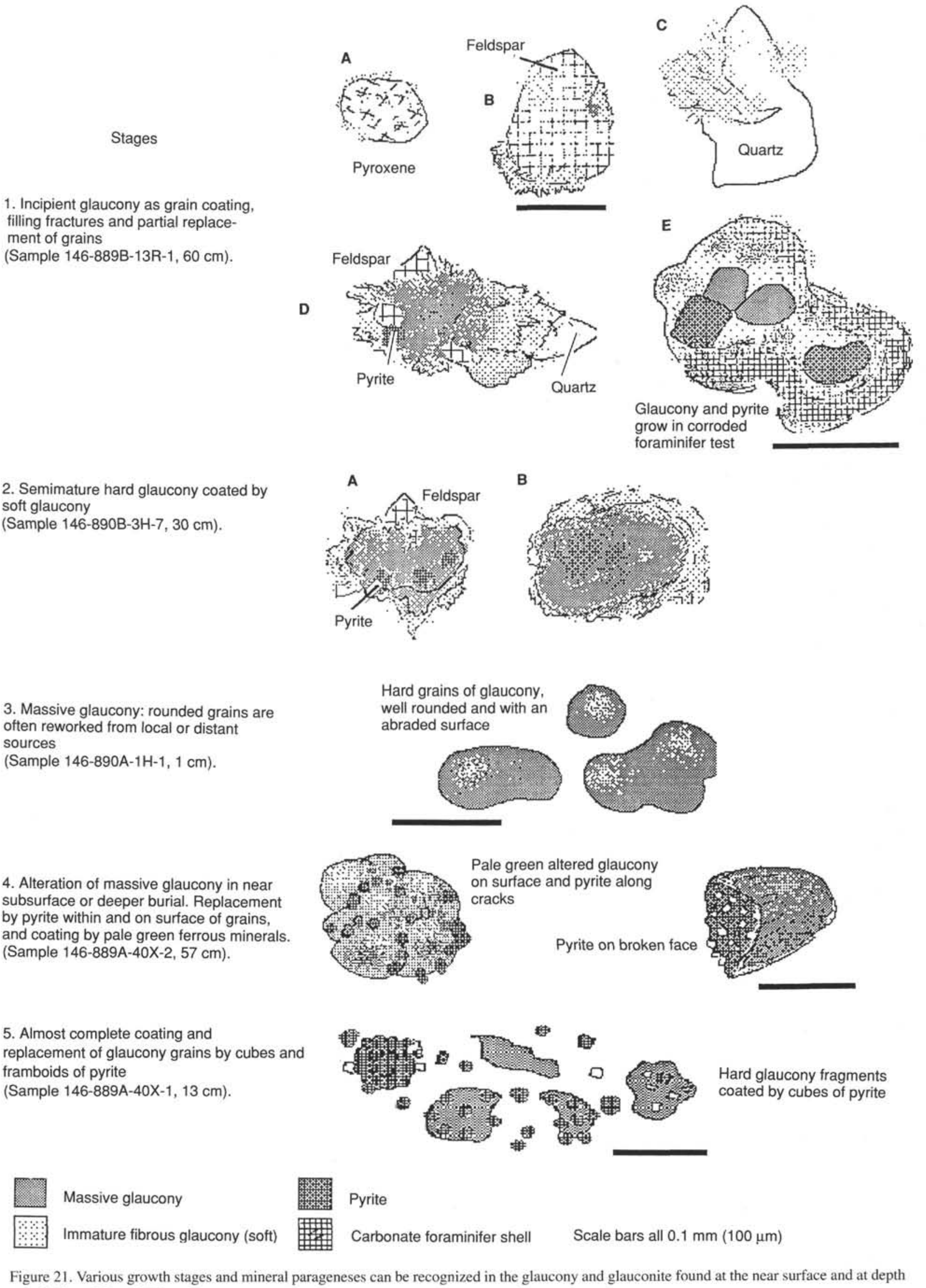

Figure 21. Various growth stages and mineral parageneses can be recognized in the glaucony and glauconite found at the near surface and at depth at both Sites 889 and 890.

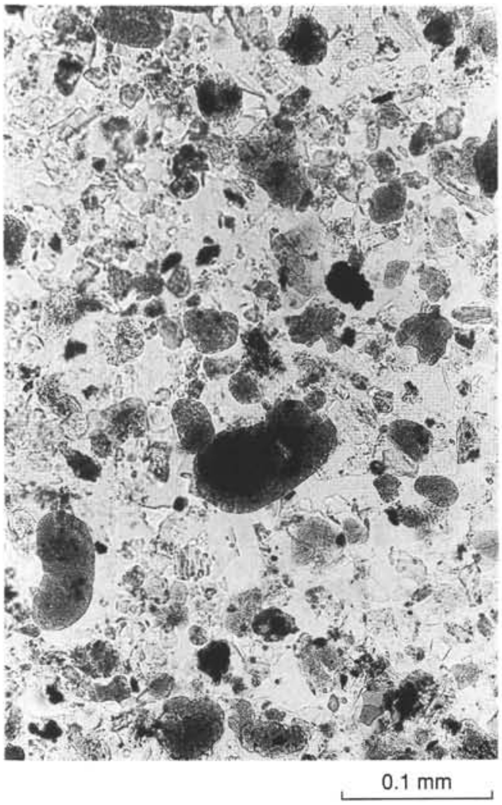

Figure 22. Photomicrograph of a typical glaucony pellet, slightly pyritized (Sample 146-889A-40X-1, 13 cm).

Figure 23. Photomicrograph of glaucony coats on detrital feldspar (Sample 146-890B-3H-7, 30 cm).

16% diatoms, 2% sponge spicules, and 2% radiolarian tests. More than 15% biogenic silica was recorded in several other samples from this interval, notably in Sample 146-889A-26X-1, 13 cm, where 25% diatoms and 3% sponge spicules were estimated to be present in the smear slide. There is a progressive decrease in the amount of siliceous skeletal material below Core 146-889A-34X (264 mbsf). From Core 146-889A-36X to the base of Hole 889A, only 1%–2% skeletal silica was found. In Hole 889B, the same changes with depth were found. Diatoms make up 30% of Section 146-889B-6R-1, 20% of Section 146-889B-6R-2, and 15%–16% of Section 146-889B-6R-3 (249 mbsf), whereas only small amounts of biogenic silica (up to 3%) occur in the slides from the deeper cores in Hole 889B.

Occurrence of "Glauconite" (Glaucony) at Sites 889 and 890

The term "glauconite," as used historically by geologists, loosely encompasses a variety of green-colored sheet silicates found in sediments. Chemical and X-ray studies reveal that these green minerals include (Odin, 1985):

1. Chlorites–both detrital and authigenic varieties, most typically early alteration products of micas.
2. The chamosite-berthierine series, which has a 7 Å chlorite-like structure, but bears additional ferrous and ferric iron.
3. Smectites and micas with partial substitution of ferrous and ferric iron in the structure, which is stabilized by a variable potassium content, producing a nonexpandable 10–14 Å structure.

Strictly, the term "glauconite" should apply to a well-crystallized dioctahedral mica with a high proportion of the interlayer cation sites ("A" sites) occupied by potassium (Brindley and Brown, 1980). As such, its definition depends on the result of detailed XRD studies. Odin and Stephan (1981) and Odin (1985), therefore, recommended the use of the term "green grains" where the mineralogy is unknown and the term "glaucony" where the general class of the mineral has been identified as of the iron-bearing, smectite-mica series, but where the structure is not in a fully evolved stage (i.e., without maximum K^+ occupancy).

Green minerals, grouped necessarily for the purpose of counting into the category "glauconite" on the computer-generated smear slide forms, occur widely at Sites 889 and 890. Green minerals occur in the form of discrete pellets or grains, as grain coatings, and dispersed in the bulk of the clay fraction. They are distributed from the near subsurface to deep levels, but "glaucony" distribution is concentrated most strongly in three intervals:

1. At the very top of the cored interval, close to the sediment/water interface in Cores 146-890A-1H and 146-890B-1H, concentrations of glaucony grains and pellets were found. In Sample 146-890B-1H-1, 1 cm, 10% of the clayey sediment was found to consist of rounded glaucony grains, whereas in Sample 146-890B-1H-1, 12 cm, 60% granular glaucony was counted. The amount of glaucony decreases with depth, with 4% in Sample 146-890B-5H-1, 17 cm.
2. In the intermediate part of Unit II (Cores 146-889A-22X to -25X) glaucony grains, and some pellets, were found in darker sand layers and in irregular patches. Smear slides from these concentrates yielded up to 35% glaucony (Sample 146-889A-25X-3, 10 cm), with a high proportion (8%–15%) of co-occurring pyrite.
3. The highest proportions of glaucony were recorded, in both Holes 889A and 889B, at depths between 300 and 330 mbsf, at the top of Unit III. The first occurrence in Hole 889A is a trace amount in Sample 146-889A-38X-1, 5 cm (284.16 mbsf). In Core 146-889A-40X, 15%–40% glaucony pellets was found between 301.6 and 310.0 mbsf. This proportion fluctuates between trace amounts and 35% glaucony downsection to the base of Hole 889A, with 30% altered

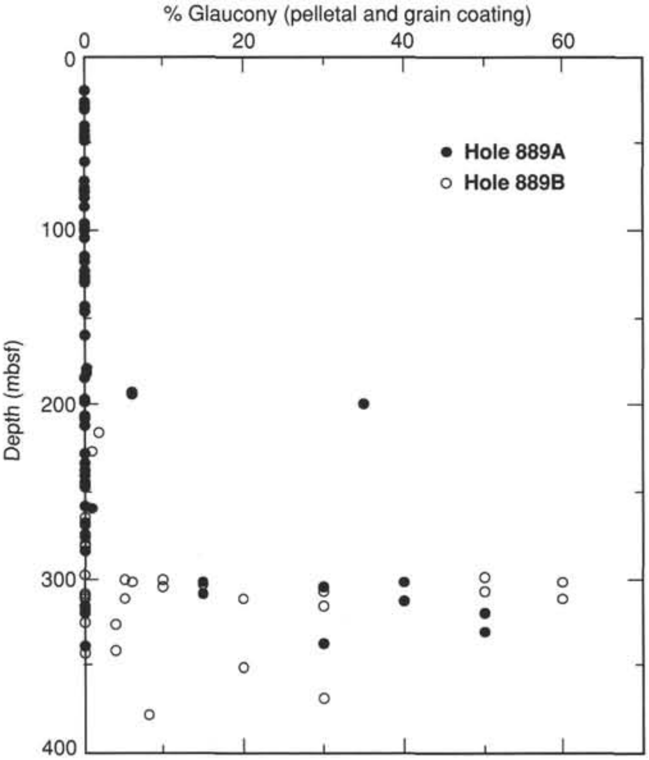

Figure 24. Abundance of glaucony vs. depth, from smear slide description of Holes 889A and 889B.

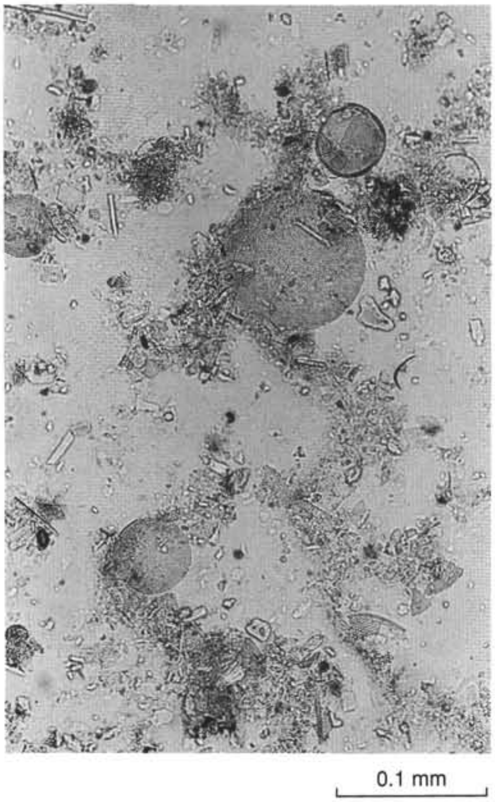

Figure 25. Photomicrograph of unusually large diatom, occurring in silt of Unit I (Sample 146-889A-9H-5, 63 cm).

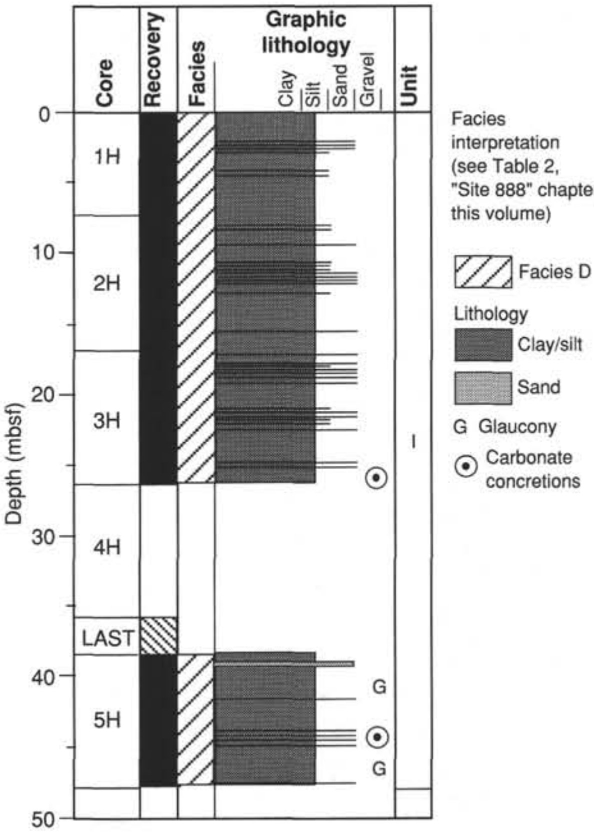

Figure 26. Sediment column and facies type for Hole 890B.

glaucony pellets found in Sample 146-889A-44X-1, 50 cm (337.7 mbsf). At the same depth in Hole 889B, recovery was more complete, and a progressive but abrupt increase in glaucony was found from 3% in Section 146-889B-10R-2 to an average of 30% in Section 146-889B-13R-1.

The glaucony in Unit III shows a coarse granular to pelletal morphology. Pellets of up to 1 cm across were found at the base of the cored interval (Sample 146-889B-21R-1, 5 cm). Most glaucony grains are between 100 and 500 µm across. This leads to a sand-sized average grain diameter for the sediments where glaucony occurs in abundance, even where it is hosted in generally fine clay or silt. The increase in incidence of glaucony generally is not accompanied by an increase in the grain size of the terrigenous sedimentary component in Unit III.

Fresh glaucony grains are included in a dolomitic concretion from Unit III (Sample 146-889B-18R-1, 14–19 cm). There is no included glaucony in a dolomitic carbonate concretion sampled from Unit II, which occurs below the level at which glaucony occurs abundantly in the free sediment of this unit (Section 146-889B-2R-1, 0–5 cm, at 206.4 mbsf).

The paragenesis of glaucony from Sites 889 and 890 is summarized in Figure 21.

Origin of Glauconite at Sites 889 and 890

Glauconite is known to occur only in marine sediments. A sister mineral, celadonite, is found associated with hydrothermal ores on land, but its distribution is limited (Brindley and Brown, 1980). Glauconite, sensu stricto, until recently was thought to be a good indicator of paleodepth in marine sediments, with its occurrence generally restricted to the seafloor above 500 mbsl. Odin and Stephan (1981) reported that glaucony, and probably mature glauconite, does occur at

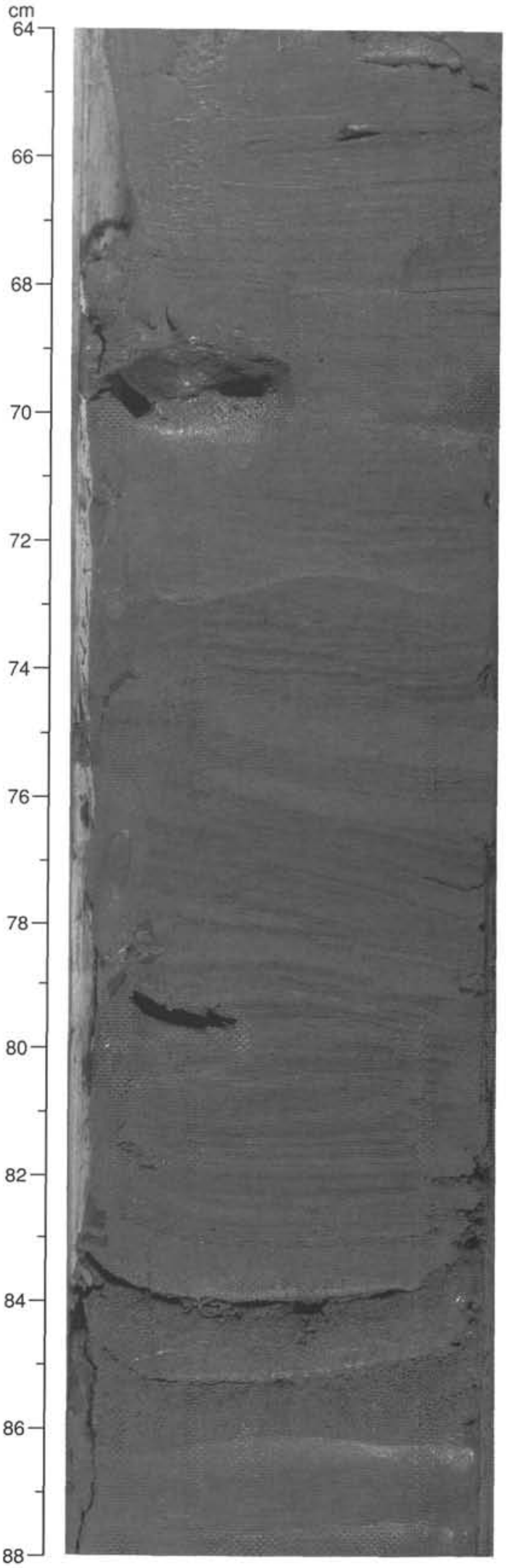

Figure 27. Fine lamination (on a millimeter scale) of green and gray clay in Hole 890A (Section 146-890A-1H-2, 64–88 cm).

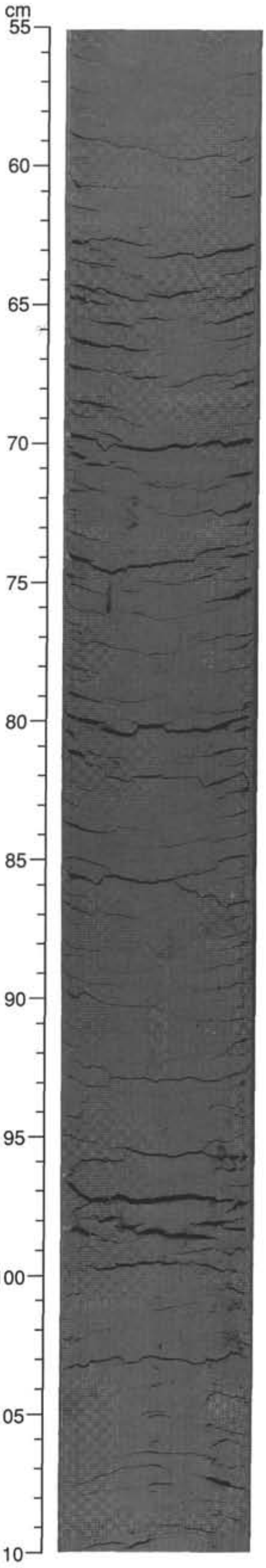

Figure 28. Horizontal fractures resulting from gas expansion in silty clay in Hole 890B (Section 146-890B-2H-5, 55–110 cm).

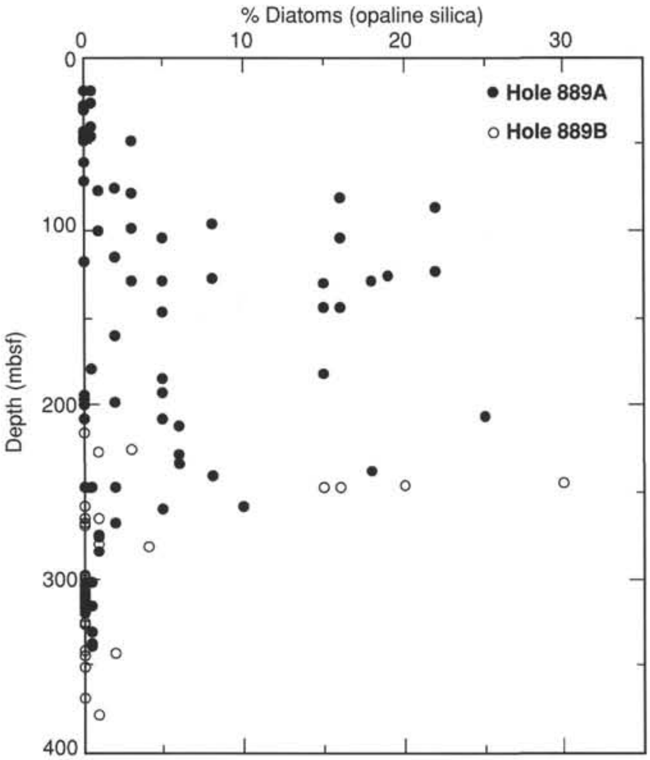

Figure 29. Abundance of diatoms vs. depth at Site 889, from smear slide description.

greater depths, particularly from 1000 to 2000 m. In a more detailed discussion, Odin (1985) argued that there is no particular reason for a depth restriction on the in-situ formation of glaucony, provided that the physico-chemical environment is suitable. The following account is based on this work.

The factors that influence the nucleation of glaucony are the availability of a substrate, typically organic matter or partly altered mineral grains, and mildly reducing conditions. Growth is sustained only if the redox balance is maintained at this level and if abundant iron and potassium are available from seawater or from pore waters. The former condition precludes the development of glaucony in areas with stagnant bottom waters that may become anoxic or in areas with highly oxygenated water. The latter conditions generally restrict the formation of glaucony to the very near surface, where iron has not yet been incorporated into pyrite during sulfate reduction and where potassium is still available from circulating seawater. Glaucony forms, and matures to glauconite, over a long time scale because of the kinetic constraints of potassium uptake (thousands of years for incipient glauconization to hundreds of thousands of years for the formation of mature glaucony pellets). For this reason, glaucony distribution is restricted largely to areas of low sedimentation rate.

Most of the glaucony found in the sediments at Sites 889 and 890 is in the form of well-rounded pellets (Fig. 22). The pellets are dense and dark green, and have provisionally been identified as mature glaucony. Some of the pellets are broken with a brittle fracture. Elsewhere, less well-crystallized and more fibrous (i.e., immature) glaucony was found. Immature glaucony occurs as grain coatings (Fig. 23), forms small grains, and is present, apparently as an alteration product, on the surface of mature glaucony grains. Grains of immature glaucony have a hackly surface where broken and are fibrous in structure.

It is possible that the pellets of mature glaucony are detrital in origin, and were carried by currents from a source area some distance away. However, a number of petrological features, listed here, suggest that at least some of the less mature glaucony either formed close by or grew in situ.

1. The grains of glaucony occur in sediments of all grain sizes, including fine silts and clays. If the glaucony grains were transported any great distance, then it is most likely that they would be carried along with other mineral grains that were hydraulically equivalent, and so be found concentrated only in restricted grain sizes.
2. Some of the pellets are very large (up to 1 cm across) and have an irregular surface morphology. This suggests that they are small concretions, formed more or less in place, and not reworked pellets.
3. Immature glaucony can be seen to form grain coats in the same intervals where the pellets are found. Some of these coated grains may have been transported, but the thinner and more delicate coating structures are unlikely to have survived transport.
4. A complete sequence (which appears to be an evolutionary progression) of coated grains to well-developed pellets, and from slightly corroded pellets to wholly altered clay lumps, can be followed in Unit III. Parts of this progression are repeated in the glaucony occurrences of Units I and II.

We concluded that strong evidence exists for the authigenic formation of glauconite at Sites 889 and 890, especially in Unit III. In view of the known paragenesis of the mineral, this indicates mildly reducing conditions close to the sediment/water interface and a slow deposition rate for a prolonged period during the accumulation of Unit III. The lack of siliceous fossils in this interval (see Fig. 26) suggests that organic productivity, and thus the pelagic accumulation rate, was low at this time. Furthermore, this deficit of biogenic material implies that iron was not removed efficiently from the sediment during the oxidation of organic matter. It is postulated that the immature glaucony formed in situ in these conditions and that a shallower source was located nearby, from which the mature glaucony was reworked.

Sedimentologic Evidence of Gas Hydrates

At Site 889, we did not find direct evidence of clathrates in the split cores. In other words, we did not observe any fragment of "bubbling ice" (observed at Site 892, and at Deep Sea Drilling Project [DSDP] Leg 66 Site 490) or simply "ice" (observed at DSDP Site 533 [Leg 76], Site 688 [Leg 112], Site 808 [Leg 131], and Site 892 [this leg]), although anomalously low temperatures were measured in some cores (see "WSTP and ADARA Temperature Measurements" section, this chapter).

In this section, we report on sediment characteristics that may be associated with the presence of gas hydrates in the sediment, and we briefly discuss their meaning.

At Site 889, we described several layers of the sediment section as affected by soupy disturbance. In Subunit IA, the soupy layers are clearly associated with sandy intervals, which have become fluid as a consequence of liquefaction induced by vibration during coring. In Subunit IB and in Units II and III, these intervals are not related to sandy layers, and they show a consistent thickness that does not exceed 1 m, with the exception of Core 146-889A-24X, which was soupy over its entire length (6.5 m, from 187.8 to 194.3 mbsf). Figure 30 shows the typical aspect of one of the soupy layers. Soupy intervals have either transitional or sharp boundaries and are composed of a homogeneous mixture of sediment and water in which fragments of firm sediments are suspended. Soupy layers are analogous in color and composition to the sediments above and below, and do not show any particular characteristics that can be related to their preferential fluidization.

The distribution with depth of soupy layers in Units II and III (Fig. 17) matches the interval of higher methane concentration found between 128 and 260 mbsf (see "Organic Geochemistry" section, this chapter), and although fluidized disturbance is not mentioned in connection with the recovery of gas hydrates on previous legs, it could have been produced at Site 889 by the melting of the solid hydrates within the sediment during core retrieval. The water sampled from two of these layers indicates the presence of fluids "diluted" by the melting of the gas hydrate (see "Inorganic Geochemistry" section,

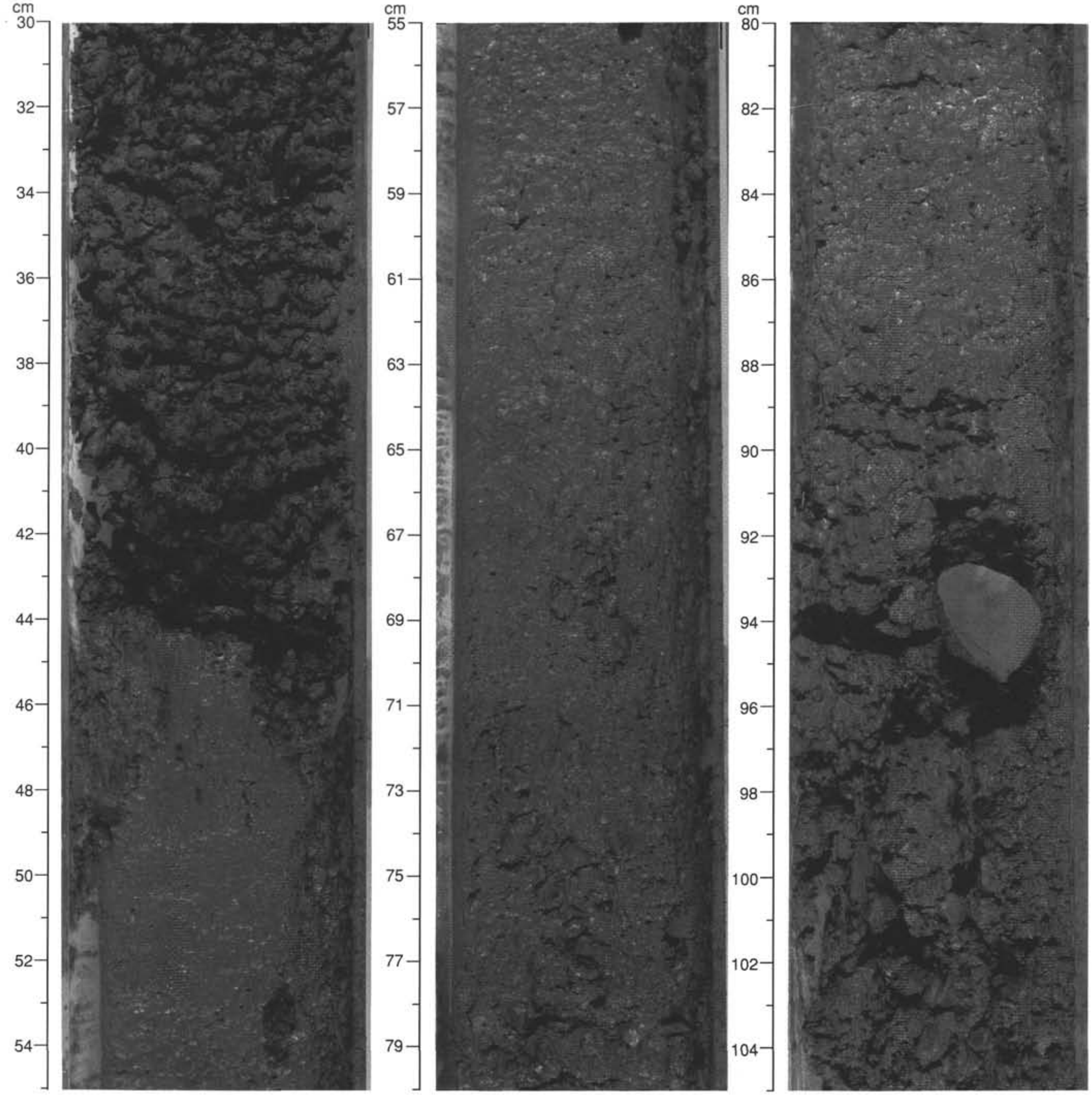

Figure 30. Example of typical soupy interval (42–112 cm) about 70 cm thick in Section 146-889A-18X-1, 30–119 cm, Unit II. The upper boundary of the interval is sharp, the lower is transitional. A carbonate concretion is present in the lower portion of the interval. The texture of the interval is extremely homogeneous and soupy.

this chapter). The disturbance induced in the sediment fabric by the sublimation of the hydrate molecules may be enhanced by the vibration of the core during drilling, and the fluidized, or soupy, texture could be the result. On DSDP Leg 76 the "fragmented character," or "disturbance texture," marked in the cores by simple cracks with small (less than 1 cm) gaps in recovery up to 20 cm long, was identified as a possible indicator of gas hydrates in the sediment.

We concede that the plot of the occurrence of soupy intervals vs. section number in which the intervals were recovered (Fig. 31) clearly shows that the majority of the intervals are in the first section of cores. Thus, some of them could be an artifact produced by disturbance of the sediment while the drill string was raised during recovery of the core barrel. Nevertheless, several soupy layers were found in deeper sections in the cores, where such disturbance can usually be excluded.

The occurrence of the soupy intervals below the present position of the BSR (base of the stability field of the gas hydrate) may indicate an origin independent of hydrate occurrence or may be explained by the presence of a "paleo-gas hydrate zone" in Unit III (see "Inorganic Geochemistry" section, this chapter).

The relationship between the carbonate concretions and the gas hydrate cannot be established at this moment, because it depends on the isotopic composition of carbon and oxygen. The downhole distri-

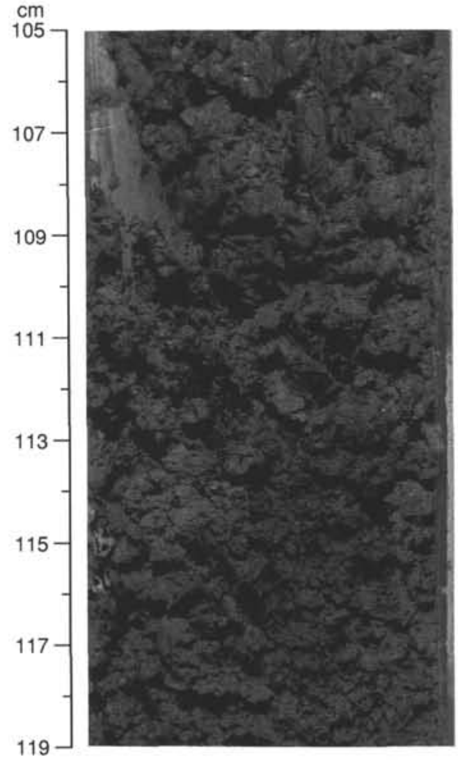

Figure 30 (continued).

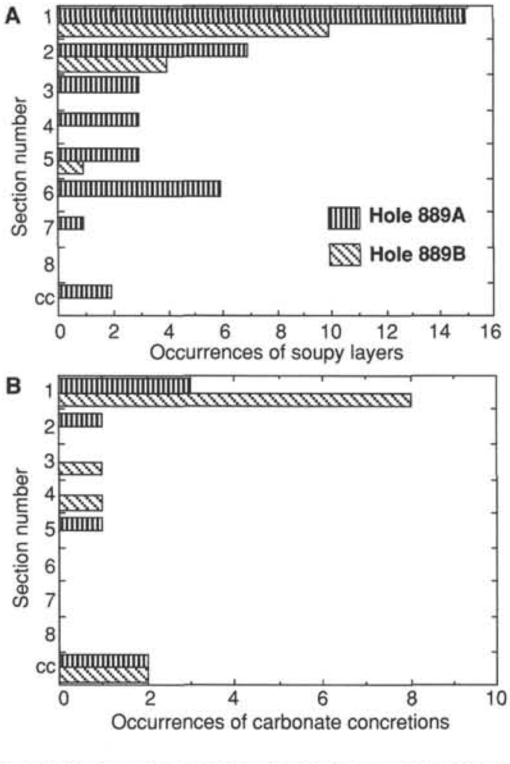

Figure 31. Distribution of core sections in which soupy layers (**A**) and carbonate concretions (**B**) were found in Holes 889A and 889B. The high abundance of soupy layers and carbonate concretions in the first sections and core catchers could indicate that soupy layers arise from drilling disturbance whereas carbonate concretions may have been reworked downhole.

bution of carbonate concretions in the sediments (Fig. 17) does not match the distribution of soupy layers. However, the carbonate clasts occur preferentially in first sections (and core catchers of low-recovery cores) (Fig. 28); they may represent reworked clasts that fell to the bottom of the hole while the bit was raised during the recovery of the core barrel.

Results of X-ray Diffractometry

Randomly oriented powders were prepared from whole-rock samples of clays and silts from various depths at Sites 889 and 890 and analyzed using the XRD methods described in the "Explanatory Notes" chapter of this volume. A preliminary interpretation of the mineral contents was derived from the diffractograms, as outlined in the following.

The data from the bulk powder diffractograms is essentially qualitative in nature, showing which minerals are present in a proportion greater than a few percent. Orientation effects, structure-factor interference, peak masking between minerals, and internal calibration problems together preclude a reliable quantitative determination of mineral proportions. Indeed, even under ideal analytical conditions, and using an internal standard, it is doubtful whether the relative amplitudes, or relative peak areas, of XRD reflections can be used to calculate the mineral proportions in sediments with any confidence (e.g., see McManus, 1991).

For the reasons outlined, no attempt was made to show quantitative changes in mineralogy. A semiquantitative measure of mineral proportion was, however, made by adopting the procedures of Froget et al. (1989). The reflections from the major clay minerals were normalized, using the intensity (square of the amplitude) of the quartz (101) reflection at 3.34 Å as an internal reference. These corrected values were then used to plot graphs of relative amplitude. In this way the most important changes in mineral abundance are displayed relative to the quartz component. Although quartz is ubiquitous, its proportion in the sediment varies, so absolute changes in abundance cannot be measured.

In contrast to the compounded errors resulting from preparation of the bulk-powder XRD mounts, the instrumentation errors are thought to be small. It was found previously (e.g., Taira, Hill, Firth, et al., 1991), that the internal reproducibility of the shipboard XRD apparatus is good, with fluctuations in peak height between duplicate runs averaging only 2%–3%.

Main Mineralogic Characteristics

Silica Minerals

All of the samples examined from Sites 889 and 890 contain an appreciable amount of quartz; the diffractograms of all samples are dominated by its characteristic reflections. Although low quartz is the overwhelmingly dominant silica mineral, the 4.1 Å reflection characteristic of tridymite is also detected at low to moderate intensity. This "tridymite" is thought to be opal-CT from the tests of siliceous organisms.

Feldspars

The second important mineral group, evident from the diffractograms of all samples, is the feldspars. The intense reflections at 4.20–4.02, 3.18, and 3.05 to 2.89 Å largely correspond, respectively, to the d(2′01), d(2′02; 2′20; 040), and d(002) planes of plagioclase feldspars. A trace of potassium feldspar is also indicated in most samples. These findings agree with the results of smear slide analysis: plagioclase is ubiquitous, and the presence of small amounts of altered potassium feldspars and/or perthites is generally indicated.

Reflections from quartz and feldspar can account for the most intense peaks, and many of the smaller peaks, on all of the diffractograms. Other minerals that were detected have relatively low-amplitude peaks, and some of their reflections coincide with those of quartz or feldspar. These factors make the exact characterization of other mineral species in the whole-rock samples difficult. Apart from quartz and feldspar, the remaining intense peaks can be explained largely as reflections from minerals of the mica-illite group, the chlorite group, kaolinite, carbonates, and sulfide minerals. Minerals of other groups are not considered to be present in any great quantity.

Clay Minerals

Clay mineral compositions are most readily distinguished using oriented powder mounts from the concentrated finer fraction of the sample, rather than from bulk, unoriented powders. The proportion of clay minerals in most of the samples was, however, sufficient for some of the stronger basal reflections to be recorded.

The most intense peaks identified from clay minerals are those of chlorites. Chlorites are accompanied by some kaolinite, but the intensity of the d(004) reflection of chlorite at 2.54 Å relative to the d(002) reflection of kaolinite at 3.58 Å shows that the former mineral is present in a greater quantity. The peak positions of the chlorites are typical of an iron-rich end-member, possibly berthierine. This observation suggests that the glaucony present in the sediments of the two sites may be a green variety of berthierine rather than true glauconite.

The mica group forms the next most intense series of reflections. It is not possible to distinguish true micas from clays with a 10 Å basal spacing (i.e., illites) in the whole-rock XRD data.

The general characteristics of the fine-grained sediments recovered from both sites (plasticity, difficulty in producing a clay dispersion for smear slides and grain-size analysis, and swelling in the core barrel) indicate that smectite is present in an appreciable quantity. Smectites were detected only in trace amounts in the unoriented powder diffractograms. This is probably a result of the tendency of the preparation technique used to mask the presence of the smectite group.

It is recommended that further studies be made on the clay mineralogy on land, employing the semiquantitative analysis of size-fractionated, oriented mounts normalized to internal standards (e.g., following the method of Froget et al., 1989).

Carbonates

There is an indication, from testing with cold dilute HCl, of small amounts of calcite in most samples from Units II and III. However, the calcite XRD trace is masked by a strong feldspar peak at 3.04 Å. Dolomite may be present in several samples from Units I, II, and III, but its peaks are partially masked by quartz and feldspars. The quantities of carbonates cannot be determined, but are probably less than 5% in all cases. This finding agrees with the smear slide determinations on material collected near the XRD samples.

Sulfides

A small peak corresponding to pyrite is present in most of the diffractograms from Sites 889 and 890. Although there is a possibility of interference from the (060) reflections of clay minerals at the same angle, smear slide and macroscopic observation of the cores both show that pyrite is present in high concentrations in several intervals throughout the succession. Pyrite is most abundant in Unit I (e.g., Sample 146-890B-2H-3, 121 cm; 11.5 mbsf), and in the lower part of Unit II to the upper part of Unit III (260.0–233.0 mbsf).

In two samples from Core 146-890B-5H, a reflection noted at 2.07 Å may be caused by pyrrhotite. This was not confirmed, because the other peaks characteristic of this mineral are in positions that would be masked by other sediment components. The observation is important because of its implications for rock magnetism (see "Paleomagnetism" section, this chapter).

Sedimentary Environments

Significant sediment disturbance and poor preservation of the original sedimentary structures cause difficulty in the interpretation of the depositional environment at Sites 889 and 890.

Sediments recovered in Units III and II do not display any significant difference in sedimentary fabric and are highly disturbed by fracturing and brecciation. Mainly facies type G (Fig. 7), and rarely type D (which is present in Core 146-889D-4N), have been identified, with terrigenous silt prevailing over fine sand and hemipelagic mud (Mutti and Ricci Lucchi, 1972). Although the sedimentary characteristics are insufficient to diagnose a particular sedimentary environment, the suggested agents of transport and deposition are distal, low-energy turbidity currents. We postulate that the sediments were deposited in an abyssal plain environment for the following reasons:

1. The sedimentologic evidence is consistent with the "basin plain association" of facies proposed by Mutti and Ricci Lucchi (1972).
2. Based on known plate motion rates, the age of the sediments recovered in Units II and III (Pliocene to early Pleistocene) suggests a paleogeographic position at the time of deposition from 120 to 80 km westward of the present position, in the Cascadia Basin abyssal plain.
3. Pliocene and Pleistocene abyssal plain silts were recovered at DSDP Site 174 located on the distal fringe of the Astoria Fan (Kulm, von Huene, et al., 1973), and seismic stratigraphic correlation suggests analogous deposits in the northern Cascadia Basin (Carlson and Nelson, 1987).
4. Based on preliminary biostratigraphic data (see "Biostratigraphy" section, this chapter), the rate of sediment accumulation in Units II and III is low (11–14 cm/k.y.). Low values of accumulation rates (about 40 cm/k.y.) are assumed to be typical for the Pliocene and Pleistocene abyssal plain units of the Cascadia Basin (Carlson and Nelson, 1987).
5. Evidence of postdepositional tectonic disturbance of Unit II and III is suggested by the structural fabric of the sediment and by FMS data (see "Structural Geology" and "Downhole Logging" sections, this chapter).

The possibility that Units II and III were deposited in a slope sedimentary environment cannot be ruled out, but there is little evidence to support this interpretation.

In Subunit IB of Site 889 the tilted beds and the sediments including mud clasts between 91.5 and 115 mbsf contain reworked fauna (see "Biostratigraphy" section, this chapter). The upper part of this reworked interval coincides with a sharp decrease in sediment bulk density, and in the lower part the density data are scattered (see "Physical Properties" section, this chapter, and Fig. 32). The variability of density in this interval supports the reworked origin of the sediment. We therefore suggest that the tilted beds and mud clasts present in Subunit IB represent a series of sediment gravity-flow deposits (creep, mud flows, debris flows, slumps, etc.) caused by tectonic uplift of the deformation front (synsedimentary tectonism). Subunit IB could thus represent a transition between the abyssal plain sedimentation of Units II and III to the subsequent deposition of Subunit IA.

In Subunit IA of Site 889, Bouma sequences (T_{cde}) occur commonly and suggest a type D depositional facies (Mutti and Ricci Lucchi, 1972). However, couplets of fine to medium sand layers and clayey silt layers are also suggestive of classical facies C turbidites. Furthermore, a coarsening-up sequence can be identified in Subunit IA from base to top. The physiographic setting and the seismic stratigraphic record of Site 889 (see "Downhole Logging" section, this chapter) permit relation of the depositional sequence of Subunit IA to the filling of a slope sedimentary basin. Although we cannot apply the deep-sea fan facies association model to this sedimentary unit, the presence of overbank deposits resulting from local lobe development and migration is inferred. The biostratigraphic hiatus

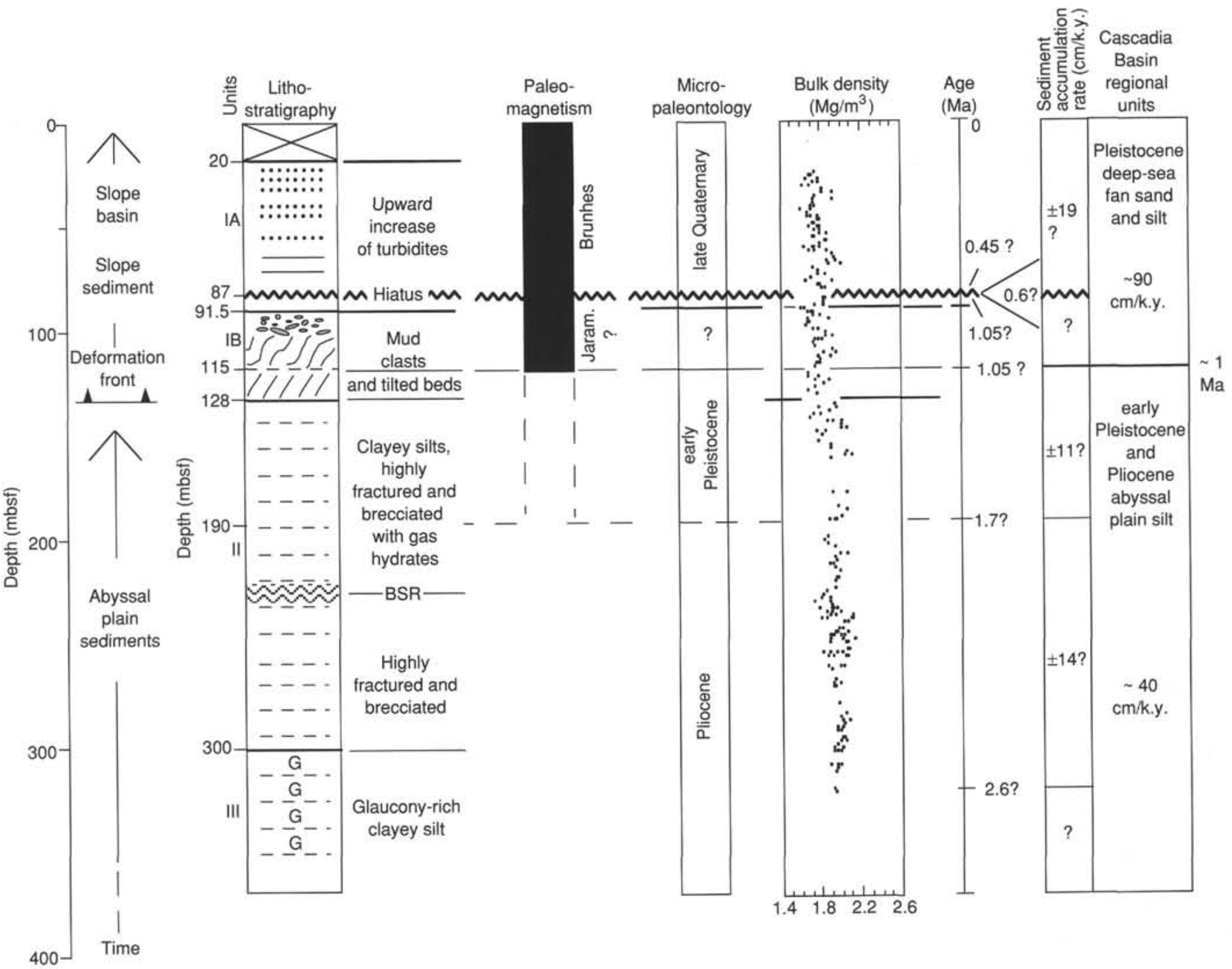

Figure 32. Flow diagram of the possible sedimentary environment and tectonic setting of Site 889. Dating of events is preliminary. The columns to the right represent the regional division of lithostratigraphic units in the Cascadia Basin (Carlson and Nelson, 1987) and average accumulation rates.

present at the base of Subunit IA (87 mbsf) can be related to the synsedimentary tectonism observed in Subunit IB.

In Unit I of Site 890, horizontal lamination, normal grading in silt and sand layers, incomplete T_{cde} Bouma sequences, and a lower sand/clayey silt ratio than in Subunit IA at Site 889 allow the identification of type D turbiditic facies belonging to a more distal depositional environment than that at Site 889 in Subunit IA. The two sites are located in different positions on the continental slope with respect to the distributary channels (Fig. 33), and Site 889 is most likely to receive the coarsest material deposited in the slope basin. The rate of sediment accumulation is thus expected to be lower at Site 890 than at Site 889.

In the interpretation of the depositional environments described herein and summarized in Figure 32, Sites 889 and 890 contain the sedimentary record of the transition from the abyssal plain to the slope environment. Such transition, recorded by the sediment reworking and redeposition observed in Subunit IB and by the biostratigraphic hiatus observed at the base of Subunit IA, represents the uplift of the sedimentary column at the deformation front. The uplift at the deformation front was followed by the development of a slope sedimentary basin.

The magnetic reversal identified in Subunit IB (see "Paleomagnetism" section, this chapter, and Fig. 32) coincides roughly with the base of the reworked section. It follows that the reversal cannot be the Brunhes/Matuyama, because its age is included in the hiatus of Subunit IA; the reversal could be the base of the Jaramillo Chron. In this case, the timing of the slumped section could be fixed to 1.05 Ma. More likely, the magnetic reversal recorded in Hole 889A is caused by the basal contact between the normal polarity sediments slumped on a reverse polarity sedimentary section. In this case, the age of Subunit IB would be >1.05 Ma (see Fig. 32).

Finally, if we assume that the plate convergence rate is 42 mm/yr, and that Subunit IB was deposited at about 1 Ma (see Fig. 32), it follows using the model of Westbrook (this volume), that the distance between the present toe of the accretionary prism and the present position of the sediments that were deformed at the deformation front 1 m.y. ago is 24 km, which is the distance between Site 889 and the present deformation front.

BIOSTRATIGRAPHY

A discontinuous sequence of upper Pliocene through uppermost Quaternary sediments was cored at Site 889, and an apparently continuous uppermost Quaternary sequence was cored at Site 890. Planktonic foraminifers, benthic foraminifers, and radiolarians are rare to abundant at these sites. Diatoms are common to abundant in

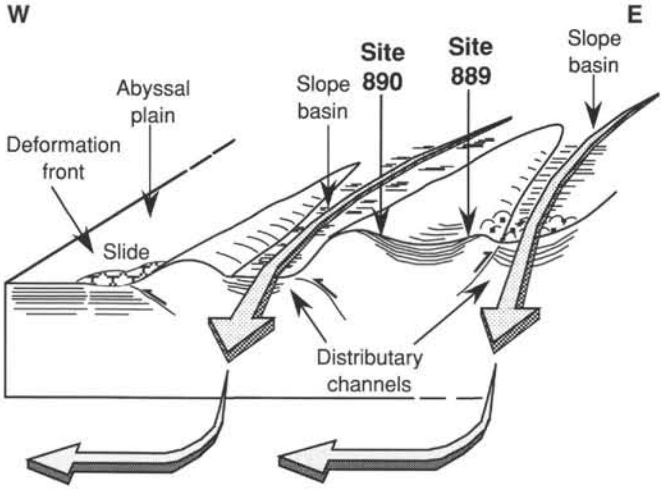

Figure 33. Sketch of the physiography and sediment-dispersal pattern in the area of location of Sites 889 and 890.

radiolarian-bearing samples. A dominantly middle bathyal environment is interpreted for these sites. Figures 34 and 35 summarize the biostratigraphic and paleoenvironmental results at Site 889.

A hiatus at 88 mbsf, inferred by the absence of the radiolarian *Stylatractus universus* Zone, separates uppermost Quaternary sediments from lower Pleistocene through upper Pliocene sediments (*Eucyrtidium matuyamai* Zone). Lithostratigraphic Subunit IB (91.5–128.0 mbsf), just below the hiatus, contains a mixture of upper Pliocene radiolarians and foraminifers and radiolarians characteristic of the late Pliocene through early Pleistocene, and is interpreted as a series of slump deposits or debris flows (see "Lithostratigraphy" section, this volume). Upper Pliocene radiolarians and foraminifers are present in Unit II of both Holes 889A and 889B. Most samples from Unit III from these holes are either barren or contain rare radiolarians and foraminifers.

Cold to temperate planktonic foraminifers and arctic radiolarians, both characteristic of North Pacific assemblages, were found at Sites 889 and 890. Radiolarian species characteristic of upwelling areas were found in several intervals.

Hole 889A

Radiolarians

All core-catcher samples from Hole 889A were examined for radiolarians. Some extra samples from Samples 146-889A-8H-CC (94.6 mbsf) through -12H-CC (127.5 mbsf) were processed for additional observations.

Well-preserved radiolarians are rare to abundant in Samples 146-889A-1H-CC (30.2 mbsf) to -37X-CC (275.4 mbsf). Samples 146-889A-38X-CC (284.2 mbsf) to -44X-CC (345.8 mbsf) are barren of radiolarians.

Samples 146-889A-1H-CC (30.2 mbsf) through 146-889A-8H-2, 96–101 cm (89.0 mbsf) contain a well-preserved assemblage dominated by *Cycladophora davisiana, Lychnocanoma grande,* and *Pterocorys clausus.* This assemblage is correlated with the late Pleistocene *Botryostrobus aquilonaris* Zone. The radiolarian assemblage observed in this interval is characteristic of the North Pacific area. Radiolarian species indicative of upwelling environments, such as *Lamprocyrtis nigriniae, Pterocanium auritum,* and *Pterocanium grandiporus* (Nigrini and Caulet, 1992) were found in Samples 146-889A-2H-CC (39.9 mbsf), -3H-CC (50.0 mbsf), and -7H-CC (86.4 mbsf).

The occurrence of *Eucyrtidium matuyamai, Stylatractus universus,* and *Lamprocyrtis neoheteroporos* places Sample 146-889A-8H-2, 114–145 cm (89.2 mbsf), in the late Pliocene/early Pleistocene *E. matuyamai* Zone. Consequently, a hiatus lasting about 0.6 m.y. is inferred at about 88 mbsf. Samples 146-889A-8H-2, 114–145 cm (89.2 mbsf), through -25X-CC (200.7 mbsf) are assigned to the *E. matuyamai* Zone. The first occurrence of *E. matuyamai* is located between Sample 146-889A-25X-CC (200.7 mbsf) and Sample 146-889A-26X-CC (215.4 mbsf). This interval is characterized by typical North Pacific species. Reworked specimens of early Pliocene species, such as *Cycladophora davisiana* (old form), *Stichocorys peregrina,* and *Sphaeropyle langii,* occur in many samples within this interval (Fig. 34), suggesting erosional and transportation processes during the early to late Pleistocene. Radiolarian species indicative of upwelling environments such as *P. grandiporus, L. nigriniae,* and *Phormostichoartus crustula,* were found in Samples 146-889A-10H-1, 140–144 cm (105.4 mbsf), 146-889A-11H-3, 88–92 cm (117.4 mbsf), and 146-889A-12H-4, 124–128 cm (123.9 mbsf). The evolutionary transition between *Lamprocyrtis neoheteroporos* and *L. nigriniae* is located between Samples 146-889A-12H-4, 124–128 cm (123.7 mbsf), and -12H-CC (127.5 mbsf).

Rare to few radiolarians assign the interval between Samples 146-889A-26X-CC (215.4 mbsf) and -38X-CC (284.2 mbsf) to the late Pliocene *Lamprocyrtis heteroporos* Zone. Rare representatives of the upwelling radiolarian marker *P. crustula* suggest an upwelling influence in sediments of Samples 146-889A-30X-CC and -31X-CC between 235 and 247 mbsf. No reworked fauna were observed.

Samples 146-889A-39X-CC through -44X-CC (294.0–345.8 mbsf) are barren of radiolarians.

Planktonic Foraminifers

Poorly to well-preserved upper Pliocene through upper Quaternary planktonic foraminifers are rare to abundant in 30 core-catcher samples from Hole 889A. Five core-catcher samples are barren of planktonic foraminifers. Additional samples from 77 to 125 mbsf were also examined for foraminifers (Fig. 34).

With the exception of Sample 146-889A-2H-CC (39.9 mbsf), which contains rare planktonic foraminifers, samples in the interval from 30.2 to 78.4 mbsf are dominated by few to common *Globigerina bulloides, Neogloboquadrina pachyderma* (sinistral), and *Globigerina quinqueloba* with sporadic occurrences of the other taxa listed in Table 2. Dextrally coiled *N. pachyderma* are rare in Samples 146-889A-2H-CC (39.9 mbsf) and -3H-CC (50.0 mbsf) and are few in Sample 146-889A-7H-5, 105–107 cm (83.6 mbsf). An insufficient number of specimens of *N. pachyderma* is present to enable one to generate coiling ratios throughout the interval from 20 to 87 mbsf (at least 50 specimens/sample are needed). However, this interval is assigned to the CD1–CD7 coiling zone (see "Explanatory Notes" chapter, this volume), based on the occurrence of both dextral and sinistral *N. pachyderma* and the lack of evolutionary markers, and is further constrained by the occurrence of radiolarians that are diagnostic of this age (see the previous section). Dominantly cold surface waters are inferred for this interval.

The interval from 89.2 to 119.0 mbsf contains moderately to well-preserved, rare to common *G. bulloides,* mixed populations of dextral and sinistral *N. pachyderma,* and rare to frequent occurrences of *G. quinqueloba* and *Neogloboquadrina asanoi* (Table 2).

Rare to few, poorly to well-preserved *G. bulloides, N. pachyderma* (sinistral and dextral), and *N. asanoi* occur sporadically in the interval from 123.9 to 345.8 mbsf. Within this interval, Sample 146-889A-41X-CC (316.4 mbsf) contains a mixture of *Globorotalia inflata* primitive form and *G. inflata praeinflata* (Table 2). The first occurrence of *G. inflata praeinflata,* a transitional form between the *G. inflata* primitive and *G. inflata* modern forms, coincides with the end of the Gauss Chron (Keller, 1980), which makes this sample no older than 2.6 Ma following the Cande and Kent (1992) time scale. This interval is therefore assigned to the CD12–CD14 zone based on the presence of *N. asanoi, N. pachyderma,* (dextral and sinistral), *G. inflata* primitive form, and *G. inflata praeinflata.* This is consistent

Table 2. Distribution of planktonic foraminifers in core-catcher samples and additional samples from Hole 889A.

Core, section, interval (cm)	Depth (mbsf)	Abundance	Preservation	*Globigerina bulloides*	*Globigerina quinqueloba*	*Globigerina umbilicata*	*Globigerinita glutinata*	*Globigerinita uvula*	*Globorotalia inflata* (modern form)	*Globorotalia inflata* (primitive form)	*Globorotalia praeinflata*	*Globorotalia scitula*	*Neogloboquadrina asanoi*	*Neogloboquadrina dutertrei*	*Neogloboquadrina pachyderma* (d)	*Neogloboquadrina pachyderma* (s)	*Orbulina universa*	*Pulleniatina obliquiloculta*	Paleotemperature	Coiling dominance zone	Epoch
146-889A-																					
1H-CC	30.2	A	G	A	F	C	F									A			Cold	CD1 to CD7	Quaternary
2H-CC	39.9	R	M												R						
3H-CC	50.0	A	G	C	F		R								R	C					
4H-CC	59.4	A	G	A												A					
5H-CC	68.2	A	G	C	R											C					
6H-CC	78.4	C	G	F								R				F					
7H-5, 105–107	83.2	C	G	F											F	R					
7H-CC	86.4	R	P	R																	
8H-2, 96–101	89.0	F	G	R											R	R					
8H-2, 114–115	89.2	C	G	R	R			R					R		R	R			Cold/cool	CD9 to CD11	early Pleistocene to late Pliocene
8H-4, 64–70	91.6	A	M	F	F	R	R						F		C	F					
8H-1, 18–123	93.5	A	G	C		F							R	R	C	F					
8H-CC	94.6	A	M	C	R				R				F		C	C					
9H-4, 69–74	98.5	C	G	F	R								F		F	F					
9H-7, 61–66	102.7	C	M	F									F		F	F					
9H-CC	104.8	F	G	R											R	R					
10H-1, 140–144	195.4	A	G	F	F							R			C	C					
10H-4, 108–114	109.3	F	G												R	F					
10H-CC	114.1	C	G	F									R		F	F					
11H-3, 85–92	117.4	C	M	F									R		F	F					
11H-CC	118.8	F	G										R		R	F					
12H-4, 124–128	123.9	F	M	R			R								R	R					
12H-CC	127.5	F	G	R																	
13H-CC	127.6	F	G	R																	
15P-CC	129.5	F	M	R												R					
16H-CC	130.0	F	M												R	R					
18X-CC	147.3	F	G										R		F	R					
22X-CC	186.1	R	G	R												R					
24X-CC	197.7	F	G	R											F	R					
25X-CC	200.7	C	G	F									F						Cool	CD12 to CD14	
26X-CC	215.4	C	G	F												F					
30X-CC	235.1	R	G												R						
31X-CC	246.8	R	M										R		R	R					
32X-CC	250.8	C	G	R											F						
34X-CC	261.7	R	P												R						
36X-CC	268.1	R	M													R					
37X-CC	275.4	F	M	F		F							R		F	R					
38X-CC	284.2	R	P	R									R								
41X-CC	316.4	F	M							F	R				R			R			
42X-CC	320.2	R	P	R						R							R				
44X-CC	338.7	R	M												R						

Notes: Zonations and surface-water paleotemperatures are also given. Dextral (d) and sinistral (s) N. pachyderma are listed separately. A = abundant, C = common, F = few, R = rare, G = good preservation, M = moderate preservation. See "Explanatory Notes" chapter (this volume) for an explanation of the categories.

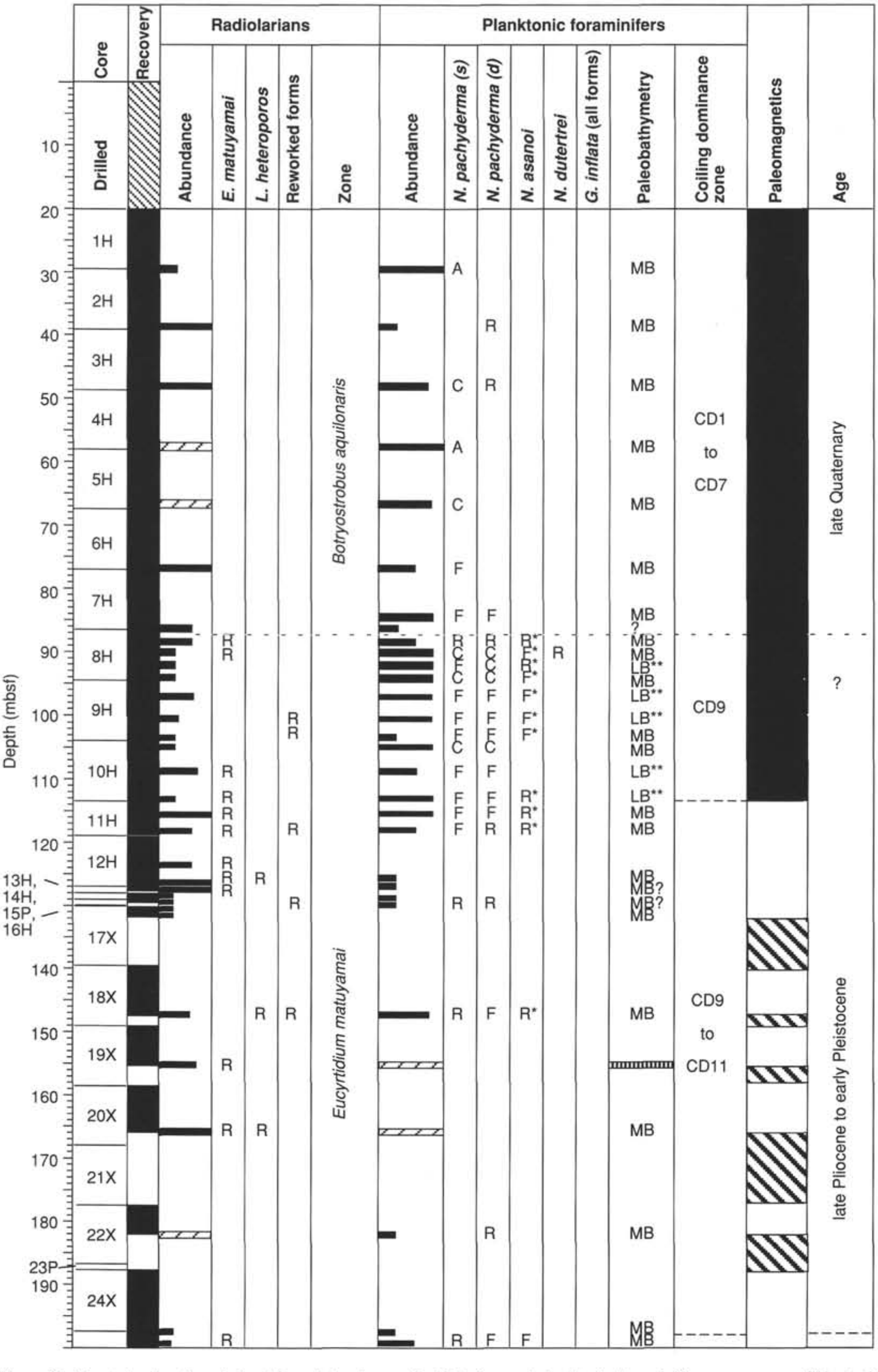

Figure 34. Chart showing the relationships of abundance of radiolarians and planktonic foraminifers, occurrence of biostratigraphic markers, coiling zonation, paleobathymetry, and paleomagnetics for Hole 889A. The hiatus at 88 mbsf is shown. See the "Explanatory Notes" chapter (this volume) for an explanation of the categories represented by the symbols.

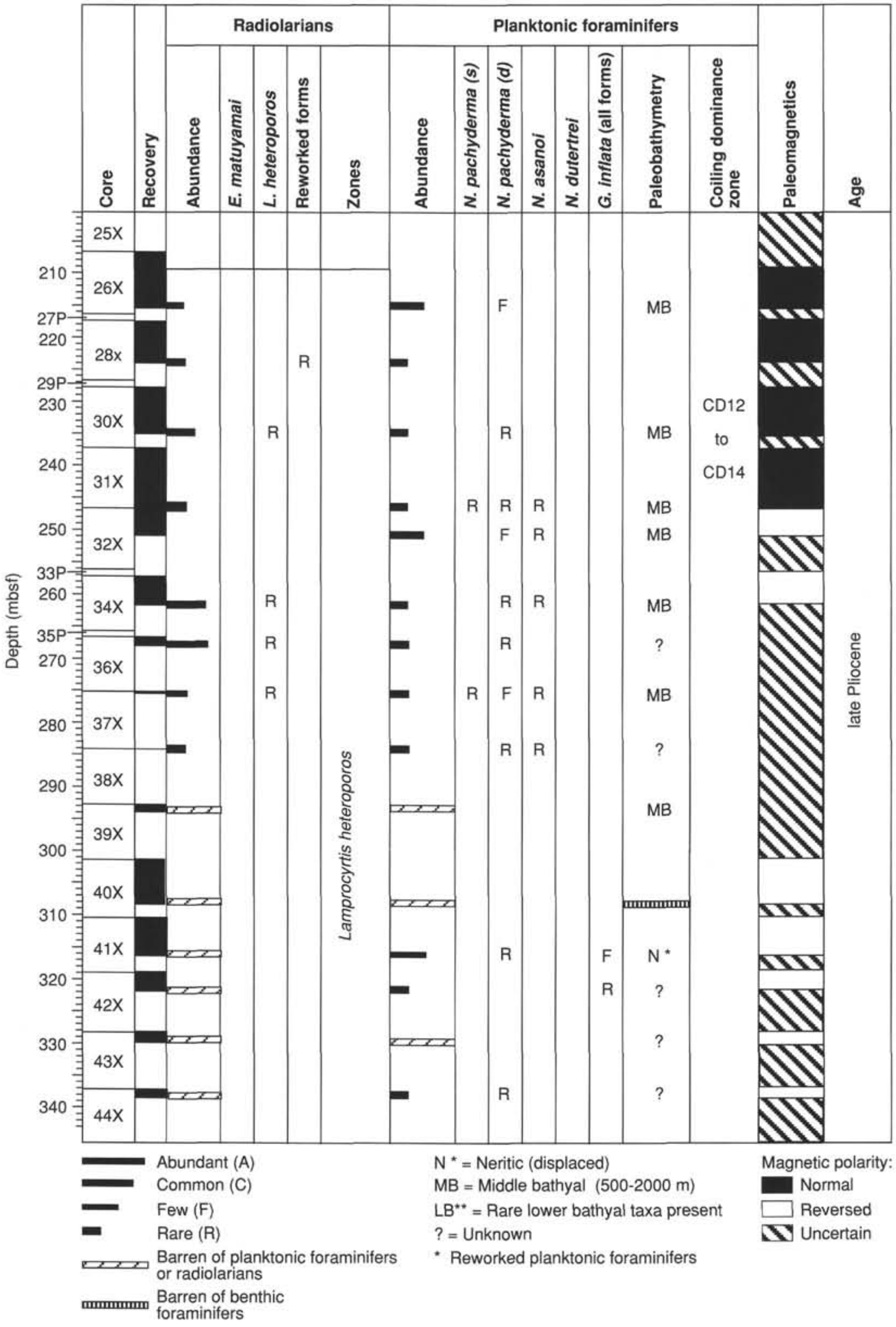

Figure 34 (continued).

with the normal paleomagnetic signature of these sediments (see "Paleomagnetism" section, this chapter).

Benthic Foraminifers

All core-catcher samples except Samples 146-889A-19X-CC (155.3 mbsf) and -40X-CC (308.7 mbsf) contain moderately to well-preserved benthic foraminifers. Benthic foraminifers are common to abundant in the interval from 20 to 128 mbsf, rare to common from 128 to 300 mbsf, and rare to few below 300 mbsf. A preliminary list of benthic foraminifers identified at this site is provided in Table 3.

Most assemblages from 20 to 92 mbsf are dominated by *Bolivina spissa, Bulimina subacuminata, Cassidulina translucens, Epistomi-*

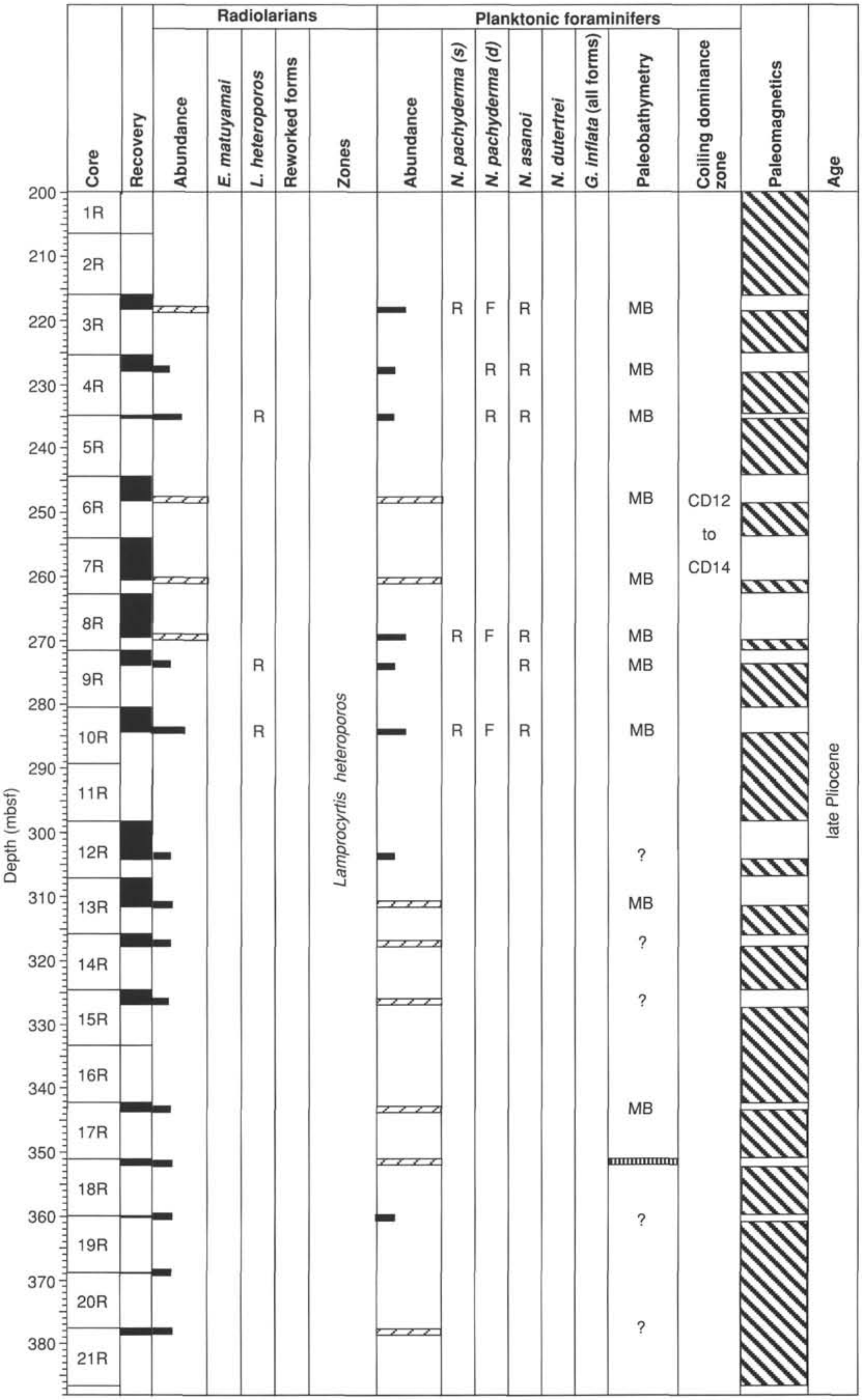

Figure 35. Chart showing the relationships of abundance of radiolarians and planktonic foraminifers, occurrence of biostratigraphic markers, zonation, paleobathymetry, and paleomagnetics for Hole 889B. Symbols as in Figure 34.

Table 3. Preliminary list of benthic foraminifers recovered in Holes 889A, 889B, and 889D.

Benthic foraminifers	Holes		
	889A	889B	889D
Bolivina interjuncta	X		X
Bolivina seminuda			X
Bolivina subadvena			X
Bolivina spissa	X	X	X
Bolivinita quadrilatera	X		
Buccella tenerrima	X		
Bulimina striata	X	X	X
Bulimina subacuminata	X		
Buliminella curta			X
Buliminella exilis	X		X
Buliminella subfusiformis	X		
Cassidulina cushmani	X		
Cassidulina limbata	X		
Cassidulina minuta	X	X	X
Cassidulina spp.	X	X	X
Cassidulina translucens	X	X	X
Cassidulinoides bradyi	X	X	X
Chilostomella czizeki		X	
Chilostomella oolina	X		
Cibicides floridanus	X		
Cibicides spp.	X		
Cibicidoides mckannai	X		
Cibicidoides wuellerstorfi	X	X	X
Dentalina spp.	X	X	
Elphidiella hannai	X		
Elphidium batialis	X		
Elphidium excavatum clavatum			X
Elphidium spp.	X		
Epistominella pacifica	X	X	X
Eponides sp.	X		
Fissurina sp.	X		
Glandulina laevigata	X		
Globobulimina affinis	X	X	
Globobulimina pacifica	X	X	X
Globobulimina sp.	X	X	
Globocassidulina subglobosa	X		X
Guttulina sp.	X		
Gyroidina multilocula	X	X	X
Lagena spp.	X		
Lagena melo	X		
Lagena striata	X		
Lenticulina sp.	X		
Martinotiella communis	X	X	
Melonis barleeanum	X		X
Melonis pompilioides			X
Nodosaria tornata	X	X	
Nonionella miocenica	X		
Nonionellina labradorica	X		X
Oridorsalis umbonatus	X	X	X
Plectofrondicularia advena	X	X	X
Pullenia bulloides	X		
Pullenia salisburyi	X	X	X
Pyrgo spp.		X	X
Quinqueloculina spp.	X	X	
Rhabdammina-Bathysiphon	X	X	
Saccammina sphaerica	X		
Stilostomella advena	X		
Tosaia hanzawai	X		
Trifarina fluens	X		
Uvigerina dirupta	X		
Uvigerina hispida	X		X
Uvigerina peregrina	X	X	X
Uvigerina senticosa			X
Valvulineria araucana	X		
Valvulineria sp.			X

nella pacifica, Globobulimina pacifica, Oridorsalis umbonatus, and *Uvigerina peregrina.* The occurrence of *B. spissa, B. subacuminata, E. pacifica,* and *O. umbonatus* indicates deposition in a middle bathyal environment for this interval. Common upper bathyal taxa such as *C. translucens, G. pacifica,* and *U. peregrina* and rare neritic faunas suggest transport mainly from upper bathyal environments.

In addition to containing the assemblage described herein, the interval from 92 to 128 mbsf, which corresponds to lithostratigraphic Subunit IB, contains rare lower bathyal *Cibicidoides wuellerstorfi* and *Pullenia bulloides,* which are probably reworked (see below).

Benthic foraminiferal assemblages in the interval from 128 to 300 mbsf are rare to common and are dominated by the taxa listed previously. This is indicative of deposition in a middle bathyal environment. Samples 146-889A-17X-CC (132.0 mbsf), 146-889A-22X-CC (186.1 mbsf), and 146-889A-26X-CC (215.4 mbsf) contain rare, poorly preserved, and probably reworked specimens of *C. wuellerstorfi* and *Plectofrondicularia advena.*

With the exception of Sample 146-889A-41X-CC (316.4 mbsf), samples below 300 mbsf are either barren or contain rare benthic foraminifers. Sample 146-889A-41X-CC (316.4 mbsf) consists of common *Dentalina, Globocassidulina subglobosa, C. californica, Fissurina* sp., *Lenticulina* sp., and *Pyrgo* sp., indicating the transport of neritic taxa into a middle bathyal environment.

Discussion

It is difficult to determine the age of the interval from 89.2 to 119.0 mbsf because of the association of *E. matuyamai, N. asanoi,* mixed sinistral and dextral populations of *N. pachyderma,* and reworked lower Pliocene radiolarians. The first occurrence of *E. matuyamai* and the last occurrence datum for *N. asanoi* are at 1.9 Ma according to the time scale of Cande and Kent (1992). It is unlikely that the sediments within the interval from 89.2 to 119.0 mbsf were deposited within the overlap in ranges of these taxa because of the presence of mixed populations of dextral and sinistral *N. pachyderma.* The short overlap in ranges of *E. matuyamai* and *N. asanoi* occurs within a zone of sinistrally coiled *N. pachyderma,* not one with mixed coiling. Like the lower Pliocene radiolarians, the rare to few specimens of *N. asanoi* found in samples within the interval from 89.2 to 119.0 mbsf are thus considered to be reworked. Therefore, based on the occurrence of *E. matuyamai* and the mixed dextral and sinistral *N. pachyderma,* the interval from 89.2 to 119.0 mbsf is considered to be in the CD9 coiling zone. This is consistent with the assignment to the *E. matuyamai* Zone based on radiolarians and the normal paleomagnetic signature (see "Paleomagnetism" section, this chapter).

In addition, within the interval between 89.2 and 119.0 mbsf, rare benthic foraminifers indicative of a lower bathyal environment (*C. wuellerstorfi* and *P. bulloides*) are present in some, but not all, of the samples examined. Other benthic assemblages in this interval suggest deposition in a middle bathyal environment. The rare lower bathyal benthic foraminifers are probably reworked.

The interpretation of the biostratigraphy and paleoenvironment of this interval is as follows: upper Pliocene sediments that were deposited in a lower bathyal environment were uplifted to a middle bathyal or shallower environment and then eroded, transported, and mixed and redeposited with lower Pleistocene faunas. This is consistent with the interpretation of a series of slumps/debris flows that have been interpreted in this interval based on sedimentological evidence (see "Lithostratigraphy" section, this chapter).

Hole 889B

Radiolarians

All core-catcher samples from Hole 889B were examined for radiolarians. Sample 146-889B-3R-CC (218.2 mbsf) is barren of radiolarians. Rare to few representatives of the North Pacific radiolarian assemblage were found in Samples 146-889B-4R-CC and -5R-CC (228.2 and 235.2 mbsf, respectively). The occurrence of *L. heteroporos* and the absence of *E. matuyamai* suggest a late Pliocene age for this interval. Samples 146-889B-6R-CC through -8R-CC (248.2–269.5 mbsf) are barren of radiolarians. Rare radiolarians of late Pliocene age were observed in Samples 146-889B-9R-CC and -10R-CC (273.9 and 284.4 mbsf, respectively). Further downhole in Hole 889B, all core-catcher samples contain very rare radiolarians. No stratigraphic markers were recognized. Radiolarian species characteristic of upwelling environments such as *Acrosphaera murrayana* and *Phormostichoartus crustula* were found in Sample 146-889B-14R-CC (317.8 mbsf).

Planktonic Foraminifers

Eight of the 16 core-catcher samples from Hole 889B examined for planktonic foraminifers contain rare to few, poorly to well-preserved *G. bulloides* and *N. pachyderma* (dextral). *Globorotalia scitula, G. quinqueloba, N. asanoi,* and *N. pachyderma* (sinistral) are rare in this hole. The presence of *N. asanoi* in the intervals from 235.2 to 253.9 mbsf and 269.5 to 284.4 mbsf indicates a late Pliocene age for these sediments. Below 284.4 mbsf planktonic foraminifers are rare or the samples are barren (Table 3).

Benthic Foraminifers

Well-preserved, common to abundant benthic foraminifers dominated by *B. spissa, E. pacifica, O. umbonatus,* and *U. peregrina* occur from 235 to 285 mbsf in Hole 889B along with the other taxa listed in Table 3. Sediments in this interval were deposited in a middle bathyal environment. Below 285 mbsf, benthic foraminifers are rare and their preservation is poor to moderate.

Hole 889D

Radiolarians

All core-catcher samples from Hole 889D were examined for radiolarians. Rare to few radiolarians were found in Samples 146-889D-1H-CC through -3X-CC (89.7–141.2 mbsf). No stratigraphic markers were recognized. Sample 146-889D-4N-CC (151.9 mbsf) is barren of radiolarians.

Planktonic Foraminifers

Samples 146-889D-1H-CC (89.7 mbsf) and 146-889D-4N-CC (151.9 mbsf) have common to abundant, well-preserved planktonic foraminifers. Sample 146-889D-1H-CC (89.7 mbsf) contains abundant *N. pachyderma* (sinistral), common *G. bulloides,* rare *N. pachyderma* (dextral), and rare *G. scitula,* which together indicate cold surface waters and deposition within a left-coiling zone. Samples 146-889D-2W-CC (115.0–140.0 mbsf) and 146-889D-3X-CC (141.2 mbsf) contain rare *G. bulloides* and *N. pachyderma* (sinistral and dextral). Sample 146-889D-4N-CC (151.9 mbsf) contains few *G. bulloides,* common *N. pachyderma* (dextral), and rare *N. pachyderma* (sinistral), indicating temperate surface waters and deposition within a right-coiling zone. Analyses on additional samples are needed to apply the *N. pachyderma* coiling zonation.

Benthic Foraminifers

Core-catcher samples from Hole 889D contain common to abundant, well-preserved benthic foraminifers. Samples 146-889D-1H-CC (89.7 mbsf) and 146-889D-2W-CC (washed from 105.0 to 140.0 mbsf) contain a diverse benthic foraminiferal fauna (Table 3) including *C. translucens, E. pacifica, G. pacifica, G. subglobosa,* and *U. peregrina.* Samples 146-889D-3X-CC (141.2 mbsf) and 146-889D-4N-CC (151.9 mbsf) contain low-diversity assemblages with *C. translucens, E. pacifica,* and *G. pacifica.* The occurrence of *U. senticosa, C. wuellerstorfi,* and *Melonis pompilioides* in Sample 146-889D-1H-CC (89.7 mbsf) and *P. advena* in Samples 146-889D-2W-CC (115.0–140.0 mbsf), 146-889D-3X-CC (141.2 mbsf), and 146-889D-4N-CC (151.9 mbsf) suggests deposition in a lower bathyal environment.

Holes 890A and 890B

Radiolarians

All core-catcher samples from Site 890 were examined for radiolarians. Sample 146-890A-1H-CC (3.7 mbsf) contains a well-diversified radiolarian assemblage assigned to the late Pleistocene *B. aquilonaris* Zone.

Few radiolarians, representative of the late Pleistocene *B. aquilonaris* Zone, were found in Sample 146-890B-1H-CC (7.3 mbsf). Samples 146-890B-2H-CC to -5H-CC (17.5–48.8 mbsf) are barren of radiolarians.

Planktonic Foraminifers

The five core-catcher samples from Holes 890A and 890B contain planktonic foraminiferal assemblages consisting of abundant, well-preserved *G. bulloides, Globigerina umbilicata, N. pachyderma* (sinistral), and *G. quinqueloba.* There are also rare to few occurrences of *G. scitula, Globigerinita glutinata,* and *N. pachyderma* (dextral). No definite age determinations can be made from this section based on planktonic foraminifers. The dominance of sinistral *N. pachyderma* suggests cold surface waters.

Benthic Foraminifers

Core-catcher samples from Holes 890A and 890B contain assemblages dominated by *B. spissa, Buliminella exilis, Cassidulina californica, Cassidulinoides bradyi, Chilostomella oolina, Elphidium excavatum clavatum, E. pacifica, G. pacifica, Quinqueloculina* spp., and *U. peregrina.* These assemblages indicate downslope transport of neritic through upper bathyal faunas into a middle bathyal environment. Additional taxa identified from Site 890 are listed in Table 4.

PALEOMAGNETISM

Paleomagnetic study of undisturbed split cores and discrete samples from Holes 889A, 889B, and 890B was conducted to constrain the ages of the lithostratigraphic units at this site. Alternating-field (AF) demagnetization up to 15 mT of the split cores did not yield a clearly interpretable magnetostratigraphy on account of the presence

Table 4. Preliminary list of benthic foraminifers recovered in Holes 890A and 890B.

Bolivina spissa
Bolivina subadevena
Bulimina aculeata
Bulimina striata
Bulimina subacuminata
Buliminella curta
Buliminella exilis
Buliminella subfusiformis
Cassidulina californica
Cassidulina cushmani
Cassidulina minuta
Cassidulina spp.
Cassidulina translucens
Cassidulinoides bradyi
Chilostomella czizeki
Chilostomella oolina
Cibicidoides mckannai
Cibicidoides wuellerstorfi
Elphidium batialis
Elphidium excavatum clavatum
Elphidium spp.
Epistominella pacifica
Eponides sp.
Fissurina lucida
Globobulimina auriculata
Globobulimina pacifica
Gyroidina multilocula
Lagena spp.
Lagena striata
Nonionellina labradorica
Oridorsalis umbonatus
Pullenia bulloides
Pullenia salisburyi
Pyrgo spp.
Pyrgo rotalaria
Quinqueloculina spp.
Trifarina fluens
Uvigerina dirupta
Uvigerina peregrina
Valvulineria araucana

of a strongly magnetized, high-coercivity mineral throughout most of the cored section. Rock-magnetic study indicated that the high-coercivity phase in these rocks is pyrrhotite and/or greigite. Because these minerals are of diagenetic origin, the remanence that they carry is by definition a secondary magnetization. The magnetostratigraphy below 120 mbsf was constructed largely by means of vector difference diagrams. A preliminary magnetostratigraphy is shown in the master chart (see Fig. 104).

Paleomagnetism

Declination, inclination, and intensity plots for the split-core sections taken at Sites 889 and 890 are shown in Figure 36. Two types of remanence were observed at this site. The first type, in which intervals of consistent inclination can be identified, occurs in the interval from 0 to 120 mbsf. From 0 to 60 mbsf the inclination is steeply inclined downward (normal polarity) after removal of a steeply inclined upward overprint. Steeply upward (reversed polarity) directions were found from 60 to 120 mbsf. Below 120 mbsf, the second type of remanence is observed, with both the declination and inclination of the split-core sections highly scattered.

Examination of the demagnetization behavior of the split-core sections from Sites 889 and 890, particularly those from below 120 mbsf, found little or no drop in remanence intensity during demagnetization to a nominal value of 15 mT in the 2-G magnetometer. Later examination of discrete samples from Site 891 led to an investigation of the AF demagnetization coils in the 2-G magnetometer, and found that the peak AF generated by the coils was less than 5 mT, which accounts for the lack of intensity drop observed in the split-core section data from Sites 889 and 890. A more detailed study of the remanence using higher alternating fields was conducted with two or more discrete samples from each intact core. The samples were demagnetized up to 80–100 mT using steps of 5 or 10 mT. Demagnetization behavior using alternating fields above 30 mT showed stable, decreasing remanence intensity, from which well-defined characteristic remanence directions were obtained. The discrete samples from the interval 0–125 mbsf have well-grouped directions, with positive inclinations observed from 0 to 112 mbsf, and negative inclinations from 113 to 125 mbsf (Figs. 37–38). This is in contrast to the behavior of the split-core sections after partial (5 mT?) demagnetization, in which the interval from 60 to 120 mbsf has negative inclinations. The paleontologic results (see "Biostratigraphy" section, this chapter) indicate that the Brunhes/Matuyama boundary should occur at about 87 mbsf in lithostratigraphic Subunit IB, based on the appearance of the radiolarian *Eucyrtidium matuyamai* along with older, reworked radiolarians. The sediments in this unit are interpreted as sediment-slump/debris-flow deposits (see "Lithostratigraphy" section, this chapter). The occurrence of both normal and reversed polarity intervals within Subunit IB indicates that this unit does not, however, represent a single slump/flow event, but that it represents several depositional events over time. The depositional age of these slump/flow events is entirely within the Matuyama (R) Chron, based on the occurrence of the unreworked *E. matuyamai,* so the normal polarity results from 87 to 113 mbsf must represent one of the normal polarity subchrons within the upper part of the Matuyama (R) Chron. We therefore assign the interval from 87 to 113 mbsf to the Jaramillo (N) Subchron, with the onset of the Jaramillo occurring at 113 mbsf, providing an age of 1.049 Ma (Cande and Kent, 1992) for the core at this depth.

Below 125 mbsf, the remanence results from discrete samples are scattered. Examination of the samples from this interval finds that in the majority of samples the remanence is either of constant intensity or increases in intensity during AF demagnetization (Fig. 38), in contrast to the stable demagnetization behavior observed in the samples from above 125 mbsf. The AF demagnetization behavior of the samples from below 125 mbsf is consistent with observations of ineffective AF demagnetization of high-coercivity magnetic sulfides using high-frequency (>300 Hz) alternating fields (Dekkers, 1988).

To determine if magnetic sulfides are present in these rocks, isothermal remanent magnetization (IRM) acquisition and multicomponent IRM (mIRM) thermal demagnetization (Lowrie, 1990) experiments were conducted. The majority of the IRM is acquired between 0.02 and 0.01 T (Fig. 39), with little increase in IRM intensity above 0.2 T. These coercivity ranges are found in coarse-grained magnetite and pyrrhotite (Dekkers, 1988). To determine which of these minerals is present, mIRM thermal demagnetization was conducted. IRMs of 1.2, 0.4, and 0.2 T were applied to sample cubes in three orthogonal directions, and then the samples were thermally demagnetized in steps up to 650°C. The 0.2 T component carried the majority of the remanence, whereas the two higher coercivity components carried little of the sample's magnetization. The results show two thermal unblocking temperatures for the 0.2 T component, one between 250° and 320°C and the other between 550° and 580°C (Fig. 40). Coarse-grained pyrrhotite has a coercivity lower than 0.2 T and an unblocking temperature between 250° and 300°C. The coercivity of greigite is less well known, but is probably similar to that of pyrrhotite for coarse grain sizes. Greigite thermally decomposes at temperatures of about 200° to 300°C (Krs et al., 1990; Musgrave et al., 1993; R.L. Reynolds, pers. comm., 1991). Only magnetite has coercivity lower than 0.2 T and an unblocking temperature between 550° and 580°C. From these observations, we know that both magnetic sulfides and magnetite occur in these rocks. Furthermore, because the samples below 120 mbsf either remain at constant intensity or increase in intensity during AF demagnetization, it is likely that the magnetic sulfides carry the majority of the remanence in these samples. Because both greigite and pyrrhotite are secondary minerals, the remanence that they carry is by definition a secondary remagnetization. The inclination of the remanence in the discrete samples from below 120 mbsf is predominantly positive, indicating normal polarity. This observation, combined with the occurrence of the base of the Jaramillo Subchron at 113 mbsf, leads us to conclude that the magnetic sulfides formed diagenetically during the Brunhes Chron, placing a maximum age of sulfide mineral diagenesis at 0.78 Ma (Cande and Kent, 1992).

Several of the samples display significant increases in intensity during AF demagnetization. Many of these samples also show no corresponding change in direction as the intensity increases (Figs. 38C and 38D). This behavior indicates that the AF demagnetization is removing a direction that is antipodal to that carried in the magnetic sulfides and that is carried in a low-coercivity mineral. This low-coercivity direction can be recovered by analysis of the vector difference between successive demagnetization steps. The results of this exercise (Fig. 41), although noisy, show that the majority of the vectors removed by AF demagnetization are of reversed polarity. Because this direction is easily removed by AF demagnetization, and is carried by a low-coercivity mineral, we conclude that magnetite is the carrier of this reversed polarity direction, and that this direction represents the primary remanence of these rocks. We have placed the termination of the Olduvai (N) Subchron (1.757 Ma; Cande and Kent, 1992) at 210 mbsf, based on our vector-difference results and on constraints from paleontology (see "Biostratigraphy" section, this chapter). A more reliable and detailed magnetostratigraphy awaits shore-based work, using thermal demagnetization on discrete samples to determine the remanent directions carried by magnetite in the cores below 120 mbsf and the nature of the magnetic sulfides present in these rocks.

Rock Magnetism

Anhysteretic remanent magnetization (ARM) acquisition studies (Fig. 42) found two distinct types of ARM behavior in these rocks. Samples from 0 to 50 mbsf in Holes 889A and 890B show significant ARM acquisition in alternating fields of 0 to 24 mT. Below 50 mbsf, little ARM is acquired by the samples. IRM studies of the same samples from Hole 890B found similar results (Fig. 43), with nearly all of the IRM acquired between 0.02 and 0.2 T in samples from 0 to 50 mbsf. Samples from depths below 50 mbsf had a larger proportion

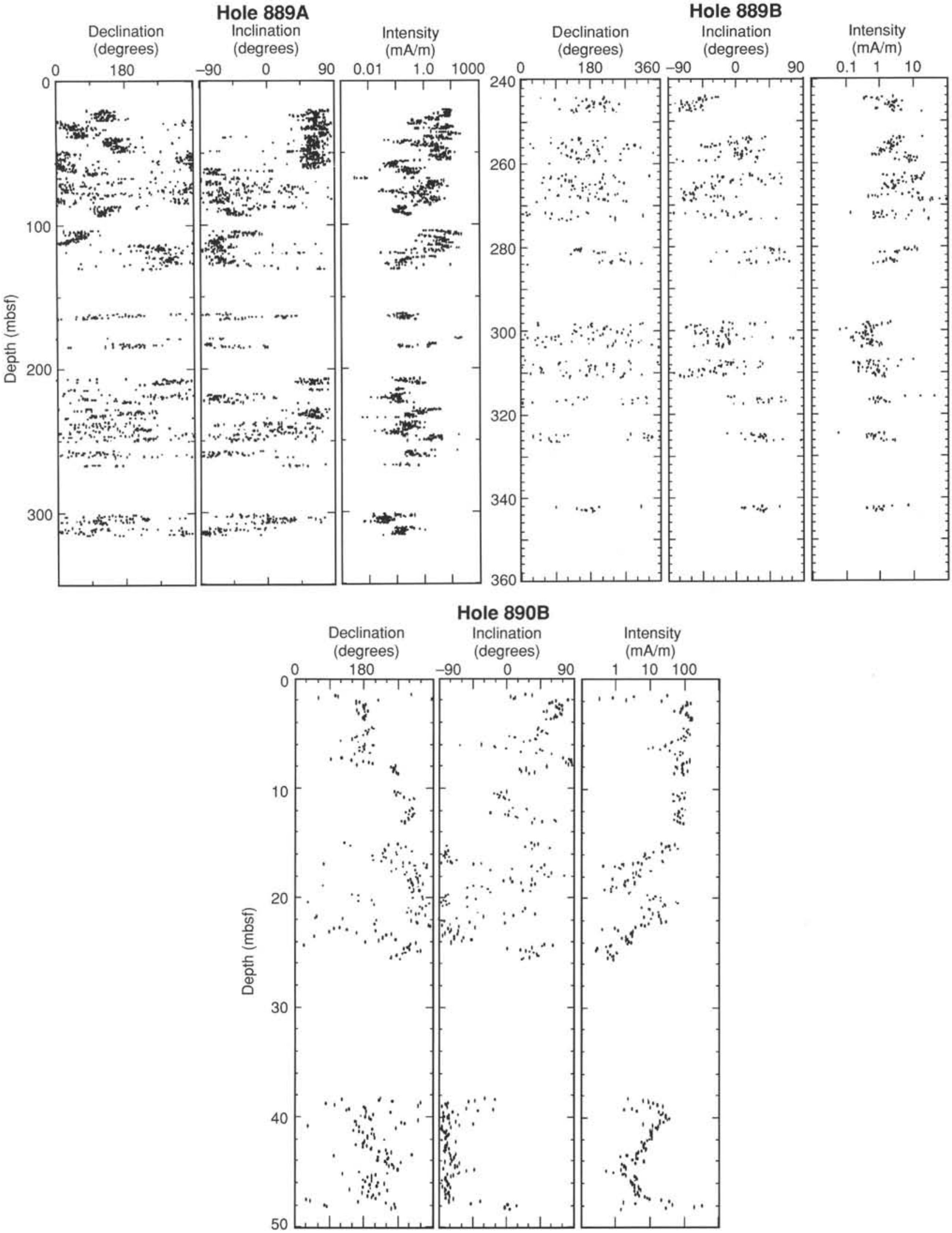

Figure 36. Declination, inclination, and intensity plots of split-core section remanence after (nominal) 15-mT AF demagnetization for Holes 889A, 889B, and 890B. From 20 to 128 mbsf in Hole 889A, the data are corrected for orientation using Tensor or Eastman-Whipstock multishot data.

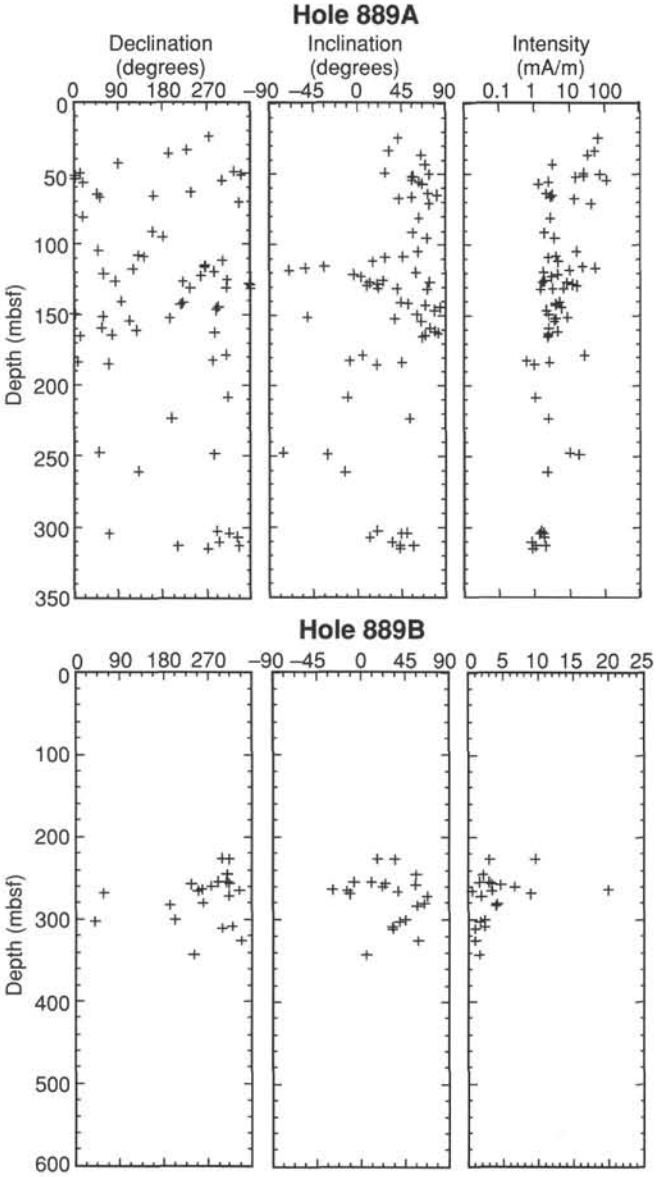

Figure 37. Declination, inclination, and intensity plots for discrete samples after 30-mT AF demagnetization for Holes 889A and 889B. The results are corrected for orientation from 20 to 128 mbsf.

of IRM acquisition above 0.2 T, indicating the presence of higher coercivity material in the sediments below 50 mbsf. The mIRM results indicated that magnetic sulfides are present in these sediments; the growth of magnetic sulfides below 50 mbsf would account for both the higher coercivity observed below 50 mbsf and the change in AF demagnetization behavior observed in this interval.

Magnetic susceptibility from the multisensor track (MST) shows a decrease in susceptibility between lithostratigraphic Units I and II. The susceptibility of Unit I varies between 10×10^{-8} and 300×10^{-8} SI units, and for Unit II the susceptibility ranges from 5×10^{-8} to 60×10^{-8} (Fig. 44). Cryogenic susceptibility tests were performed to identify the primary contributors to the low-field susceptibility. Three samples from Hole 889A were cooled to 77 K in liquid nitrogen, and were placed in an insulated sample holder. As the sample heated to room temperature (293 K), magnetic susceptibility was measured with the SI-2 device and sample temperature was measured with a

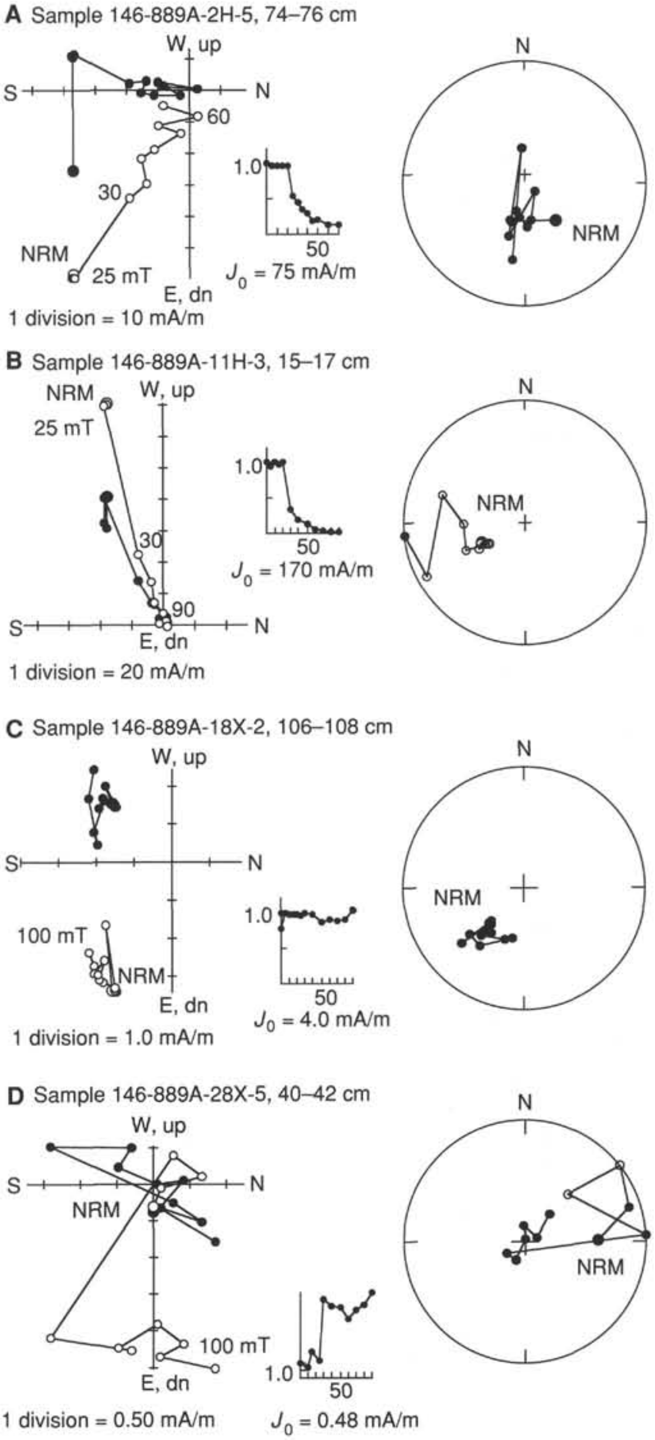

Figure 38. Demagnetization plots for discrete samples from Hole 889A. The magnetization vectors are plotted on stereographic projections (open symbols are up, filled symbols are down), as Zijderveld diagrams (filled symbols are on the horizontal plane, open symbols on the vertical plane), and as intensity vs. demagnetization plots. Samples from above 120 mbsf display well-behaved normal polarity (**A**) and reversed polarity (**B**) directions. Below 120 mbsf, the results are less well behaved and usually show no change in direction and either constant intensity (**C**) or an increase in intensity (**D**) during AF demagnetization to 90 mT. An apparent failure to demagnetize significantly during AF treatment up to 25 mT arose from a malfunction of the AF coils in the 2-G magnetometer, which prevented the coils from reaching their nominal field values.

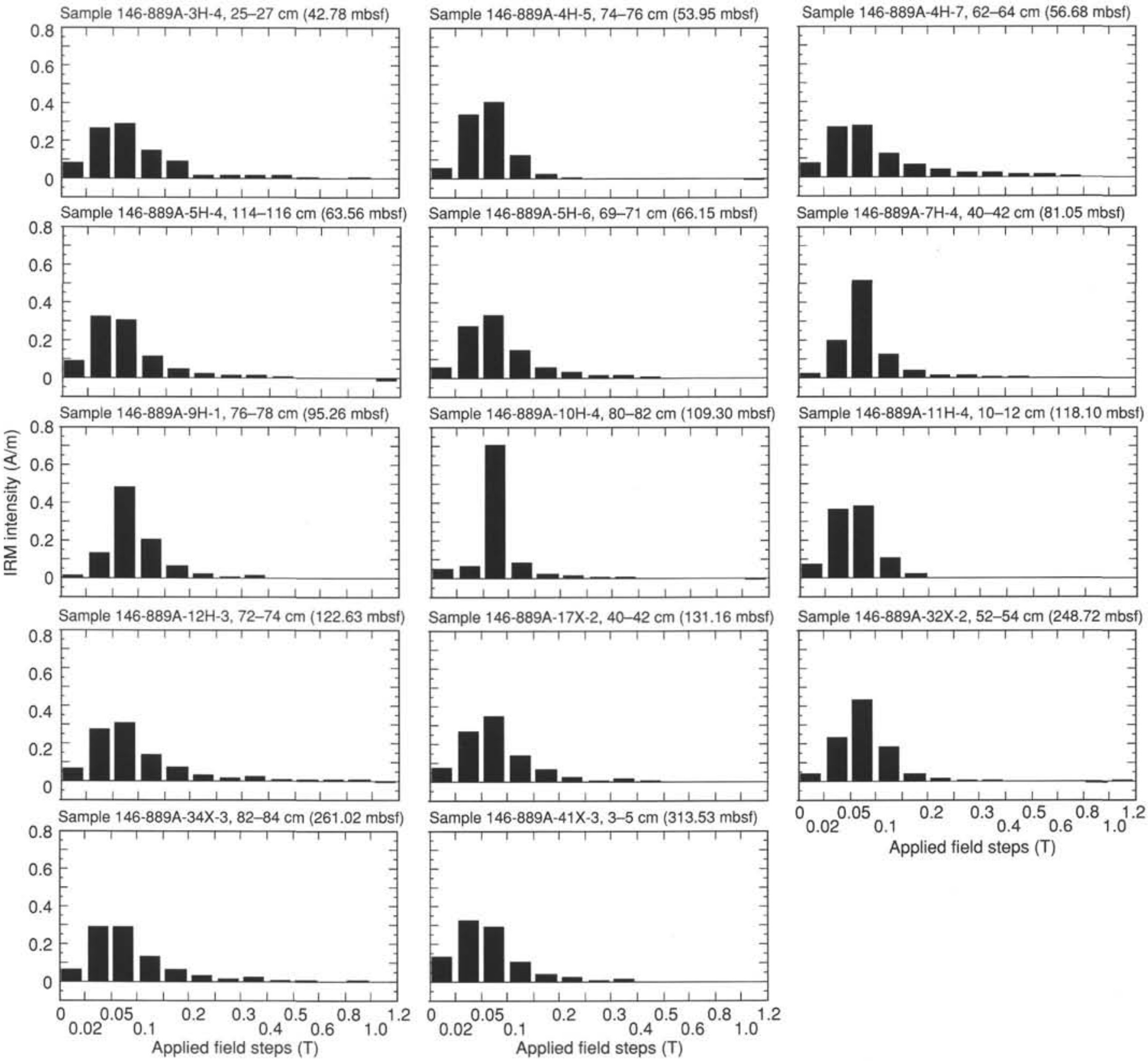

Figure 39. Isothermal remanent magnetization acquisition results for samples from Hole 889A. The vertical axes are IRM intensities (A/m), and the horizontal axes are the pulse-field steps (T). The majority of the IRM in all samples are acquired below 0.2 T, indicating predominately low-coercivity magnetic minerals in these sediments.

thermocouple. The inversely proportional relationship between the measured susceptibility and temperature (Fig. 45) indicate that paramagnetic minerals, most likely clay minerals, account for nearly all of the low-field susceptibility. This indicates that the anisotropy of magnetic susceptibility (AMS) results (see "Structural Geology" section, this chapter) measure the preferred orientation of clay minerals (Richter et al., 1993) at this site.

STRUCTURAL GEOLOGY

Introduction

Sites 889 and 890 penetrated undeformed slope deposits and into partially lithified, pervasively fractured silts representing either accreted abyssal plain sediments or deformed older slope basin deposits. Below 130 mbsf, the cores were typically disaggregated into subcentimeter-size angular mud chips, probably because of in-situ fractures, providing little intact material on which to base structural observations.

The intervals drilled at Sites 889 and 890 comprise three distinct structural domains. Structural measurements are tabulated in Tables 5 and 6. The characteristics of these three domains are:

Domain I: Subhorizontal to shallowly dipping, poorly indurated and little-deformed slope basin turbidites and pelagics, with minor subvertical faulting.

Domain II: Moderate to steeply westward-dipping bedding, similar in composition and degree of induration to Domain I.

Domain III: Pervasively fractured silts and siltstones with variable dips. The degree of lithification varies downhole but generally increases with depth. Numerous sets of fractures are developed with a wide range of inclinations from about 20° to about 70°, commonly

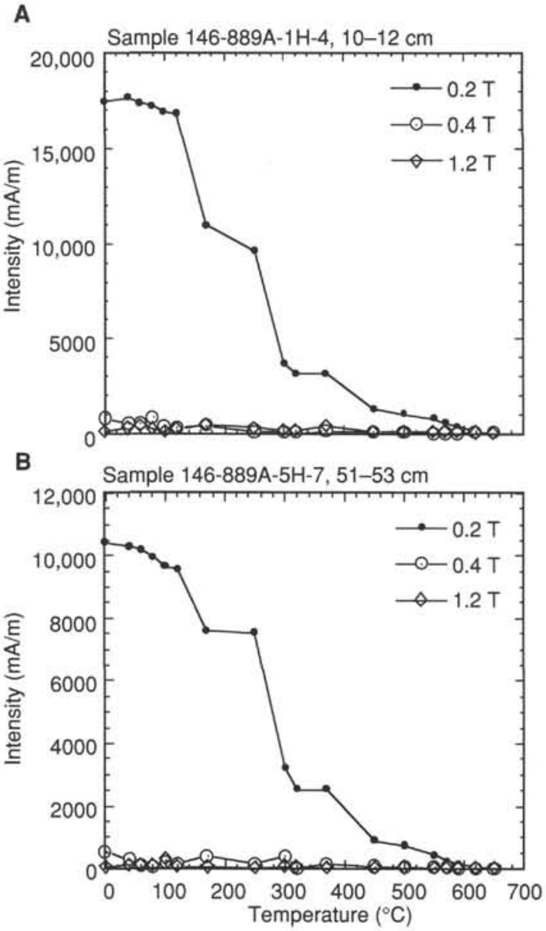

Figure 40. Multicomponent IRM thermal demagnetization results. Three orthogonal IRMs were given to each sample. Remanence is in each of the three orthogonal directions is plotted vs. thermal demagnetization steps. Two unblocking temperatures are observed for the 0.2 T component, one between 250° and 320°C, the other between 550° and 580°C. This pattern indicates that both magnetic sulfides and magnetite are present as remanence carriers in these rocks.

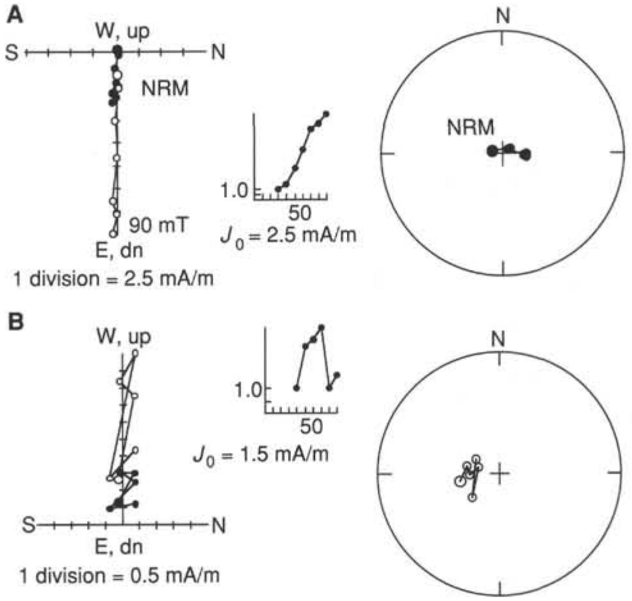

Figure 41. **A.** Results of vector-difference analysis of a typical sample (146-889A-20X-3, 107–109 cm [162.67 mbsf]) from below 120 mbsf that displayed increasing remanence intensity and constant remanence direction during AF demagnetization. **B.** The vector difference between successive demagnetization steps was determined for this same sample. Conventions for the plots of both the total vectors and the difference vectors are as in Figure 38. The majority of the removed remanence is reversed polarity in this interval.

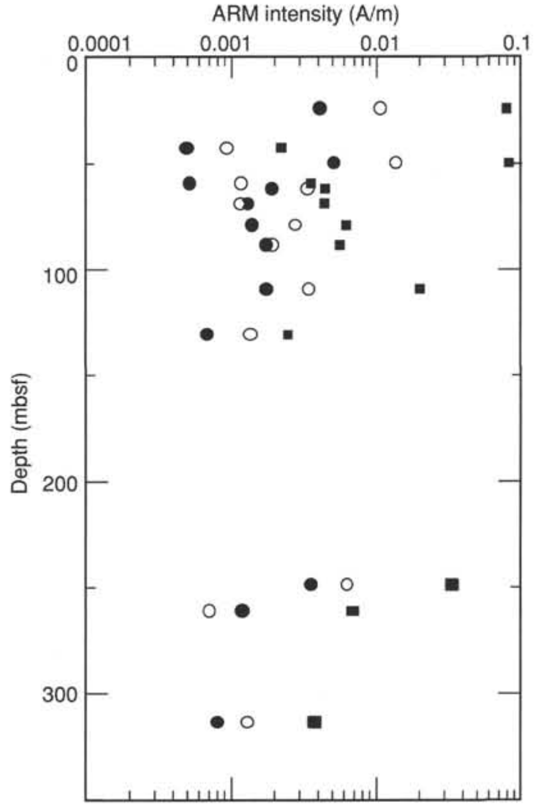

Figure 42. Results of ARM acquisition for samples from Hole 889A. Results for AF levels of 3 mT are plotted as filled dots, 6-mT results as open dots, and 20-mT results as filled squares. Note that the highest intensity ARM occurs in the 20-mT coercivity range, and that samples above 50 mbsf acquire a much stronger ARM than those below 50 mbsf.

exhibiting weakly developed, polished curviplanar surfaces and slickenlines of varying orientation. We interpret these fractures as an expression of incipient scaly foliation. The fracturing is remarkably consistent downhole; it is well-developed from about 130 mbsf to the TD of 386.5 mbsf.

This site is characterized by an overall downward progressive increase in the intensity of deformation, with relatively sharp boundaries to the three domains (Fig. 46). However, even in the most deformed intervals of Domain III, incipient scaly foliation is the only extensively developed core-scale structure. Other observable structural evidence is limited to two occurrences of shear zone deformation bands and two of stratal disruption (all in Domain III). Bedding was very rarely identifiable in Domain III, and bedding attitudes, where present, were typically destroyed by drilling-induced disturbance of the cores. Healed fractures were not observed. Thus, structural information from these sites is inherently limited.

Structural Description

Domain I

Domain I, from 0 to 104 mbsf (Cores 146-890B-1H to -5H and 146-889A-1H to -9H), roughly corresponds to lithostratigraphic Subunit IA of Site 889. It is composed of subhorizontally bedded turbidite sequences. The sediments of Domain I are mostly clayey silt to silty clay, interbedded with some sandy layers. The silts and clays are not

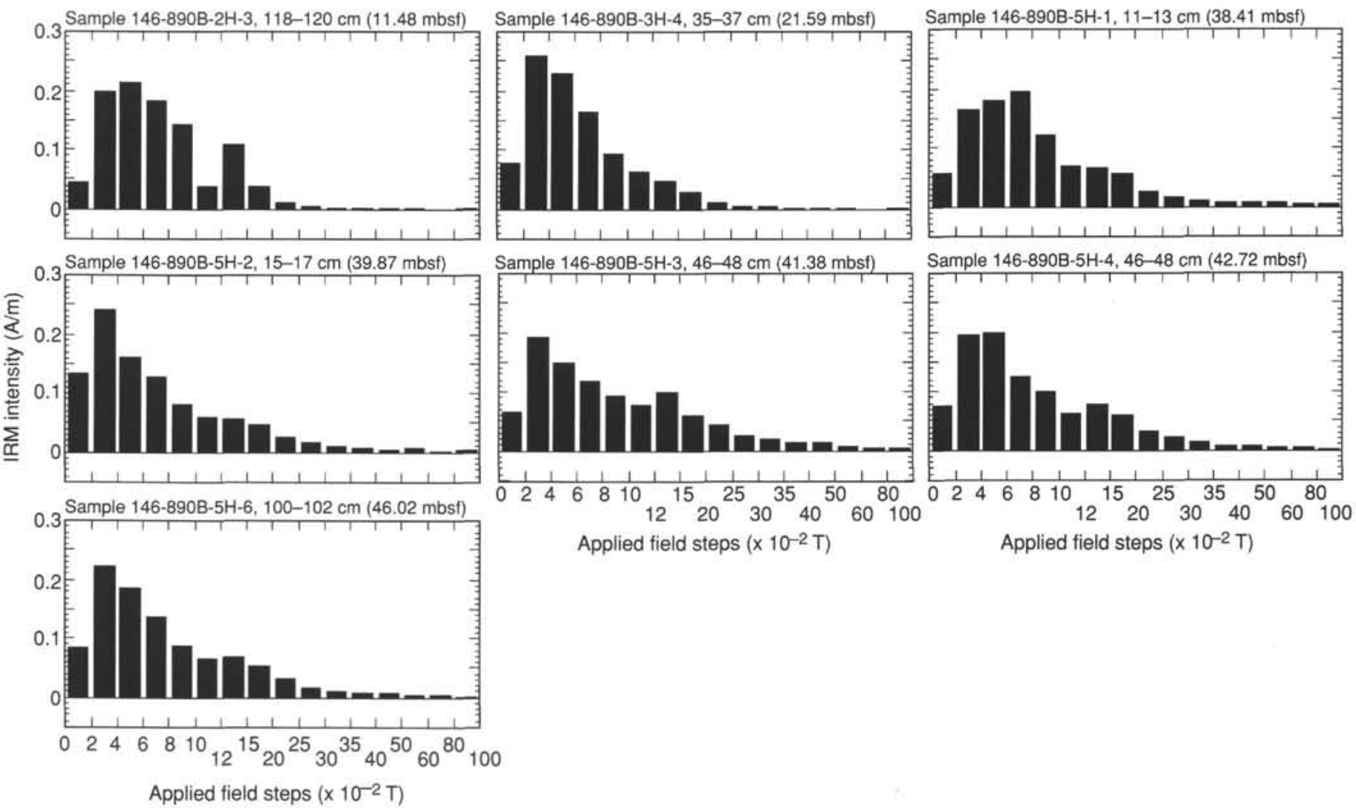

Figure 43. IRM acquisition results from Hole 890B samples. Conventions as in Figure 39.

lithified and deform plastically. Bedding attitudes range from horizontal to 24° true dip (Fig. 47). At 72 mbsf in Section 146-889A-6H-3, a single near-vertical, curving fault is developed, vertically offsetting sand layers by 1 to 2 cm on the core face and extending along the core for 74 cm (Fig. 48). Both apparent normal and high-angle reverse offset are observed because the fault is nonplanar. Bedding in this interval strikes from 270° to 290° in corrected geographic coordinates, and dips as much as 24° to the north (see Table 5). No other core-scale faulting is observed in this domain, although subvertical faulting may be well developed but not well sampled by the vertical drill hole.

We interpret Domain I as little-deformed upper Quaternary (see "Biostratigraphy" and "Paleomagnetism" sections, this chapter) slope basin deposits. The shallowly dipping bedding and small-scale vertical faulting in Cores 146-889A-6H through -9H may represent the initial deformation of these sediments as they are transported in the hanging wall of a much deeper reverse fault system, or they may represent synsedimentary deformation resulting from slumping or local bed-loading. In the multichannel seismic (MCS) data for this site (see Fig. 4 and the "Downhole Logging" section, this chapter), a zone of steep reverse faulting occurs just below Domain I, indicating that the minor faulting and related folding in this domain may be the result of tectonic deformation.

No fractures are present in Domain I that have been interpreted as having formed in situ. However, the cores are commonly disrupted by open fracture surfaces perpendicular to the core axis and associated voids spaced a few to a few tens of centimeters apart, the faces of which exhibit a hackly parting-surface texture. These voids appear to be the product of gas exsolution and expansion during recovery of the cores.

Domain II

The transition to Domain II (104–127 mbsf) is marked by the onset of moderately to steeply dipping beds at 104 mbsf in Core 146-889A-10H (Fig. 49). The transition between Domains I and II is transitional over about 3 m in the base of Core 146-889A-9H and the top of Core 146-889A-10H. Because identifiable bedding surfaces are spaced as much as 2 m apart in this interval, it is not clear whether a sharp unconformity or gradual steepening of attitudes exists between the two domains. Domain II corresponds roughly to lithostratigraphic Subunit IB. No great lithologic or rheologic contrast is present between this interval and Domain I above.

Bedding planes are consistently inclined in Domain II. Attitudes measured in the core reference frame were geographically corrected using orientation data from the multishot tools (see "Explanatory Notes" chapter, this volume). All of the corrected attitudes indicate westward dips of 36° to 74° (Fig. 49). The mean of the measured attitudes strikes 187° and dips 51° to the west, which agrees well with the macroscopic structural trend exhibited in the multibeam bathymetry and seismic imaging of the site. Identifiable bedding planes are sparse in this domain, which is mostly homogeneous clay and silt. No other structural features were observed.

The consistent development of steeply inclined bedding over a 23-m interval suggests a tectonic origin for Domain II deformation. Gravitational slumping may also have occurred; however, no small-scale features (such as tight folds or en echelon extensional microfaults) typically associated with slumping were observed. The depth interval corresponding to Domain II on the MCS data is a zone of reverse faulting (see Fig. 4). There is no direct evidence in the cores that the drill hole intersected one of these faults; however, the MCS data indicate a possible fault intersection at the base of Domain II.

The inclination of bedding in Domain II is steeper than would be predicted from the overall apparent dip on the seismic section. We interpret the observed inclination in the cores as a locally strong tilting in the vicinity of a nearby fault; the bulk inclination accomplished across the whole zone is modest, producing the general shallow apparent dip of the reflectors between the locations of Holes 889A and 889B.

Inspection of the FMS images from Hole 889A (see "Downhole Logging" section, this chapter) corroborates the conclusion that Do-

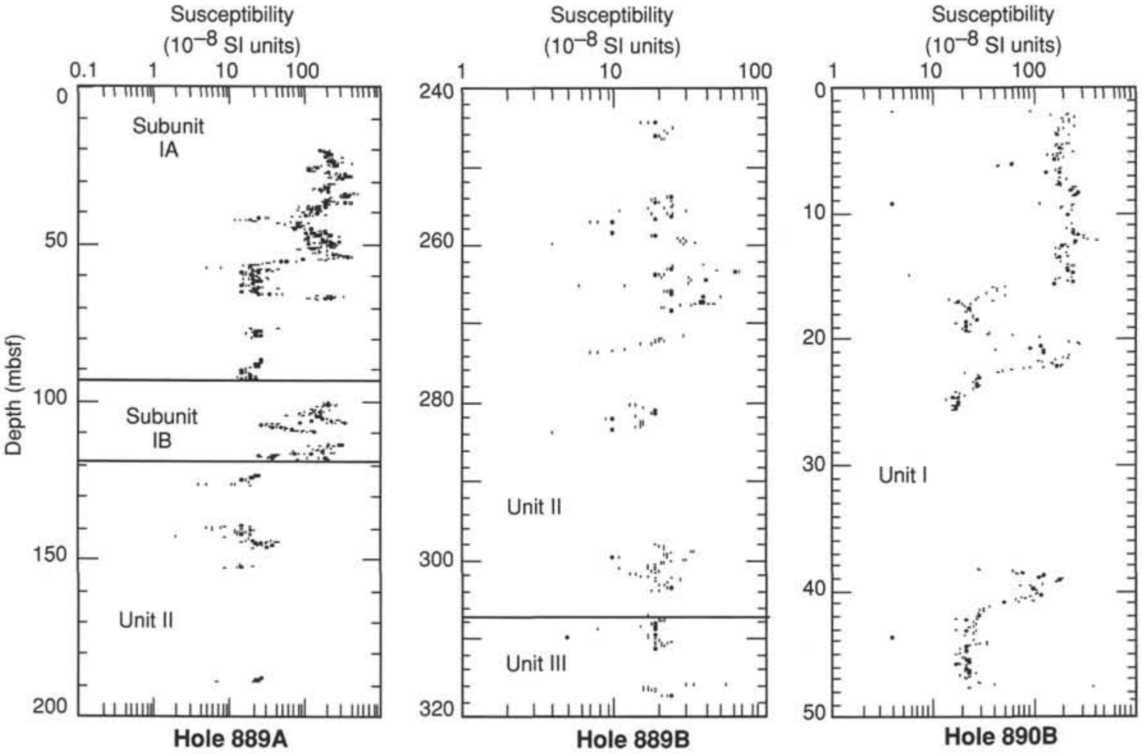

Figure 44. Susceptibility vs. depth for Holes 889A, 889B, and 890B.

main II contains westward-dipping beds. Planar sharp contrasts in resistivity generally exhibit moderate westward dips.

Domain III

Structural features in Domain III include inclined bedding, sheared fractures (small faults), joints, shear zone deformation bands, and stratal disruption. Partial core recovery and the destruction of original fabric by strong drilling disturbance limits observable structures to those that can be seen in coherent intervals (usually no more than 1 m long). Up to 80% of the recovered material is too disturbed to preserve structural information. In the following paragraphs, each of the features listed herein will be discussed in detail.

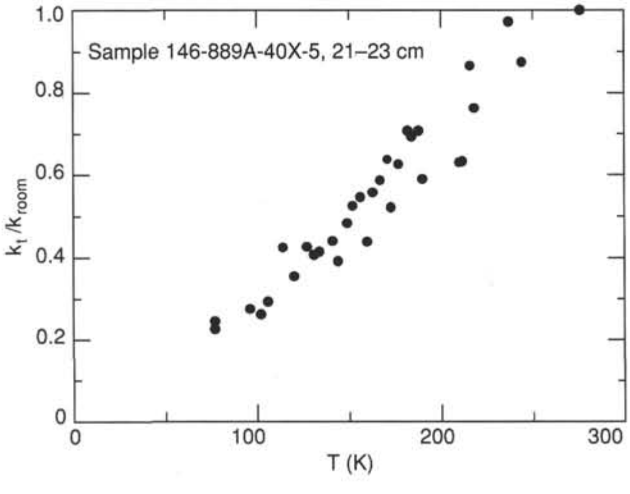

Figure 45. Results of cryogenic susceptibility experiments. The vertical axis is the measured susceptibility at a given temperature normalized by the room-temperature susceptibility. The linear trend in the normalized susceptibility to zero at 0 K indicates that the sample behaves as a bulk paramagnet.

Fractures

Structural development in Domain III is dominated by pervasive open fractures present from Core 146-889A-13H to the deepest recovery. The fractures can be divided into two prevalent types: (1) polished and lineated curviplanar to planar surfaces, commonly developed in sets at a low angle to one another, but typically at a moderate to high angle to the horizontal; and (2) planar tensional fractures resembling joints, some of which exhibit plumose structure, usually occurring in conjugate sets. As many as four fracture systems may be coincident in a single interval of cored material. No timing relationships between the various fracture systems have been identified, and offsets have not been identified across any of these fractures, owing to the lack of identifiable markers in the monotonous sediments.

The transition from Domains II to III is placed at the top of the pervasively fractured zone, below 127 mbsf in Hole 889A and extending to 386.5 mbsf (TD of Hole 889B). A transition zone that extends from 127 to about 140 mbsf is present between the two structural domains. This zone exhibits interlayered intervals of plastic sediments and sediments sufficiently stiff to form discrete fractures between Cores 146-889A-12H and -18X. Over this interval, the development of brittle fractures progressively increases. The zone of weakly polished and slickensided fracture surfaces begins in Core 146-889A-17X, at about 130 mbsf, and is developed throughout the recovered interval below. Slight changes in the degree of lithification apparently control the presence or absence of discrete fractures. Intervals of fractured material and softer unfractured sediment alternate throughout Domain III.

Within intervals in which the fragments of fractured siltstone have been recovered with a relatively intact fabric, we were able to measure the orientation of the well-developed fractures (Table 5). These intact regions are well preserved in Cores 146-889A-22X, -26X, -28X, -32X, and -41X. Where such intact fractures were found, a dominant

Table 5. All structural data collected at Site 889, tabulated on a section-by-section basis.

			Core face orientation		Corrected core reference frame				Corrected geographic reference frame			
Core, section, interval (cm)	ID	Description	Apparent dip (degrees)	Direction (degrees)	Strike (degrees)	Dip (degrees)	Direction	Reorientation method	Strike (degrees)	Dip (degrees)	Direction	Comments
146-889A-												
1H-3, 147–149		Bedding	13	270								May be drilling deformation
1H-6, 51		Bedding	13	270	163	14	W	Tensor	161.5	14	W	
1H-4, 46		Bedding	2	270								
1H-3, 130		Gas escape fracture	15	270								Gas escape feature hackly parting surfaces
2H-2, 41		Bedding	0	0	0	0			33.0	0		Horizontal bedding
2H-6, 70		Bedding	3	270								Horizontal bedding
6H-3, 93		Bedding	11	90	48	16	S	Tensor	276.0	16	N	
6H-4, 30		Bedding	11	90	62	24	S	Tensor	290.0	24	N	
9H-2, 65–66		Bedding	4	270	180	4						Loaded bed
9H-2, 91		Bedding	2	90	0	2						
9H-6, 70–71		Bedding	7	90	8	7						Subhorizontal
9H-8, 60–63		Bedding	23	90	20	24						Sketchy
10H-1, 60–76		Bedding	71	270								
10H-2, 102–112		Bedding	71	270	149	74	W	Multishot	160.0	74	W	
10H-3, 55–67		Bedding	66	270								
10H-5, 91–101		Bedding	57	270	203	59	W	Multishot	214.0	59	W	
11H-1, 45–50		Bedding	43	90	310	55	N	Multishot	145.0	55	SW	
12H-3, 46–49		Bedding	36	270	172	36	W	Tensor	238.0	36	N	
12H-4, 48		Bedding	38	270	126	53	S	Tensor	192.0	53	W	
12H-4, 40–50		Color change	54	90								At a high angle to apparent bedding
18X-3, 102–112		Fracture	72	90								These three are coexisting joint sets
18X-3, 102–112		Fracture	18	90								
18X-3, 102–112		Fracture	65	270								
18X-3, 125–130		Fracture	70	270								
18X-3, 140–147		Fracture	60	270								Pair of joints in fractured unit
18X-3, 140–147		Fracture	65	90								
18X-3, 116–120		Fracture	48	90	25	51						Moderate lithification; fracturing well developed
18X-4, 50–52		Fracture	41	270	194	42						
18X-4, 10–18		Fracture	75	90								Pair of joints
18X-4, 10–18		Fracture	50	270								
19X-4, 10–20		Fracture	60	90								Joints in fractured unit
19X-4, 45–50		Fracture	45	90								
19X-4, 118		Fracture	20	90	67	43						Fairly indurated
19X-4, 130–145		Fracture	60	90								
20X-3, 96–100		Color change	46	90								Irregular in cross section, no plane identified
20X-3, 45		Interfracture angle	107									
20X-4, 110–115		Fracture	61	90	330	64						Scaly fracture surface
20X-4, 80–85		Fracture	50	90	328	55						Conjugate present, but more poorly developed
22X-2, 15		Fracture	27	90	316	35	E					Set of apparently tectonic fractures
22X-2, 45		Fracture	88	90	0	88	E					Exhibits polished surface, undulose, faint slicks
22X-6, 51		Fracture	19	270	248	43	N					Excavated fracture
22X-6, 51		Joint/fracture	43	90	15	44	E					Pair of drill-induced conjugates?
22X-6, 52		Joint/fracture	50	270	199	52	W					
22X-6, 123–130		Fracture	64	270	226	71	N					Steep fracture near plane of cut face
22X-6, 123–130		Lineation			T:135	P:16						Weakly developed slickenlines on fracture surface near strike-parallel
22X-5, 75		Joint/fracture	59	90	369	E						
22X-5, 75		Joint/fracture	14	270	180	14	W					No slickenlines
22X-5, 75		Joint/fracture	66	90	40	71	W					No slickenlines
22X-5, 17–21	A	Fracture	43	270	174	43	W					Scaly fractures, set of four co-occurring
22X-5, 17–21	B	Fracture	58	90	18	59	E					Scaly fractures
22X-5, 17–21	C	Fracture	51	270	112	73	S					Scaly fractures
22X-5, 17–21	D	Fracture	33	90	42	41	E					Scaly fractures
22X-6, 130		Bedding	~0									Subhorizontal bedding (?)
26X-1, 35		Fracture	45	90	0	45	E					Apparent dominant fracture set
26X-2, 88–90	A	Fracture	37	90	49	49	S					Both strike in this core's dominant trend
26X-2, 91–94	B	Fracture	29	90	294	54	N					Conjugate set? Neither dominant

			Core face orientation		Corrected core reference frame				Corrected geographic reference frame			
Core, section, interval (cm)	ID	Description	Apparent dip (degrees)	Direction (degrees)	Strike (degrees)	Dip (degrees)	Direction	Reorientation method	Strike (degrees)	Dip (degrees)	Direction	Comments
26X-6, 56–59		Fracture	90	0	0	90	E					? Unreliable apparent dips-slicked surface
28X-1, 50–52		Fracture	25	90	339	26	E					
28X-2, 48–50		Fracture	23	90	78	64	S					
28X-2, 31–37		Fracture	44	90	314	54	N					
28X-3, 42–46		Fracture	43	90	324	49	E					
28X-5, 14–20		Fracture	54	270	128	66	S					
28X-5, 76–80	A	Fracture (fabric)	37	270	207	40	W					A and B appear to be dominant scaly fabric directions
28X-5, 71–74	B	Fracture (fabric)	41	270	152	45	W					
28X-1, 38–45		Fracture	59	90	354	59	E					
28X-2, 62–64		Fracture	28	90	67	54	S					Good fracture face
28X-2, 70–71		Fracture	16	90	78	55	S					} These three fractures form bounding faces of one rhomb of mudstone
28X-2, 73–77		Fracture	43	90	330	47	E					}
28X-2, 70–75		Fracture	68	90	312	75	N					}
30X-2, 77–81		Fracture	41	90								Second dip not possible
30X-2, 52–57		Fracture	64	90								Second dip not possible
30X-4, 34–38		Fracture	37	240	155	40	W					Second dip measured on another (parallel) fracture
30X-4, 27		Fracture	23	270	117	43	S					Two fractures bounding a rhomb in scaly fabric
30X-4, 27		Fracture	59	270	164	60	W					
31X-5, 0–14		Fracture	12	270								Second orientation not possible in many cases
31X-5, 0–14		Fracture	50	270								
31X-5, 0–14		Fracture	60	90								
31X-5, 115–120		Fracture	65	270								
31X-5, 124–126		Fracture	12	90								
32X-2, 95–100		Fracture	50	270								
32X-2, 115–116		Fracture	15	270	213	18	W					
32X-2, 132–135		Fracture	45	90								
32X-2, 135–136		Fracture	15	270	213	18	W					
32X-3, 16–18		Fracture	12	270								
32X-3, 17–25		Fracture	65	90								
32X-3, 25–26		Fracture	14	90								
32X-3, 52–55		Fracture	40	270	235	56	N	Paleomagnetism				
32X-3, 56–58		Fracture	30	90	32	34	E					
32X-1, 103–105		Bedding	14	90	313	20	N	Paleomagnetism	58.0	20	S	Black layer—possibly bedding (?)
32X-1, 39–40		Bedding (? color change)	19	90								
32X-2, 99–103		Fracture	45	270	225	55	W	Paleomagnetism	130.0	55	S	Makes angle with a fracture in plane of core of ~115°
32X-2, 93–95		Fracture	49	270	214	54	W	Paleomagnetism	119.0	54	S	
32X-3, 54–58		Fracture	35	270	201	37	W					} Conjugate pair?
32X-3, 56–58		Fracture	24	90	314	33	N					}
32X-3, 71–80		Fracture	80	90								
40X-2, 28–31		Fracture/fabric	38	90								
40X-2, 59–61		Fracture	36	90	54	51	S					Scaly fabric in glauconite interval
40X-1, 41–45		Fracture	36	270	146	41	W	Paleomagnetism	216.0	41	W	
40X-4, 16–21		Fracture	83	270	199	83	W	Paleomagnetism	244.0	83	W	
40X-4, 69		Fracture	3	90	271	80	N	Paleomagnetism	316.0	80	N	
40X-4, 69		Lineation			T:???	P:8						Possibly a strike-parallel trend
40X-4, 140		Fracture	0	90	90	60	S	Paleomagnetism	135.0	60	S	
40X-4, 77–82		Fracture	70	270	210	73	W	Paleomagnetism	255.0	73	N	
40X-4, 77–82		Lineation			T:000	P:50		Paleomagnetism	T:45	P:50		Slickenlines on preceding fracture
41X-2, 103–106		Fracture	9	90	59	17	S	Paleomagnetism	144.0	17	W	
41X-2, 103–106		Bedding (?)	9	90	277	51	N	Paleomagnetism	2.0	51	E	Fracture surface with piece of wood lying in plane
41X-2, 112–114		Fracture	21	90	63	40	S	Paleomagnetism	148.0	40	W	
41X-2, 28–31		Fracture	33	270	233	47	N	Paleomagnetism	318.0	47	E	Dominant fracture in fabric at this interval
41X-2, 44–53		Fracture	68	270	151	71	W	Paleomagnetism	236.0	71	N	
41X-3, 99–101		Fracture	26	90	346	27	E	Paleomagnetism	146.0	27	W	
41X-3, 99–101		Lineation			T:120	P:23		Paleomagnetism	T:280	P:23		Slickenlines on preceding fracture surface
41X-3, 100–103		Fracture	51	270	114	72	S	Paleomagnetism	274.0	72	N	Forms set with preceeding lineated fracture
41X-3, 100–103		Lineation			T:180	P: 70		Paleomagnetism	T:340	P:70		Slickenlines on preceding fracture
41X-4, 014		Fracture	68	270	154	70	W					
41X-4, 56–65		Fracture	62	270	163	63	W					

			Core face orientation		Corrected core reference frame				Corrected geographic reference frame			
Core, section, interval (cm)	ID	Description	Apparent dip (degrees)	Direction (degrees)	Strike (degrees)	Dip (degrees)	Direction	Reorientation method	Strike (degrees)	Dip (degrees)	Direction	Comments
41X-4, 62–67		Fracture	48	270	180	48	W					
41X-4, 16–18		Deformation band	74	270	186	74	W					Dark seams parallel to fabric in adjacent broken zone
146-889B-												
7R-4, 84–88		Fracture	35	270	148	40	W					Approximate orientation on carbonate layer
7R-4, 88–90		Fracture	38	90	67	63	S					Not intact, but close to in situ
8R-?, 56–85		Melange										Steep (~70°) zone of disaggregated blocks in dark seam
12R-4, 84–87		Fracture	41	90	33	46	E					
12R-1, 14–17		Fracture	30	90	52	43	S					Dominant fracture; downdip slickenlines
12R-1, 12–14			30	90	28	270	N					Another fracture in same location—oblique slickenlines toward ~225°
14R-1, 98–100		Fracture	39	90	46	49	S					Only somewhat intact; low confidence
146-889D-												
2W-6, 113–116		Bedding	23	270	230	34	N					Core 2 is a wash core: depth indeterminate but appears to be from Subunit IB (Domain II)
2W-4, 82–83		Bedding	21	270	155	23	W					
4N-1, 80–81		Bedding	17	90	73	46	S					MDCB core; recovered very fine sand beds, not much disturbed
4N-1, 25–26		Bedding	89	0	82	44	S					
4N-1, 94–100		Fracture	71	90	317	76	E					Pair of fractures in same location
4N-1, 96–97		Fracture	21	90	345	22	E					Slightly polished and lineated

Note: "T" and "P" refer to trend and plunge of linear features.

Table 6. All structural data collected at Site 890, tabulated on a section-by-section basis.

Core, section, interval (cm)	Description	Core face orientation: Apparent dip (degrees)	Core face orientation: Direction (degrees)	Comments
Hole 890B-				
1H-2, 93	Bedding	5	90	Horizontal bedding
1H-2, 135	Bedding	2	135	Horizontal
1H-3, 22	Bedding	1	270	Horizontal
1H-4, 50	Bedding	4	90	Horizontal
2H-7, 10	Bedding	2	270	Horizontal
3H-1, 14	Bedding	0		
3H-1, 21–23	Bedding	22	270	Base of core has imploded liner
3H-1, 30–32	Bedding	8	270	Upper half does not appear disturbed
3H-3, 45	Bedding	3	270	

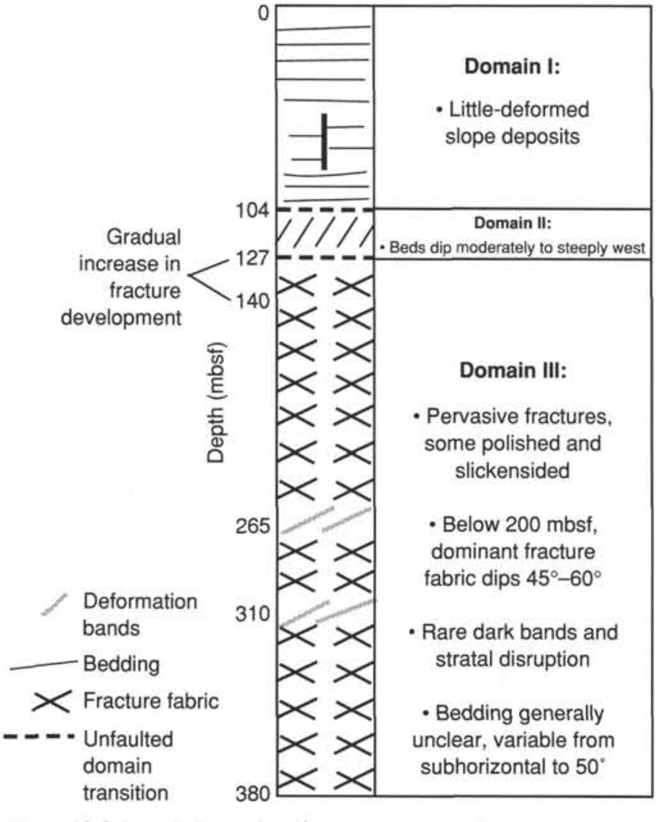

Figure 46. Schematic illustration of structural domains developed at Sites 889 and 890.

fracture orientation was typically observed, wherein one fracture set or two sets at low angles to each other are through-going and consistent in orientation within the interval (Fig. 50). Fracture inclination data (Fig. 51) indicate variable orientations, clustered about a 45° to 60° inclination. Note that reorientation into true geographic coordinates is not possible until viscous remanent magnetism orientations for the relevant sections are determined. The strongly preferred inclination shown in Figure 51 agrees well with the visual observation of a dominant fracture orientation in the cores of about 45°–50°, illustrated in Figures 50 and 52. This dominant orientation is first observed at about 200 mbsf in Hole 889A and is consistently well developed in coherent intervals downhole. The oriented fracture fabric is especially well developed in Core 146-889A-41X, at 310–319 mbsf.

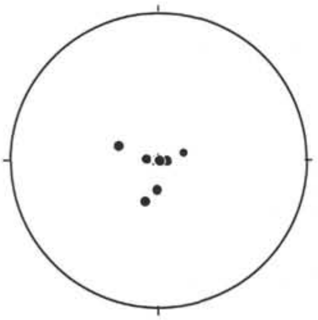

Figure 47. Equal-area lower hemisphere projection of poles to bedding in Domain I.

Close examination of this fracture fabric indicates that it is composed of several intersecting sets of fractures that define individual trapezoidal fragments of siltstone. The surfaces of the siltstone rhombs are typically slightly polished and weakly striated. These striations, in- terpreted as slickenlines, are unsystematic and indicate a range of trans- port directions, from dip parallel to strike parallel, even on various faces of the same fragment. Fracture spacing ranges from a few millimeters to 10 cm. No unfractured pieces larger than 10 cm were recovered.

Visual inspection and measurement of fracture orientations (Table 5) indicate that the rhombs are typically bounded by three intersecting fracture sets: one dipping at about 45°; one which is steeper, dipping 60°–70°, and intersects the first at a low angle; and a third oriented obliquely to both of the first two. The intersection of the acute fractures produces the dominant fabric in the cores.

In Core 146-889A-41X, where the largest intact fragments were recovered, pieces up to 10 cm long in the core liner are bounded by several centimeters of densely fractured siltstone, perhaps representing zones of concentrated shear (Fig. 52). The occurrence of this distinct structure is associated with the presence of shear bands, discussed subsequently in this section.

As on previous DSDP and ODP legs that found similar fractured material, the origin of these fractures was the subject of some discussion during Leg 146, regarding whether they may be induced during drilling and recovery rather than being of tectonic origin. Following criteria identified by Arthur et al. (1980) and by Lundberg and Moore (1986), we conclude that the majority of the open fractures in the cores are natural features. Several observations argue for in-situ formation of the fractures: (1) the presence of two distinct types of fractures implies multiple mechanisms of formation; (2) polished fractures in coherent intervals indicate significant shear strain that does not appear to be rotationally induced, typically form sets with a dominant orientation oblique to the horizontal (Fig. 50), are consistent downhole, and are not symmetric with respect to the long axis of the core (cf. Lundberg and Moore, 1986); and (3) the shear bands (see the following) recovered in Core 146-889A-41X, which are clearly a predrilling feature, are planar and parallel to the dominant open fracture orientation at that depth. The recovery process disaggregates pieces bounded by the intersecting fracture sets and may induce many of the planar joints. The slickenlines developed on the mud chips may be natural, or they may be produced by drilling disturbance as well.

Bedding

Identification of bedding proved extremely difficult in Domain III. The lack of distinct bedding planes and the association of sandy intervals with poor and disturbed recovery precluded the routine measurement of attitudes. Only six bedding measurements were made in Domain III; they indicate variable bedding attitudes, with 45° dips in Core 146-889D-4N (140 mbsf), subhorizontal to moderate dips in Core 146-889A-32X (248 mbsf), and 52° bedding dips in Core 146-889-41X (300 mbsf). Bedding in the latter case was identified by a flat-sided wood fragment lying in the plane of a parting surface. This

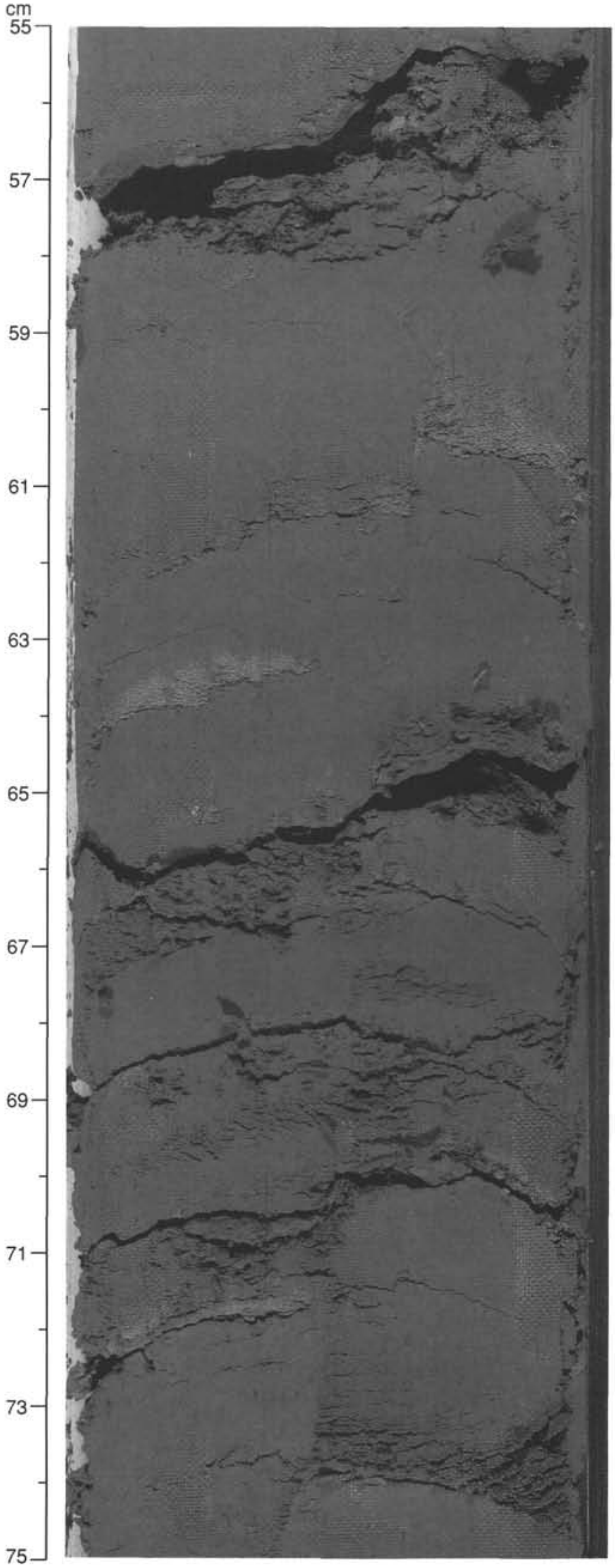

Figure 48. Curving steep fault in Section 146-889A-6H-3, 55–75 cm. Note ~2 cm offset of shallowly dipping turbidite sand layers. In this interval, the fault shows a normal sense of offset, but it curves to a high-angle reverse in adjacent intervals.

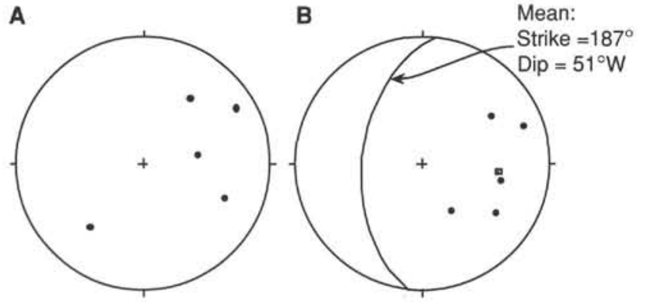

Figure 49. Equal-area lower hemisphere projection of poles to bedding in Domain II. **A.** Poles in core reference frame. **B.** Poles rotated into true geographic coordinates.

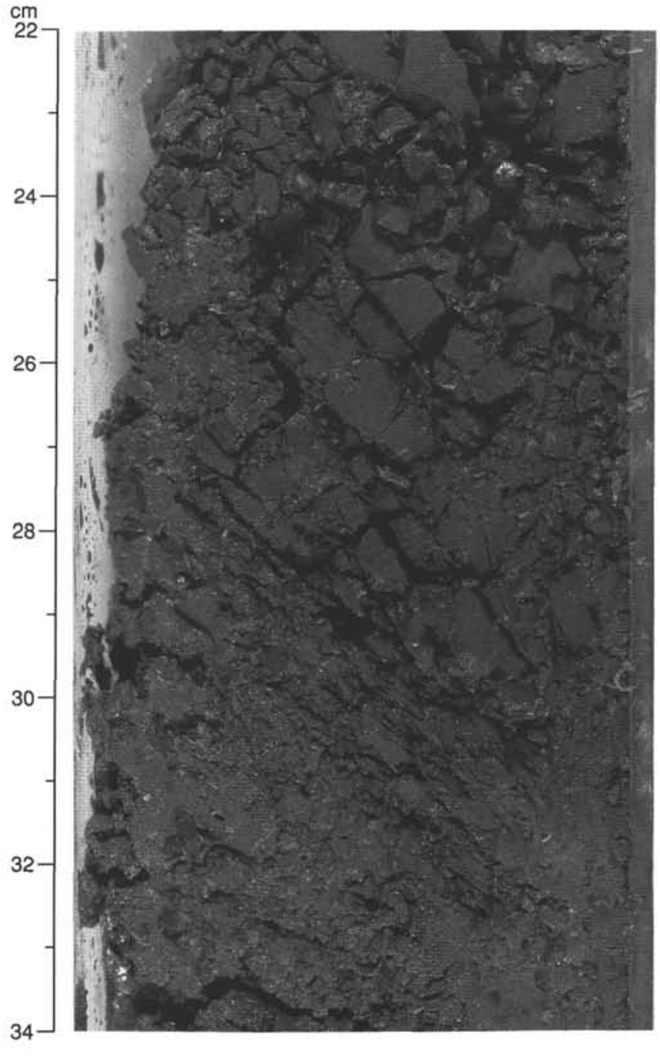

Figure 50. Example of the dominant orientation of fractures in a relatively intact interval below 200 mbsf in Hole 889A (Section 146-889A-26X-1, 22–34 cm). Two sets of well-developed fracture fabric cross from the upper left to lower right; one has an apparent inclination of about 50°, the other about 70°. These fracture sets define the dominant fabric orientation in Domain III.

is the only indication anywhere in Domain III of a bedding plane parting. At this location in Core 146-889A-41X, this bedding-parallel parting is in the dominant fracture orientation displayed by the core, suggesting that one of the fracture systems is locally controlled by bedding. We speculate that the locations where a single fracture fabric orientation is dominant are those locations where bedding is favorably

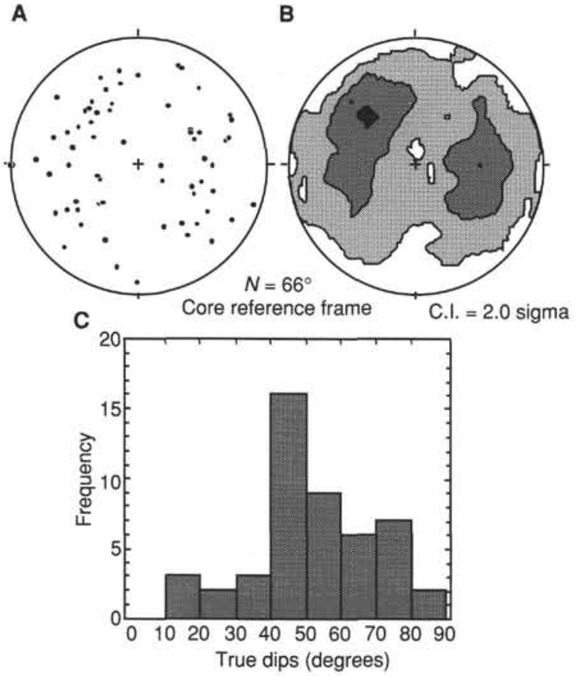

Figure 51. Orientation data for 66 fractures measured in Domain III. **A.** Equal-area lower hemisphere projection of poles to fracture planes in the core reference frame. **B.** Kamb contour plot of the density of poles, same projection. Darker fields indicate higher concentration of poles. Note the concentration in moderate dips between 40° and 70°. Azimuth directions are not meaningful in these uncorrected plots. **C.** Histogram of fracture inclinations for same data set. Fractures dip dominantly from 40° to 60°.

oriented for exploitation by a fracture set; in all other locations, several fracture sets are equally well developed, so that no dominant trend is evident.

Core 146-889D-4N (recovered with the motor-driven core barrel) was especially interesting, as it recovered intact sand beds in an interval where the depth-equivalent Core 146-889D-18X recovered no intact bedding, suggesting that there is more bedded sand in the subsurface than is recovered with the XCB or RCB techniques.

Deformation Bands

Very faint submillimeter to 1-mm-wide anastomosing sets of dark bands are present in Section 146-889A-41X-4 in several locations (Fig. 53). Thin-section analysis of the one well-developed specimen indicates that they are similar to the feature referred to variously as "shear bands" (Taira, Hill, Firth, et al., 1991), "deformation bands" (Karig and Lundberg, 1990; Behrmann, Lewis, Musgrave, et al., 1992), or "kink bands" (Lundberg and Moore, 1986). Herein we will follow the usage on Leg 141 and that of Maltman et al. (1993), and refer to them as deformation bands. These bands are not as well developed as examples from the Nankai Margin, perhaps because of the more silty (as opposed to clay-rich) lithology here at Site 889 (Karig and Lundberg, 1990). They appear to be very similar to those described in siltstones on Leg 141.

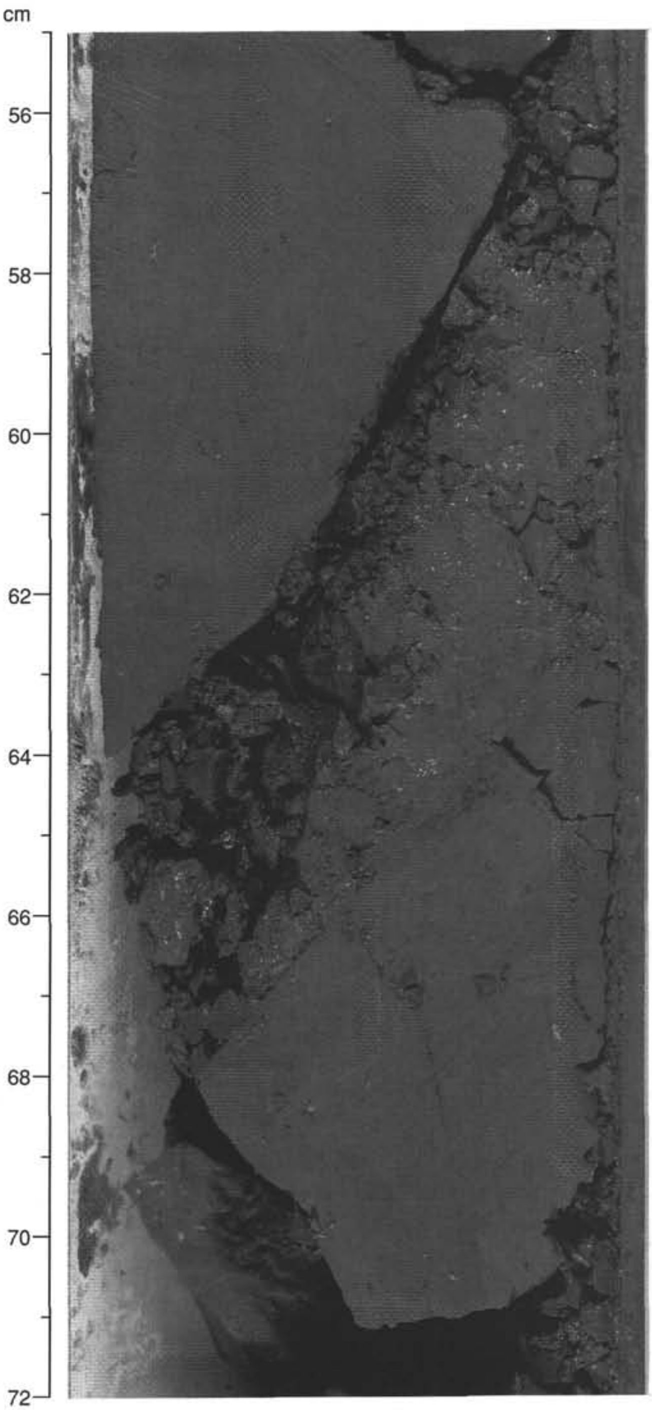

Figure 52. Interval illustrating large unfractured pieces of siltstone with a band of closely spaced fractures in between (Section 146-889A-41X-4, 55–72 cm). Fragments between the large blocks are polished and lineated, do not appear to have been injected, and are in their relative subsurface disposition, based on the interlocking of individual fragments. This zone of heterogeneous fracture concentration was found adjacent to the only well-developed deformation bands at Site 889, which are oriented subparallel to this fabric. Faint deformation bands can be seen from 56 to 61 cm.

The anastomosing sets dip 74°, parallel to the strongly developed dominant fracture fabric in this core. The shear bands at Site 889 are made up of a network of 0.03- to 0.25-mm-wide zones exhibiting strong preferred orientation of phyllosilicates and are at right angles to a weak foliation, interpreted as bedding. The margins of the bands are sharp. The mineralogy of these zones is identical to the adjacent rock, and there is no evidence for vein fill or for cataclasis. About 0.4 mm of reverse-sense offset of a bed is observed across one deformation band (see Fig. 53). Measurements of the AMS were determined to characterize the phyllosilicate fabrics further (see "Paleomagnetism" section, this chapter). Samples from intervals with observed deformation bands displayed weakly to well-developed lineation fabrics (Fig. 54), in contrast to samples from fractured intervals, in which planar fabrics were found. Deformation bands of this type have been interpreted to record zones of contractile shear deformation, and

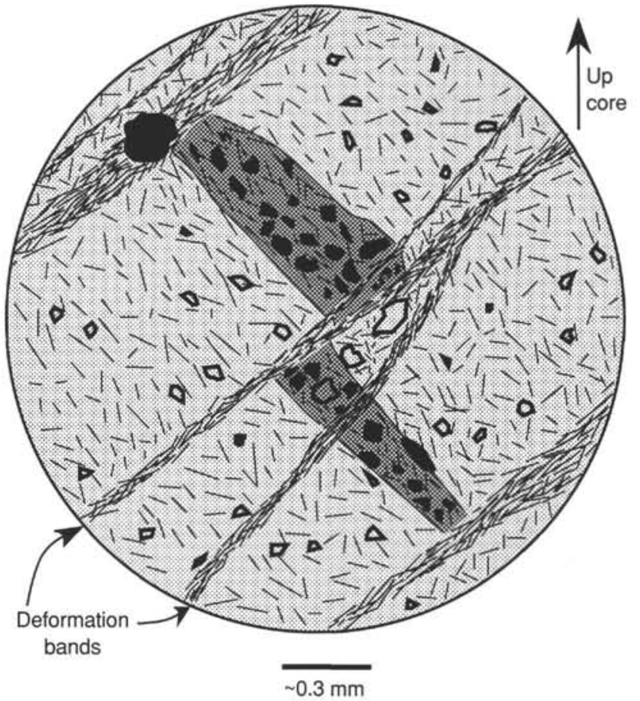

Figure 53. Sketch made from thin section of Sample 146-889A-41X-4, 16–18 cm. Shear-zone-type deformation bands exhibiting strong preferred orientation of phyllosilicates cross an opaque-mineral-rich bed, producing about 0.4 mm of apparent reverse offset. A weakly developed foliation of phyllosilicates, which we interpret as a bedding fabric, is present in the matrix; deformation bands are at right angles to the bedding foliation.

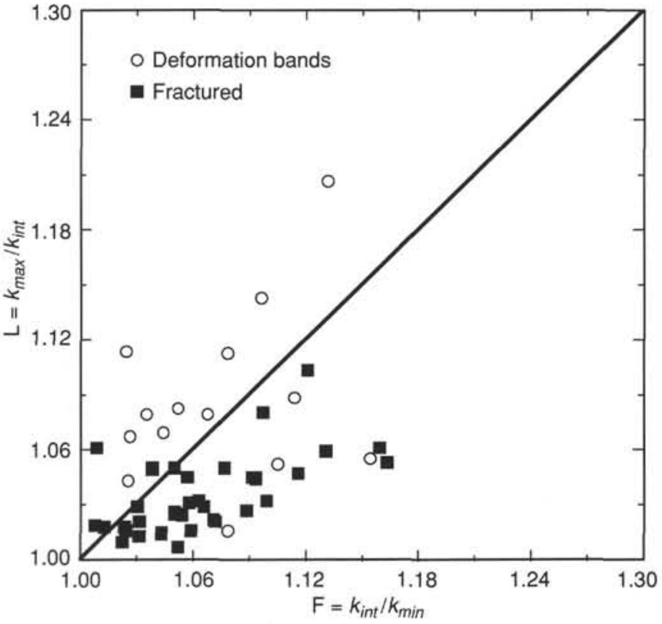

Figure 54. Flinn-type diagram of AMS ellipsoid shape for Hole 889A samples. The vertical axis is magnetic lineation, the horizontal axis magnetic foliation. Prolate ellipsoids plot in the upper left portion of the diagram, oblate ellipsoids in the lower right.

some are associated with faulting (Taira, Hill, Firth, et al., 1991). Taken together, the coincident deformation bands, strong fracture orientation, and stratal disruption in Hole 889B at nearly the same depth suggest a possible thrust fault at about 310 mbsf.

Stratal Disruption

Stratal disruption, as defined in Lundberg and Moore (1986), was identified in two locations in Hole 889B in Domain III, in Sections 146-889B-8R-2, 74–97 cm, and -13R-CC, 7–12 cm. In the first instance, at 265 mbsf, it is represented by an interval of blocks of siltstone in a finer grained darker matrix. The texture of this interval borders on Type I mélange (Cowan, 1985). The base of this disrupted interval dips at least 52°, and is above structureless clayey silt. The second interval, at 311 mbsf, is composed of light brown blocks of silt in a dark, muddy matrix, with a subhorizontal orientation. It may represent drill biscuiting and not tectonic deformation, but the texture is similar to the stratally disrupted interval above.

Summary and Conclusions

The absence of well-developed structural features at the depths penetrated by drilling limits the interpretation of deformation at Sites 889 and 890. The dominant structural feature is the pervasive shear fracturing in Domain III. The almost complete lack of healed fractures, microfaults, deformation bands, fault offsets, and other typical structural features of weakly lithified accretionary-wedge sediments suggests that the strain accumulated in this interval is minor. We found little direct evidence of zones of concentrated shear. The intervals of stratal disruption and deformation bands at 310–312 mbsf in Holes 889A and 889B and at 265 mbsf in Hole 889B may represent discrete concentrated shear zones. Magnetic fabric anisotropy supports this interpretation.

The pervasive fracturing in Domain III is indicative of bulk distributed strain. Based on the interpretation of the MCS data (see "Downhole Logging" section, this chapter), the sediments of Domain III probably developed this strain as they were transported upward in the hanging wall of a deeper reverse fault that was not intersected by drilling. Both of the potential fault zones at 265 and 310 mbsf probably are internal zones of localized shear within the hanging wall, based on the consistency of fracturing above and below each of them. The lack of offset features and the incipient nature of the scaly foliation suggests that the finite strain recorded in Domain III has been relatively small.

Few constraints can be placed on the timing of the deformation. Sediments of Domain III are probably material accreted at the trench, overlain by early slope basin sediments of Domain II (see "Lithostratigraphy" section, this chapter). Deformation could have begun at any time during or since deposition of the Domain III sediments (about 2 Ma at the base of Hole 889B). The structural transitions to Domains I and II are not abrupt, and could simply represent progressively younger and less lithified sediments that record less of the strain history during continuing deformation. The onset of fracture formation at the Domain II/III transition appears to represent an induration-related rheological boundary rather than a significant time gap. Because some deformation is present in Domain I above the biostratigraphically defined hiatus in Core 146-889A-8H, deformation must have continued until at least 0.4 Ma. The reverse fault interpreted on the MCS line (see "Downhole Logging" section, this chapter) apparently offsets the seafloor, suggesting present-day, active deformation.

ORGANIC GEOCHEMISTRY

Overview

The sediments encountered during the drilling of Sites 889 and 890 consist of two main types: basin fill and possibly slumped material in the interval shallower than 128 mbsf (the boundary between lithostratigraphic Units I and II) and accreted material below this level (Units II and III). In contrast to the reference site (Site 888), headspace (HS) and expansion void gas (EVG) methane concentrations rise sharply immediately below the shallow sulfate-reduction zone, which extends down only to about 10 mbsf. The third highest HS methane concentration at

Table 7. Carbon, nitrogen, and sulfur sediment data (based on total dry sediment), Sites 889 and 890.

Core, section, interval (cm)	Depth (mbsf)	Inorganic carbon (wt%)	$CaCO_3$ (wt%)	Total carbon (wt%)	Organic carbon (wt%)	Total nitrogen (wt%)	Total sulfur (wt%)
146-889A-							
1H-2, 1–6	21.50	0.90	7.50	1.69	0.79	0.09	0.11
1H-4, 145–150	25.95	0.88	7.30	1.82	0.94	0.16	0.16
2H-5, 145–150	36.95	0.10	0.80	0.49	0.39	0.04	0.17
3H-5, 1–6	44.04	0.10	0.80	1.16	1.06	0.16	0.23
4H-5, 143–150	54.64	0.76	6.30	1.36	0.60	0.05	0.19
5H-3, 143–150	62.44	0.18	1.50	0.53	0.35	0.04	0.61
6H-5, 145–150	74.07	0.25	2.10	1.11	0.86	0.15	0.25
7H-2, 143–150	79.93	0.20	1.70	1.09	0.89	0.11	1.37
8H-3, 140–150	90.90	0.19	1.60	1.41	1.22	0.14	0.86
9H-6, 137–150	102.14	0.05	0.40	0.49	0.44	0.06	0.12
10H-4, 140–150	109.90	0.10	0.80	0.82	0.72	0.15	0.16
11H-1, 140–150	114.90	0.24	2.00	0.72	0.48	0.07	0.06
12H-4, 140–150	124.81	0.23	1.90	1.36	1.13	0.15	0.81
13H-1, 0–5	127.32	0.12	1.00	1.22	1.10	0.22	0.78
14H-1, 153–158	128.56	0.06	0.50	1.26	1.20	0.14	2.46
15P-1, 6–13	129.07	3.26	27.20	3.58	0.32	0.12	0.50
17X-2, 70–80	131.46	0.14	1.20	1.20	1.06	0.15	1.02
18X-4, 36–46	144.41	0.37	3.10	1.24	0.87	0.16	0.30
22X-7, 0–20	185.60	0.31	2.60	1.31	1.00	0.19	0.49
24X-5, 120–140	194.32	0.22	1.80	1.09	0.87	0.19	0.31
25X-2, 0–20	198.80	0.40	3.30	1.48	1.08	0.13	0.36
26X-4, 130–150	212.47	0.20	1.70	1.24	1.04	0.14	0.56
28X-4, 80–100	222.60	0.17	1.40	1.23	1.06	0.19	1.01
30X-4, 130–150	233.60	0.39	3.20	1.65	1.26	0.15	0.55
31X-5, 140–160	244.70	0.35	2.90	1.62	1.27	0.20	0.62
32X-1, 130–150	248.00	0.32	2.70	0.74	0.42	0.06	0.00
36X-1, 99–114	267.69	0.60	5.00	1.76	1.16	0.13	0.64
40X-4, 45–65	306.45	0.21	1.70	0.84	0.63	0.08	0.95
41X-3, 130–150	314.80	0.36	3.00	1.16	0.80	0.14	0.86
42X-1, 44–52	319.94	0.22	1.80	1.12	0.90	0.19	0.99
43X-1, 0–5	329.80	0.03	0.20	1.30	1.27	0.13	0.88
44X-2, 0–15	337.20	0.13	1.10	1.34	1.21	0.20	0.44
146-889B-							
3R-1, 79–94	216.77	0.23	1.90	0.80	0.57	0.13	0.25
4R-1, 61–76	225.99	0.14	1.20	0.84	0.70	0.09	0.08
4R-2, 45–60	227.33	0.10	0.80	0.84	0.74	0.12	0.14
5R-1, 26–36	235.11	0.29	2.40	1.58	1.29	0.25	0.74
6R-1, 54–69	244.92	1.09	9.10	1.95	0.86	0.14	0.19
7R-1, 103–126	255.05	0.10	0.80	0.80	0.70	0.17	0.20
8R-2, 130–150	265.60	0.42	3.50	1.42	1.00	0.20	0.28
9R-1, 0–20	271.70	0.47	3.90	1.37	0.90	0.10	0.99
10R-2, 0–20	282.00	0.63	5.20	1.38	0.75	0.17	0.42
12R-1, 130–150	299.60	0.13	1.10	0.94	0.81	0.17	0.91
13R-2, 35–55	309.50	0.15	1.20	0.83	0.68	0.14	0.97
14R-1, 111–136	317.04	0.05	0.40	1.37	1.32	0.16	1.02
15R-1, 125–150	325.98	0.03	0.20	1.33	1.30	0.15	0.89
17R-1, 0–15	342.18	0.05	0.40	1.13	1.08	0.14	0.89
18R-1, 0–10	351.05	0.03	0.20	1.18	1.15	0.13	1.01
20R-1, 0–3	368.70	0.11	0.90	1.08	0.97	0.13	0.71
146-890B-							
1H-2, 145–150	2.98	0.34	2.80	0.98	0.64	0.12	0.18
1H-3, 145–150	4.48	0.40	3.30	0.61	0.21	0.02	0.02
2H-2, 63–68	9.36	0.32	2.70	0.74	0.42	0.04	0.09
2H-3, 53–58	10.76	0.47	3.90	0.86	0.39	0.04	0.02
2H-6, 145–150	16.18	0.42	3.50	0.72	0.30	0.03	0.41
3H-2, 143–150	19.77	0.21	1.70	0.41	0.20	0.02	0.84
3H-6, 150–155	25.83	0.27	2.20	0.71	0.44	0.05	0.45
5H-5, 0–10	44.35	0.30	2.50	0.83	0.53	0.04	0.81

Sites 889 and 890 (82,417 ppmv) occurs at only 24 mbsf, even though the organic carbon contents of the shallow sediments, down to 50 mbsf, are low, ranging between 0.20 and 0.64 wt%. The disparity between organic source material and methane concentration suggests an allochthonous contribution of thermogenic methane from depth mixed with autochthonous biogenic methane.

Beneath the near-surface zone, the HS methane concentration profile can be divided into three zones: an upper zone (20–125 mbsf), where concentrations decrease with depth; a middle zone, where methane concentrations are high; and a deep zone (247 mbsf to TD), where the concentrations are variable with depth.

Apart from this tripartition of the methane profile, and local high HS nitrogen and carbon dioxide spikes, the most striking aspects of the organic geochemical data set from these sites are zones of minimum HS ethane and propane at depths between 283 and 311 mbsf. The presence of gas hydrates and/or molecular stripping associated with upward migration of the hydrate stability zone over time are possible models that may explain these observations.

Introduction

Shipboard organic geochemical analyses of sediments from Holes 889A, 889B, and 890A included volatile hydrocarbon and nonhydrocarbon gases; sediment total carbon; organic carbon, nitrogen, and sulfur; fluorescence intensity; total hexane-soluble lipid/bitumen analysis; and Rock-Eval/Geofina analysis. The instrumentation, operating conditions, and procedures are summarized in the "Explanatory Notes" chapter (this volume). The organic geochemistry results from the three holes are combined here because they were drilled within the same general area and because they overlap vertically. Although the geochemical trends in the two vertically overlapping holes (889A and 889B) are similar, the geochemical results were difficult to correlate between them. Hole 889A was sampled from 21.5 to 337.2 mbsf, Hole 889B from 198.5 to 378.3 mbsf, and Hole 890A from 0.4 to 44.3 mbsf.

At Site 889 samples were also taken from Hole 889D. These results are reported here in tabular form only. No sediment samples were obtained from Hole 889C.

Organic Carbon

Organic carbon content (C_{org}) is intermediate to low at Sites 889 and 890 (Table 7). In Unit I (0–128.0 mbsf), C_{org} fluctuates between 0.20 and 1.22 wt% (Fig. 55). In the upper part of Unit II (128–242 mbsf), C_{org} generally fluctuates at about 1.0 wt%. At 230–245 mbsf, a marked drop occurs in C_{org}, from a high of 1.26 wt% at 242 mbsf (Hole 889A) to a low of 0.41 wt% at 248 mbsf (Hole 889A). Thereafter, C_{org} is variable with a local maximum of 1.32 wt% at 317 mbsf.

The boundary between Units II and III is marked by a local low C_{org} value of 0.65 wt%.

Total Nitrogen

The total nitrogen (N_{tot}) generally varies sympathetically with the organic carbon contents at Holes 889A, 889B, and 890B (Table 7 and Fig. 55). The lowest N_{tot} values were recorded in Subunit IA (0.05 wt%). The highest N_{tot} in Hole 889A (0.22 wt%) is located at the boundary between Units I and II. In Hole 889B the maximum value (0.25 wt%) corresponds with a local C_{org} high at 238 mbsf.

Regression of C_{org} with N_{tot} yields a C/N ratio of 1:0.14, which is indicative of a source more influenced by marine organic matter than the terrestrially dominated detritus at the reference site (Site 888; Fig. 56). Considerable scatter is observed in the C/N ratio owing to the variations in the lithologies drilled.

Total Sulfur

Total sulfur (S_{tot}) in Holes 889A, 889B, and 890B fluctuates between <0.1 wt% at 6, 115, and 248 mbsf and two maxima that occur at 83 mbsf (S_{tot} = 1.33 wt%) and at 129 mbsf (S_{tot} = 2.46 wt%) (Table 7 and Fig. 55). The sulfur in the sediments is derived mainly from the reduction of SO_4^{2-}. The highest values correspond to zones of pyrite reported in the "Lithostratigraphy" section (this chapter).

Headspace Gases

Volatile gases (hydrocarbons, CO_2, H_2S, N_2, and O_2) released by the sediments recovered at Sites 889 and 890 were measured by gas chromatography. The results are listed in Table 8 and illustrated in Figure 57.

The methane concentrations in the HS volumes range between 13 and 112,901 ppmv (Fig. 57). In the uppermost part of Unit I, the methane increases rapidly from 88 ppm at 0.4 mbsf to 82,417 ppm at 24.3 mbsf (the third highest HS value recorded at these sites).

Ethane and higher hydrocarbons up to C_7 (heptane) were also detected. The downhole profiles for HS ethane and propane are shown in Figure 57. Both C_2 and C_3 compounds are absent shallower than

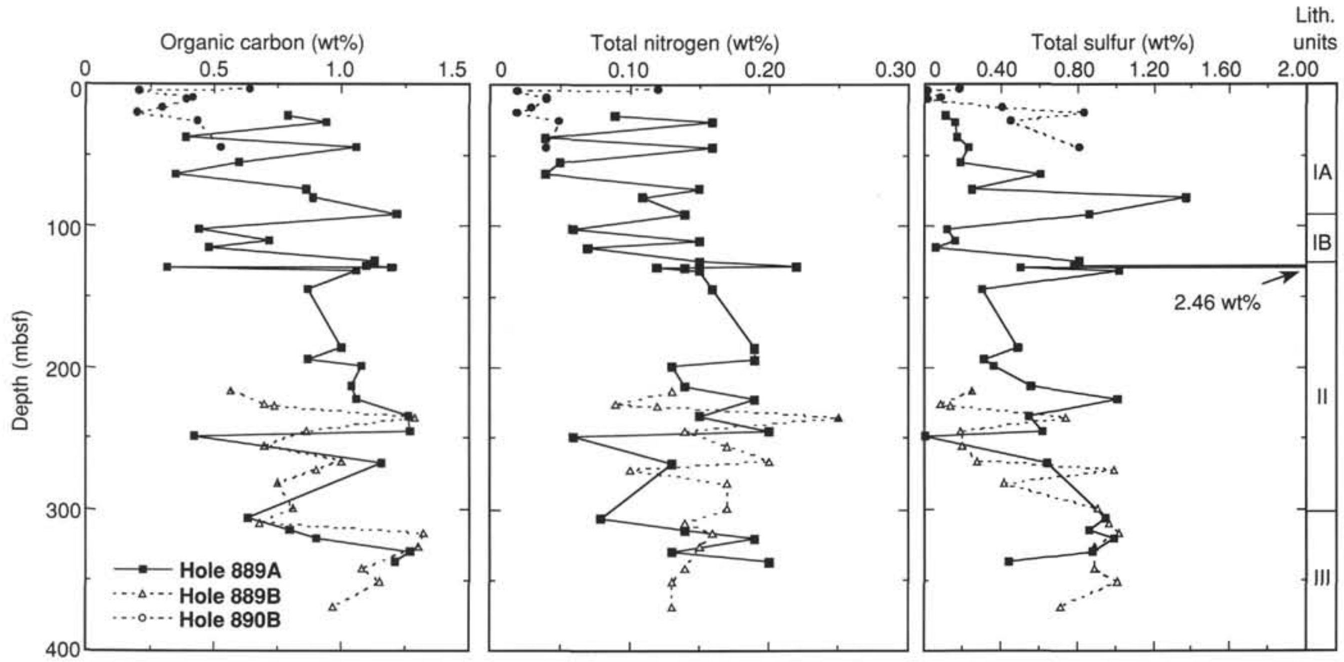

Figure 55. Depth distribution at Sites 889 and 890 of organic carbon, total nitrogen, and total sulfur.

16.1 mbsf. At this depth ethane appears and is constant at low values to about 130 mbsf, below which it increases in concentration with depth, gradually at first, but abruptly to above 200 ppm toward the base of Hole 889A. The profile for HS ethane in Hole 889B is similar, except for an "ethane minimum zone" between 283 and 311 mbsf, where the concentrations are low. Headspace propane is present below 130 mbsf and shows a similar depth vs. concentration trend to ethane. For propane, too, a "local minimum zone" exists between 283 and 311 mbsf in Hole 889B.

No H_2S was detected in the samples collected at this site.

The HS methane concentration profile (Fig. 57) can be divided into three zones. In the upper zone (from about 20 to 125 mbsf), the concentration generally decreases with depth. The middle zone (from 125 to about 245 mbsf in Hole 889A and to about 300 mbsf in Hole 889B) is characterized by generally high methane concentrations (10,053–76,498 ppmv). In the deepest zone (from about 245 mbsf in Hole 889A and from about 300 mbsf in Hole 889B to the deepest sample at 378 mbsf), the methane content is variable. In the same depth zone, propane content is variable and ethane content generally increases with depth (Fig. 57).

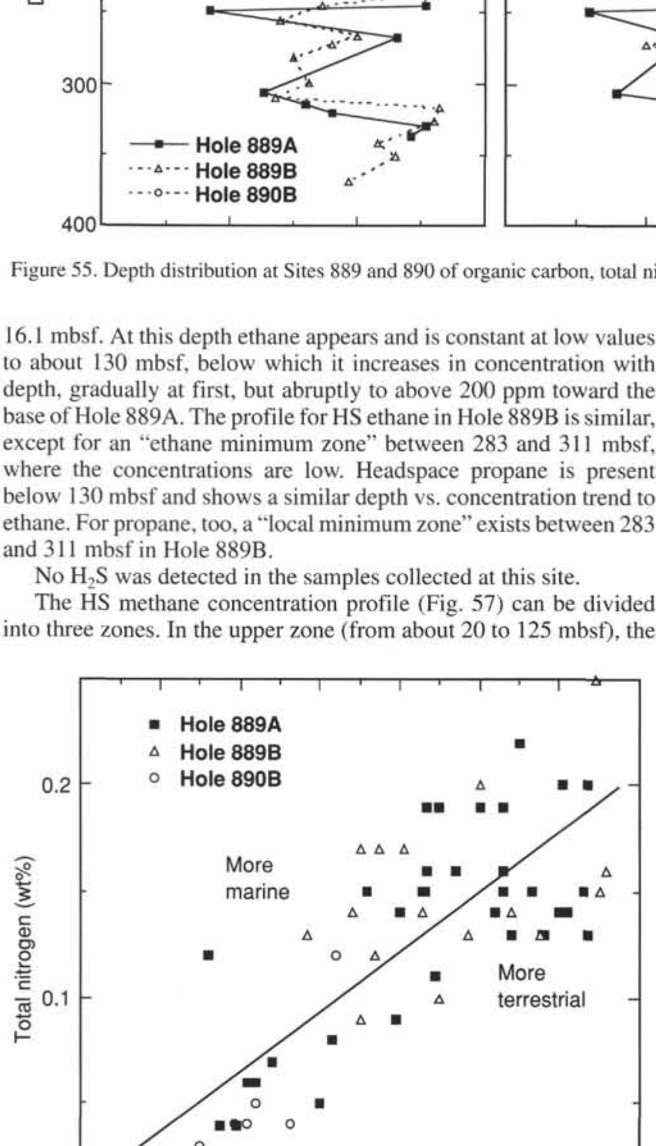

Figure 56. Cross plot of C_{org} and N_{tot} illustrating a relatively strong terrigenous-hemipelagic influence at Sites 889 and 890.

In the middle zone, where the methane concentrations are relatively high, ethane and propane concentrations peak to local highs (C_2 to 39 ppmv at 231 mbsf in Hole 889A and to 103 ppmv at 255 mbsf in Hole 889B; C_3 to 3.4 ppm at 195 mbsf in Hole 889A and to 1.3 ppmv at 247 mbsf in Hole 889B).

Systematic deviations exist from these general trends in the methane, ethane, and propane profiles: intervals that could be termed "gas minimum zones" are observed in the C_1–C_3 profiles. In these minimum zones, the HS concentrations decrease abruptly to a local low value, before increasing to a higher value. In the methane profile (Fig. 57), a typical minimum zone is present from 248 to 260 mbsf. In the ethane and propane profiles for Hole 889B, minimum zones are clearly present from 283 to 311 mbsf.

The C_1/C_2 ratio profile for HS methane and ethane is shown in Figure 57. Generally, it shows the trend of increasing ethane relative to methane with depth, reflecting a probable deeper source of thermogenic hydrocarbons. However, two zones of anomalous trends are present: (1) a sharp relative increase in ethane at the boundary between Units I and II, which causes a prominent local inversion of the C_1/C_2 gradient; and (2) a similar, but more extensive, event between 240 and about 300 mbsf in both Holes 889A and 889B, although the profile for Hole 889B is more distinct.

A vertical profile of HS carbon dioxide is compared in Figure 58 with the profile of HS methane. The HS carbon dioxide concentration generally varies between 8×10^2 and 4×10^3 ppmv. An anomalous peak is present at 230 mbsf in Hole 889A, where the HS carbon dioxide concentration is 3.3×10^4 ppmv. This also corresponds with a local maximum zone in Hole 889B at the same depth (see Fig. 58).

No HS nitrogen was found, other than what could be accounted for by contamination from the air during HS sampling.

Table 8. Molecular composition of headspace gases at Sites 889 and 890.

Core, section, interval (cm)	Depth (mbsf)	O_2	N_2	C_1	CO_2	C_2	C_3	iC_4	nC_4	iC_5	nC_5	iC_6	nC_6	C_1/C_2
146-889A-														
1H-2, 0–6	22	19	114	58980	1	1				2	3	4	5	42129
1H-5, 0–5	26	96	585	60149	4	2				2			2	40099
2H-1, 145–150	31	1295	1231	50134	2	2								20889
2H-5, 140–145	37	94	577	31452	4386	1								24194
3H-1, 145–150	40	353	713	30622	3	2			2					19139
3H-6, 6–10	47	79	491	49953	823	2		4	1					26291
4H-3, 0–5	52	35	208	11914	66	1						1		10831
4H-6, 0–5	56	416	724	22312	48	2								13945
5H-4, 0–5	63	60	369	33126	16	2								13803
6H-6, 0–5	75	78	481	48830	66	3								16838
7H-2, 0–5	79	42	268	23922	7	2								9968
8H-4, 0–5	91	25	150	12225	1	1							1	1114
9H-4, 0–5	99	2217	3501	21412	24	2								9310
10H-4, 150–152	110	3661	9217	9652	39	2								4387
11H-2, 0–5	115	6093	26875	27858	1662	5							1	6056
12H-2, 0–5	121	4143	13472	9652	1921	2								4387
13H-1, 0–5	127	9055	40702	76498	1634	14								5425
14H-1, 148–153	130	8356	36951	10053	1770	11								898
15P-1, 45–50	129	2103	3089	51184	1898	33								1532
17X-2, 75–80	132	50123	208641	60798	3644	20	0							3010
18X-4, 31–36	144	58023	237429	46432	6325	13	2							3715
19X-3, 145–150	154	25010	109405	48534	1923	19	1		10		1	1		2521
220X-3, 133–138	163	33101	140520	54756	1758	13	1							4346
22X-2, 0–5	179	4255	15273	30784	1383	10	1							3240
24X-6, 0–5	195	4061	12777	47330	3792	22	3	2		0				2122
25X-2, 145–150	200	3965	11814	48662	3185	16	2							3041
26X-3, 0–5	210	2926	6447	47192	3300	21	2	1				2		2302
28X-3, 0–5	220	3748	10249	71222	2035	33	3		5					2139
30X-3, 0–5	231	3141	7260	45859	33229	39	2			1				1182
31X-3, 0–5	240	1986	2669	74882	3294	36	1					1		2086
32X-1, 125–130	248	2161	3223	10042	0	13	0							786
32X-3, 0–5	250	60347	249019	10055	982	12	0							828
34X-2, 145–150	260	25160	108685	16271	1824	25	1							657
36X-1, 94–99	268	184462	860777	23299	10299	36	2							653
37X-1, 0–1	275	2522	4859	34004	2449	35	1							963
38X-1, 0–1	284	73520	300328	42402	1054	49	1						2	867
39X-1, 45–50	293	15283	66932	10077	1898	36	1				3			281
40X-3, 0–5	302	4173	14104	25619	1811	58	1							439
40X-4, 39–44	302	3298	7850	26463	2487	134	2						1	197
41X-5, 0–5	311	7872	34327	38529	1124	83	1		1		2			464
42X-1, 42–44	320	51386	212776	8929	963	109	2							82
43X-2, 0–5	328	43413	180977	44390	2109	110	1					1	1	403
44X-1, 101–106	337	16318	71628	29687	2233	225	1							132
146-889B-														
1R-1, 145–150	198	230910	1097203	64626	12227	2			1	1		6	13	37573
3R-2, 0–5	217	198310	873525	35312	5802	14				1	2		3	2579
4R-2, 63–64	227	161321	738874	61427	15267	33	1						2	1867
5R-1, 0–5	235	176654	798531	49357	11602	14	0						2	3546
6R-2, 0–5	246	131424	718084	43158	15875	68	1	3	4	2				634
6R-3, 35–40	248	146392	927214	27888	5367	59	1	4	4	4			1	472
7R-2, 0–5	255	207305	1011742	28839	10114	103	1	2					1	280
8R-2, 0–5	264	163208	759977	67465	9187	58	0						1	1161
9R-1, 145–150	273	101609	469949	65875	10670	24	1							639
10R-3, 0–5	283	162303	728905	69143	9888	13		2		1				5360
12R-3, 0–5	301	145663	747170	36791	5318	13								2787
13R-3, 55–60	311	175063	785710	19090	4566	11								1735
14R-1, 106–111	317	185165	824346	112901	3102	104	3							1086
15R-1, 145–150	326	143873	730833	28757	5614	126	1							229
17R-1, 15–20	342	180084	765612	64376	8900	147								437
18R-1, 95–100	352	193343	825475	26877	5106	85	1							317
19R-1, 0–2	360	183056	755846	51328	3501	99								521
20R-1, 0–2	369	207771	882333	63010	9789	217	4	5	3	4			2	290
21R-1, 66–68	378	191447	820846	42934	3722	178	8	10	6	7			2	241
146-889D-														
1H-4, 0–5	89	170135	748743	121928	3127	6								18800
2W-6, 0–5	118	224972	980834	58846	14032	3								18600
3X-1, 0–5	140	199311	824730	29877	6854	8								3940
4N-2, 0–5	153	189864	860546	36828	13387	21								1750
146-890B-														
1H-1, 40–45	0	88800	360232	88	6725									U/D
1H-1, 62–65	1	189222	799331	119	1973									U/D
1H-1, 113–116	1	178505	760692	106	66					1				U/D
1H-2, 45–48	2	176298	753622	569	4046									U/D
1H-3, 0–5	3	206693	855828	13	1333									U/D
2H-2, 60–63	9	209789	903761	20813	4099									U/D
2H-3, 50–53	11	237536	1025934	19897	9986									U/D
2H-6, 140–145	16	194231	816172	55558	7923	1								55558
3H-2, 140–142	20	170908	789043	72308	4203	2								45193
3H-5, 145–150	24	187232	800940	82417	10029	2								43377
4H-1, 0–1	26	149244	708312	48109	10871	1		1						37007
5H-5, 0–5	44	258114	1078394	68532	9741	2				1		1		38073

Note: C_X = *n*-alkanes, iC_X = iso-alkanes, nC_X = normal alkanes, and U/D = $C_1/C_2 > 10^6$. Hydrocarbon gases given as ppmv; other gases are uncorrected for sample volumes

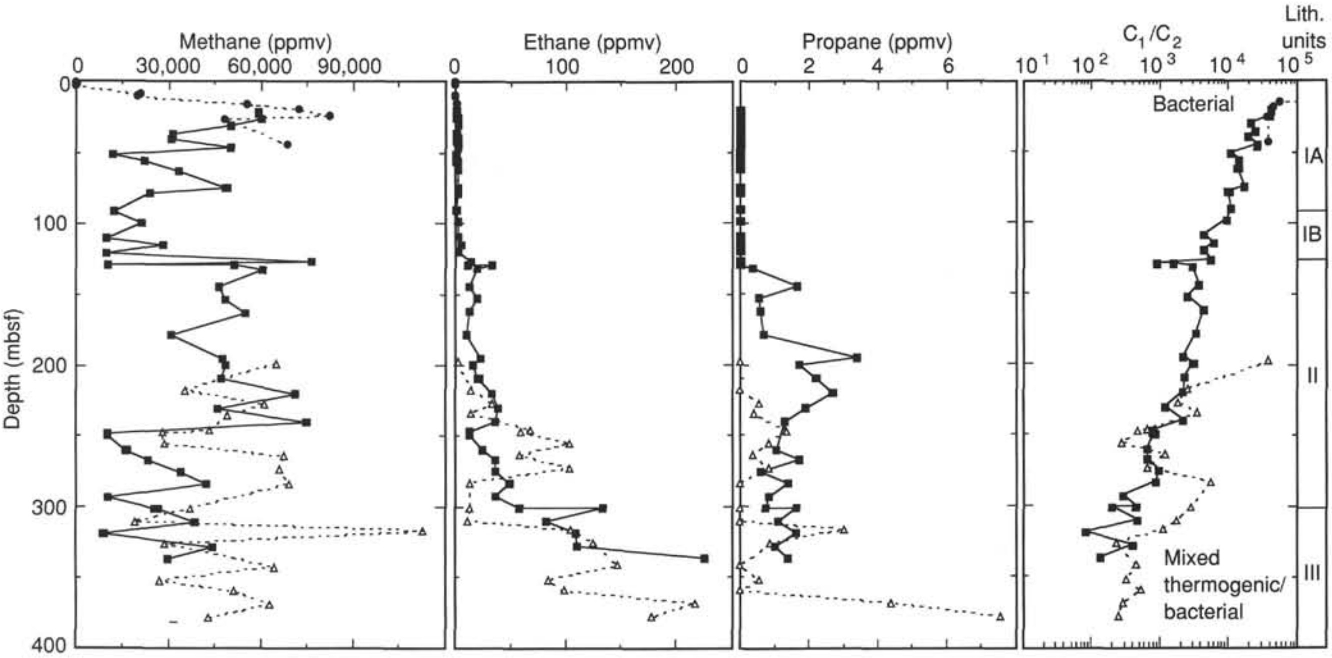

Figure 57. Depth distribution at Sites 889 and 890 of headspace gases, including methane, ethane, propane, and ratio of C_1/C_2 (squares = Hole 889A, triangles = Hole 889B, and circles = Hole 890B).

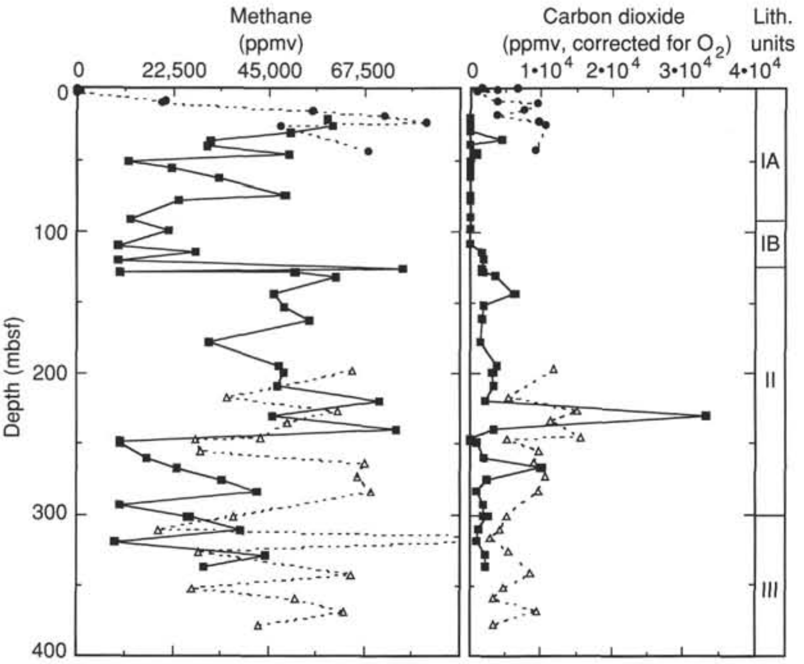

Figure 58. Comparative depth distribution of headspace methane and carbon dioxide (symbols as in Fig. 57).

Expansion Void Gas

Gas expansion voids were often observed in the core liner after its retrieval on deck. These gases were sampled as explained in the "Explanatory Notes" chapter (this volume). The EVGs were found to contain hydrocarbons in the C_1 to C_7 range. All EVG results obtained from Holes 889A, 889B, 889D, and 890B are shown in Table 9. Whereas 74 HS samples were collected from the three holes, a total of only 36 EVG samples was obtained. This disparity resulted from either the absence of voids or poor core recovery. For Hole 889A, no EVG observations were made between 240 and 300 mbsf; however, this gap is covered by a relatively dense series of observations at Hole 889B. The vertical profiles for the EVG hydrocarbon gases methane, ethane, and propane are shown in Figure 59.

The EVG hydrocarbon contents are significantly higher (up to 999,000 ppmv; i.e., 99.9 vol%) than those of HS gas but present similar gas ratios for equivalent depths. The EVG methane profiles are shown in Figure 59. The HS methane shows the same general trends as the EVG methane profile, although perhaps more generalized by fewer observations. For HS ethane (Fig. 59), a high concentration of 3099

Table 9. Molecular composition of expansion void gases at Sites 889 and 890.

Core, section, interval (cm)	Depth (mbsf)	O_2	N_2	C_1	CO_2	C_2	C_3	iC_4	nC_4	iC_5	nC_5	iC_6	nC_6	C_1/C_2
146-889A-														
1H-1, 41–42	20.42	27339	150634	812419	11592	31.8	0.3							25548
1H-3, 12–13	23.13	13570	58505	980794	1407	38.7	0.4	1.9	2.2	3.3	3.8	6.7	8.7	25357
1H-6, 27–28	27.78	1170	1126	944008	1712	47.7	0.5							19791
2H-7, 3–4	38.54	9422	65704	998701	7483	55.6	0.5							17962
3H-8, 17–18	49.68	52614	226633	776254	4837	51.0	2.5							15221
4H-2, 132–133	51.33	29857	139984	962874	5384	65.8	0.6		5.3					14633
4H-7, 105–106	58.56	13711	60275	653467	54	45.9	0.4							14237
5H-7, 105–106	68.06	0	0	995485	0	83.5	0.6							11922
6H-5, 47–48	73.98	75	463	795435	0	60.8	0.4							13083
8H-5, 60–61	93.11	150100	550222	495428	2798	50.3	1.6							9849
9H-8, 91–92	105.92	4623	18829	562284	1626	62.7	1.5		13.9					8968
10H-4, 42–43	108.93	4660	19214	14394	90	4.2	0.0							3427
12H-5, 5–6	125.06	14778	64391	464676	2480	211.7	1.0	1.4	19.0			1.1		2195
17X-2, 75–76	132.36	26415	114109	253	90	5.4	0.0	1.7	42.9				1.2	47
19X-3, 140–141	144.51	78864	322235	782284	4794	607.2	2.6							1288
20X-3, 90–91	162.51	28349	146436	969920	4281	522.7	6.7		5.6			1.1		1856
22X-6, 28–29	185.29	47567	198007	892816	312	866.9	9.2	1.8				0.8	1.3	1030
24X-5, 16–17	193.97	33000	139925	655076	4242	638.2	3.9							1026
25X-2, 100–101	199.81	23958	104432	798851	203	687.4	7.7							1162
26X-4, 56–57	211.87	5749	26079	867673	694	625.4	6.5							1387
28X-4, 101–102	222.82	29491	126310	813108	1476	867.3	5.1							938
30X-2, 81–82	230.12	25265	109798	894792	1271	775.7	4.1							1154
31X-5, 51–52	243.72	2082	3044	733236	1165	412.2	3.7	2.3	0.7				1.2	1779
40X-1, 102–103	302.53	26220	113348	218779	2583	206.1	1.0							1062
41X-4, 35–36	315.36	41416	173888	860362	89	2813.5	5.0						0.8	306
146-889B-														
4R-2, 63–64	227.44	48986	209721	775376	6172	896.7	2.9	1.2		0.8	1.9	3.0	4.2	865
6R-3, 10–11	247.41	94882	353286	657636	5777	3099.0	10.4	10.0	44.2	3.0		1.1	2.1	212
7R-4, 69–70	259.10	202353	840293	232710	984	245.4	0.5		3.3					948
8R-4, 69–70	267.90	47426	210635	947194	3438	962.7	1.9	2.2		1.1				984
9R-1, 102–103	272.63	81743	339213	562309	3939	352.0	0.9	1.4	3.2					1597
10R-2, 38–39	282.29	69401	293669	679717	3555	202.9	0.4		2.7					3350
12R-3, 11–12	301.32	92491	324325	806928	5122	242.6	2.5	2.2	5.2		1.9		0.5	3326
13R-2, 30–31	308.91	60033	255927	836403	5643	430.0	0.9							1945
14R-2, 36–37	317.67	35485	155355	853820	9761	920.0	2.2	4.4	3.2	3.6				928
146-889D-														
1H-6, 69–70	95.38	69729	289215	693960	3480	56.9								1220
2W-7, 51–52	121.69	42308	184764	935866	3022	125.6					2.3			7450
146-890B-														
2H-4, 53–54	2.24	8293	50055	36530	2607	6.1	2.0	1.0			2.2			5989
3H-3, 112–113	20.93	4245	51669	938618	3440	33.9	1.4				2.2			27688

Note: C_X = n-alkanes, iC_X = iso-alkanes, nC_X = normal alkanes, C_X = unsaturated alkanes, and U/D = $C_1/C_2 > 10^6$. Hydrocarbon gases given as ppmv; other gases are uncorrected for sample volume.

ppmv occurs at 247 mbsf (in Hole 889B) immediately above the "ethane minimum zone." Another anomaly is recognized in comparing the HS methane and ethane profiles from Hole 889B. Whereas the methane values are seen to increase with depth in the zone between 268 and 282 mbsf, the ethane profile trends the opposite way.

The HS C_1/C_2 curve (Fig. 59) also follows the same trends as the equivalent EVG curve, that is, an anomaly at the boundary between Units I and II, and another anomaly, restricted to Hole 889B, at depths between 247 and 282 mbsf. Overall, the C_1/C_2 ratios for HS are surprisingly similar to the ratios for EVG gases, suggesting minimal molecular fractionation related to recovery, degassing, or to air exposure of EVG samples during sampling. The HS propane profile (Fig. 59) shows similar trends to those in the EVG propane profile.

The nonhydrocarbon HS profiles are shown in Figure 60. The HS concentrations of nitrogen and carbon dioxide vary sympathetically in Hole 889A, but in opposite directions in Hole 889B, which was sampled between 227 and 318 mbsf only. There are two anomalous HS nitrogen peaks: 5.5×10^5 ppmv at 93 mbsf in Hole 889A and 8.4×10^5 ppmv at 259 mbsf in Hole 889B.

Kerogen Analysis

Nine samples from Holes 889A and 890B were analyzed for kerogen by Geofina hydrocarbon meter pyrolysis. They gave low S_1 and S_2 counts (Table 10), reflecting that the organic matter is refractory. Examples of pyrolysis runs (Fig. 61) show that there is a trend towards a constant T_{max} of 402°C with depths greater than 130 mbsf.

Bitumen Analysis

A total of eight samples was extracted as described in the "Explanatory Notes" chapter (this volume). There was no visible fluorescence in any of the samples, indicating the low rank and domination of refractory material.

In contrast to Site 888, the high-resolution C_{11}–C_{40} gas chromatography of the hexane-soluble fraction in Sites 889 and 890 showed that some of the original labile hydrocarbons in the organic matter occur as *n*-alkanes and isoprenes (Figs. 62–63). Some of the most prominent peaks correspond to common alkanes and can readily be identified. Some of the residual bitumen is clearly seen as lipids from methanogenesis, and some remains as an unresolved complex mixture (UCM) of extractable material (Fig. 62). Maturation of the organic matter has been insufficient to generate significant amounts of thermogenic products. Examples of typical C_{11}–C_{40} gas chromatograms in Figure 62 illustrate the highly degraded nature of the hydrocarbons in the extracts. The C_{37}–C_{39} alkenones (Fig. 63) are resolved and determination of U^k37 is possible.

Preliminary Interpretation

Methanogenesis dominates the diagenetic sequence after sulfate is depleted by sulfate-reducing bacteria (Claypool and Kaplan, 1974). The sulfate content in the interstitial waters is low throughout Sites 889 and 890 with almost complete sulfate depletion observed at about the 5–8 mbsf level (see "Inorganic Geochemistry" section, this chap-

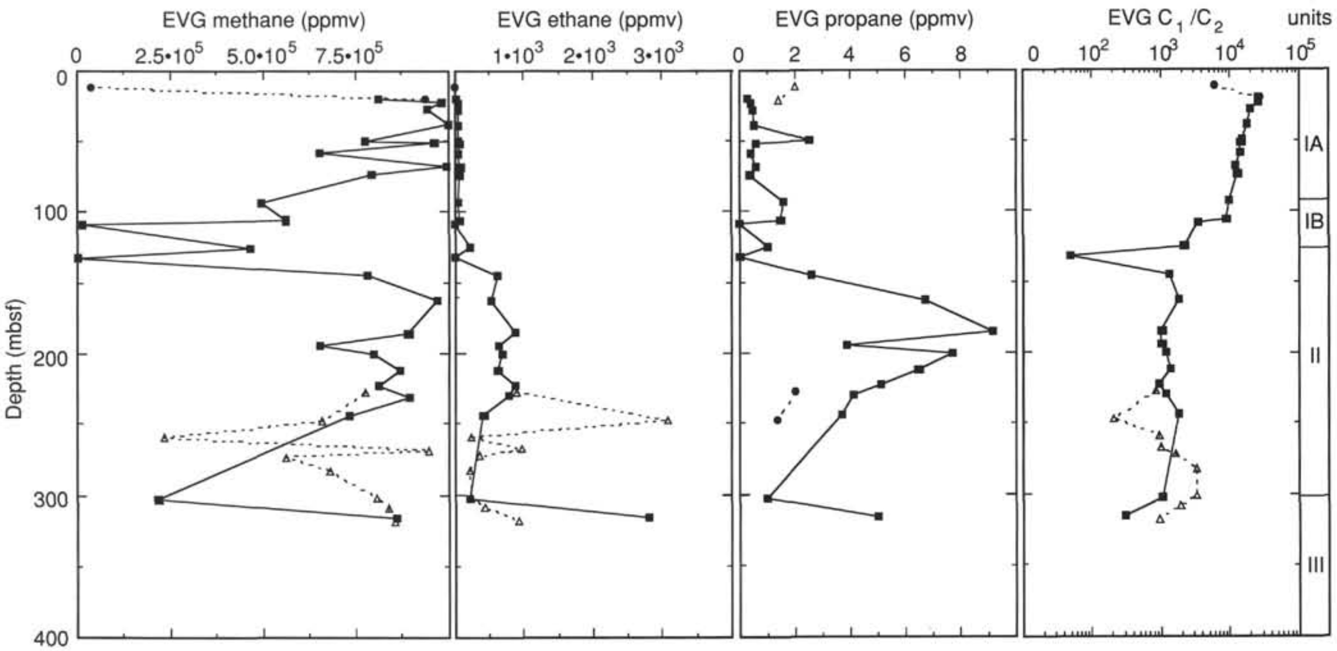

Figure 59. Depth distribution at Sites 889 and 890 of EVG methane, ethane, propane, and ratio of C_1/C_2 (symbols as in Fig. 57).

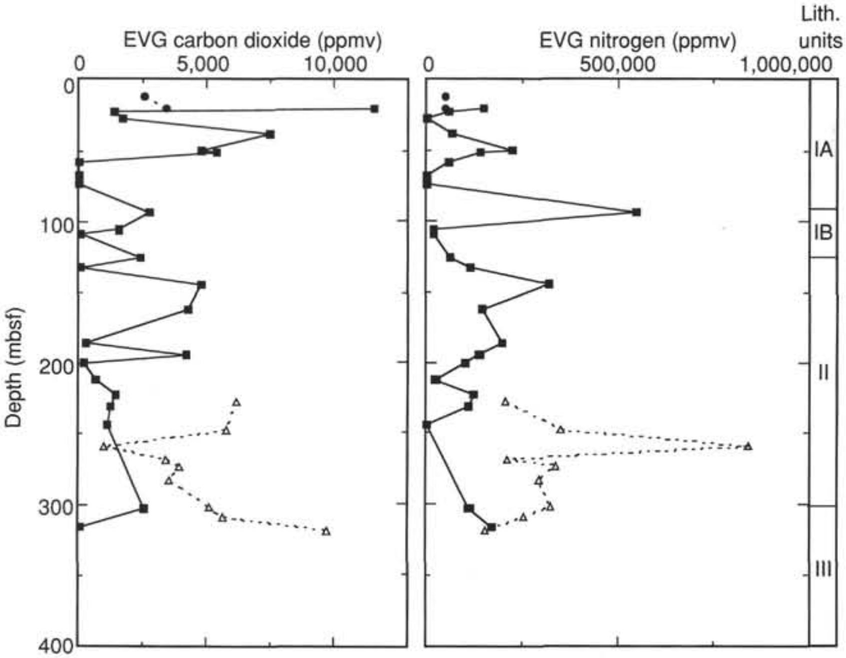

Figure 60. Comparative depth distribution of EVG carbon dioxide and nitrogen at Sites 889 and 890 (symbols as in Fig. 57).

ter). Therefore, environmental conditions for methanogenesis by way of CO_2 reduction are probably favorable for biogenic methane generation in the sedimentary column (e.g., Whiticar et al., 1986). There is a strong correlation between the organic carbon distribution and the methane concentrations suggesting autochthonous production of bacterial methane in the sediments.

The increase of ethane and propane below 200 mbsf and the C_1/C_2 trends indicate that allochthonous thermogenic hydrocarbons have migrated and probably still migrate into the sediments below this depth. We anticipate that the isotopic signature of the hydrocarbons sampled at Sites 889 and 890 will show a mixed bacterial/thermogenic origin, but final confirmation awaits shore-based stable isotope analyses.

Despite the generalized situation described here, some interesting features are present in the distribution of organic compounds at these sites, some of which possibly relate to the expected (but not directly observed) presence of gas hydrates at Holes 889A, 889B, and 890B.

The shallowest geochemical anomaly is found between 120 and 130 mbsf, that is, at the transition between Units I and II, where the EVG and HS methane concentrations increase sharply with depth and where there is a marked local inversion in the EVG and HS C_1/C_2

Table 10. Results of Geofina hydrocarbon meter pyrolysis at Sites 889 and 890.

Core and section	S_1 (mg C/g)	S_2 (mg C/g)	Calculated T_{max} (°C)	Measured T_{max} (°C)
146-889A-				
1H-2	0.21	0.49	407	488
6H-5	0.21	0.41	337	404
10H-4	0.29	1.00	375	449
17X-2	0.19	1.35	401	480
31X-5	0.28	1.31	401	481
43X-2	0.18	1.07	401	481
146-889B-				
20R-1	0.17	1.44	402	482
146-890B-				
1H-2	0.14	0.48	415	497
3H-2	0.03	0.07	346	414

curves. This local increase in ethane relative to methane probably indicates hydraulic communication with deeper layers richer in thermogenic hydrocarbons.

At depths greater than 200 mbsf there are three zones that seem to be geochemically significant: (1) the zone from 220 to 240 mbsf, where there is an EVG carbon dioxide anomaly in both Holes 889A and 889B; (2) the zone from 247 to 260 mbsf, where the EVG methane concentrations drop abruptly to a local low (a methane minimum zone) before increasing with depth, where the HS ethane spikes up to a local high, and where the EVG and HS C_1/C_2 ratios start increasing with depth in Hole 889B (but not in Hole 889A); and (3) the zone from 283 to 311 mbsf, where the EVG ethane and propane concentrations in Hole 889B drop and remain low (an ethane/propane minimum zone) and where the HS methane and ethane concentration gradients in Hole 889B vary in opposite directions. The geochemical distributions observed from 220 to 311 mbsf are unusual. The formation or decomposition of gas hydrates may play a role in the stripping and accumulation of gas species and may explain some of these observations.

According to previous laboratory results, field measurements, and theoretical calculations (Hitchon, 1974), gas hydrates have varying stability fields according to hydrate structure (I or II) and the presence and composition of guest molecules. If both Structure I and II gas hydrates containing methane, ethane, and propane guest molecules (Hitchon, 1974) occur at Sites 889 and 890, then the observed hydrocarbon anomalies may be explained by the formation of Structure I and II hydrates somewhere within the 220- to 311-mbsf interval.

At this stage, use of the organic geochemical profiles as indicators for gas hydrates is highly speculative. However, two interpretative models seem possible:

1. Structure I and II gas hydrates may be present in the sediment column above the methane minimum zone (i.e., above a depth of 247 mbsf). The minimum zones represent concentration gradients that are anomalous because there is no accompanying significant change in lithology. A strong concentration gradient then suggests either active pore-water flow or upward molecular flow (diffusion) from higher concentrations existing below the minimum zone toward a zone of gas accumulation or hydrate formation, located above the minimum zone at 247 mbsf.

Likewise, Structure II hydrates, containing ethane and propane, would be expected to form at about 283 mbsf (at least in Hole 889B), according to Hitchon (1974), immediately above the ethane/propane minimum zones.

This model would mean that the EVG and HS gases sampled shallower than the respective minimum zones may have evolved from disseminated gas hydrates that decomposed as a result of pressure release upon sampling. It would also mean that the gases obtained from the sediments below the minimum zones would have been stored either as dissolved gas in the pore water or as free (occluded) gas in the sediments. If this model is correct, the existence of the gas minimum zones is suggested to be diagnostic for in-situ gas hydrate formation.

2. The other way of explaining some of the peculiarities we observed in the organic geochemical data at Sites 889 and 890 is by reconstructing the history of the gas hydrate stability zone. Gas hydrates have probably been forming in the sediments at Sites 889 and 890 from the time they were accreted, that is, for about 0.8–1.1 $\times 10^6$ yr (Westbrook, this volume). Therefore, one would expect that a geochemical fingerprint would still exist in the sediment zones where gas hydrates previously had been stable, but where they have now decomposed because of sedimentation and increased temperature. The anomalies in the EVG and HS profiles mentioned previously could thus be the signatures remaining in the sediments from a complex history of gas hydrate formation and decomposition.

It is expected that onshore analysis of the sorbed gases in the sediments and of the stable carbon isotopes of hydrocarbon gases and of CO_2 will shed more light on these issues.

GAS HYDRATE STUDIES

Low Temperature Measured on Core 146-889B-3R on the Catwalk

Temperature measurements were conducted in Core 146-889B-3R on the catwalk after sediment was found to be unexpectedly cold to the touch. About 10 measurements at the base and section ends of the 2.27-m-long core were taken with a portable, digital thermometer that has a precision of 0.1°C. Temperatures were measured between –0.9° and –1.4°C. The measurements indicated a rather uniform temperature both along the core and from its axis to its outer edge inside the liner. The measured temperature of –0.9° to –1.4°C is much lower than any in-situ temperature the core could have met on its way from the bottom of the hole to the catwalk. In particular, it is 3.6° to 4.1°C lower than the bottom-seawater temperature of about 2.7°C, which is the lowest temperature the core could have met inside the drill pipe (see "WSTP and ADARA Temperature Measurements" section, this chapter). For comparison, the temperature measured on the catwalk in subsequently recovered cores was between 7° and 10°C.

Internal heat consumption caused by hydrate dissociation is thought to be the only reasonable explanation for the low temperature measured in Core 146-889B-3R. One gram of methane hydrate requires about 700 J to dissociate (using a mole weight of 120 g and a dissociation heat of 85000 J/mol, after Makogon, 1981). If we assume that a unit volume of the core contained x grams of methane hydrates at the time of drilling, the heat required for the total dissociation of these x grams of methane hydrate before the core reaches the catwalk is then $700x$ J. If all of this heat is derived from the core itself (for simplicity in this preliminary analysis, no heat exchange is assumed between the core and the surrounding medium), the core temperature is predicted to drop by $\Delta T = 700x/\rho c$, where ρc is the volumetric heat capacity of the wet sediment.

When applied to Core 146-889-3H, with $\rho c = 2500 \times 10^3$ J/m^3°C and $\Delta T = 10$°C, the formula yields a hydrate content of $x = 0 \times 036$ Mg/m^3. Taking the hydrate density as 0.9 Mg/m^3 and the porosity as 0.49 (see "Physical Properties" section, this chapter), the fraction of the pore space occupied by hydrates is then estimated at 8.2%. As noted earlier, this figure rests on the assumption that heat exchange between the core and its surrounding medium can be neglected. Measurements were taken between 5 and 10 min after the core had been brought to the catwalk. Allowing for an additional 10 min to account for the core trip from the bottom of the hole to the catwalk, the time during which the core and its surroundings could exchange heat was probably near 20 min. This is of the order of the time constant of thermal equilibration of the core (the time constant, τ[s], of an infinite circular cylinder of diameter $2R$[m] and thermal diffusivity k[m^2/s] is given by $0.2R^2/k$, after Carslaw and Jaeger (1959); taking $2R = 0.07$ m as the core diameter and $k = 3 \times 10^{-7}$ m^2/s as its thermal

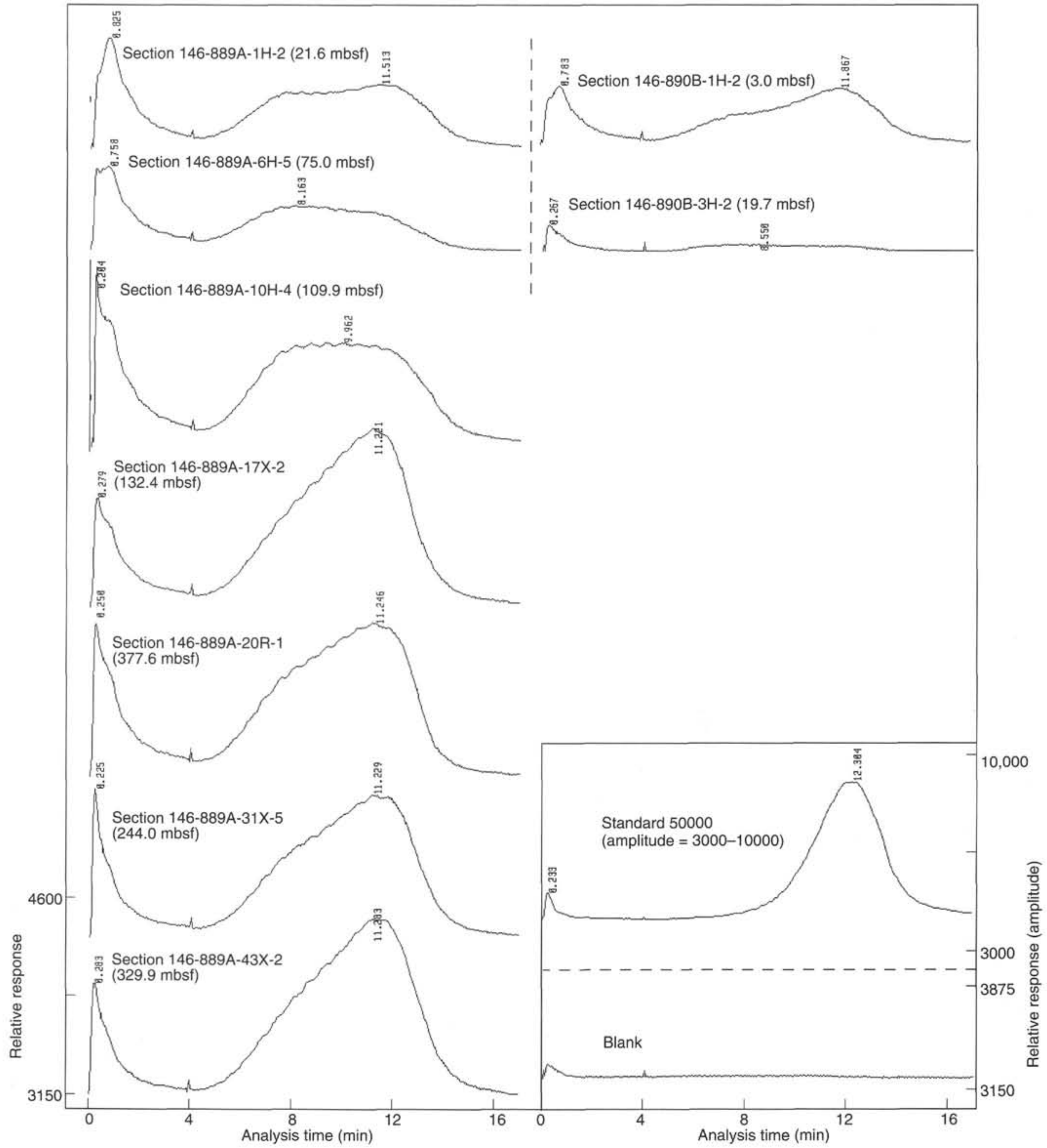

Figure 61. Example of Geofina hydrocarbon meter pyrograms at Sites 889 and 890.

diffusivity, $\tau = 816$ s). A corrected figure for the fraction of pore space occupied by hydrates could be therefore substantially more than 8%.

INORGANIC GEOCHEMISTRY

Introduction and Operation

The main objectives of the pore-fluids program at Sites 889 and 890 were (1) to determine if gas hydrates are present above the prominent BSR, and if present, to sample both the gas hydrates and the in-situ pore fluids with the PCS, and to determine the depth profile of gas hydrate concentration above the BSR and the mechanism of its formation; (2) to determine the relation between fluid flux and gas hydrate formation; (3) to test the hypothesis that dispersed fluid expulsion is associated with compaction in this segment of the Cascadia convergent margin; and (4) to document the decomposition of organic matter by anaerobic microbial processes and their control on carbonate dia-

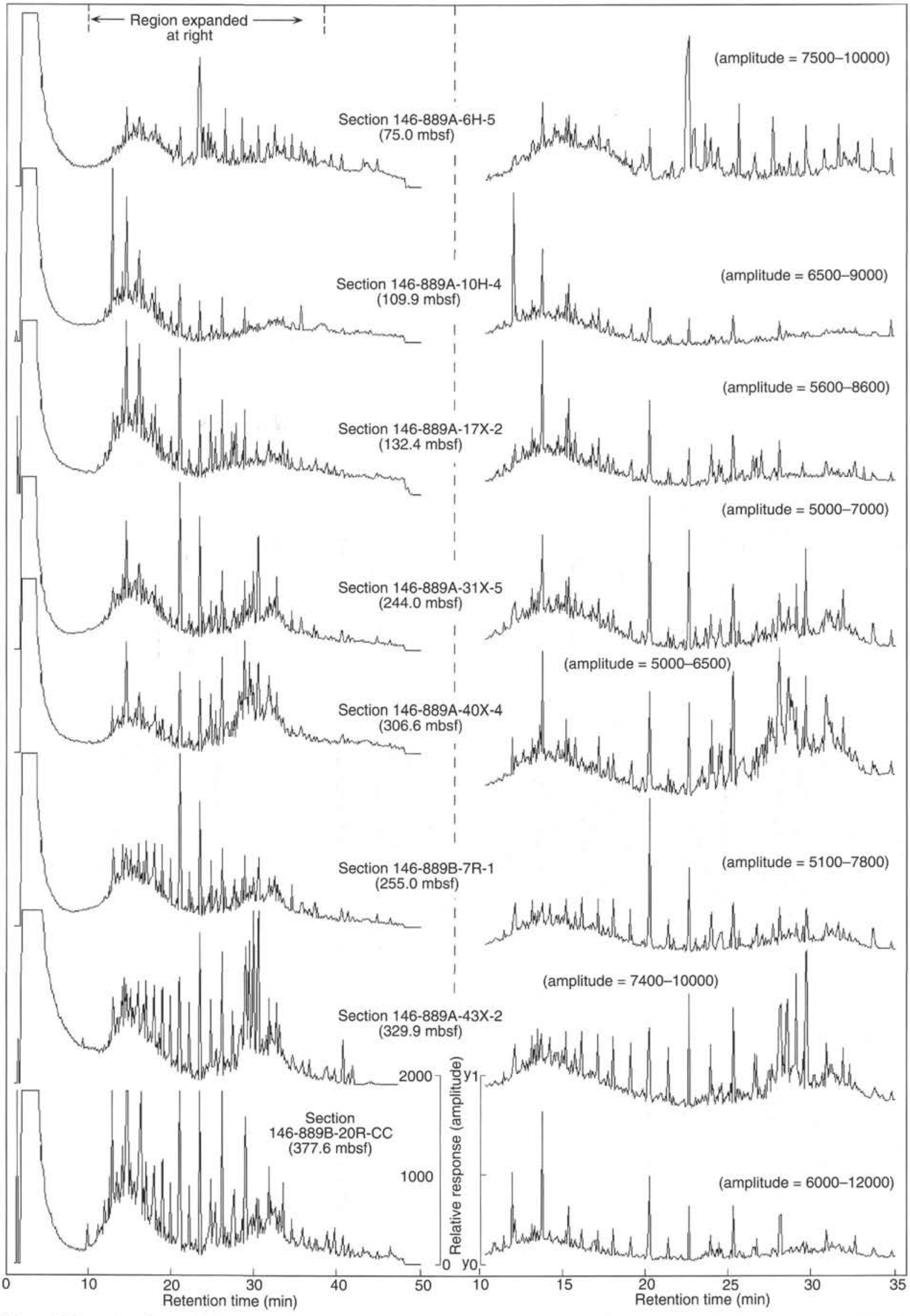

Figure 62. Examples of typical C_{11}–C_{40} gas chromatograms at Site 889. The central part of each chromatogram is shown on an expanded scale on the right.

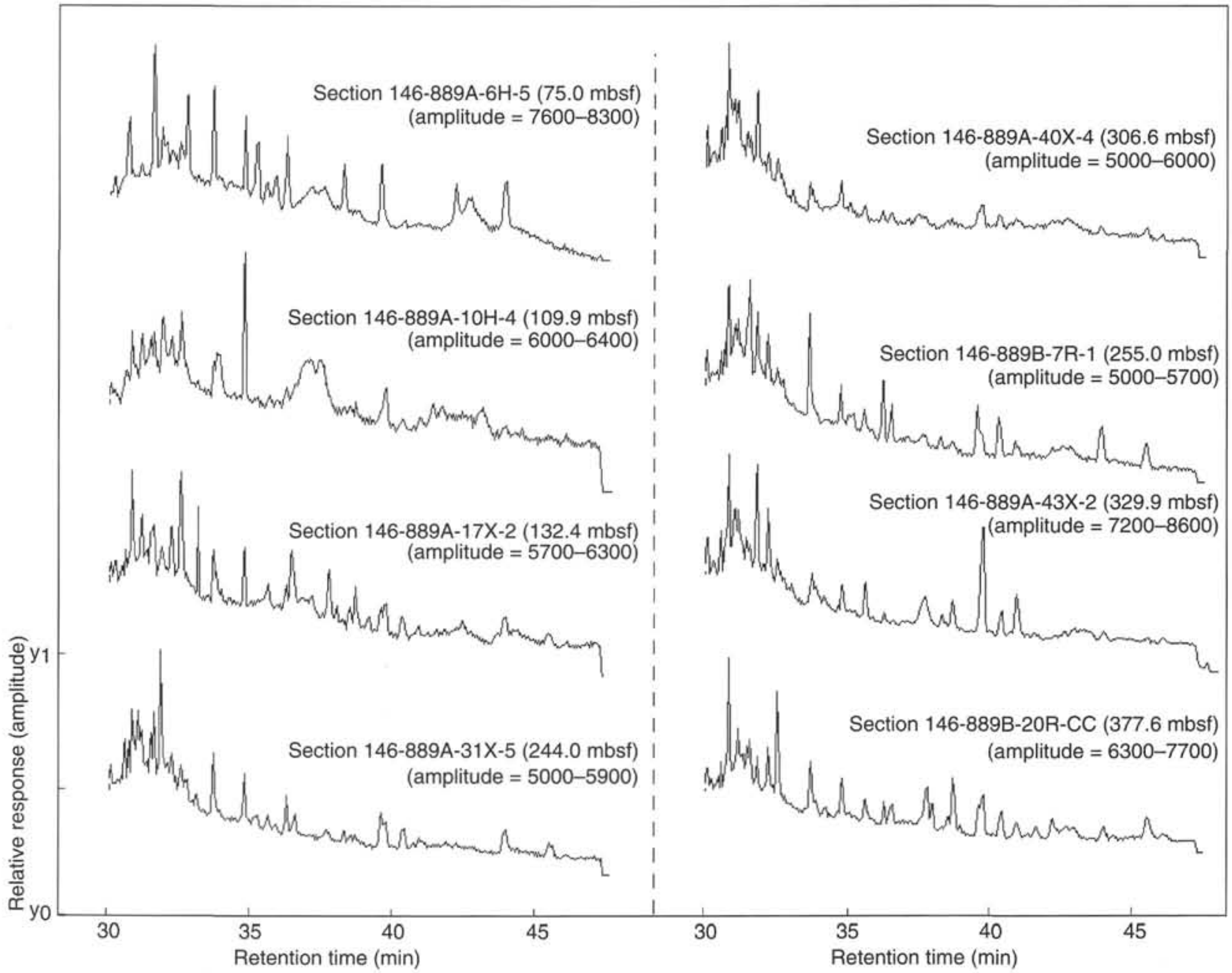

Figure 63. Examples of typical C_{23}–C_{40} gas chromatograms ("alkenone fraction") at Site 889.

genesis, especially in the uppermost 80–100 m of the sediment section, as well as the influence of fluid advection and gas hydrate formation on carbonate precipitation throughout the section drilled.

Holes 889A, 889B, and 890B were sampled for inorganic chemical analyses of the pore fluids. Only pore-fluid samples squeezed from whole-round core samples (5–20 cm length) were analyzed at these sites. The squeezed pore fluids were analyzed for salinity, Cl^-, Ca^{2+}, Mg^{2+}, K^+, Na^+ (only Hole 889A samples), Li, sulfate, ammonia, phosphate, pH, alkalinity, and silica. The data are presented in Tables 11 and 12. The Na^+ data in Holes 889B and 890B were calculated by charge balance.

One in-situ pore fluid sample (WSTP 10M), at 101 mbsf, was collected in Hole 889A. Water was recovered from the two coils (Ti and stainless steel), as well as from the overflow chamber. The Cl^-, SO_4^{2-}, Ca^{2+}, and Mg^{2+} concentrations and the alkalinities of the three WSTP subsamples indicated approximately 94% contamination with surface seawater (the drilling water). The overflow water was also diluted by the nanopure water displaced from the two coils by the drilling water.

The PCS was run six times in Hole 889A. Cores 146-889A-15P (PCS #1, at 129.5 mbsf) and 146-889A-29P (PCS #4, at 227.8 mbsf) retained a pressure approximately equal to the in-situ hydrostatic pressure while on deck. Gases were recovered only from Core 146-889A-15P, but no pressure increase was observed on the pressure gauge that monitors the core-barrel pressure after depressurization, which indicated that gas hydrates were not present. The core barrel of Core 146-889A-15P contained 45 cm of sediment. The interval from 7 to 13 cm in the core was squeezed and analyzed for all the aforementioned components (Table 11). The only observed distinct difference in chemistry relative to the adjacent squeezed pore fluids is the high alkalinity value obtained in the PCS sample. In Core 146-889A-29P, upon expansion through the gas manifold, all pressure was rapidly lost and the core barrel contained only water. Chemical analyses identified the water as drilling water. The other four PCS cores neither retained a pressure nor recovered sediment in the core barrel, with each recovering only drilling water.

Clearly, we failed to achieve the first main objective outlined herein. No in-situ pore fluids and no gas hydrates were recovered at these sites.

Although great care was taken when preparing the sediment samples for squeezing to avoid contamination by the surface seawater used for drilling, in several of the deeper, highly fractured samples some contamination was unavoidable. At Site 889, the sediments prone to drill-water contamination occur below the sulfate-reduction zone. Contamination by surface seawater, introduced by drilling, is therefore easily monitored and quantified by sulfate analysis. But in order to be certain that each observed elevated sulfate value indeed represents contamination with surface seawater, the concentration of every other major seawater constituent (i.e., Cl^-, Mg^{2+}, Ca^{2+}, Na^+, and K^+) must also be checked for consistency with the assumption of contamination by surface seawater. When a sample was found to be contaminated with surface seawater, the percent contamination was determined and the concentrations of all major constituents of the contaminated sample were corrected for the amount of admixed seawater. Table 11 shows the sulfate-corrected values.

Table 11. Interstitial-water geochemical data, Holes 889A and 889B.

Core, section, interval (cm)	Depth (mbsf)	Water (mL)	pH	Alkalinity (mM)	Salinity (g/kg)	Cl^- (mM)	Mg^{2+} (mM)	Ca^{2+} (mM)	Mg/Ca	SO_4^{2-}(mM)		PO_4^{3-} (µM)	NH_4^+ (µM)	SiO_2 (µM)	K^+ (mM)	Na^+ (mM)	Na/Cl	Li^+ (µM)
										Measured	Corrected[a]							
146-889A-																		
1H-2, 0–6	21.52	38	8.0	32.60	33.8	528	40.61	3.47	11.7	0.00	0.00	92.6	2141	558	9.36	461	0.87	9.7
1H-4, 145–150	25.97	38	8.3	34.95	32.0	521	39.31	2.98	13.2			88.3	2226	570	10.74	458	0.88	13.0
2H-5, 145–150	36.95	28	8.2	40.83	30.0	499	33.95	3.06	11.1	0.00	0.00	110.4	1786	465	10.54	453	0.91	
3H-6, 0–6	45.54	22	8.3	31.35	29.0	488	29.08	2.88	10.1	0.00	0.00	123.7	2901	608	13.61	439	0.90	11.8
4H-5, 143–150	54.64	28	8.4	24.79	27.5	462	25.84	2.03	12.7	0.00	0.00	83.0	2673	537	9.31	419	0.91	11.2
5H-3, 137–147	62.32	30	8.4	24.05	26.0	456	23.55	1.21	19.5	0.00	0.00	94.7	2598	650	8.80	419	0.92	12.0
6H-5, 145–150	73.69	40	8.5	26.83	25.0	442	22.13	2.22	10.0	0.00	0.00	85.1	3439	655	9.00	408	0.92	14.7
7H-2, 143–150	79.95	40	8.2	27.33	25.0	432	21.18	2.62	8.1	0.00	0.00	73.3	3182	743	8.24	400	0.93	18.5
8H-3, 140–150	90.91	42			26.5	424	20.15	3.08	6.5	0.00	0.00	53.0	3942	901	8.29			19.7
9H-6, 125–130	101.89		8.3	28.32	30.0	412	18.16	3.63	5.0	0.00	0.00	39.0	4890	680	7.93	384	0.93	22.3
10H-4, 140–150	109.57	28	8.4		24.5	405	17.64	3.83	4.6	0.00	0.00	33.7	4904	695	8.59			23.4
11H-1, 140–150	114.90	38	8.3	27.94	24.0	401	17.60	3.95	4.5	0.00	0.00	25.1	5889	655	8.70	371	0.93	29.0
11H-2, 130–150	116.40	50																
12H-4, 140–150	124.05	20	8.2	27.08	26.0	398	17.13	3.94	4.3	0.00	0.00	28.3	5750	851	8.67	369	0.93	34.6
13H-CC, 15–22	127.37	20	8.4	25.78	23.5	391	16.86	4.05	4.2	0.00	0.00	23.7	6463	889	7.83	361	0.92	34.5
14H-1, 53–58	128.53	9	8.4	27.07	22.2	378	15.27	4.03	3.8	0.00	0.00	12.8	4801	686	7.16	355	0.94	34.9
15P-1, 7–13	129.07	6	8.1	35.56	28.9	363	10.53	4.41	2.4	0.54	0.00	9.4	6876	950	7.16	355	0.98	
17X-2, 70–80	131.46	5			21.2	379	14.54	3.64	4.0	1.92	0.00	16.8	6828	898	7.95			34.5
18X-4, 36–46	144.41	9			24.4	388	16.29	3.36	4.8	0.21	0.00	15.8	7056	776	6.47			36.8
22X-7, 0–20	184.95	7			21.5	378	11.42	4.02	2.8	1.12	0.00	10.9	6621	758	6.14			40.2
24X-5, 120–140	194.27	8	8.2	19.49	24.8	366	10.93	4.36	2.5	2.70	0.00	12.2	7131	730	6.78	341	0.93	50.1
25X-2, 0–20	198.80	9	8.3	19.73	21.8	364	11.12	3.89	2.9	3.02	0.00	10.4	7086	866	8.24	338	0.93	52.0
26X-4, 130–150	212.47	20	8.1	17.18	20.8	370	11.90	4.18	2.8	1.61	0.00	14.0	5517	878	7.34	342	0.92	59.6
28X-3, 80–100	221.12	22	8.2	19.45	22.1	372	12.78	4.13	3.1	0.95	0.00	10.9	6336	799	8.83	343	0.92	63.6
30X-4, 130–150	233.60	20	8.0	19.57	21.9	358	12.25	4.05	3.0	0.69	0.00	11.8	5826	832	6.47	333	0.93	63.5
31X-5, 140–160	244.01	15	8.3	17.92	24.4	352	11.40	3.75	3.0	0.33	0.00	6.9	6504	628	11.13	322	0.92	66.5
32X-1, 130–150	248.00	11	8.2	18.31	21.5	360	12.94	4.12	3.1	0.08	0.00	0.0	5044	466	7.11	332	0.92	69.4
36X-1, 99–114	267.69	7			21.5	364	10.97	4.26	2.6	1.16	0.00	7.1	5728	909	6.34			81.2
40X-4, 45–65	306.47	12	8.1	15.98	20.5	365	12.17	4.37	2.8	0.10	0.00	8.1	4798	307	6.39	337	0.92	74.6
41X-3, 130–150	314.80	26	7.9	17.44	24.1	362	9.01	5.03	1.8	1.31	0.00	10.1	4920	600	6.78	340	0.94	110.4
42X-1, 44–52	319.94	1			19.0	314												
43X-2, 0–20	329.80	5			22.5	367	10.44	5.72	1.8	1.26	0.00	5.9	5313	811	6.14			
44X-1, 0–15	337.20	2			25.7	376	3.40	5.62	0.6	3.18	0.00	0.0	5120	600	7.47			
146-889B-																		
3R-1, 79–94	216.50	3			22.8	368	13.47	3.59	3.8	0.60	0.00	8.12	5027	746	6.37			
4R-2, 45–60	227.76	14	8.14	19.94	22.9	380	12.18	4.43	2.7	0.23	0.00	8.12	5647	631	8.85	352	0.93	
5R-1, 26–36	235.06	5			21.6	370	11.95	4.43	2.7	0.96	0.00	8.75	4237	1078	6.60			
6R-1, 35–40	244.65	25	8.18	21.02	21.9	365	12.98	4.27	3.0	0.24	0.00	8.12	5138	881	6.83	340	0.93	
7R-1, 95–118	254.85	10	8.25	20.00	21.0	362	12.68	4.19	3.0	0.00	0.00	6.88	4777	707	9.03	334	0.92	
8R-2, 130–150	265.50	8			21.8	372	12.11	4.28	2.8	0.41	0.00	8.12	4855	767	10.05			
9R-1, 130–150	272.90	10	8.08	17.85	21.9	370	9.51	4.13	2.3	0.14	0.00	5.62	4985	967	7.14	348	0.94	
10R-2, 0–20	281.90	3			21.8	371	10.88	4.78	2.3	0.51	0.00				6.50			
12R-1, 130–150	299.50	11	8.11	18.46	22.0	364	11.30	4.40	2.6	0.00	0.00	8.75	4982	570	8.54	338	0.93	
13R-2, 35–55	308.95	9		0.00	20.5	365	11.76	4.74	2.5	0.00	0.00	5.00	4355	559	9.04			
14R-1, 111–136	316.91	7			19.5	375	11.47	5.05	2.3	1.06	0.00	6.25	3877	953	5.78			
15R-1, 125–150	325.85	5			21.6	368	12.50	5.53	2.3	0.96	0.00	6.88	3274	1036	5.37			
17R-1, 0–15	342.10	7			21.9	379	12.44	5.91	2.1	1.49	0.00	6.88	3806	952	5.75			
18R-1, 0–10	351.00	6			21.6	369	12.09	5.21	2.3	0.91	0.00	6.25	3667	950	5.47			
20R-CC, 0–3	368.70	6			21.8	366	11.11	6.37	1.7	0.63	0.00	5.00	3725	1127	6.06			

[a] Corrected for contamination by drilling water; percent sulfate contamination used for correction of other species. All samples were interstitial water samples.

Table 12. Interstitial-water geochemical data, Hole 890B.

Core, section, interval (cm)	Depth (mbsf)	Water (mL)	pH	Alkalinity (mM)	Salinity (g/kg)	Cl^- (mM)	Mg^{2+} (mM)	Ca^{2+} (mM)	Mg/Ca	SO_4^{2-} (mM)	PO_4^{3-} (µM)	NH_4^+ (µM)	SiO_2 (µM)	K^+ (mM)	Na^+ (mM)	Na/Cl
146-890B-																
1H-2, 145–150	2.95	45	7.7	11.47	33.5	544	45.09	6.90	6.5	14.29	45.5	1004	560	12.58	466	0.86
1H-3, 145–150	4.45	25	7.9	16.43	32.0	541	41.49	5.06	8.2	7.13	68.0	997	534	10.95	452	0.84
2H-2, 63–68	9.43	24	7.8	24.04	31.0	532	37.85	3.32	11.4	0.00	79.8	1822	530	10.33	451	0.85
2H-3, 53–58	10.89	25	7.9	24.86	31.5	526	37.87	3.30	11.5	0.00	86.2	1471	590	10.13	457	0.87
2H-6, 145–150	16.52	10	8.3	28.21	30.5	522	37.05	2.20	16.8	0.00	92.6	2282	412	11.00	430	0.82
3H-2, 143–150	19.67	34	8.2	29.22	30.5	515	34.45	1.53	22.5	0.00	124.7	2275	491	11.10	459	0.89
3H-6, 150–155	25.74	30	8.1	30.94	30.0	508	31.77	1.87	17.0	0.00	152.6	2548	681	12.33	457	0.90
5H-5, 0–10	43.62	30	8.1	30.43	28.0	473	25.48	1.44	17.7	0.00	123.7	2634	663	10.64	436	0.92

Results

The concentration-depth profiles of the pore fluids from Sites 889 and 890 define two distinct geochemical zones:

Zone 1, from the sediment/water interface to 130 mbsf, is delineated at its base by chemical concentration anomalies in Cl^-, Mg^{2+}, Ca^{2+}, Na^+, K^+, alkalinity, phosphate, and silica and is situated almost wholly within lithostratigraphic Unit I (see "Lithostratigraphy" section, this chapter).

Zone 2, from 130 mbsf to the bottom of the drill hole, is a low-Cl^- zone, which most probably reflects the dissociation of modern and glacial gas hydrates. It encompasses the modern, active gas hydrate interval, which extends to the depth of the BSR at 225 mbsf (see "Downhole Logging" section, this chapter), to the depth interval of the pressure–temperature-calculated base of the CH_4-H_2O gas hydrate zone located at about 260 (±15) mbsf (see "WSTP and ADARA Temperature Measurements" section, this chapter), and perhaps to a paleo(glacial)-gas hydrate interval below the BSR.

Zone 1

The concentration-depth profiles show systematic variations downhole, with distinct maxima and minima. The most pronounced of these downhole variations are the decreases in Cl^-, Mg^{2+}, Ca^{2+}, Na^+, K^+, and SO_4^{2-} concentrations, as opposed to the increases in alkalinity, ammonia, phosphate, and silica concentrations (Fig. 64). These concentration-depth profiles are controlled primarily by two types of processes: (1) microbially mediated decomposition reactions of organic matter and the resultant carbonate diagenetic reactions; and (2) a physico-chemical diffusional communication with an advected, chemically distinct fluid, introduced at about 130 mbsf. Microbial decomposition is typically reflected in the SO_4^{2-}, alkalinity, Ca^{2+}, Mg^{2+}, and phosphate concentration–depth profiles. (Interestingly, ammonia, which is intimately related to organic matter degradation processes, mimics the silica depth profile in this zone and attains maximum values only in Zone 2.) The diffusion process is best observed in the concentration-depth profile of the conservative component Cl^- and is also in the Na^+, K^+, and silica profiles.

Microbially Mediated Reactions

Microbially mediated organic-matter decomposition processes are the dominant diagenetic reactions in Zone 1, especially between the sediment/water interface and 70–90 mbsf. Sulfate reduction is complete at about 10 mbsf (Fig. 64) and is immediately underlain by the zone of methanogenesis (Claypool and Kaplan, 1974) (see "Organic Geochemistry" section, this chapter). The sulfate-reduction rate is mainly a function of the nature of the substrate organic matter, the burial flux of organic matter, and the sedimentation rate. The observed depth zonation between the sulfate- and carbonate-reduction zones reflects the system's dynamic balance between the rate of sulfate reduction, diffusional supply of sulfate, and sedimentation rates.

Sulfate reduction is accompanied by alkalinity production (Fig. 64). The removal of sulfate, an inhibitor of carbonate diagenesis (particularly dolomite formation; Baker and Kastner, 1981), and the concomitant production of the carbonate ion conducive to carbonate formation, are responsible for the steep downhole variations in dissolved Ca^{2+} and Mg^{2+} concentrations and in alkalinity in the uppermost 70–90 m of Zone 1 (Fig. 64). The two extreme maxima in the Mg^{2+}/Ca^{2+} molar ratios (Fig. 64), the first at about 20 mbsf in Hole 890B (22.5, about 4 times the seawater value), and the second at 62.3 mbsf in Hole 889A (19.5 times the seawater value), correlate with Ca^{2+} minima (Fig. 64). Immediately beneath such Mg^{2+}/Ca^{2+} maxima dolomite usually forms. Below the zone of intense microbially mediated carbonate diagenesis, carbonate formation probably continues, but at a considerably reduced rate. The Ca^{2+}, Mg^{2+}, and alkalinity profiles at this site do not clearly indicate significant enhancement of carbonate diagenesis in the gas hydrate stability field (<225 mbsf). Shore-based geochemical and mineralogical analyses are required for the detection of the small amounts of authigenic carbonates that have formed in this zone. Consequently, the depth profiles of Ca^{2+}, Mg^{2+}, and alkalinity are considerably less perturbed by carbonate diagenesis below 70–90 mbsf.

Carbonate diagenesis may, however, again be enhanced, by transport of Ca^{2+}, Mg^{2+}, and/or the carbonate ion, as seen, for example, at about 130 mbsf (Fig. 64), or in the vicinity of gas hydrates through in-situ production of the carbonate ion.

The total amount of diagenetic carbonate produced should be inversely proportional to the sedimentation rate. Carbonate diagenesis depends on the diffusional supply of Mg^{2+} and in carbonate-poor sediments, such as those at Sites 889 and 890, also on the diffusional supply of Ca^{2+}.

In-situ production of Mg^{2+} and Na^+ by ion exchange with NH_4^+ in the subzone of organic-matter-mediated carbonate diagenesis (in the uppermost 70–90 m at Sites 889 and 890) is most probably at least partially responsible for the apparent "advective" profile of Mg^{2+} and Na^+ in this subzone (Fig. 64).

Diffusional Communication with an Advected Fluid

The low-Cl^- fluid at about 130 mbsf is also considerably depleted in Na^+, Mg^{2+}, and phosphate, but enriched in Ca^{2+}, K^+, silica, and alkalinity relative to the adjacent in-situ pore fluids. (From all the species analyzed on board, only ammonia does not show a maximum or a minimum at this depth interval. This may be the result of in-situ ammonia production, which reaches its peak at 150–200 mbsf.) The depth profiles of the aforementioned components normalized to Cl^- indicate that these maxima and minima do not simply reflect dilution with H_2O; Na^+, K^+, Ca^{2+}, alkalinity, and silica are enriched relative to Cl^-, whereas Mg^{2+} and phosphate are depleted. Based on its major element chemistry, this fluid could have been derived from the underlying section (Zone 2). Shore-based isotopic analyses, however, are essential to determine the origin and depth of formation of the fluid. The advective plumbing system of fluid transport to this level, by way of a fault or perhaps the pervasive fracturing observed in the core, is not obvious from the seismic-reflection section.

The most striking feature observed in Zone 1 is the systematic pore-fluid dilution, from the sediment/water interface to about 130 mbsf, seen most clearly in the Cl^- concentration-depth profile (Fig. 64). This Cl^--dilution profile does not reflect the in-situ production of H_2O from the smectite-to-illite transformation reaction. The onset of this reaction occurs at about 600°C, at least 1 km below the base of Zone 1, assuming a linear geothermal gradient of 54°C/km (see "WSTP and ADARA Temperature Measurements" section, this chapter). The Cl^- profile in Zone 1 probably was produced and is maintained by a gradient between the low-Cl^- fluid at about 100 mbsf and bottom seawater. The minimum time needed to establish the long Cl^- diffusion profile between the sediment/water interface and 100 mbsf (Fig. 64), assuming a bulk diffusion coefficient of 1×10^{-5} cm^2/s or 5×10^{-6} cm^2/s, is 1.6×10^5 yr or 2.1×10^5 yr, respectively.

Zone 2

Between about 130 mbsf and the bottom of the drill hole is a low-Cl^- zone, which most plausibly represents a modern and a paleo(glacial)-gas hydrate dissociation zone. It thus includes the modern gas hydrate depth interval delineated by a BSR at 225 mbsf and perhaps a glacial-gas hydrate subzone below the BSR. The calculated base of the modern CH_4-H_2O gas hydrate stability field (e.g., Katz et al., 1959; Kvenvolden and McMenamin, 1980) lies within the presumed glacial-hydrate subzone, at 260 mbsf (±15 m) (for details see "WSTP and ADARA Temperature Measurements" section, this chapter).

The most distinct geochemical characteristics of this zone are the almost constant low-Cl^- concentrations in the depth profile and the similar, almost constant depth profiles of Na^+, Mg^{2+}, and phosphate concentrations and of Mg/Ca molar ratios (Fig. 64). Interestingly, distinct but subtle discontinuities in the concentrations of some dissolved components analyzed occur near the calculated depth interval of the CH_4-H_2O gas hydrate stability field; particularly, note the subtle discontinuities observed in the Cl^-, Na^+, and Mg^{2+} depth profiles at 240–270 mbsf and the stronger discontinuity in the Ca^{2+}-concentration profile at 300 mbsf (Figs. 64–65). The concentration profiles of Cl^-

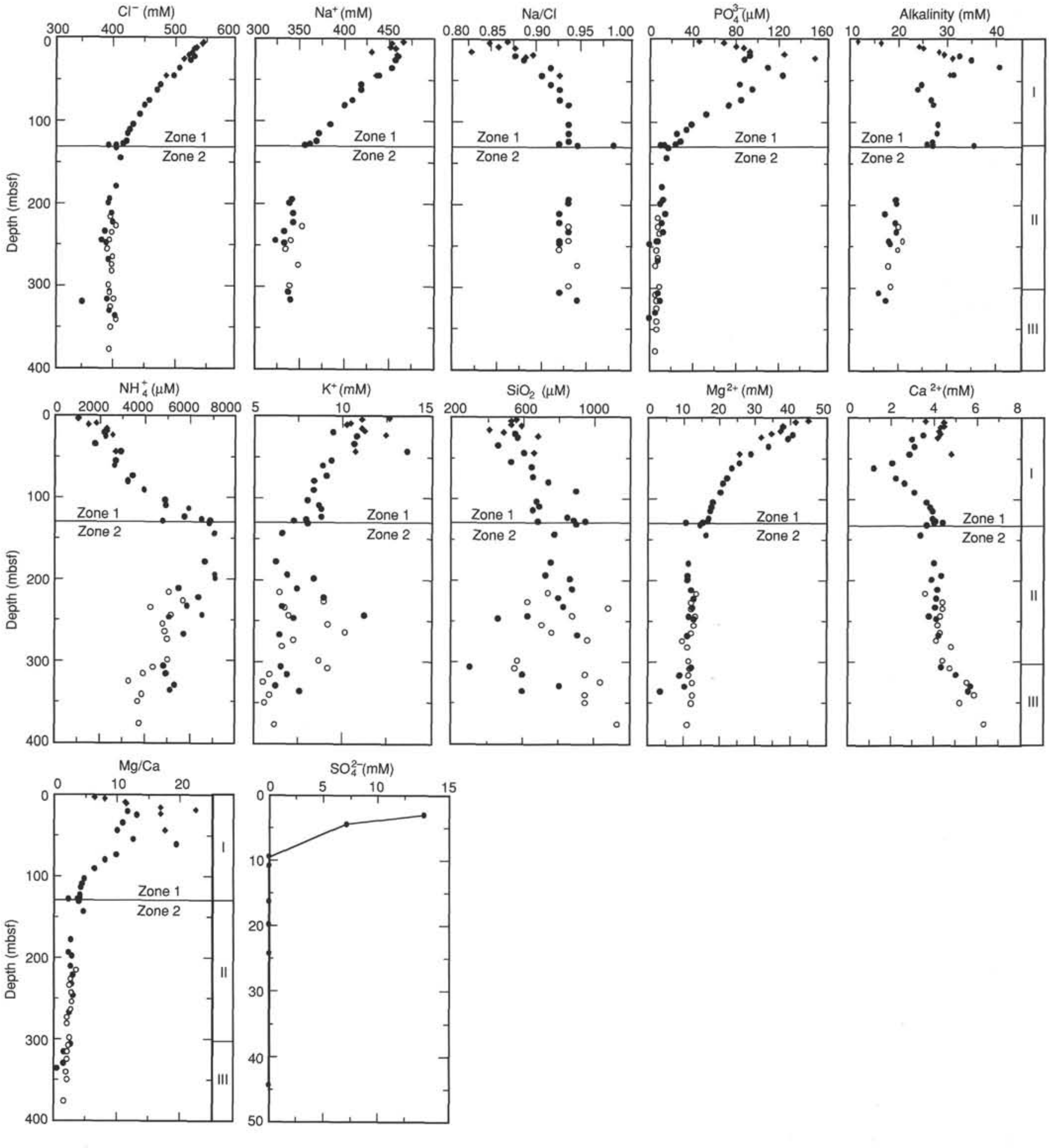

Figure 64. Concentration vs. depth profiles for chloride, sodium, phosphate, alkalinity, ammonium, potassium, silica, magnesium, calcium, and sulfate; Na/Cl and Mg/Ca molar ratios are also illustrated (filled circles = Hole 889A, open circles = Hole 889B, and filled diamonds = Hole 890B). The three lithostratigraphic units are shown in the right column. Zones 1 and 2 are geochemically defined intervals. Note change in depth scale for sulfate profile.

and Na^+ are most revealing because within the physico-chemical environment drilled at this site both are expected to behave conservatively.

The full significance of these observations is as yet unclear. The low-velocity zone (see "Downhole Logging" section, this chapter) between the BSR at 225 mbsf and the base of the CH_4-H_2O gas hydrate stability zone, at about 260 mbsf, may reflect an upward migration of the gas hydrate stability field. Another geochemical characteristic of Zone 2 is the observed change in the trend of the Ca^{2+}, Si, K^+, and NH_4^+ concentration profiles at and below about 300 mbsf, across the lithologic boundary between lithostratigraphic Units II and III, which may result from differential diagenesis within the two lithologies.

The depth profile of Cl^- concentration is the most distinctive geochemical feature of Zone 2. The Cl^- concentrations are low, ranging from 388 mM at 145 mbsf in Hole 889A, equivalent to 31% seawater dilution, to minima of 352 mM at 244 mbsf in Hole 889A and 362 mM at 255 mbsf in Hole 889B, equivalent to 37% and 35% seawater dilution, respectively (Table 11 and Fig. 64). The squeezed low-Cl$^-$ pore fluids from this zone contained considerable amounts of dissolved gas. Within the fluid containers, gas bubbles rapidly evolved at the laboratory-ambient temperature and pressure, suggesting that these fluids may have been saturated in situ with respect to dissolved gases.

Pore fluids with Cl$^-$ concentrations lower than seawater are ubiquitous in convergent margin sediments. But seawater dilution of 37%, as determined in Zone 2, has been observed previously only once in accretionary complex pore fluids, in the Middle America Trench, DSDP Leg 84 (Hesse et al., 1985); massive gas hydrates were recovered from these sediments. The maximum seawater Cl$^-$ dilution reported to date, 55%, was measured in the fluids recovered from the "mud pie" mud volcano, located seaward of the Barbados accretionary complex (Le Pichon et al., 1990); methane gas hydrate is widespread in this area. It thus seems that in the marine environment extreme seawater dilution is associated with gas hydrates.

Despite the preceding observations that strongly suggest the existence of gas hydrates in Zone 2, none were recovered. Nevertheless, the −0.9 to −1.4°C temperature measured on the catwalk in Core 146-889B-3R, at 217 mbsf, probably resulted from gas hydrate dissociation (for discussion see "Gas Hydrate Studies" section, this chapter). The coincidental observations of low Cl$^-$ concentrations in the associated pore fluids and high HS methane concentrations strongly suggest that methane gas hydrates are present in situ. These observations are to be anticipated from dissociation of gas hydrates during core recovery. Because massive hydrates would probably have been recovered, it is suggested that finely disseminated gas hydrates occur at this site.

Indirect evidence for the presence of gas hydrates in Zone 2 is provided by the occurrence of highly fluid sections of sediment. The pore fluids from two "soupy layers" (see "Lithostratigraphy" section, this chapter) in Core 146-889A-24X-1, at 50–55 and 140–147 cm (between 188 and 197 mbsf), were analyzed for Cl$^-$, SO_4^{2-}, and other major constituents of seawater. These fluids were significantly contaminated by surface seawater. A mixing of two fluid end-members was assumed; one end-member is the adjacent uncontaminated, squeezed, and analyzed pore fluid that contains no dissolved sulfate, and the other is surface seawater at this site, which was analyzed on board. On the basis of the Cl$^-$ analyses of the soupy layer pore fluids, their sulfate concentrations were predicted. The actual sulfate concentrations were, however, more than 20% lower than predicted. The lower values imply that the Cl$^-$ concentration of the squeezed pore fluid end-member used for this calculation, is lower than the in-situ pore fluid chlorinity. The only available in-situ diluent is gas hydrate.

If gas hydrates exist within this depth interval, the low chlorinity values observed should reflect dilution of the in-situ pore fluids by H_2O from the dissociated gas hydrates. Hence, the Cl$^-$ dilution should estimate the amount of gas hydrate present in the pore space. The in-situ chemical baseline for this calculation is, however, unknown and therefore was assumed. Assuming a bottom-water Cl$^-$ concentration of 548 mM as the Cl$^-$-concentration baseline (derived from extrapolation of the Site 890 Cl$^-$ profile to the seafloor) and a density of 0.92 Mg/m^3 for methane hydrate, it is inferred that a maximum of 39% of the pore space is occupied by the gas hydrate. All other chemical constituents must have been diluted to the same extent. Consequently, the Cl$^-$-normalized concentration-depth profiles of all the chemical constituents not included in methane hydrate and their corresponding unnormalized concentration-depth profiles should be, and indeed are, identical, as seen for example, in the Ca^{2+}, Na$^+$, and silica depth profiles (cf. Figs. 64 and 66).

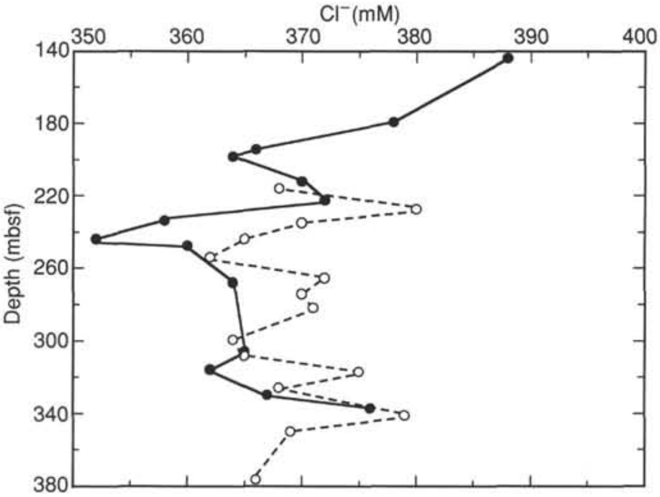

Figure 65. Depth profile of Cl$^-$ concentration in Zone 2 (symbols as in Fig. 64).

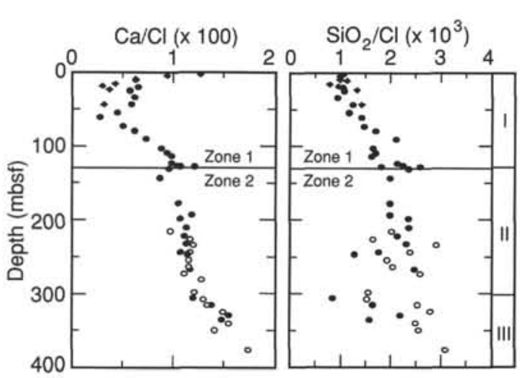

Figure 66. Depth profiles of Ca/Cl and Si/Cl molar ratios (symbols and units as in Fig. 64).

Other possible origins of the low-Cl$^-$ pore fluids are (1) mixing with meteoric water; (2) dehydration of hydrous minerals, particularly smectite and opal-A; and (3) clay-membrane ion filtration. The geological setting does not support option 1. Option 3 is an inefficient process and its geological importance is not documented. Option 2 has been shown to be geologically important. From preliminary X-ray diffraction (XRD) data of the bulk sediments, the dominant clay minerals in the section cored are illite and chlorite (± kaolinite?). A mixed-layer smectite/illite clay mineral is present in varying amounts throughout the section, but does not seem to be the dominant clay mineral at any interval. Its average concentration in these sediments and its composition (i.e., the ratio of smectite to illite layers) could not be evaluated on board from the X-ray diffractograms of the untreated bulk-sediment samples. From all the clay minerals present, only the smectite component, upon its transformation to illite, would dilute the pore fluids, according to the following schematic reaction (Perry and Hower, 1972):

$$\text{smectite} + K + Al = \text{illite} + \text{silica} + H_2O.$$

At a geothermal gradient of 54°C/km (see "WSTP and ADARA Temperature Measurements" section, this chapter) the reaction window spans a depth interval between 1.1 and 2.8 km. Assuming that sufficient smectite is available below the cored section to dilute the pore fluids recovered, fluid advection from a sub-bottom depth >1.5 km must be invoked. Shore-based isotopic analyses of these dilute fluids should distinguish between the hypotheses for gas hydrate dissociation and smectite dehydration.

The most interesting geochemical characteristic of the Cl$^-$-concentration profile is the persistence of the low-chlorinity fluid beneath both the BSR and the calculated CH_4-H_2O gas hydrate stability field to the bottom of the cored section. Does the low-Cl$^-$ pore fluid below the gas hydrate stability zone indicate advection of a low-Cl^- fluid from a greater depth? The Ca^{2+}, SiO_2, K^+, and ammonia concentration-depth profiles do not support this hypothesis. For example, the Ca^{2+}-concentration profile at about 270 mbsf shows a subtle but abrupt discontinuity (Figs. 64 and 66). Below 300 mbsf the Ca^{2+} profile is even more distinct from the overlying section. In Zone 2, below about 300 mbsf, Ca^{2+} concentrations increase with depth and approximate a diffusion profile or a mixing profile with a high-Ca^{2+} deeper seated fluid. The silica concentrations below 300 mbsf show a similar gradient, and the K concentrations show the opposite gradient (Fig. 64). Deeper seated fluids in subduction zones are typified by high Ca^{2+} and Si and by low Cl^-, Mg^{2+}, and K^+ concentrations. Because Mg^{2+}, SO_4^{2-}, and phosphate concentrations have been extensively depleted in Zone 1, their concentration-depth profiles show little structure in Zone 2 (Fig. 64). Therefore, the Mg^{2+}, SO_4^{2-}, and phosphate depth-concentration profiles do not provide new insights into the discussion on the origin of the low-Cl^- fluids, particularly below the BSR depth.

If advection is excluded as the source of the low-Cl^- fluid in the deeper section of Zone 2, another plausible explanation for its origin is the dissociation of gas hydrate. It is thus suggested that the base of the gas hydrate stability field may have been deeper during the latest glacial maximum, and migrated upward during the postglacial period (see "Summary and Conclusions" section, this chapter). This process has been predicted before, for example, by Revelle (1983).

PHYSICAL PROPERTIES

Introduction

Sediment physical properties were measured on cores recovered from Holes 889A, 889B, and 890B. Sample recovery varied greatly throughout both holes and sample quality was degraded by the coring artifacts described for Site 888: flow-in after partial penetration of the APC, liquefied sand samples, and severe shearing of XCB and RCB samples during the drilling process. Owing to these factors, the physical property record is incomplete and biased toward the fine-grained sediment end-member.

The physical properties are described in relation to the three major lithostratigraphic units (see "Lithostratigraphy" section, this chapter). Major changes in physical property-depth functions occur over the same intervals as the lithostratigraphic boundaries.

Measurements for Sites 889 and 890 include index properties, electrical resistivity, shear strength, acoustic velocity, and thermal conductivity. Only a sparse data set of shear strength (S_u) and acoustic velocity (V_p) for Site 889 was collected because of the poor sample quality. No trends in S_u or V_p could be interpreted as a function of depth for Site 889. The S_u data are plotted for Site 890 and reported in tabular form for Site 889. The methods used for these measurements are described in the "Explanatory Notes" chapter (this volume). The MST was only run on selected cores for magnetic susceptibility because of the poor quality of core collected.

Index Properties

Relatively high core recovery in the fine-grained sediments of lithostratigraphic Unit I (20.0–128.0 mbsf) allowed measurement of a full suite of index properties within this interval. Unit I is dominated by interbedded silts, clays, and fine sand. The sediment was disturbed by gas expansion and intervals with the least disturbance were selected for measurement. Unit I is subdivided into Subunits IA and IB (see "Lithostratigraphy" section, this chapter). In Subunit IA (0–91.5 mbsf), which is dominated by subhorizontal, interbedded silts, clays, and fine sands, water content and porosity decrease and bulk density increases (Fig. 67 and Tables 13–14), as expected for gravitationally compacting sediment (Athy, 1930). Sharp lithologic or diagenetic-related excursions to higher bulk densities occur locally in this interval.

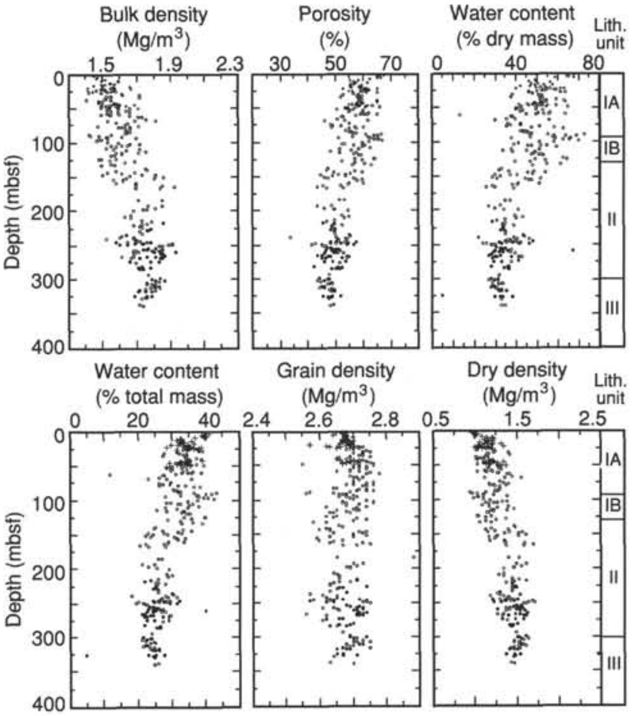

Figure 67. Index properties (bulk density, porosity, water content [as percentages of dry and total mass], grain density, and dry density) vs. depth (filled circles = Hole 889A, open circles = Hole 889B, and plus signs = Hole 890B).

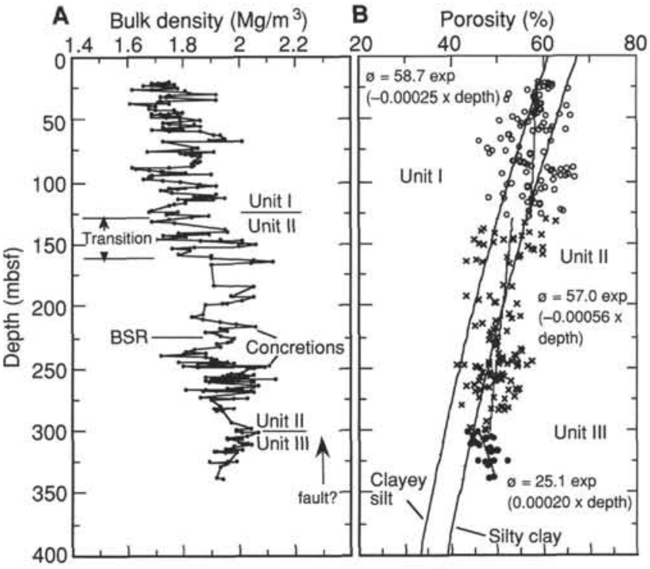

Figure 68. **A.** Bulk density plotted with depth; key intervals are noted. **B.** Porosity as a function of depth for Site 889. The thick lines are Brückmann's (1989) normally consolidated porosity-depth functions for clayey silt and silty clay derived from DSDP and ODP data. Best fits are also shown for lithostratigraphic Units I, II, and III as thinner lines (open circles = Unit I data, crosses = Unit II data, and closed circles = Unit III data).

Subunit IB (91.5–128.0 mbsf) is predominantly silty clay with some matrix-supported mud clasts, silts and sands, that are interpreted as debris-flow deposits (see "Lithostratigraphy" section, this chapter). The debris flows are marked by slightly more scatter in the index property data. The boundary between Units I and II at 128.0 mbsf can be described as transitional in physical properties (Fig. 68). At 128

Table 13. Summary of index property data, Site 889.

Depth (mbsf)	Bulk density (Mg/m^3)	Porosity (%)	Water content (%)		Grain density (Mg/m^3)	Dry- bulk density (Mg/m^3)
			Dry mass	Total mass		
20.20	1.75	59.1	51.6	34.0	2.70	1.15
21.10	1.71	61.1	56.2	35.9	2.69	1.10
21.70	1.69	60.2	56.0	35.8	2.66	1.09
22.60	1.77	61.9	54.7	35.3	2.71	1.14
23.30	1.66	61.2	59.1	37.1	2.72	1.05
23.90	1.77	61.7	54.5	35.2	2.73	1.14
24.70	1.73	59.9	53.5	34.8	2.72	1.13
25.40	1.78	59.1	50.2	33.4	2.72	1.19
26.50	1.69	65.2	63.8	38.9	2.68	1.03
26.80	1.62	61.0	61.1	37.9	2.70	1.01
27.85	1.81	56.6	45.9	31.4	2.74	1.24
29.80	1.82	58.1	47.5	32.2	2.75	1.23
30.60	1.92	52.6	38.1	27.5	2.73	1.39
31.30	1.75	58.1	50.4	33.5	2.73	1.16
31.95	1.74	59.3	52.5	34.4	2.70	1.14
32.60	1.72	58.0	51.3	33.9	2.70	1.14
34.20	1.92	52.0	37.4	27.2	2.73	1.40
35.80	1.72	58.2	51.8	34.1	2.72	1.13
36.50	1.71	58.7	52.7	34.5	2.73	1.12
37.40	1.75	59.2	51.8	34.1	2.75	1.15
37.80	1.61	59.3	59.3	37.2	2.69	1.01
39.40	1.70	65.1	62.8	38.5	2.66	1.05
39.75	1.68	58.6	54.5	35.2	2.69	1.09
41.40	1.68	59.1	54.8	35.4	2.68	1.09
42.15	1.70	58.5	53.4	34.7	2.73	1.11
42.80	1.77	59.6	51.5	33.9	2.73	1.17
43.30	1.77	57.6	48.9	32.8	2.72	1.19
44.30	1.80	56.0	45.7	31.3	2.74	1.23
45.10	1.75	57.9	50.1	33.3	2.71	1.17
45.60	1.72	58.6	52.5	34.4	2.71	1.13
46.00	1.69	58.0	53.1	34.6	2.72	1.10
46.50	1.73	63.4	58.9	37.0	2.69	1.09
47.00	1.78	58.0	48.8	32.7	2.75	1.20
47.50	1.79	60.7	51.8	34.1	2.72	1.18
48.00	1.69	65.7	64.8	39.3	2.55	1.02
48.50	1.74	57.3	49.8	33.2	2.76	1.16
48.90	1.79	53.4	42.9	30.0	2.76	1.26
50.60	1.86	54.4	41.7	29.4	2.76	1.31
51.65	1.79	50.6	39.7	28.4	2.72	1.28
52.30	1.73	56.6	49.3	33.0	2.74	1.16
53.25	1.75	60.0	52.6	34.4	2.70	1.15
54.10	1.84	55.2	43.3	30.2	2.72	1.28
55.20	1.86	55.0	42.2	29.7	2.74	1.31
56.65	1.79	59.4	50.4	33.5	1.54	1.19
57.10	1.73	62.0	56.3	36.0	2.69	1.11
58.60	1.80	59.0	49.3	33.0	2.72	1.21
58.70	1.74	61.5	55.6	35.7	2.69	1.12
58.95	1.69	64.8	63.3	38.7	2.72	1.03
59.40	1.75	60.5	53.3	34.7	2.65	1.14
59.75	1.86	57.6	45.2	31.1	2.75	1.28
60.45	1.44	16.8	13.2	11.7	2.75	1.27
62.35	1.91	52.5	38.4	27.7	2.74	1.38
62.85	1.93	52.3	37.6	27.3	2.78	1.40
65.60	1.95	50.7	35.4	26.1	2.69	1.44
66.70	1.89	53.1	39.5	28.3	2.73	1.35
67.45	2.01	45.9	29.8	22.9	2.70	1.55
68.00	1.73	61.5	55.9	35.8	2.71	1.11
72.45	1.85	54.8	42.4	29.7	2.70	1.30
74.05	1.83	47.8	35.8	26.3	2.76	1.25
75.50	1.67	49.0	42.0	29.6	2.70	1.01
75.80	1.91	51.7	37.3	27.1	2.74	1.39
77.25	1.79	60.1	51.2	33.8	2.68	1.18
77.50	1.86	48.5	35.5	26.2	2.76	[a]1.37
78.20	1.81	57.1	47.1	32.0	2.70	[a]1.23
79.00	1.83	57.2	57.7	36.5	2.74	[a]1.24
79.50	1.86	54.6	62.2	38.3	2.73	[a]1.30
83.50	1.84	53.6	42.5	30.4	2.65	[a]1.30
84.00	1.84	53.4	42.4	30.3	2.64	[a]1.30
84.20	1.86	54.9	43.5	30.9	2.72	[a]1.29
84.50	1.85	55.7	44.5	31.4	2.74	[a]1.28
85.00	1.85	55.0	43.7	31.0	2.72	[a]1.29
86.00	1.83	56.0	45.5	31.9	2.71	[a]1.26
86.80	1.84	56.6	46.0	32.1	2.74	[a]1.26
87.50	1.83	57.4	47.2	32.7	2.76	[a]1.24
88.50	1.75	60.9	55.3	36.5	2.69	[a]1.13
89.20	1.62	66.4	72.5	43.3	2.57	[a]0.94
90.00	1.63	65.0	68.8	41.9	2.56	[a]0.97
90.70	1.68	63.8	63.5	39.9	2.64	[a]1.03
91.40	1.72	61.8	58.2	37.7	2.66	[a]1.09
92.10	1.73	61.6	57.1	37.2	2.68	[a]1.10
92.80	1.81	56.2	46.6	32.4	2.67	[a]1.23
93.50	1.73	62.3	58.3	37.8	2.70	[a]1.09
94.30	1.90	50.9	37.9	27.9	2.68	[a]1.38
94.80	1.69	65.3	65.6	40.7	2.71	[a]1.02
95.70	1.69	63.6	62.4	39.4	2.66	[a]1.04
96.40	1.68	64.8	65.2	40.6	2.68	[a]1.02
97.45	1.66	66.7	69.9	42.4	2.69	[a]0.98
99.25	1.73	62.1	58.0	37.6	2.70	[a]1.10
100.05	1.79	59.4	51.4	34.7	2.74	[a]1.18
102.00	1.86	53.1	41.3	29.7	2.67	[a]1.32
103.00	1.92	52.2	38.6	28.3	2.76	[a]1.38
104.20	1.85	56.6	45.8	32.0	2.76	[a]1.27
104.60	1.75	60.3	54.5	36.1	2.67	[a]1.13
105.10	1.81	56.6	47.0	32.6	2.68	[a]1.23
105.80	1.78	59.4	51.8	34.9	2.72	[a]1.17
107.20	1.72	62.3	58.8	38.0	2.68	[a]1.08
109.40	1.76	58.1	51.2	34.6	2.62	[a]1.16
110.50	1.92	51.3	37.7	27.8	2.74	[a]1.39
111.70	1.84	55.5	44.8	31.5	2.71	[a]1.27
112.80	1.95	48.0	33.6	25.5	2.70	[a]1.46
114.20	1.78	57.3	49.0	33.6	2.65	[a]1.20
114.50	1.91	51.6	38.3	28.2	2.72	[a]1.38
115.20	1.81	57.5	48.3	33.2	2.71	[a]1.22
117.30	1.81	56.7	47.4	32.8	2.68	[a]1.23
117.85	1.77	58.2	50.8	34.4	2.64	[a]1.17
118.20	1.77	59.2	52.0	35.0	2.69	[a]1.17
119.30	1.75	59.2	53.1	35.5	2.63	[a]1.14
123.20	1.69	63.6	62.6	39.5	2.65	[a]1.04
123.80	1.68	64.1	64.1	40.1	2.65	[a]1.02
124.50	1.78	57.0	48.9	33.5	2.62	[a]1.19
125.90	1.74	59.6	53.8	35.8	2.64	[a]1.13
127.12	1.89	52.2	39.4	28.7	2.71	[a]1.36
128.34	1.83	56.9	46.6	32.4	2.74	[a]1.25
130.60	1.75	60.5	54.7	36.2	2.70	[a]1.13
132.00	1.69	62.7	61.5	39.1	2.62	[a]1.05
133.00	1.77	56.0	48.0	33.1	2.58	[a]1.20
138.10	1.95	47.1	32.9	25.1	2.66	[a]1.46
139.80	1.96	46.6	32.2	24.7	2.67	[a]1.48
141.20	1.78	56.7	48.5	33.3	2.62	[a]1.48
142.40	1.89	49.4	36.5	27.2	2.63	[a]1.20
143.70	1.73	59.3	54.0	35.9	2.60	[a]1.12
144.35	1.81	55.2	45.6	31.9	2.63	[a]1.24
145.90	1.70	53.4	47.5	32.9	2.36	[a]1.15
146.80	1.93	51.1	37.3	27.6	2.74	[a]1.40
147.50	2.01	44.8	29.5	23.1	2.72	[a]1.56
147.70	1.86	53.4	40.6	28.8	2.64	1.35
149.16	2.01	49.0	32.5	24.5	2.73	1.52
150.40	2.06	46.0	28.8	22.4	2.70	1.60
151.80	2.00	47.1	31.1	23.7	2.74	1.52
152.60	1.84	56.4	44.6	30.8	2.70	1.27
153.30	1.76	59.6	51.9	34.1	2.70	1.16
154.20	1.82	57.2	46.2	31.6	2.63	1.25
155.00	1.82	57.9	47.2	32.0	2.59	1.24
158.85	1.78	59.8	51.0	33.7	2.60	1.18
159.85	1.90	54.8	41.0	29.1	2.67	1.35
161.20	1.90	54.6	40.6	28.9	2.64	1.35
161.85	1.90	52.0	38.1	27.6	2.63	1.37
163.25	2.05	45.4	28.7	22.3	2.73	1.59
164.50	2.12	43.2	25.8	20.5	2.75	1.69
165.40	2.04	46.6	29.9	23.0	2.71	1.57
166.20	1.90	52.7	38.7	27.8	2.67	1.37
183.92	1.91	51.3	37.2	27.1	2.65	1.39
184.30	2.05	53.0	35.1	25.9	2.88	1.52
192.16	1.97	48.4	32.8	24.7	2.73	1.49
193.10	2.05	43.4	27.1	21.3	2.70	1.61
196.00	2.01	46.0	29.9	23.0	2.71	1.55
197.95	1.94	49.4	34.4	25.6	2.68	1.45
198.00	1.96	49.5	34.1	25.4	2.69	1.46
198.82	1.88	54.2	40.9	29.0	2.69	1.33
206.95	1.87	52.5	39.3	28.2	2.64	1.34
209.20	1.83	54.8	43.2	30.1	2.65	1.28
210.76	1.87	53.0	40.0	28.6	2.66	1.33
213.05	1.93	49.6	34.9	25.9	2.66	1.43
215.00	1.99	46.8	31.0	23.7	2.71	1.52
216.60	2.06	45.3	28.5	22.1	2.71	1.60
218.10	1.93	49.7	34.9	25.8	2.66	1.43
219.58	1.96	49.1	33.8	25.2	2.69	1.46
220.95	1.88	52.2	38.6	27.8	2.64	1.36
222.00	1.92	48.5	34.0	25.4	2.63	1.43
223.60	1.93	48.3	33.7	25.2	2.63	1.44
225.50	1.98	49.7	33.7	25.2	2.74	1.48
228.10	1.97	48.0	32.5	24.5	2.66	1.49
228.55	1.96	49.8	34.3	25.5	2.67	1.46
230.00	1.92	49.5	34.9	25.8	2.65	1.43

Table 13 (continued).

Depth (mbsf)	Bulk density (Mg/m³)	Porosity (%)	Water content (%) Dry mass	Water content (%) Total mass	Grain density (Mg/m³)	Dry-bulk density (Mg/m³)
233.30	1.93	49.7	34.9	25.8	2.63	1.43
234.83	1.84	55.0	43.1	30.1	2.68	1.29
237.30	1.81	55.1	44.1	30.5	2.57	1.26
238.35	1.88	33.7	22.0	18.0	2.61	1.54
239.20	1.80	50.1	39.0	28.0	2.34	1.29
240.30	1.72	53.7	45.9	31.4	2.35	1.18
240.90	1.88	53.9	40.6	28.8	2.65	1.34
242.25	1.90	51.0	37.0	27.0	2.62	1.39
243.10	1.92	50.4	36.0	26.4	2.65	1.41
243.90	1.90	51.0	37.2	27.1	2.62	1.38
244.60	1.96	50.4	34.9	25.8	2.63	1.45
244.72	1.78	57.4	48.0	32.4	2.67	1.21
245.00	1.90	53.0	39.1	28.1	2.58	1.36
245.90	1.85	54.1	41.9	29.5	2.67	1.30
246.00	1.98	48.0	32.2	24.3	2.72	1.50
246.75	1.89	54.4	40.6	28.8	2.64	1.35
246.80	1.93	50.2	35.6	26.2	2.63	1.42
246.90	1.89	52.0	38.4	27.7	2.57	1.36
247.60	1.94	48.0	33.1	24.8	2.64	1.46
247.90	2.11	42.7	25.6	20.4	2.74	1.68
248.35	2.11	41.2	24.4	19.6	2.74	1.70
248.40	1.80	56.4	46.3	31.6	2.62	1.23
248.82	1.85	54.1	41.7	29.4	2.64	1.31
249.40	2.09	45.1	27.8	21.7	2.73	1.63
250.10	2.05	45.5	28.7	22.3	2.92	1.60
250.55	2.03	46.1	29.5	22.8	2.75	1.57
253.95	2.01	46.7	30.4	23.3	2.68	1.55
254.30	1.97	48.2	32.6	24.5	2.68	1.49
255.60	2.05	51.0	33.4	25.0	2.91	1.54
255.65	1.96	50.2	34.7	25.7	2.72	1.45
256.60	1.94	48.7	33.8	25.2	2.69	1.45
257.40	1.88	51.3	37.9	27.4	2.61	1.36
257.50	1.99	48.3	32.4	24.4	2.71	1.50
257.76	2.03	46.3	29.7	22.9	2.73	1.56
258.10	1.90	49.9	35.8	26.3	2.64	1.40
258.85	1.91	50.8	36.6	26.8	2.65	1.40
259.16	2.13	84.6	67.2	40.2		1.27
259.50	2.00	50.3	33.9	25.3	2.73	1.49
260.35	1.88	50.7	37.1	27.0	2.66	1.37
260.85	2.04	49.3	32.2	24.3	2.70	1.54
261.18	2.05	46.0	29.1	22.5	2.71	1.59
261.30	1.89	52.9	39.3	28.2	2.66	1.36
264.30	2.07	45.0	27.9	21.8	2.74	1.62
264.80	2.05	43.3	26.9	21.1	2.72	1.62
266.30	1.96	48.0	32.7	24.6	2.71	1.48
266.70	2.01	47.3	31.0	23.7	2.73	1.53
266.75	1.88	54.8	41.6	29.3		1.33
267.35	1.81	53.8	42.6	29.8	2.56	1.27
267.80	2.04	46.3	29.7	22.9	2.71	1.57
268.20	1.92	52.4	37.9	27.4	2.73	1.39
268.30	1.87	54.2	41.3	29.2	2.62	1.32
269.08	2.05	45.1	28.4	22.1	2.72	1.60
273.30	1.86	53.5	40.9	29.0	2.62	1.32
273.80	1.98	49.1	33.3	24.9	2.67	1.48
274.30	2.03	45.9	29.4	22.7	2.66	1.57
275.30	1.90	51.6	37.5	27.2	2.61	1.38
280.70	1.93	42.2	28.1	21.9	2.70	1.51
281.60	1.93	50.8	36.1	26.5	2.69	1.42
282.15	1.91	50.6	36.3	26.6	2.66	1.40
282.70	1.98	52.3	36.3	26.6	2.69	1.45
283.60	1.92	48.6	34.1	25.4	2.63	1.43
284.20	1.92	50.3	35.7	26.3	2.65	1.42
284.40	1.94	51.5	36.4	26.6	2.68	1.42
293.16	1.97	47.5	31.9	24.2	2.67	1.49
298.50	2.04	44.2	27.8	21.7	2.69	1.60
299.30	1.99	47.2	31.2	23.8	2.74	1.52
300.25	1.99	47.5	31.7	24.0	2.69	1.51
301.30	2.01	45.7	29.7	22.9	2.70	1.55
301.55	2.07	43.5	26.8	21.1	2.71	1.63
304.30	2.03	44.8	28.6	22.2	2.70	1.58
305.80	1.96	48.5	33.2	24.9	2.73	1.47
306.20	2.01	47.6	31.3	23.8	2.75	1.53
306.70	1.96	49.1	33.6	25.1	2.70	1.47
307.80	1.99	47.3	31.3	23.8	2.71	1.52
309.85	2.00	45.0	29.1	22.5	2.72	1.55
310.70	2.03	45.0	28.6	22.2	2.68	1.58
311.25	2.01	45.8	29.6	22.8	2.73	1.55
311.70	2.04	44.1	27.8	21.7	2.68	1.60
313.05	1.98	46.0	30.4	23.3	2.70	1.52
314.25	1.95	48.4	33.3	24.9	2.69	1.46
315.60	2.01	47.8	31.5	23.9	2.75	1.53
316.26	1.92	49.7	35.3	26.1	2.67	1.42
316.80	1.91	49.8	35.6	26.2	2.65	1.41
317.35	1.95	48.6	33.4	25.0	2.69	1.46
317.60	1.99	48.3	32.2	24.4	2.68	1.51
324.72	2.60	12.5	5.0	4.8	2.65	2.47
324.85	1.96	49.0	33.6	25.1	2.67	1.47
324.90	1.99	45.6	29.9	23.0	2.67	1.53
325.16	1.89	52.1	38.3	27.7	2.67	1.37
325.65	1.95	47.4	32.3	24.4	2.67	1.48
326.05	1.96	48.1	32.8	24.7	2.71	1.47
326.28	1.95	48.3	33.2	24.9	2.67	1.46
328.70	1.93	47.7	33.1	24.8	2.64	1.45
337.70	1.92	49.2	34.9	25.8	2.63	1.42
338.90	1.94	48.1	33.2	24.9	2.70	1.46

[a] Calculated from volumetric wet and dry measurements and dry mass.

mbsf, there is a sharp, local decrease in bulk density, which does not remain low below this boundary. This interval is also associated with distinct changes in fluid geochemistry and sonic velocities (see "Inorganic Geochemistry" and "Downhole Logging" sections, this chapter). Between 128 and 160 mbsf, however, there is a transition in index properties represented in bulk density by a general increase with depth. Bulk density generally varies from 1.65 to 1.95 Mg/m^3 above this transitional boundary and from 1.8 to 2.1 Mg/m^3 below the boundary. Overall there is a general trend in Unit II of small decreases in porosity and water content (and increasing bulk density) with depth. Superimposed on this slight general trend are several large fluctuations in index properties. These fluctuations are particularly well defined in the bulk density data between 200 and 255 mbsf. Peaks in bulk density of 2.1–2.15 Mg/m^3 at 215 and 250 mbsf correspond to regions in which concretions are developed. The concretion intervals are separated by a region of lower bulk density (1.7 to 1.8 Mg/m^3). The fluctuations in bulk density and water content correlate with changes in seismic velocity as measured by the wireline sonic tool (see "Downhole Logging" section, this chapter), with high bulk density (low porosity) corresponding to high velocity. The density decrease near 230 mbsf corresponds to the approximate position of the BSR as seen on seismic-reflection sections.

The boundary between Units II and III (301 mbsf) also shows an offset in index properties with an increase in bulk density and a decrease in porosity and water content. Below the unit boundary, a normal trend of decreasing porosity and increasing bulk density with depth is not observed. Rather, the trend is opposite to normal, suggesting either a consistent trend of decreasing grain size with depth or a structural discontinuity between Units II and III.

Grain density ranges from 2.6 to 2.8 Mg/m^3, with a mean of 2.67 Mg/m^3. Within Unit III grain density tends to increase with depth (Fig. 67). Dry-bulk density increases with depth from 1.1 to 1.5 Mg/m^3 within Unit I and the top of Unit II. Below 150 mbsf, the dry-bulk density remains relatively constant with depth.

Porosity-depth functions were approximated for each lithostratigraphic unit and compared with the normally consolidated clayey silt and silty clay functions of Brückmann (1989) (Fig. 68). Unit I goes from slightly overconsolidated at the top to slightly underconsolidated at the base of the unit in comparison with the normally consolidated functions. Unit II follows a similar pattern to Unit I, going from slightly overconsolidated at the top of the unit to underconsolidated at the base. The porosity-depth function for Unit III shows an anomalous reverse trend. This unit lies predominantly in the underconsolidated range in comparison to either the clayey silt or the silty clay normally consolidated profiles.

Table 14. Summary of index property data, Hole 890B.

Depth (mbsf)	Bulk density ($\mathrm{Mg/m^3}$)	Porosity (%)	Water content (%)		Grain density ($\mathrm{Mg/m^3}$)	Dry-bulk density ($\mathrm{Mg/m^3}$)
			Dry mass	Total mass		
1.40	1.65	67.3	70.2	41.2	2.68	0.97
2.30	1.65	65.9	67.7	40.3	2.67	0.98
3.40	1.67	64.8	64.0	39.0	2.67	1.02
4.90	1.66	64.9	65.2	39.4	2.68	1.01
5.75	1.66	66.2	67.7	40.3	2.64	0.99
6.40	1.71	62.3	58.3	36.8	2.68	1.08
11.65	1.79	56.3	46.3	31.6	2.68	1.22
12.00	1.75	57.5	49.3	33.0	2.67	1.17
13.20	1.74	61.7	55.9	35.8	2.68	1.11
8.55	1.79	58.1	48.8	32.8	2.70	1.20
9.70	1.69	55.1	48.7	32.7	2.68	1.14
15.00	1.77	56.4	47.3	32.1	2.68	1.20
16.25	1.65	59.5	57.4	36.4	2.67	1.05
16.75	1.70	55.3	48.7	32.7	2.69	1.14
13.48	1.69	55.8	49.9	33.3	2.67	1.13
14.30	1.71	57.0	50.5	33.5	2.70	1.14
17.00	1.70	58.5	53.2	34.7	2.66	1.11
17.88	1.76	55.7	46.8	31.8	2.69	1.20
18.38	1.86	55.0	42.3	29.7	2.68	1.31
19.24	1.61	55.7	53.7	34.9	2.57	1.05
19.90	1.77	58.4	49.6	33.1	2.69	1.19
20.95	1.69	64.8	63.1	38.6	2.62	1.04
21.47	1.87	52.7	39.6	28.3	2.68	1.34
22.48	1.61	60.6	61.1	37.9	2.63	1.00
22.97	1.76	60.3	52.6	34.4	2.70	1.16
23.57	1.71	62.0	57.6	36.5	2.66	1.08
24.63	1.64	55.9	52.3	34.3	2.65	1.08
25.03	1.75	54.9	46.3	31.6	2.69	1.20
41.40	1.68	64.8	63.6	38.8	2.65	1.03
42.30	1.76	59.8	52.1	34.2	2.66	1.16
43.12	1.78	57.8	48.5	32.6	2.70	1.20
43.90	1.89	54.9	41.5	29.3	2.69	1.33
45.15	1.80	57.5	47.5	32.1	2.69	1.22
46.35	1.84	57.7	46.2	31.6	2.68	1.26
45.90	1.74	61.5	55.3	35.5	2.67	1.12
48.55	1.74	60.8	54.5	35.2	2.67	1.12
49.45	1.91	53.9	39.7	28.4	2.70	1.36

Electrical Resistivity

Resistivity was measured in core samples collected in Holes 889A, 889B, and 890B (Table 15). The measurement interval varied with the amount and quality of recovered sediment. Electrical resistivity is reported here both directly and in its nondimensional form as the ratio of saturated sediment resistivity to the calculated pore fluid resistivity, known as the formation factor (see "Explanatory Notes" chapter, this volume). At Site 889, Archie coefficients were determined by assuming a fixed value for the cementation coefficient (m) of −1.76 (Wang et al., 1976) and fitting an exponential curve to the data (Figs. 69–70). The resulting tortuosity coefficient, a, is 2.07. The correlation coefficient for this regression is 0.7. The Archie equation was then used to calculate a derived porosity (Fig. 70 and Table 15).

Formation factor and calculated porosity show trends with depth that are similar to the discrete index-property measurements. Within Unit I, the resistivity-derived porosity decreases with depth, and is generally equal to or higher than the directly measured porosity (Fig. 70). No measurements were made in the top of Unit II because the samples either were too small for the probes or would crack during measurement. At the base of Unit II and in Unit III, the resistivity-derived porosity is generally lower than the measured porosity, indicating a change in composition or cementation somewhere between Unit I and the lower half of Unit II.

Undrained Shear Strength

The undrained shear-strength measurements were made using a motorized miniature vane-shear device and a pocket penetrometer in cores from Holes 889A, 889B, and 890B (see "Explanatory Notes" chapter, this volume). All data were collected from lithostratigraphic Unit I within the limited intervals from 0 to 50 mbsf (Hole 890B) and from 79 to 125 mbsf (Site 889), where sample quality was sufficiently high to perform the measurement (Table 16). Because the data are sparse, trends with depth in the section can be interpreted only for Hole 890B. A comparison of undrained sediment strength (S_u) with effective overburden stress (P_o') (Fig. 71) can provide an estimate of the sediment consolidation history. At Site 890, the strength data, in terms of S_u/P_o', show overconsolidation in the upper 10 m and normal to slightly underconsolidated behavior from 10 to 50 mbsf.

Thermal Conductivity

Thermal conductivity was measured on sediment samples using the needle-probe method in the full-space mode (see "Explanatory Notes" chapter, this volume). Measurements were usually taken at four points per core in sections with good recovery. The measured values are given in Table 17 and plotted as a function of depth in Figure 72.

Thermal conductivities range from 0.88 to 1.46 W/(m · K), with a mean of 1.15 W/(m · K). There is no apparent trend with depth. The isolated high value of 1.46 W/(m · K) at 35.1 mbsf was measured in a fine-sand layer where a high quartz content considerably increases thermal conductivity.

There is a large scatter of the measured values at all depths. The scatter does not appear to relate to changes in porosity or mineralogy. Instead, it probably reflects the overall poor quality of the core samples. Gas expansion and drilling disturbance produce bubbles and cracks that are filled with a mixture of gases and pore fluid. Because of the insulating properties of the gases and the low thermal conductivity of water, disturbances decrease the bulk thermal conductivity. Measurements were taken only in those sections of the cores that appeared to be preserved best. Nevertheless, a large part of the scatter in the measured values is probably related to mechanical disturbance of the cores. If so, the measured thermal conductivity is a lower bound to the in-situ value.

Thermal conductivity at Sites 889 and 890 is significantly lower than at Site 888, for comparable porosities. The main reason for this is the lack of high-conductivity quartz-rich sand layers at Sites 889 and 890 as compared with Site 888. The low thermal conductivity at Sites 889 and 890 is consistent with clay-rich sediment. Another difference at Site 888 is that thermal conductivity at Sites 889 and 890 shows little variation with depth over the upper 100 m. This difference simply parallels the difference in the porosity curves at the two sites (see "Site 888" chapter, this volume). The bulk thermal conductivity of a water-saturated porous sediment is controlled mainly by porosity and mineralogy (Brigaud and Vasseur, 1989).

Acoustic Velocity

Because of the poor sample quality at Sites 889 and 890, few measurements of acoustic velocity were made (Table 18). Velocity data were corrected to in-situ temperature.

WSTP AND ADARA TEMPERATURE MEASUREMENTS

Introduction

In-situ sediment temperatures were measured at Sites 889 and 890 with both the WSTP and ADARA tools (see "Explanatory Notes" chapter, this volume). The primary purpose of the measurements was to detect and analyze possible thermal effects associated with pore-fluid flow. In particular, temperature measurements were intended to test the rate of upward pore-fluid advection. Upward pore-fluid advection has been proposed to be a major process across much of the Vancouver margin (Davis et al., 1990). High advection rates, as estimated by Davis et al. (1990), are predicted to generate a temperature profile with a relatively pronounced curvature downward with depth (see "Leg 146 Introduction: Cascadia Margin" chapter, this volume). Whether the predicted curvature could be confirmed by temperature observations was a major objective at Sites 889 and 890.

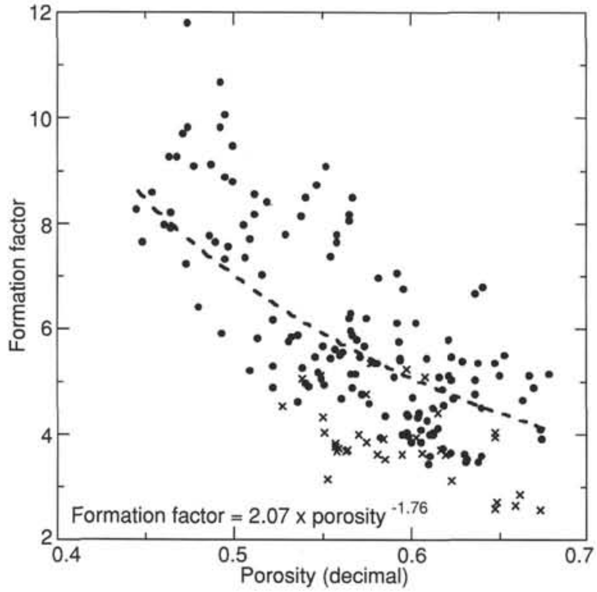

Figure 69. Formation factor plotted vs. measured porosity. The solid circles are data from Site 889 and the crosses are data from Site 890. A best fit was calculated for these data, assuming a cementation coefficient of –1.76. The resulting tortuosity coefficient is 2.07, with a correlation coefficient of 0.7.

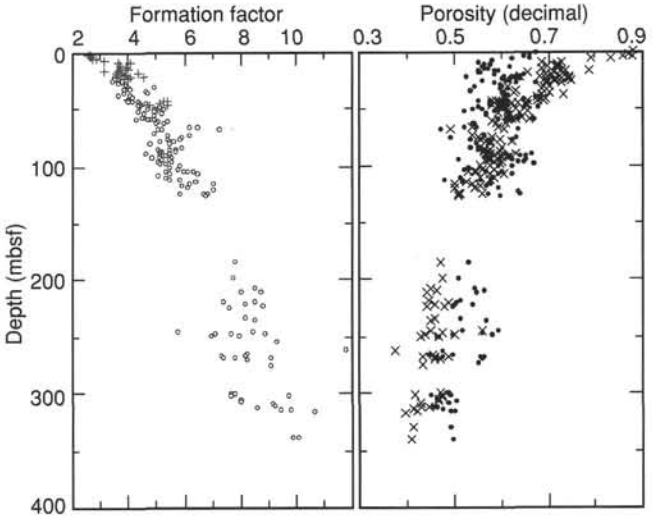

Figure 70. Formation factor (the ratio of sediment resistivity to pore fluid resistivity) and porosity derived from formation factor plotted with depth for Sites 889 and 890. On the formation factor plot, the circles are data from Site 889 and the crosses are data from Site 890. On the porosity plot, the crosses are porosity derived from formation factors and the circles are porosity data calculated from index measurements.

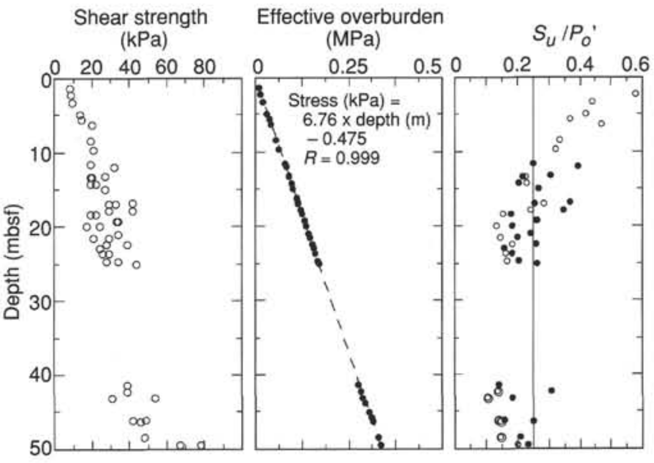

Figure 71. Undrained shear strength, effective overburden stress calculated from discrete bulk density measurements, and S_u/P_o' plotted as a function of depth for Site 890. Normally consolidated sediment should have an S_u/P_o' value of approximately 0.25 (indicated by vertical line on S_u/P_o' plot).

Another specific objective of the temperature measurements at Sites 889 and 890 was to determine the temperature at the BSR. The BSR is currently interpreted to mark the base of a hydrate layer. Temperature-pressure stability conditions of hydrates have been determined accurately in the laboratory (e.g., Sloan, 1990). Yet, how closely the laboratory results describe field conditions and how the BSR relates to the stability field of hydrates remain poorly assessed (Hyndman et al., 1992). A new opportunity was given at Sites 889 and 890 to document the stability field of natural hydrates and calibrate the BSR as a temperature indicator. In addition, temperature measurements were important at Sites 889 and 890 to estimate heat flow in relation to the tectonic processes of formation of the Vancouver margin (Ferguson, 1991; Davis et al., 1990).

Temperature was successfully measured at six depths from 29.5 to 168.0 mbsf at Sites 889 and 890 with either the WSTP or the ADARA tool. All of the attempted measurements are summarized in Table 19.

WSTP Temperature Measurements

WSTP measurements were attempted at six depths between 104.0 and 244.3 mbsf (Table 19). Two measurements were successful. Three were rejected because of clear indications of bad in-situ temperature determinations. The one other is of doubtful quality.

The tool was first deployed at 104 mbsf in Hole 889A in the version that includes the pore-water sampler (see "Explanatory Notes" chapter, this volume). The temperature record while the probe was in sediment (Fig. 73) shows a high drift, from 5.5° to 6.2°C, indicating unstable sediment temperature conditions. Probable explanations are that either the probe did not penetrate beyond the borehole fill or the formation was cracked and invaded by the cool drilling fluid at the time of penetration. In either case, the description of the transient thermal processes is too poorly constrained to allow the equilibrium temperature to be estimated. The measurement was rejected.

Following the unsuccessful deployment at 104 mbsf, the WSTP probe was modified to its configuration that does not include the pore-water sampler (see "Explanatory Notes" chapter, this volume) and uses a smaller diameter probe tip. It was anticipated that this configuration would induce less cracking of the formation upon penetration of the sediment than the configuration that include the pore-water sampler. Two successful measurements were obtained following this modification, at 139.6 mbsf (11.57° ± 0.05°C) and 168.0 mbsf (12.99° ± 0.05°C) (Figs. 74–75).

A third measurement at 197.3 mbsf (Fig. 76A) shows large disturbances of the sediment temperature record. The disturbances were most probably caused by vertical shifts of the probe in the sediment after penetration. No frictional heat pulses are visible at penetration and withdrawal. The early part of the temperature record (1960–2100 s) suggests equilibration at near 14.5°C (Fig. 76B). A tentative calculation of the equilibrium temperature from a decay curve over the intermediate part of the record (2240–2480 s) (Fig. 76C) yields a value of 13.8° ± 0.1°C. Both determinations are of poor quality. Cool drill water could have penetrated the formation around the probe tip as a result of the vertical movements of the probe. The estimated equilibrium temperatures are doubtful.

Two measurements were subsequently attempted in Hole 889B at depths of 197 and 244.3 mbsf. Both measurements show fairly good

Table 15. Resistivity, formation factor, and derived porosity, Holes 889A, 889B, and 890B.

Depth (mbsf)	Sample resistivity (Ωm)	Formation factor	Derived porosity (%)
146-889A-			
21.10	0.738	3.479	74.45
21.70	0.777	3.661	72.33
22.60	0.767	3.605	72.96
23.30	0.746	3.529	73.85
23.90	0.743	3.487	74.36
24.70	0.791	3.735	71.50
25.40	0.727	3.454	74.76
26.50	0.825	3.916	69.61
26.80	0.765	3.644	72.52
27.85	0.832	3.944	69.33
29.80	0.852	3.983	68.95
30.60	1.052	4.918	61.16
31.30	0.817	3.855	70.23
31.95	0.860	4.022	68.56
32.60	0.858	4.044	68.35
34.20	0.988	4.636	63.25
35.80	1.006	4.724	62.58
36.50	0.826	3.872	70.06
37.40	0.768	3.605	72.97
37.80	0.857	4.040	68.39
39.40	0.881	4.103	67.80
39.75	0.875	4.108	67.75
41.40	0.846	4.017	68.61
42.15	0.911	4.343	65.64
42.80	0.869	4.119	67.64
43.30	0.845	4.005	68.73
44.30	0.974	4.614	63.42
45.10	0.926	4.395	65.20
45.60	0.933	4.420	64.98
46.40	0.911	4.357	65.52
48.15	1.091	5.153	59.56
48.75	1.069	5.114	59.82
49.70	1.115	5.292	58.67
50.45	1.019	4.893	61.34
48.90	1.054	4.955	60.90
50.60	0.997	4.690	62.84
51.65	1.040	4.891	61.35
52.30	0.925	4.351	65.57
53.25	0.974	4.581	63.68
54.10	1.099	5.168	59.46
55.20	1.039	4.905	61.25
56.65	0.957	4.520	64.17
57.10	0.953	4.498	64.34
58.70	1.010	4.767	62.25
59.40	0.992	4.682	62.89
58.95	1.033	4.877	61.45
58.60	0.908	4.287	66.12
59.75	1.146	5.411	57.93
60.45	1.070	5.051	60.24
62.35	1.054	4.977	60.74
62.85	1.115	5.265	58.83
65.60	1.307	6.171	53.76
64.80	1.374	6.488	52.25
66.70	1.097	5.178	59.39
67.45	1.536	7.252	49.05
68.00	1.067	5.036	60.34
70.65	1.036	4.890	61.36
72.45	1.315	6.210	53.57
72.70	1.138	5.374	58.15
74.05	1.251	5.907	55.11
75.50	1.141	5.387	58.08
77.25	1.085	5.120	59.78
75.80	1.240	5.855	55.39
77.50	1.192	5.629	56.65
78.20	1.182	5.494	57.43
79.00	1.026	4.772	62.22
79.50	1.179	5.481	57.51
84.20	1.090	5.066	60.14
83.50	1.264	5.877	55.27
85.00	1.222	5.682	56.34
85.55	1.184	5.504	57.37
86.50	1.109	5.157	59.53
87.90	1.097	5.102	59.90
86.80	1.092	5.098	59.93
87.50	1.218	5.684	56.33
88.50	1.174	5.440	57.76
89.20	1.005	4.646	63.17
90.00	1.113	5.134	59.69
90.70	1.161	5.358	58.25
91.40	1.054	4.852	61.63
92.10	1.108	5.090	59.98
92.80	1.197	5.567	57.00
93.50	1.179	5.483	57.49
94.30	1.120	5.209	59.19
94.80	1.210	5.507	57.35
95.70	1.113	5.054	60.22
96.40	1.182	5.358	58.25
97.45	1.131	5.125	59.74
99.25	1.279	5.811	55.63
100.05	1.200	5.439	57.76
103.10	1.267	5.775	55.82
106.10	1.385	6.437	52.49
104.20	1.149	5.309	58.56
105.10	1.323	6.115	54.04
105.10	1.234	5.994	54.66
105.80	1.185	5.458	57.64
107.20	1.092	5.038	60.32
109.40	1.163	5.356	58.27
110.50	1.261	5.828	55.54
111.70	1.181	5.459	57.64
112.80	1.390	6.423	52.55
104.70	1.359	6.304	53.11
114.50	1.518	7.032	49.92
115.20	1.332	6.204	53.60
117.30	1.265	5.883	55.24
118.20	1.319	6.118	54.02
119.30	1.510	7.058	49.81
123.20	1.438	6.675	51.42
123.80	1.461	6.791	50.92
124.50	1.248	5.800	55.69
125.90	1.465	6.772	51.00
183.92	1.656	7.788	47.10
197.95	1.652	7.723	47.33
206.95	1.829	8.488	44.85
209.20	1.723	8.055	46.21
210.76	1.899	8.743	44.11
218.10	1.814	8.546	44.68
219.58	1.585	7.369	48.61
220.95	1.759	8.146	45.91
222.00	1.895	8.809	43.92
223.60	1.636	7.575	47.85
233.30	1.758	8.174	45.83
244.60	1.814	8.432	45.02
249.40	1.704	7.920	46.65
266.75	1.758	8.174	45.83
267.35	1.588	7.381	48.56
268.30	1.676	7.794	47.08
275.30	1.955	9.090	43.14
301.55	1.643	7.652	47.58
304.30	1.718	7.988	46.43
306.70	1.718	7.988	46.43
307.80	1.971	9.129	43.04
310.70	1.985	9.262	42.68
311.70	1.842	8.599	44.52
313.05	2.100	9.820	41.29
314.25	1.985	9.458	42.18
315.60	2.286	10.671	39.38
337.70	2.100	9.838	41.24
338.80	2.16	10.051	40.75
146-889B-			
234.83	2.032	8.490	44.85
244.72	1.379	5.761	55.90
246.00	1.793	7.648	47.59
246.90	1.671	7.131	49.52
247.60	2.039	8.898	43.67
248.40	1.604	6.988	50.10
261.18	2.538	11.801	37.19
264.80	1.776	8.256	45.56
266.30	1.576	7.327	48.76
267.80	1.953	9.082	43.16
269.25	1.767	8.215	45.69
253.32	1.993	9.268	42.67
299.30	1.709	7.778	47.13
300.25	1.678	7.637	47.63
301.30	2.131	9.698	41.58
146-890B-			
1.40	0.549	2.590	88.04
2.30	0.567	2.655	86.82
3.40	0.562	2.600	87.84
4.90	0.590	2.715	85.71
5.75	0.620	2.857	83.27
6.40	0.685	3.146	78.83
11.65	0.772	3.685	72.06
12.00	0.820	3.881	69.97
13.20	0.787	3.723	71.64
8.55	0.774	3.642	72.55
9.70	0.856	4.035	68.44
15.00	0.782	3.720	71.67
16.25	0.764	3.635	72.62
16.75	0.669	3.159	78.64
13.48	0.785	3.697	71.93
14.30	0.851	4.011	68.67
17.00	0.774	3.558	73.51
17.88	0.820	3.770	71.13
18.38	0.918	4.342	65.65
19.24	0.810	3.832	70.47
19.90	0.831	3.929	69.48
20.95	0.856	4.051	68.29
21.47	0.987	4.554	63.89
22.48	0.792	3.655	72.39
22.97	0.856	3.951	69.26
23.57	0.787	3.631	72.66
24.63	0.820	3.763	71.21
41.40	0.849	3.953	69.24
42.30	1.128	5.255	58.90
43.12	1.154	5.374	58.15
43.90	1.103	5.136	59.67
45.15	1.026	4.777	62.18
46.35	1.154	5.374	58.15
45.90	0.949	4.419	64.99
48.55	1.095	5.100	59.91
49.45	1.087	5.064	60.15

Note: Values for derived porosity were calculated using the Archie equation with coefficients of tortuosity and cementation of 2.07 and –1.76, respectively.

data (Fig. 77), but recorded anomalously low temperatures with respect to the main temperature trend with depth. They do not show well-developed penetration heat pulses and decay curves. The two measurements were probably taken in borehole fill, in agreement with the strong suspicion held by the drillers that borehole fill could have been as much as 3 to 6 m thick at these deployments. The two measurements were rejected.

ADARA Temperature Data

Twelve ADARA deployments were attempted along the APC-cored sections of the holes, down to 128 mbsf. Only four were successful (Table 19).

Three successful measurements were obtained in Hole 889A at 29.5, 48.5, and 67.5 mbsf, as well as two additional measurements

Table 16. Undrained shear strength, Hole 889A (lithostratigraphic Unit I).

Depth (mbsf)	Undrained s hear strength (kPa)	Method
79.4	94.8	Miniature vane
83.9	124.0	Miniature vane
86.8	29.4	Pocket penetrometer
87.5	49.0	Pocket penetrometer
88.5	34.3	Pocket penetrometer
89.2	36.8	Pocket penetrometer
91.4	34.3	Pocket penetrometer
92.1	37.3	Pocket penetrometer
92.8	33.3	Pocket penetrometer
93.5	34.3	Pocket penetrometer
94.3	37.3	Pocket penetrometer
94.9	78.5	Pocket penetrometer
95.7	110.3	Pocket penetrometer
96.4	85.8	Pocket penetrometer
97.5	134.8	Pocket penetrometer
99.3	105.4	Pocket penetrometer
100.1	117.7	Pocket penetrometer
103.1	122.6	Pocket penetrometer
106.1	156.9	Pocket penetrometer
104.2	117.7	Pocket penetrometer
105.1	215.7	Pocket penetrometer
105.8	152.0	Pocket penetrometer
107.2	112.8	Pocket penetrometer
109.4	152.0	Pocket penetrometer
111.0	147.1	Pocket penetrometer
111.7	191.2	Pocket penetrometer
112.8	127.5	Pocket penetrometer
114.2	215.7	Pocket penetrometer
115.2	215.7	Pocket penetrometer
117.3	215.7	Pocket penetrometer
119.3	196.1	Pocket penetrometer
121.7	183.9	Pocket penetrometer
123.8	205.9	Pocket penetrometer
124.5	220.6	Pocket penetrometer

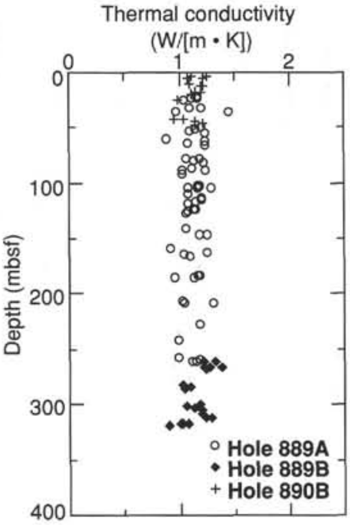

Figure 72. Thermal conductivity, plotted as a function of depth, for Sites 889 and 890.

that were obtained over the same depth interval in Hole 890B, at 35.8 and 47.8 mbsf (Fig. 78). Equilibrium temperatures for all these deployments, except that at 35.8 mbsf in Hole 890B, were calculated from the decay curves with an accuracy estimated at 0.2°–0.3°C. The sediment temperature record at 35.8 mbsf in Hole 890B is abnormal, showing a decay curve truncated at 3 min after penetration. At truncation time, a second heat pulse followed by a low temperature record suggests that the probe could have been partially pulled out of the sediment. The measurement is doubtful.

Table 17. Thermal conductivity data, Holes 889A, 889B, and 890B.

Depth (mbsf)	Thermal conductivity (W/[m•K])
146-889A-	
22.20	1.17
23.40	1.17
23.50	1.11
25.30	1.04
31.77	1.09
32.72	1.20
35.10	1.46
36.10	0.97
49.70	1.21
51.67	1.16
52.73	1.09
54.31	1.24
60.18	0.89
61.97	1.24
63.24	1.08
65.02	1.24
77.75	1.20
78.72	1.06
79.73	1.14
80.60	1.22
87.01	1.12
87.66	1.24
88.87	1.03
92.25	1.04
101.79	1.18
101.79	1.18
103.31	1.16
103.73	1.08
103.86	1.18
104.43	1.29
109.28	1.08
112.74	1.21
115.26	1.20
117.25	1.15
118.20	1.08
123.81	1.15
124.41	1.14
125.06	1.07
126.71	1.07
142.13	1.06
146.41	1.25
146.61	1.19
159.10	0.93
162.10	1.27
164.98	1.04
165.68	1.10
183.67	1.17
184.02	1.18
184.60	1.13
184.70	0.96
207.24	1.02
207.74	1.32
208.95	1.04
228.30	1.20
242.26	0.99
258.20	1.00
259.20	1.19
260.70	1.12
261.07	1.16
146-889B-	
259.35	1.22
259.65	1.32
264.77	1.37
266.32	1.27
266.35	1.22
267.70	1.23
281.30	1.03
283.77	1.09
284.22	1.03
299.00	1.18
300.80	1.06
301.60	1.13
303.60	1.20
307.66	1.20
309.55	1.21
310.67	1.23
310.95	1.28
316.02	1.02
316.09	1.01
317.32	1.08
317.59	0.90
146-890B-	
2.50	1.10
3.50	1.26
5.00	1.08
5.70	1.22
9.70	1.10
11.22	1.19
12.03	1.21
16.55	1.15
17.50	1.19
19.14	1.11
23.69	0.98
41.67	0.96
42.66	1.03
44.46	1.15
45.52	1.22
47.20	1.14

A series of four measurements over the depth interval from 86.5 to 128.0 mbsf in Hole 889A unfortunately did not recover any usable data as a result of tool failure. Two later deployments over the same depth interval in Hole 889D, at 89.5 and 105 mbsf, were also unsuccessful. The measurement at 86.5 mbsf in Hole 889A made with probe 12 recorded only 25 scans (total record of 125 s). The measurement at 104 mbsf made with probe 15 recorded only 219 scans (18 min). The measurement at 119 mbsf made with probe 12 recovered a full record of erratic data. No data were recorded at 128 mbsf with probe 19. Partial records of 131 and 20 scans (11 and 2 min, respectively) were obtained at 89.5 mbsf in Hole 889D and 16.8 mbsf in Hole 890B, respectively, both with probe 15. Following an extensive investigation, weak batteries were suspected as the most probable reason why the measurements failed repeatedly. The reason for the sudden onset of such serious battery problems is still not understood. The power-supply board inside the ADARA tool was, however, modified in order to increase the power available to the tool as a whole. To do this, the clock battery pack was connected to the main tool battery pack to feed the electronics circuits. The last measurement made with the ADARA tool, at 105 mbsf in Hole 889D, used this modification. It recovered a full temperature record. The measurement was, however, rejected because the deployment of the core barrel was unsuccessful (Fig. 79).

Table 18. Acoustic compressional-wave velocity measurements, Holes 890B and 889B.

Core, section, interval (cm)	Depth (mbsf)	Lithology	Velocity (m/s)
146-890B-			
1H-1, 140	1.40	Silty clay	1466.20
1H-2, 80	2.30	Silty clay	1464.60
1H-3, 40	3.40	Silty clay	1464.60
1H-4, 40	4.90	Silty clay	1470.90
1H-4, 125	5.75	Silty clay	1461.50
2H-5, 40	6.40	Silty clay	1475.70
1H-1, 125	8.55	Silty clay	1463.00
146-889B-			
3H-1, 2	215.90	Carbonate concretion	3551.31
7H-4, 76	259.16	Carbonate concretion	1738.17
19H-1, 12	324.72	Mudstone biscuit	2983.51

Note: Velocity corrected to in-situ temperature.

Temperature Profile with Depth

The near-bottom seawater temperature was measured on each of the WSTP and ADARA deployments. The measure was taken usually while the probe was held for 10 min at about 20 m above seafloor inside the drill string. WSTP probes measured a bottom seawater temperature of 4.0° ± 0.1°C. ADARA probes measured a bottom seawater of 2.7° ± 0.1°C, except for the deployment to 105 mbsf in Hole 889D that recorded a near-bottom seawater temperature of 2.4°C. For consistency with the intercalibration procedure at Site 888, the ADARA reading of 2.7°C was used as the reference bottom-seawater temperature at Sites 889 and 890 and a constant correction of −1.3°C was applied to all WSTP-measured temperatures. Corrected temperature data are summarized in Table 20 and plotted as a function of depth in Figure 80. Excluding the doubtful measurements at 197.3 mbsf in Hole 889A and 35.8 mbsf in Hole 890B, a best linear fit of the temperature data with depth is obtained for a temperature gradient of 54°C/km (Fig. 80). Note that the excluded values at 197.3 mbsf, in particular the upper determination of 13.2°C, fall close to the extrapolated value of 13.35°C predicted from the 54°C/km gradient.

The two measurements at 48.5 mbsf in Hole 889A and 47.8 mbsf in Hole 890B of 4.8°C and 5.7°C, respectively, differ significantly by 0.9°C. The measurement at 47.8 mbsf in Hole 890B plots 0.5°C above the linear trend. This raises the question of whether the temperature gradient is higher in Hole 890B than in Hole 889A. It is a question that cannot be satisfactorily answered from the single data point we have in Hole 890B.

Heat Flow at Sites 889 and 890

On the basis of a temperature gradient of 54°C/km with an uncertainty of 2°C/km and a thermal conductivity of 1.15 W/(m · K) with an uncertainty of 0.1 W/(m · K) (1 standard deviation), the estimated conductive heat flow at Sites 889 and 890 is 62 ± 8 mW/m^2. This value is significantly less than the heat flow of between 84 and 110 mW/m^2 previously measured at the seabed approximately 2 nmi south of the drilling site (Davis et al., 1990). The thermal data gathered at Sites 889 and 890 do not indicate that the temperature profile is significantly curved with depth. The data therefore do not provide

Table 19. Summary of WSTP and ADARA temperature measurements, Sites 889 and 890.

Summary of WTSP temperature measurements

Core	Depth (mbsf)	Temperature above mud line (°C)	Temperature in sediment (°C)	Comments	Status
146-889A-					
10H	104.0	4.05	5.5–6.2*	High drift from 5.5° to 6.2°C while in sediment.	Rejected
18X	139.6	3.9	11.57 ± 0.05	Good measurement.	Accepted
21X	168.0	3.9	12.99 ± 0.05	Good measurement.	Accepted
25X	197.3	4.1	13.8–14.5	Disturbed thermal decay. Determination of equilibrium temperature questionable.	Doubtful
146-889B-					
1R	197.0	3.9	5.9–6.3	Fairly good data but probe probably in fill.	Rejected
6R	244.3	3.95	6.6	Good data but probe probably in fill.	Rejected

Summary of APC tool temperature measurements (ADARA measurements)

Core	Depth mbsf	Probe no.	Temperature above mud line (°C)	Temperature in sediment (°C)	Comments	Status
146-889A-						
1H	29.5	12	2.8	4.2 ± 0.2	Good data.	Accepted
3H	48.5	12	2.7	4.8 ± 0.2	Good data.	Accepted
5H	67.5	12	2.7	6.2 ± 0.2	Good data.	Accepted
7H	86.5	12			Electronics failure. No usable data.	
9H	104.0	15			Electronics failure. No usable data.	
11H	119.0	12			Electronics failure. No usable data.	
13H	128.0	19			Electronics failure. No data.	
146-889D-						
1H	89.5	15			No temperature record in sediment.	
(following 1H)	105.0	12	2.4		Failed core penetration.	Rejected
146-890B-						
2H	16.8	15			Electronics failure. No usable data.	
4H	35.8	19	2.8	5.5 ± 0.5?	Two-step penetration and decay curve. Uncertain determination of equilibrium temperature.	Doubtful
5H	47.8	19	2.7	5.7 ± 0.3	Good data.	Accepted

Notes: Measurement marked with an asterisk (*) was taken with Probe 105; other WSTP measurements were taken with Probe 108.

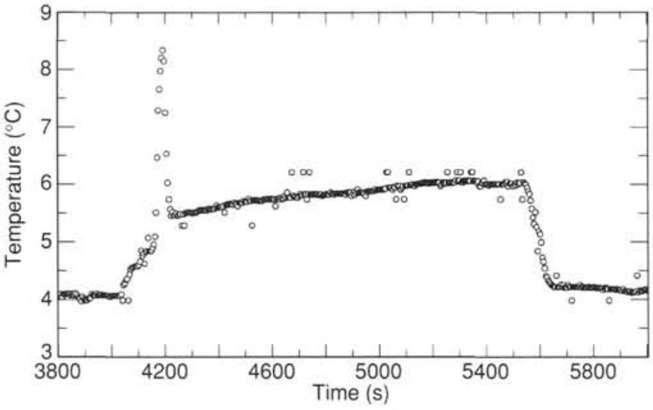

Figure 73. Temperature record in near-bottom seawater and sediment from WSTP deployment in Hole 889A at 104.0 mbsf (Core 146-889A-10H).

evidence that pore-water advection occurs at the large flow rates proposed by Davis et al. (1990). Instead, the data are compatible with a predominantly conductive process of heat transfer.

Temperature and Hydrates

The depth to the hydrate layer can be predicted from the in-situ temperature structure using experimentally derived pressure-temperature stability curves for hydrates. Stability curves vary according to the chemical composition of hydrates. The pure water-pure methane curve best describes the correlation of depth to the BSR to the in-situ temperature at three previous DSDP and ODP sites (Fig. 81; Hyndman et al., 1992). Using this stability curve and a constant temperature gradient of 54 ± 2°C/km, the base of the stability field, and by implication the BSR, is predicted at 260 ± 10 mbsf. In contrast, the VSP data indicate that the BSR lies near 224 mbsf (see "Downhole Logging" section, this chapter). For hydrates to be stable at this depth, an in-situ temperature of 16.8°C would be required, according to the pure water-pure methane stability curve. The temperature at this depth, estimated from the gradient of 54°C/km, is only 14.8°C. The 2°C discrepancy is large. Unless the pure methane-pure water hydrate stability curve used is grossly in error, the data suggest that the stability relationships for pure methane-seawater or other gas hydrate-fluid systems are more appropriate.

LAST-II

Introduction

The LAST-II was run in Hole 889D at a depth of 140 mbsf. The tool was deployed on the colleted delivery tool, pumped down the hole, and pushed approximately 3 m ahead of the bit into the formation (see "Explanatory Notes" chapter, this volume). The pumps were shut down after the tool was pushed into the formation. The tool was left in the formation for 35 min. Pore-pressure measurements were collected during the entire deployment from the rig floor to the end of

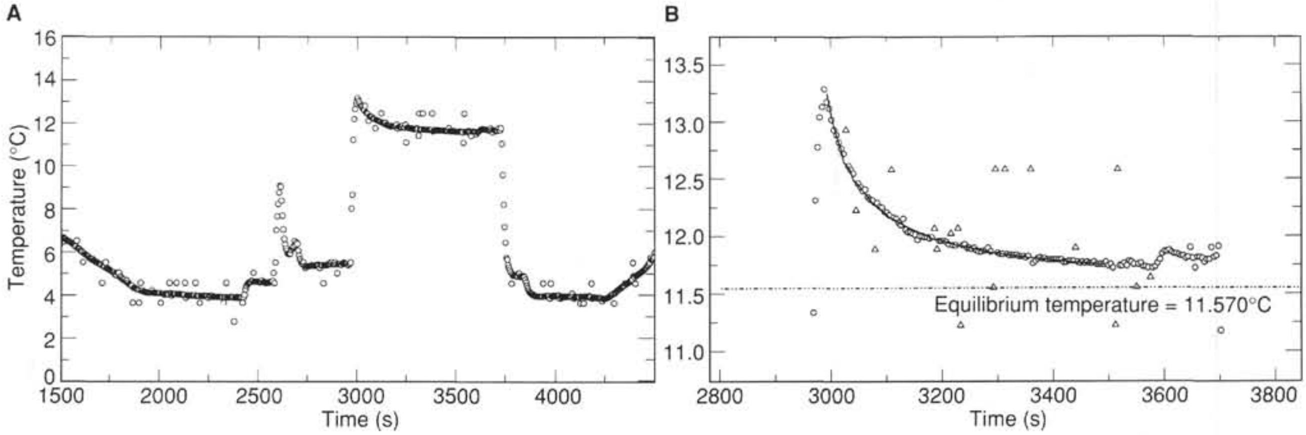

Figure 74. Temperature record from WSTP deployment in Hole 889A at 139.6 mbsf (Core 146-889A-18X). **A.** Entire run. **B.** Close-up of record in sediment. The solid line is the regression curve used to estimate the equilibrium temperature shown by the dashed line. Triangles are points not used for regression calculation.

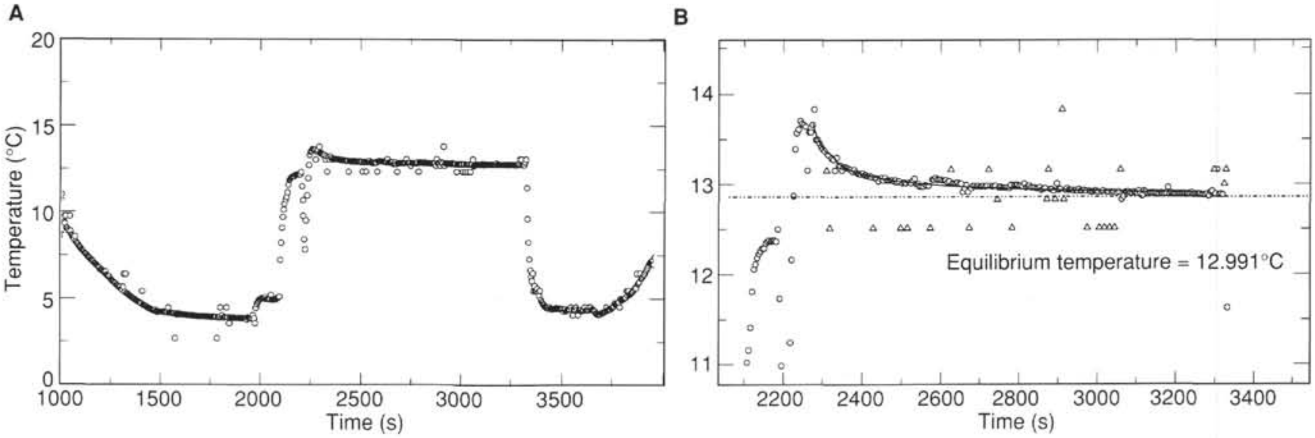

Figure 75. Temperature record from WSTP deployment in Hole 889A at 168.0 mbsf (Core 146-889A-21X). **A.** Entire run. **B.** Close-up of record in sediment. Conventions as in Figure 74.

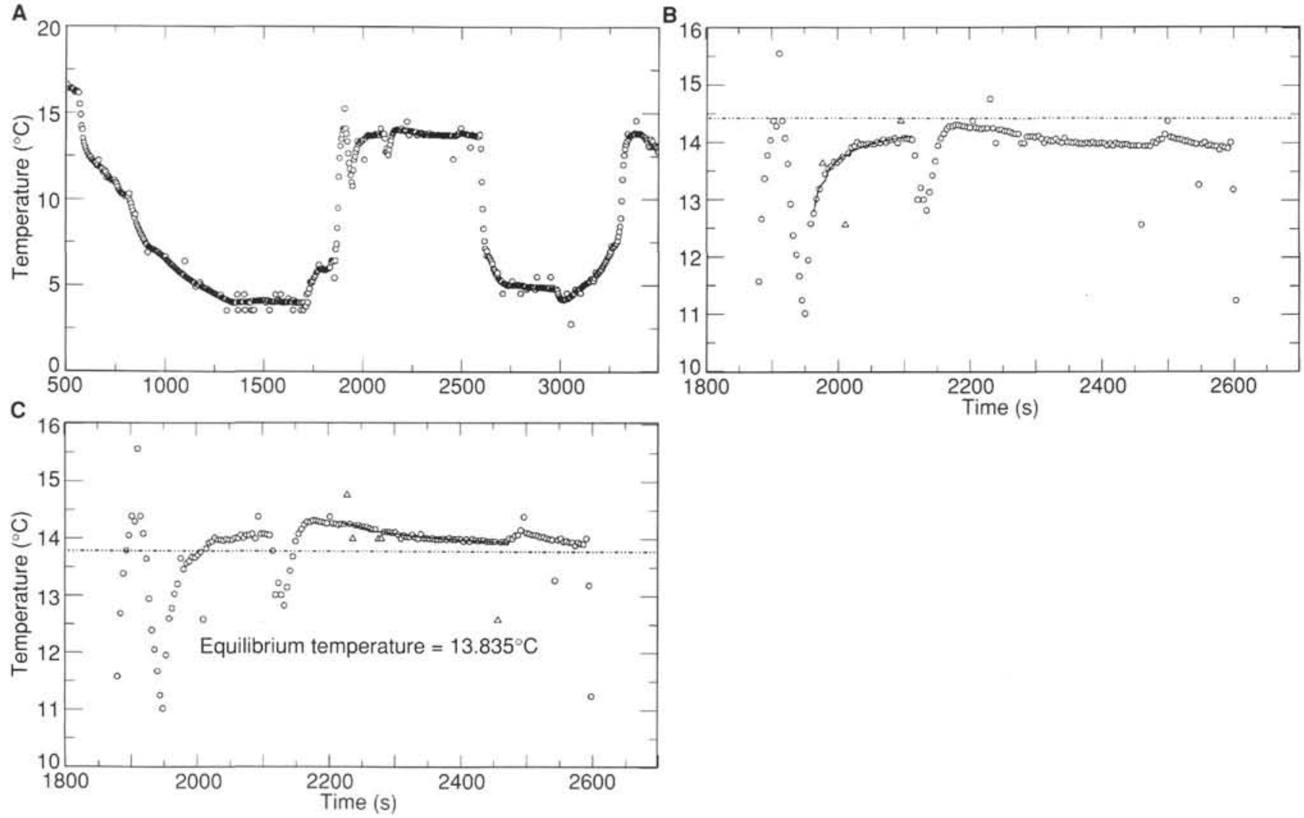

Figure 76. Temperature record from WSTP deployment in Hole 889A at 197.3 mbsf (Core 146-889A-25X). **A.** Entire run. **B.** Close-up of record in sediment with the early decay curve (1960–2100 s) used to estimate the equilibrium temperature. **C.** Close-up of record in sediment with the intermediate decay curve (2240–2480 s) used to estimate the equilibrium temperature. Conventions as in Figure 74.

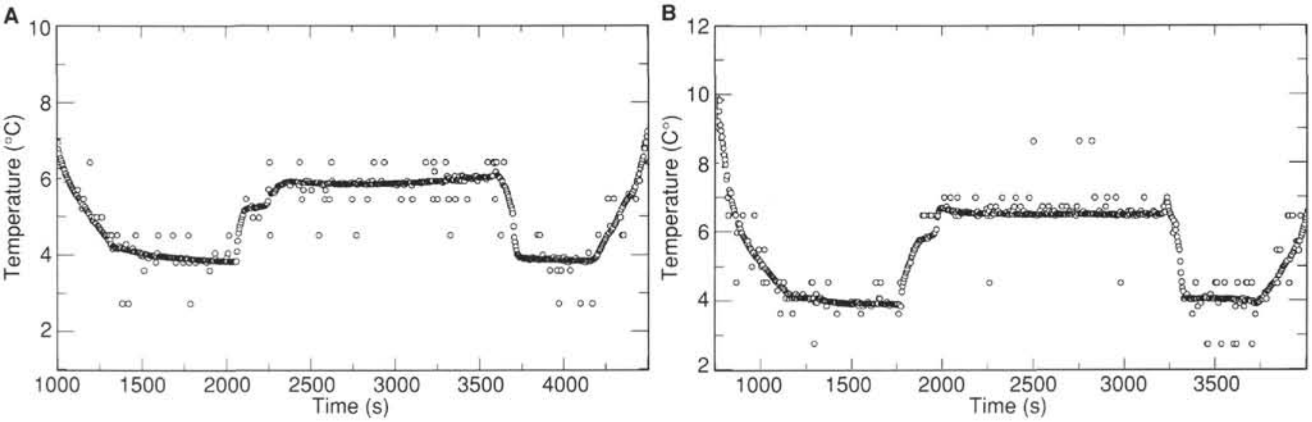

Figure 77. Temperature records from WSTP deployment in Hole 889B. **A.** Core 146-889B-1R (197.0 mbsf). **B.** Core 146-889B-6R (244.3 mbsf).

the measurement cycle. Measurements of stress and strain were made after the tool was in the formation approximately 20 min.

Preliminary Results

The pore-pressure record shows the tool's descent through the water column, its stationary position at 20 m above the seabed/water interface (mud line), and the increasing hydrostatic stress as it was lowered down the drill pipe (Fig. 82). The measured values of pressure for 20 m above the mud line and the hole depth match the calculated hydrostatic stress for these depths. Pore-pressure measurements during and following tool insertion are noisy, most likely reflecting the effects of drill-string heave on the tool (Fig. 83). However, the general trends suggest good penetration into the formation with a maximum dynamic pore-pressure response of 15,364 kPa, which decayed to hydrostatic stress at the test depth (14,671 kPa) within 16 min, suggesting a highly permeable formation at this depth interval.

Following the dissipation of excess pore pressure, the tool began the pressure meter expansion at test scan number 2625 (Fig. 84) 31 min after insertion. The lead-screw motor for pressure meter expansion is the basic parameter for the determination of volumetric strain. Initial formation strain began at test scan number 2626 at a lateral

Table 20. Summary of sediment temperatures, Sites 889 and 890.

Core	Depth (mbsf)	Measured temperature (°C)	Corrected temperature (°C)	Measured type	Status
146-889A-					
1H	29.5	4.2 ± 0.2	4.2 ± 0.2	ADARA	Accepted
3H	48.5	4.8 ± 0.2	4.8 ± 0.2	ADARA	Accepted
5H	67.5	6.2 ± 0.2	6.2 ± 0.2	ADARA	Accepted
18X	139.6	11.57 ± .05	10.3 ± 0.1	WSTP	Accepted
21X	168.0	12.99 ± 05	11.7 ± 0.1	WSTP	Accepted
25X	197.3	13.8–14.5	12.5–13.2	WSTP	Doubtful
146-890B-					
4H	35.8	5.5 ± 0.5	5.5 ±0 .5	ADARA	Doubtful
5H	47.8	5.7 ± 0.3	5.7 ± 0.3	ADARA	Accepted

total stress of 18,298 kPa. This initial stress measurement is interpreted as the average in-situ lateral stress. Based on the measured hydrostatic equilibrium pore pressure, the resulting effective lateral stress is 3627 kPa. The vertical effective stress at this test interval is 946 kPa, using the fit expression for effective overburden stress from Figure 71. This results in a high ratio of horizontal to vertical stress, K, of 3.8, suggesting a rotation of principal stress directions.

Further analysis of these test data requires the volumetric calibration of the lead screw. Once the post-cruise calibration is completed, the full stress-strain response of the formation, including maximum shear strength and shear modulus, will be reported.

DOWNHOLE LOGGING

Log Reliability

At Site 889, hole instability caused many enlarged-diameter intervals (Fig. 85), filling the basal portion of each hole and limiting the logging results to the upper 250 mbsf. Density tool measurements in Hole 889A showed many low-value spikes because of the inability of the tool's caliper to remain in contact with the borehole wall. The density tool was not run in Hole 889B because of the poor data acquired in Hole 889A and so that the sonic tool could be placed as low as possible in the tool string. The large and rapidly varying hole diameter may also have affected the quality of the neutron porosity measurements, which will be corrected post-cruise. Similarly, gamma-ray counts and resistivity may be slightly underestimated because of the large hole diameter. The absence of firm pressure on all four pads of the FMS tool is probably responsible for local degradation of the FMS data.

For Hole 889B, upcoming logs were obtained with the geophysical tool string in two logging runs: an initial run from 234 to 60 mbsf and a deeper run, made possible by using the side-entry sub, from 259 to 213 mbsf. Logs from the deeper run were depth-shifted 0.5 m upward and then merged with the initial run.

Spikes in the sonic velocity logs (Fig. 86) might be interpreted as cycle skipping. However, these high values are on both the upcoming and downgoing logs, were preserved through reprocessing (see "Explanatory Notes" chapter, this volume), and have correlative high values in the resistivity logs. Therefore, we think that these spikes are true high-velocity values. Because the sonic tool is placed higher in the tool string than the resistivity tool, resistivity data are available from 30 m deeper in Hole 889A and 15 m deeper in Hole 889B than are the sonic data. At Site 889, resistivity correlates with sonic traveltimes. Therefore, we determined the regression equation for predicting sonic traveltimes from the logarithm of resistivity for each hole, using the bottom 30 m of sonic data at Hole 889A ($R = -0.665$) and the bottom 61 m of sonic data at Hole 889B ($R = -0.710$); these correlation coefficients are negative because sonic traveltime is inversely correlated with resistivity. We then applied each regression equation to the intervals for which resistivity, but not sonic, data were available (231.6–260.1 mbsf at Hole 889A and 243.0–258.9 mbsf at Hole 889B).

The resistivity measurements (Fig. 86) are expressed as formation resistivities rather than as formation factors, because the latter requires estimation of both temperature variations and the effect of the salinity of the interstitial fluid. Although the recovered pore fluids are generally of low salinity (see "Inorganic Geochemistry" section, this chapter), these values probably reflect some dilution by melting of gas hydrate and therefore are not representative of in-situ formation fluids. Some of the resistivity data could be affected by the flushing of the borehole with seawater; temperature effects are also superimposed by drilling.

Measured hole deviations were 1°–2° to the south in Hole 889A and 2°–3° to the north in Hole 889B. Hole deviation adds inherent inaccuracy to any structural measurements taken on the cores or on FMS data, and may cause hole ellipticity.

Gamma-ray measurements are attenuated in the portion of the hole logged through pipe, which is above 62 mbsf at Hole 889A and above 60.7 mbsf at Hole 889B. Spectral gamma-ray logs from Hole 889A (Fig. 86) were approximately corrected for pipe attenuation by using the baseline shift across the pipe/open-hole transition to estimate an attenuation factor, then multiplying measurements for the through-pipe data interval by the inverse of this estimated attenuation. For the total gamma-ray log, the multiplier used was 4.4. These corrected through-pipe logs (Fig. 86) are noisier than the open-hole logs but are still capable of revealing the dominant gamma-ray trends.

Correlation of Logs to Lithostratigraphic Units

Drilling two holes separated by about 500 m provides a good opportunity to use log responses to examine the heterogeneity of an accretionary prism. Logs of sonic velocity and resistivity correlate well with subdivisions based on lithology; these logs plus neutron porosity also mark smaller scale depositional and diagenetic events (Fig. 86). Gamma-ray data indicate changes in sediment type within the lithostratigraphic units.

The gamma-ray data from Hole 889A systematically decrease from about 60 mbsf toward the surface (Fig. 86). This variation is consistent with the observed uphole increase in the proportion of sand turbidites in the recovered cores.

The velocity log at Hole 889A shows a positive deviation of about 0.1 km/s at about 88 mbsf that correlates with a biostratigraphically defined hiatus (see "Biostratigraphy" section, this chapter). Because this anomaly associated with the hiatus is a peak and not a downhole shift to higher velocities, the increase in velocity is probably the result of subtle cementation effects caused by long-term exposure of the sediments to bottom water, rather than the result of erosion of the subjacent sequence.

Lithostratigraphic Subunit IB (91.5–128.0 mbsf in Hole 889A) was observed to be reworked and is interpreted as debris flows and/or slumped sediment (see "Lithostratigraphy" section, this chapter). In the logs, this interval is readily identifiable by low velocities and resistivities (at 88–126 mbsf in the Hole 889A log and at 92–129 mbsf in the Hole 889B log), which indicate low porosity (Fig. 87). The top of this interval is more obvious in the velocity log in Hole 889B than in Hole 889A, because the overlying sediments have a much slower response in Hole 889A. In both holes, high porosities, low velocities, and low resistivities are observed at the base of this interval. The top portion of Subunit IB in both holes is a sequence, 18 m thick in Hole 889A and 11 m thick in Hole 889B, in which porosity gradually increases uphole; the gamma-ray log for this sequence exhibits no consistent pattern of fining or coarsening upward. Other than the readily correlatable top and bottom portions, few log characteristics of Subunit IB can be correlated between the holes.

The boundary between lithostratigraphic Units I and II is defined at 128.0 mbsf in cores from Hole 889A and was not cored at Hole 889B. Log responses (Figs. 86–87) indicate that the boundary is marked by a shift to higher velocity and resistivity at 126 mbsf in Hole 889A and at 129 mbsf in Hole 889B (Fig. 86). The change is more evident in Hole 889B, where it is characterized by a distinct displace-

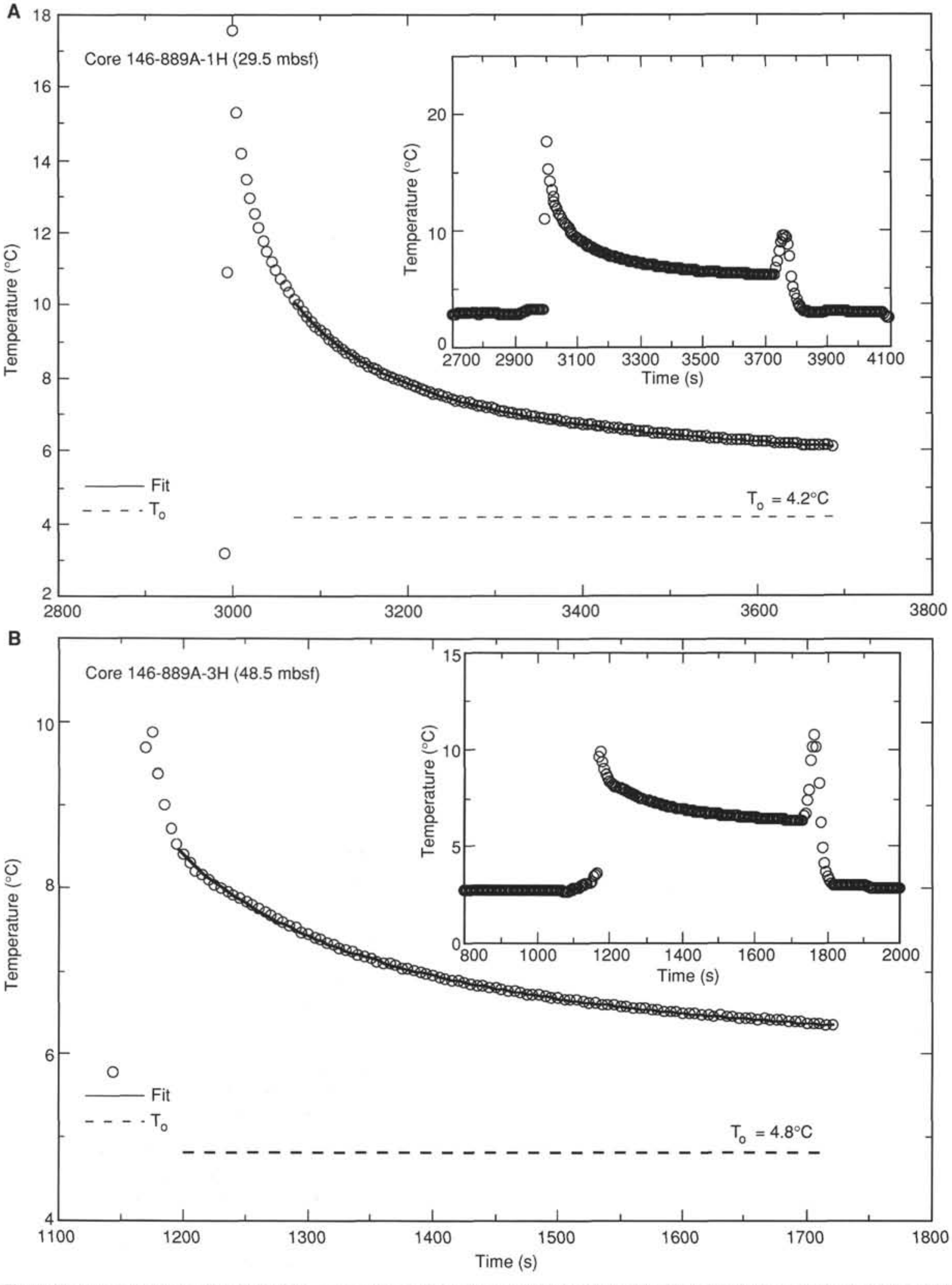

Figure 78. Temperature record in near-bottom seawater and sediment from ADARA deployments in Hole 889A. The solid line is the theoretical fitted curve used to estimate the equilibrium temperature, T_o, shown by the dashed line. The entire record of the deployment is shown in the inset. **A.** Core 146-889A-1H (29.5 mbsf). **B.** Core 146-889A-3H (48.5 mbsf). **C.** Core 146-889A-5H (67.5 mbsf). **D.** Core 146-890B-4H (35.8 mbsf). **E.** Core 146-890B-11H (47.8 mbsf).

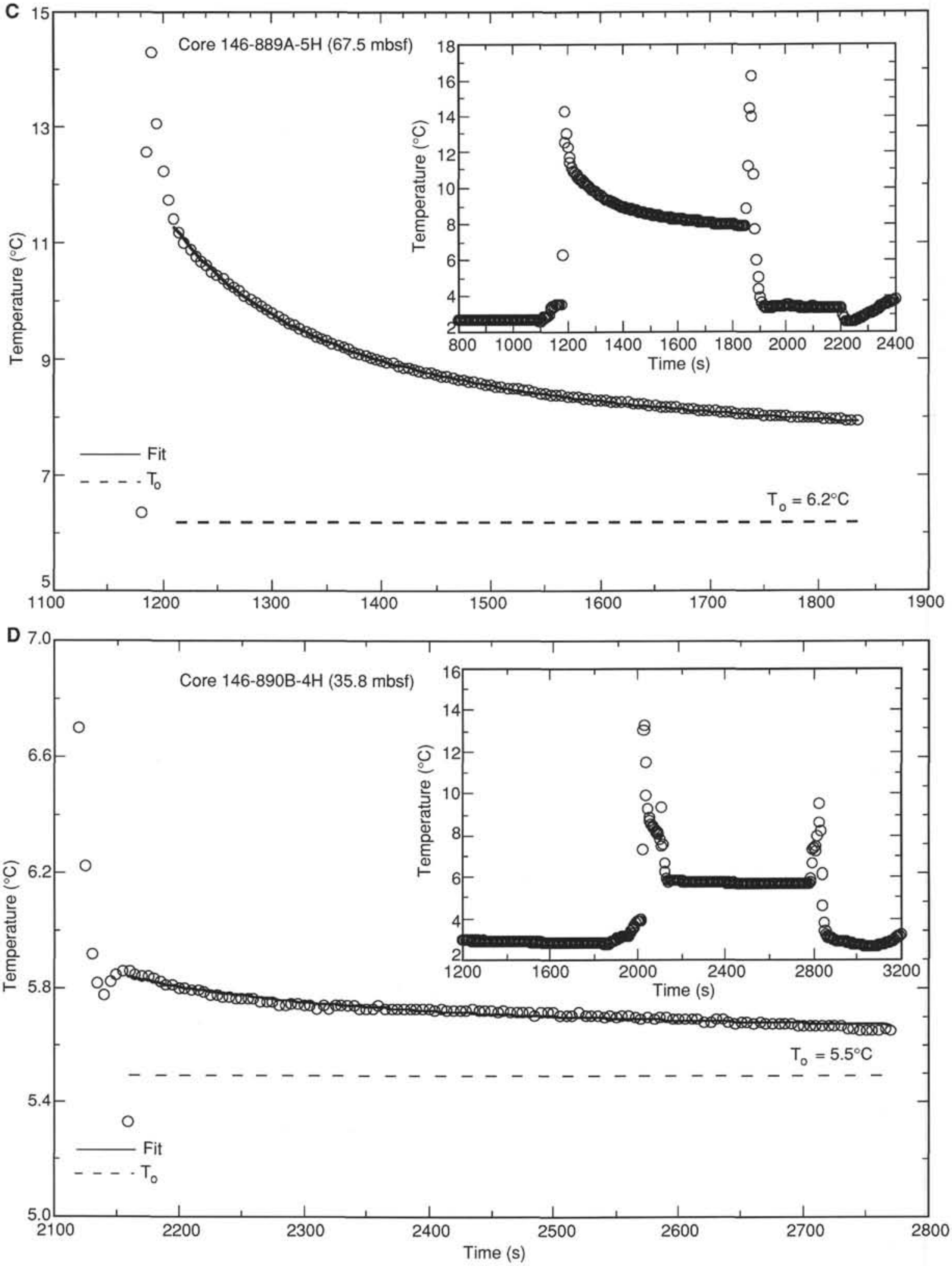

Figure 78 (continued).

ment of the baseline in both the velocity and resistivity logs. In both holes the boundary is partly obscured by the gradually increasing porosity exhibited in the top 5–10 m of Unit II. Gamma-ray logs show that this short interval is a fining-upward sequence.

The velocity and resistivity logs show peaks within lithostratigraphic Unit II, for example, at 190 and 213 mbsf in Hole 889B (Fig. 86). These peaks correlate with low values of neutron porosity and probably represent cemented zones that produced some of the cemented carbonate chunks recovered in the cores. Fractures filled with hydrate would show similar highs in velocity and resistivity, but the observation that neutron porosities are low, not high, indicates that the peaks are not because of the presence of hydrate (Mathews and von

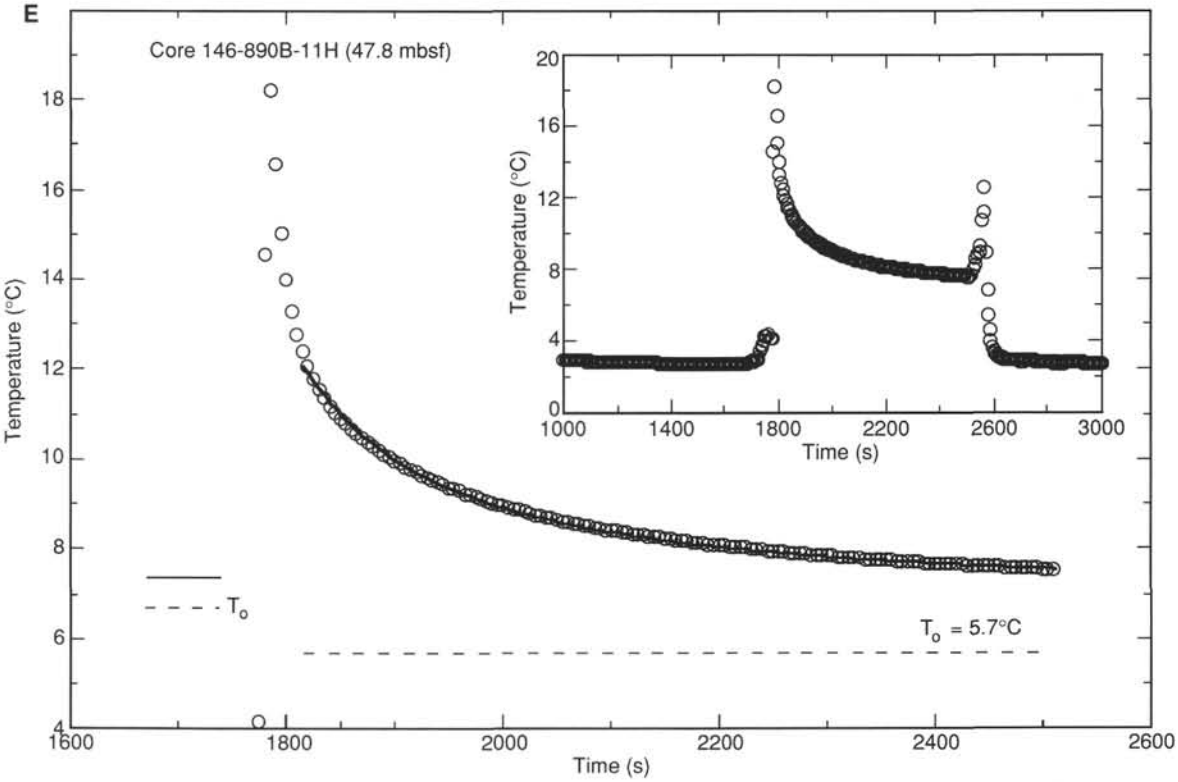

Figure 78 (continued).

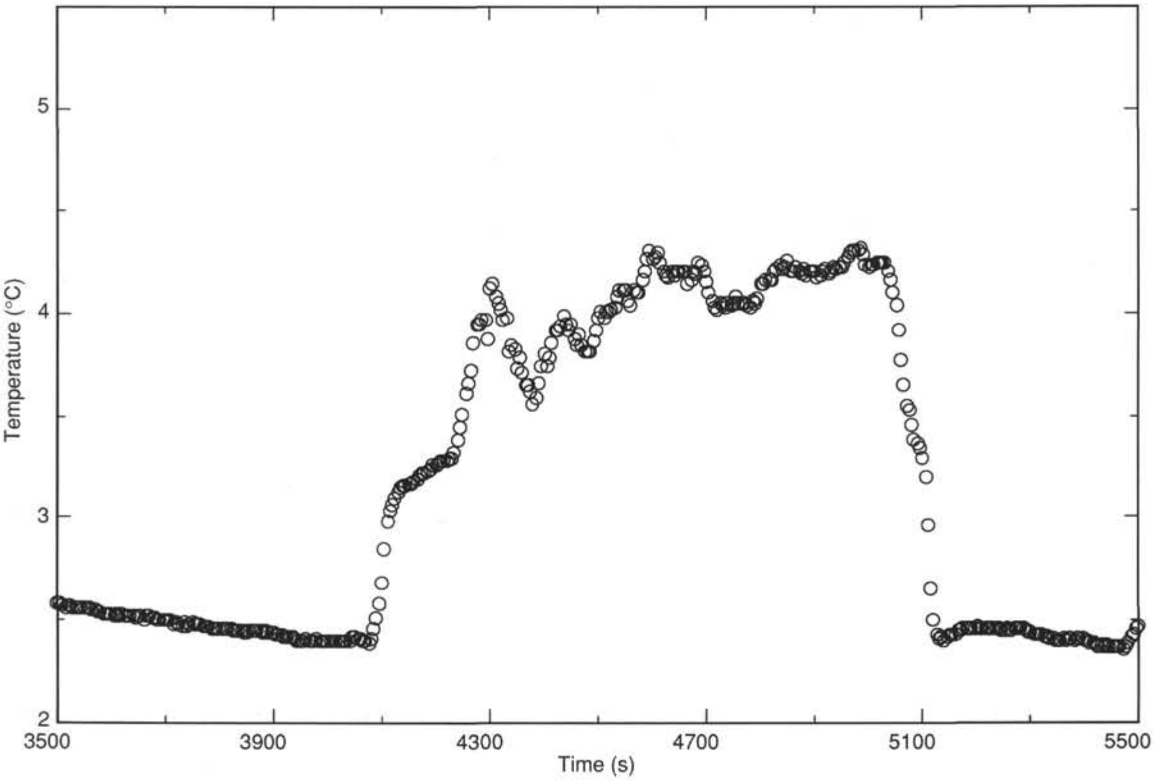

Figure 79. Temperature record in bottom seawater and sediment from ADARA deployment in Hole 889D at 105 mbsf (following Core 146-889D-1H).

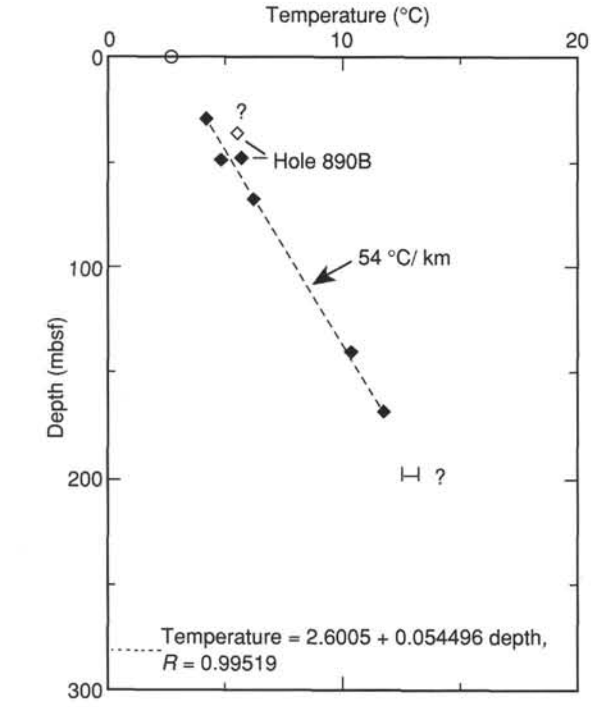

Figure 80. Bottom-seawater (open circle) and sediment (diamonds) temperatures plotted as a function of depth at Sites 889 and 890. Solid diamonds are good data points from which the linear least-squares regression line (dashed) was calculated. The range of two dubious WSTP measurements at 197.3 mbsf is indicated by the bar.

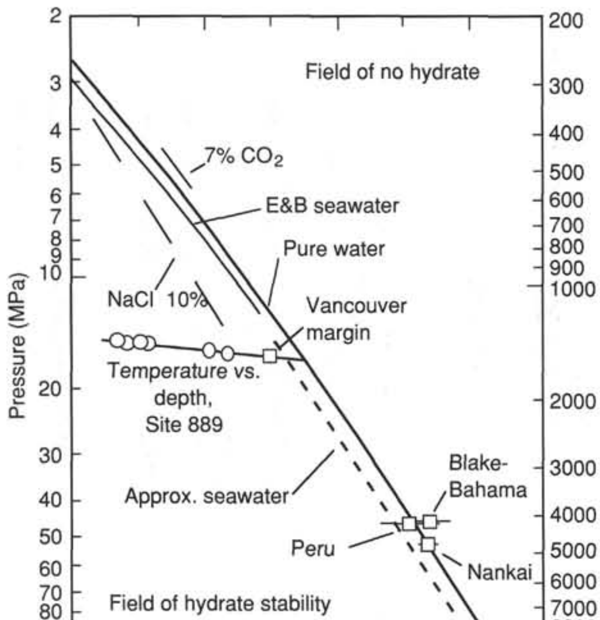

Figure 81. Diagram after Hyndman et al. (1992) showing the hydrate stability fields from laboratory data, with BSR temperatures and depths (open squares) estimated at three previous DSDP and ODP sites (Blake-Bahama outer ridge, Site 533; Peru Margin, Site 688; and Nankai accretionary prism, Site 808) and one present site (Vancouver Margin, Site 889). Error limits at Sites 889 and 890 are ±0.5°C for temperature and ±5 m for depth (error bars would plot within the square symbol). "E&B seawater" indicates the theoretical prediction for seawater by Englezos and Bishnoi (1988). Open circles are sediment temperatures at Sites 889 and 890.

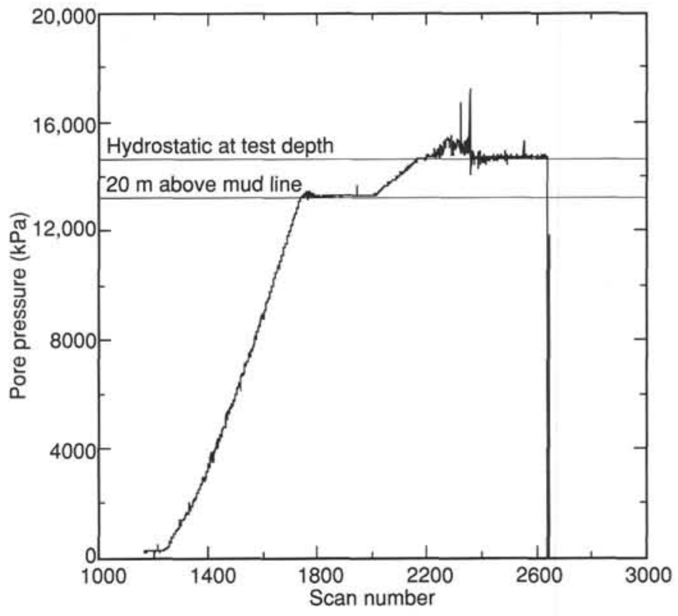

Figure 82. LAST-II pore pressure data vs. scan number in Hole 889D. The noisy response is attributed to small movements of tool resulting from drill-string heave. The tool stopped recording data after scan number 2647, approximately 40 min after insertion.

Huene, 1985). The FMS images suggest that these cemented zones dip at about 40°–50° to the north; they are probably carbonate-filled fractures rather than bedding.

A transition in log responses in Holes 889A and 889B is observed at about 150 mbsf (Fig. 88). This transition at 146 to 150 mbsf in Hole 889A and 141 to 149 mbsf in Hole 889B is characterized by high velocity–high resistivity intervals and adjacent low velocity–low resistivity intervals. The 1- to 3-m-thick high velocity–high resistivity intervals are nondiagnostic in gamma-ray response; they are probably carbonate-cemented beds. The 2- to 6-m-thick low velocity–low resistivity intervals have low gamma-ray values and may be sands. In Hole 889A, a low velocity–low resistivity interval (145–148 mbsf) overlies

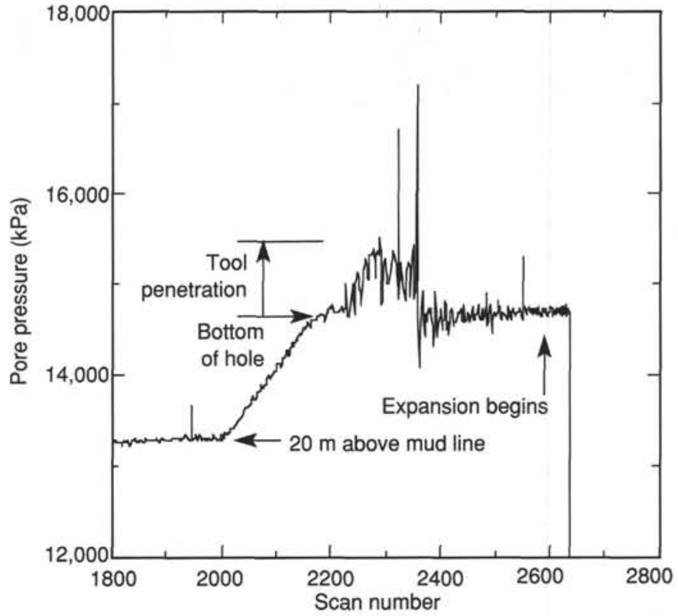

Figure 83. Pore-pressure data from LAST-II during and after tool insertion into the formation in Hole 889D.

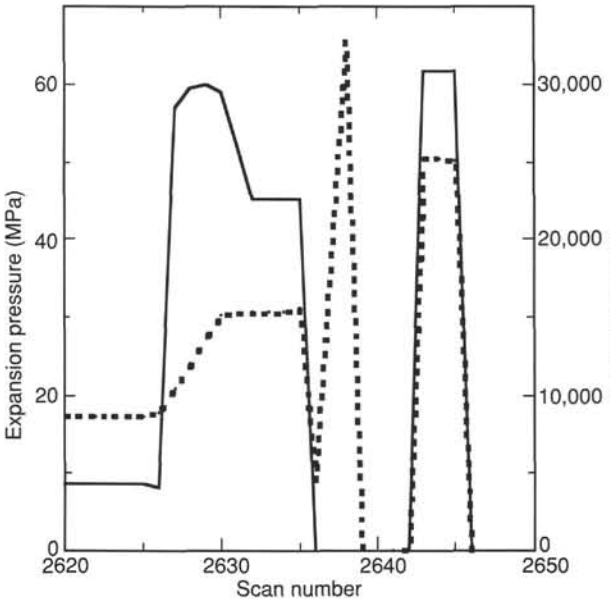

Figure 84. Lead-screw count (dashed line), which is equivalent to volumetric strain, and expansion pressure (solid line) vs. scan number during inflation of the pressure meter during the LAST-II run in Hole 889D. The large variations in stress and lead-screw count are attributed to movement of the tool from drill-string heave. Good test results were recorded from scan numbers 2625 (expansion begins) to 2631, from 31 to approximately 37 min after insertion.

a high velocity–high resistivity unit (148–150 mbsf), whereas in Hole 889B at least two thin high velocity–high resistivity units (both in the interval from 141 to 145 mbsf) overlie a low velocity–low resistivity unit (145–150 mbsf). A velocity spike at 147 mbsf within the low velocity–low resistivity unit in Hole 889B is probably real but too thin for detection on the resistivity log; it is observed in both downgoing and upcoming velocity logs in Hole 889B and in the FMS data in both Holes 889A and 889B. In Hole 889B, a sharp increase in gamma-ray values at 148–150 mbsf is associated with a small baseline increase in resistivity but not in velocity. In Hole 889A, none of the three logs exhibits a baseline shift.

Throughout the logged intervals at both holes, the small-scale variations in gamma-ray values are positively correlated with variations in resistivity and velocity. This relationship seems to imply that the silty clays/clayey silts are less porous (higher in resistivity and velocity) than the sandier beds, because K, Th, and U are normally more abundant in clay minerals than in sands. If so, this pattern is the opposite to that generally observed in porous terrigenous sediments (e.g., see "Site 888" chapter, this volume), where uncompacted clay minerals increase the porosity because of their near-random orientation of platy particles. Perhaps the silty clays/clayey silts are less porous than the sandier beds at Site 889 because of a much wider grain-size distribution, or perhaps the silty clays/clayey silts were initially more porous than the sands but have experienced a greater proportion of compression-induced dewatering. The answer to this problem has implications for the quantitative estimation of fluid flux through the Vancouver accretionary prism, based on comparison of porosity/depth trends at Sites 888 and 889.

Velocity-Porosity Relationships and Hydrate Occurrences

Velocity-porosity relationships at Site 889 are important for two purposes. First, a transform from velocity to porosity is needed to enable the conversion of seismic interval velocities into an inferred porosity structure for the prism. Second, log-based detection of methane hydrate is based on the identification of zones that have anomalously high velocity, in comparison with the velocity of other sediments with the same porosity. Theoretical relationships of velocity to porosity are of limited usefulness here, because of inappropriate assumptions (e.g., Wood, 1941) or critical parameters for which the values are unknown (e.g., Gassmann, 1951; Toksöz et al., 1976).

Log-based porosities for Site 889 can be estimated from three logs: density, resistivity, and neutron. Hole size was so large and variable

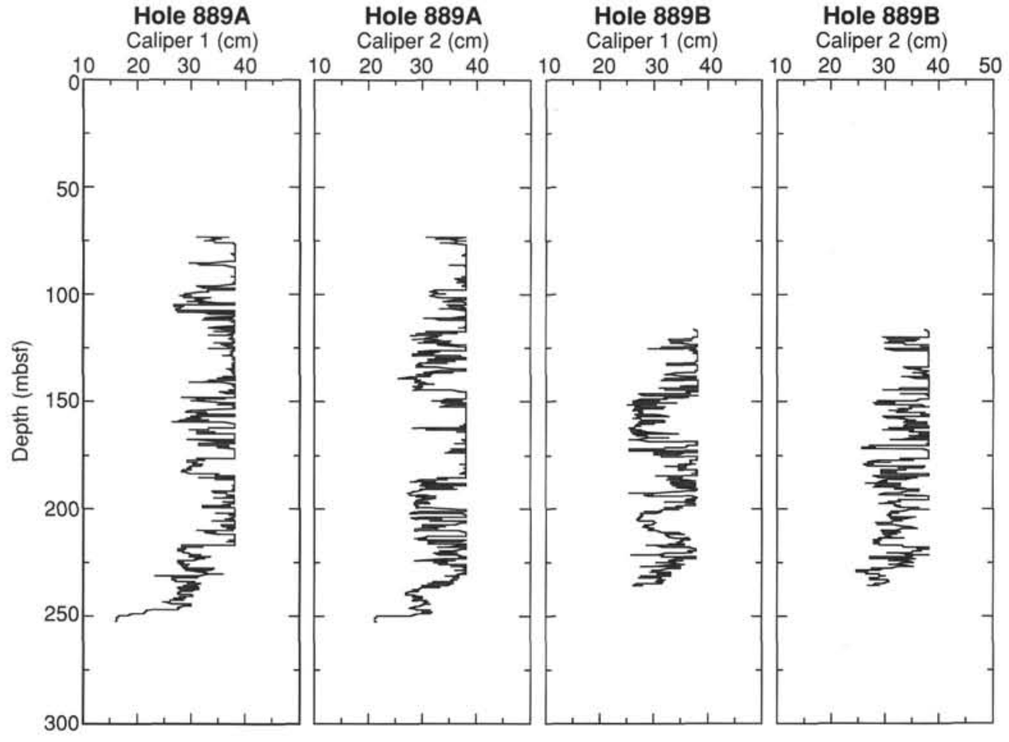

Figure 85. Caliper logs for Holes 889A and 889B.

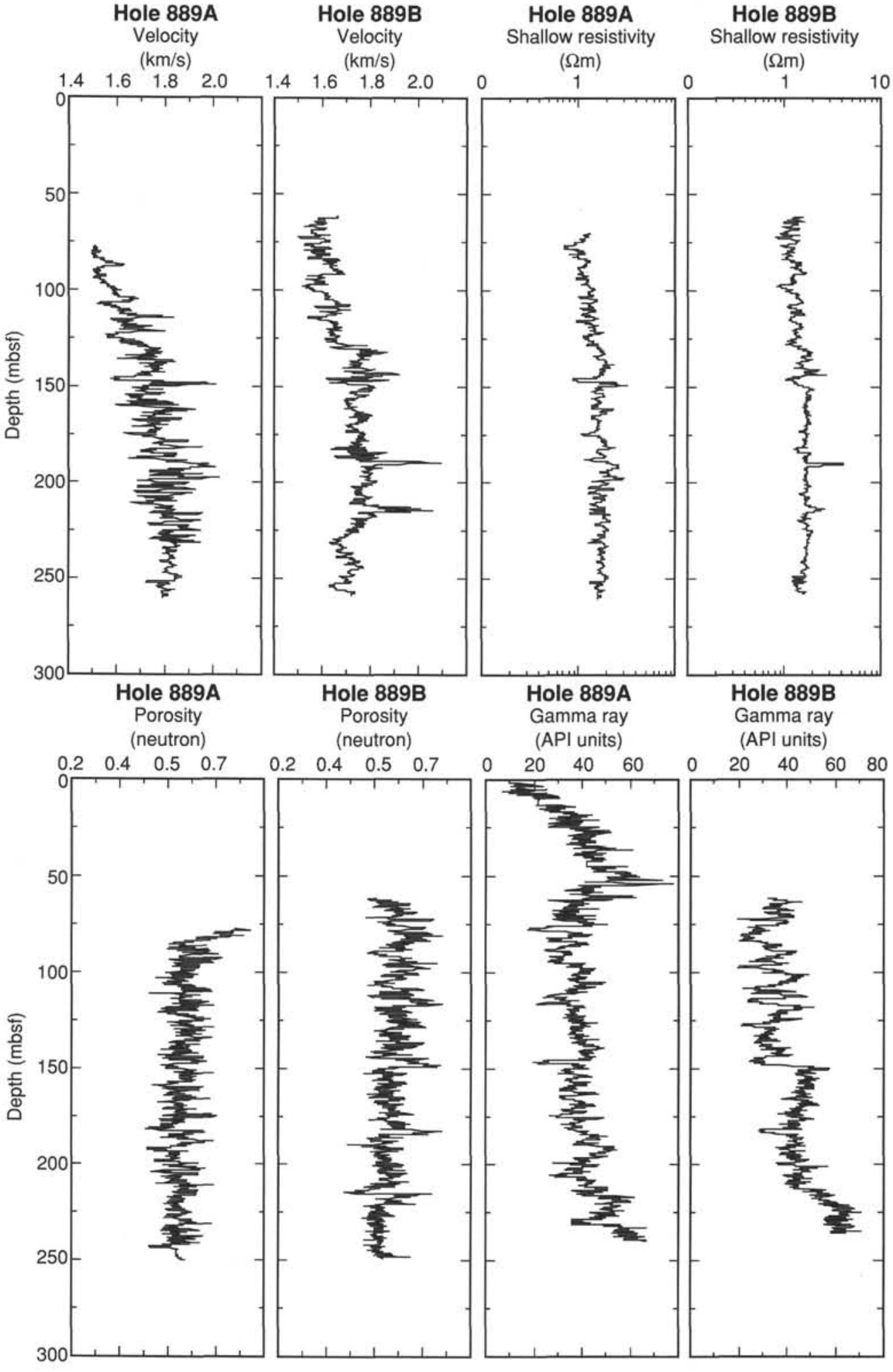

Figure 86. Sonic velocity, shallow resistivity, neutron porosity, and gamma-ray logs from Holes 889A and 889B.

that the density data from Hole 889A are almost completely spurious; for this reason, density logging was not attempted in Hole 889B. Porosity determination from resistivity logs requires estimates of both near-borehole formation temperatures and salinities, as well as calibration of the Archie (1942) coefficients a and m; this has not been attempted yet. Instead, we used neutron porosities as our most accurate shipboard estimation of in-situ porosities. These neutron porosities may be too high by as much as several percent, because of both the presence of bound water in clay minerals and the deployment of the tool without eccentralization (see "Explanatory Notes" chapter, this volume). The neutron porosities agree fairly well with core measurements of porosity below about 85 mbsf (Fig. 89), but the latter also may be slightly overestimated because of differences between laboratory and in-situ pressures (e.g., Hamilton, 1976). Velocity and neutron porosity for Units I

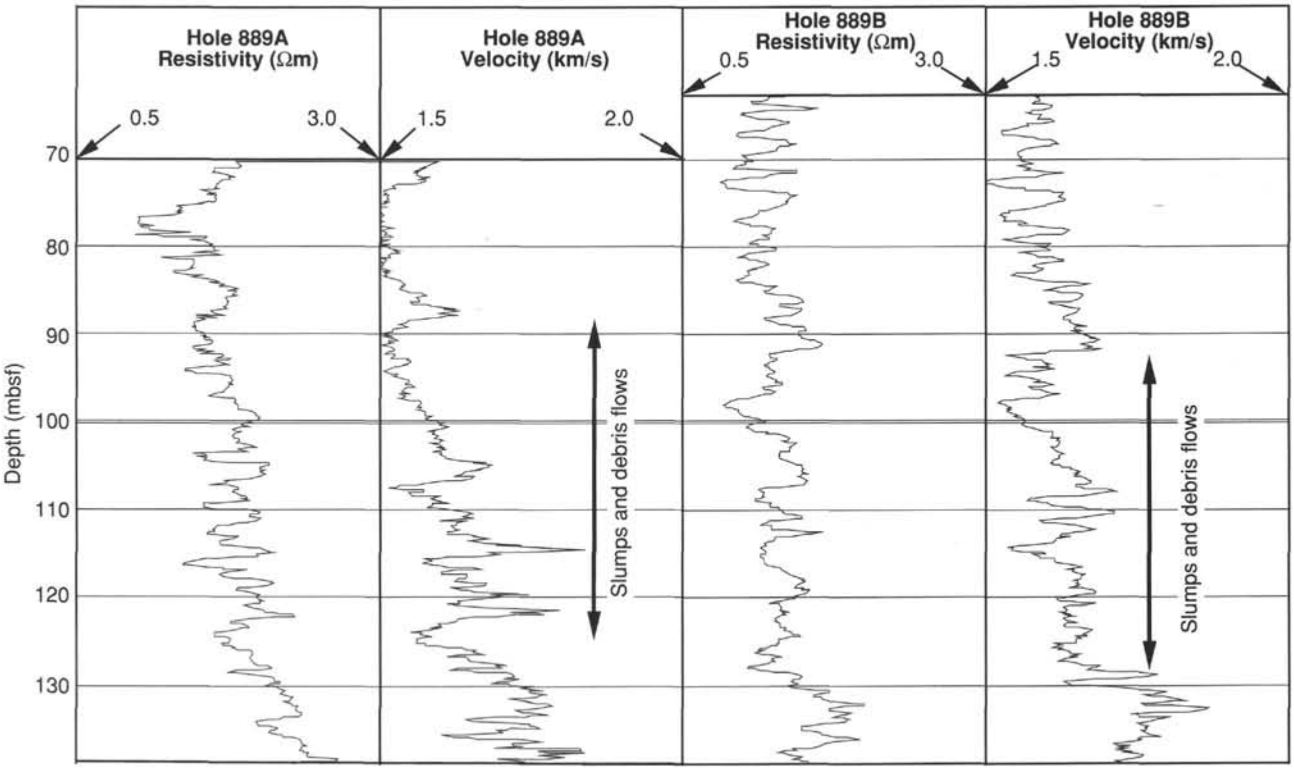

Figure 87. Resistivity and sonic velocity logs for Holes 889A and 889B from the bottom half of lithostratigraphic Unit I.

and II in Holes 889A and 889B are weakly correlated to uncorrelated (Fig. 90); these correlations may be improved with post-cruise log processing to improve the quality of the porosity data.

Log responses can be used to detect occurrences of hydrates (e.g., Mathews and von Huene, 1985). In massive methane hydrates, velocity and resistivity are very high, and density and gamma-ray response are low. Whalley (1980) calculated that the compressional-wave velocity in pure methane hydrates is about 3.8 km/s and the density is 0.91 Mg/m^3. For sediments in which the pores contain a mixture of hydrate and pore water, however, the relationships between hydrate proportion and velocity and resistivity are neither theoretically nor empirically known.

Hyndman and Spence (1992) proposed a model for the origin of hydrates and associated BSRs. Based on seismic modeling, they make several specific predictions concerning the log responses to be encountered off Vancouver Island. The BSR is a strong negative-polarity seismic reflector; therefore, a sharp decrease in impedance is expected at the BSR. Hyndman and Spence (1992), for example, predicted a 20%–30% decrease in impedance at the BSR; a decrease of this magnitude is not observed in the log data (Fig. 91). They estimated that about one-third of the pore space immediately above the BSR is filled with hydrate, and that this proportion drops gradually in the overlying 10 to 30 m. Hyndman and Spence (1992) attributed the impedance change entirely to this contrast between fluid-filled and hydrate-filled pores. They followed other investigators in assuming that the BSR is the base of the methane hydrate stability field, and they suggested that the hydrate accumulates in the 10- to 30-m-thick interval overlying the BSR owing to fluid advection.

We see no evidence for massive methane hydrates (Fig. 91) as found in Site 570 logs (Mathews and von Huene, 1985), but we cannot exclude a few percent of methane hydrate. No velocity anomaly is visible at Hole 889A, where the lack of a VSP results in a few meters of uncertainty in the estimated location of the BSR. However, at the 215.9–225.3 mbsf location of Core 146-889B-3R, which is inferred to contain methane hydrate (see "Gas Hydrate Studies" section, this chapter), the velocity is anomalously high (by about 0.1 km/s) with respect to resistivity and neutron values for the same interval. The anomalous velocity zone is capped by a steeply dipping high-velocity, high-resistivity interval that may be a carbonate-filled fracture. The base of this zone is the inferred location of the BSR based on VSP data.

An alternative model for BSR formation is that the impedance contrast is attributable primarily to the presence of free gas immediately below the BSR, rather than high-velocity hydrates (Minshull and White, 1989; Miller et al., 1991). Even 2%–4% of free gas is sufficient to lower the compressional-wave velocity of an unconsolidated sediment to less than that of water (Domenico, 1976). The implications of both the log and VSP-based velocities for the presence of free gas are discussed below.

Vertical Seismic Profile

Acquisition

The zero-offset VSP at Site 889 was shot using a 300-in.^{3} air gun and a 400-in.^{3} water gun fired alternately. Gun and receiver geometries are shown in the "Explanatory Notes" chapter (this volume). Both guns were fired at 1300 psi for most of the experiment because we were unable to fire the air gun at higher pressures. The water gun was fired at 1800 psi during the final uphole run. WST data were recorded by Schlumberger as well as on a Sun workstation. In addition, far-field (about 150 mbsf) source signatures were recorded on the Sun workstation for both guns throughout the experiment. Receiver stations (23 total) were run beginning at the bottom of the logged hole (243 mbsf) and stepping uphole at 5-m intervals without closing the clamping arm between stations. The upper three stations were spaced 7 m apart as a result of the poor hole conditions. The experiment was conducted in two runs because of problems with the water gun.

Although the first run encountered few difficulties in clamping or tool slippage, we found few secure clamping positions during the second run (water gun, 208–126 mbsf), resulting in extremely noisy

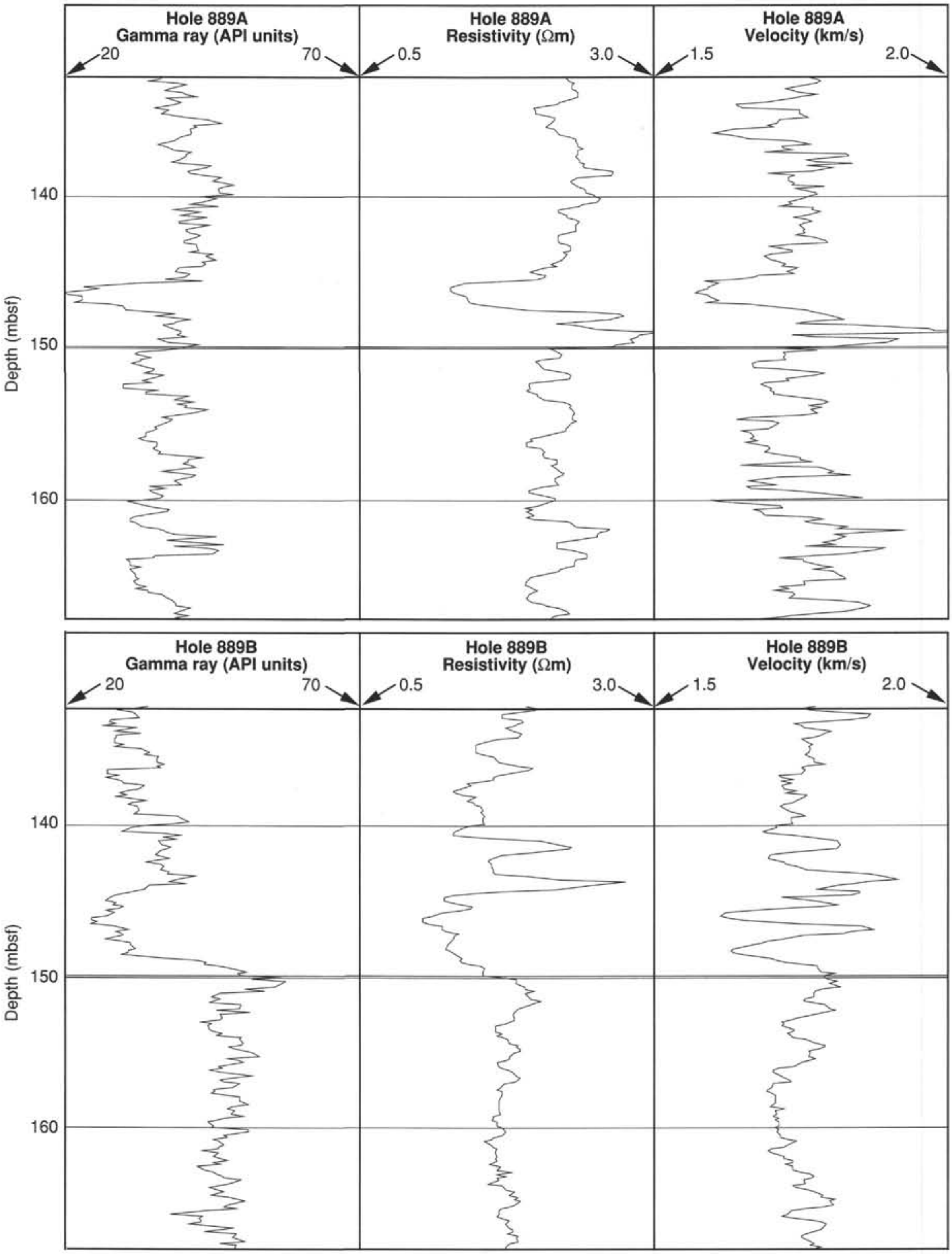

Figure 88. Gamma-ray, resistivity, and sonic velocity logs for Holes 889A and 889B from the transition interval around 150 mbsf.

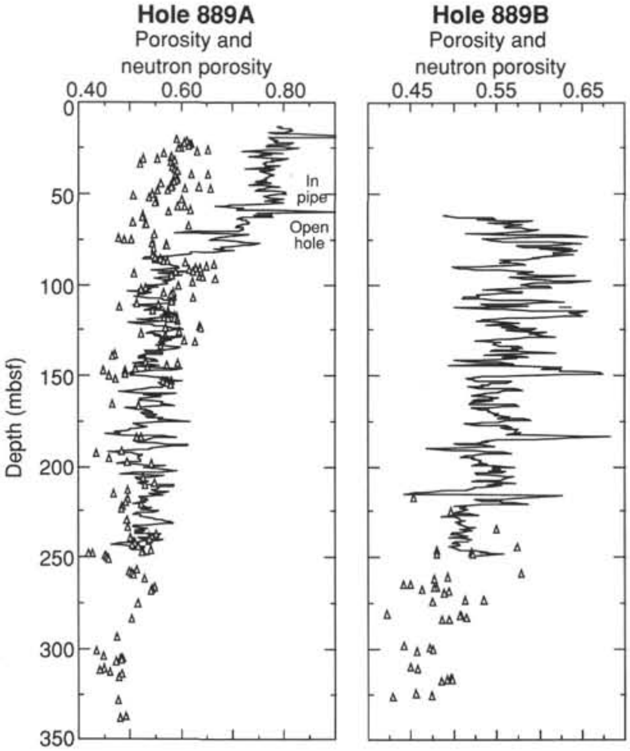

Figure 89. Comparison of porosities measured on core samples (triangles) with the neutron porosity log (continuous line), Holes 889A and 889B. Note that the high neutron porosities for the interval above 73 mbsf in Hole 889A are unreliable because of through-pipe logging.

data and greatly increased operation time. Apparently, the initial uphole trip (with clamping arm extended) caused instability in and enlargement of the borehole. Closing the clamping arm between each station would, however, have introduced considerable risk that the arm might fail to open properly, thereby jeopardizing the VSP.

Time-depth and velocity data presented here (Fig. 92) are based on air gun data alone; the water gun data require further post-cruise processing. Additional processing is also required to separate the upcoming (reflected) from downgoing (direct) events and to eliminate the prominent bubble pulse in the air gun data. The uppermost VSP station (126 mbsf) was of poor quality because of the proximity of the pipe (set at 106.7 mbsf) and is not included in the discussion.

Time-Depth Relationship

The VSP provides an unambiguous time-depth relationship in the first break time of the direct compressional-wave arrival at each receiver depth (Fig. 92). This time-depth relationship was extended by inclusion of the integrated sonic log and further confirmed by agreement between the synthetic seismogram and the multichannel seismic (MCS) data. The slope of the time-depth curve provides the velocity.

Integration of the sonic log yields a time-depth curve with respect to the shallowest log value, but the sonic log provides no information on the travel times between the seafloor and the first sonic-log measurement at 61.7 mbsf. Therefore, the sonic-log time-depth curve was shifted to sub-bottom time by using the VSP data to constrain the velocity of the unlogged interval (Fig. 92). The MCS data show flat-lying, laterally continuous reflectors in the upper portion of the hole (see "Core, Log, and Seismic Integration," this section) indicating that the VSP-derived interval velocity for lithostratigraphic Unit I should be representative of the near-borehole conditions measured in the sonic log.

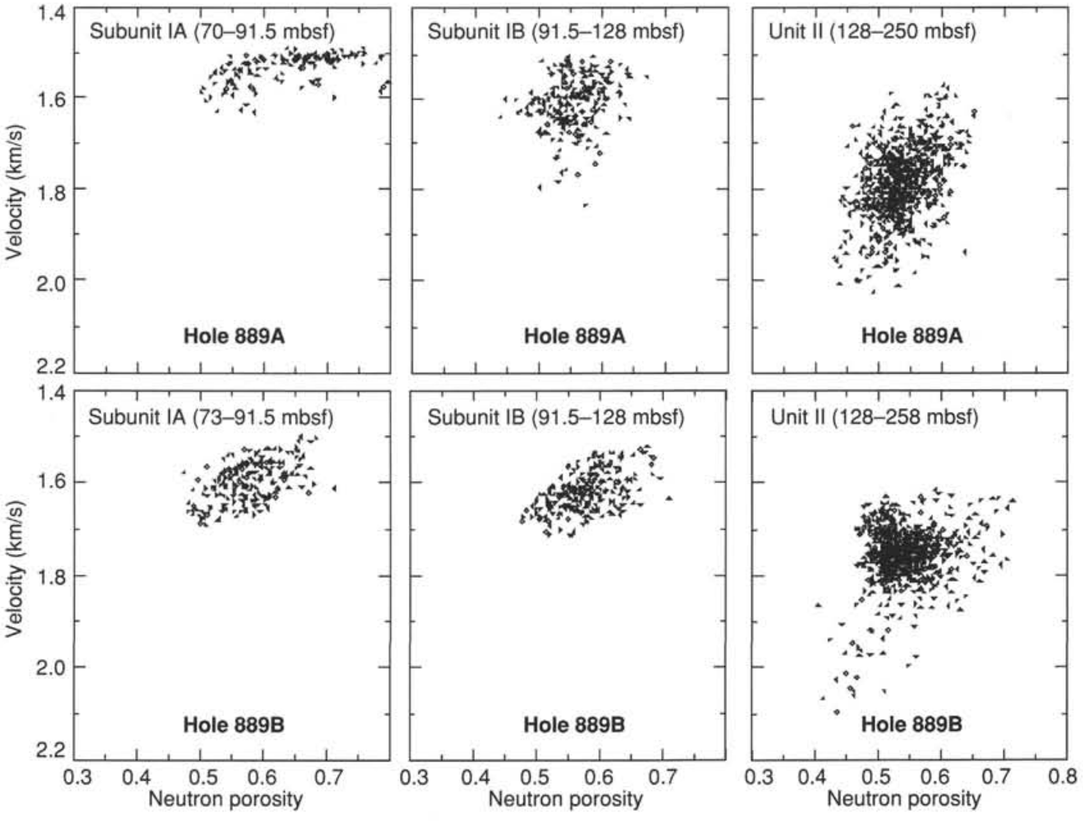

Figure 90. Cross plots of neutron porosity and velocity for Units I and II, Holes 889A and 889B.

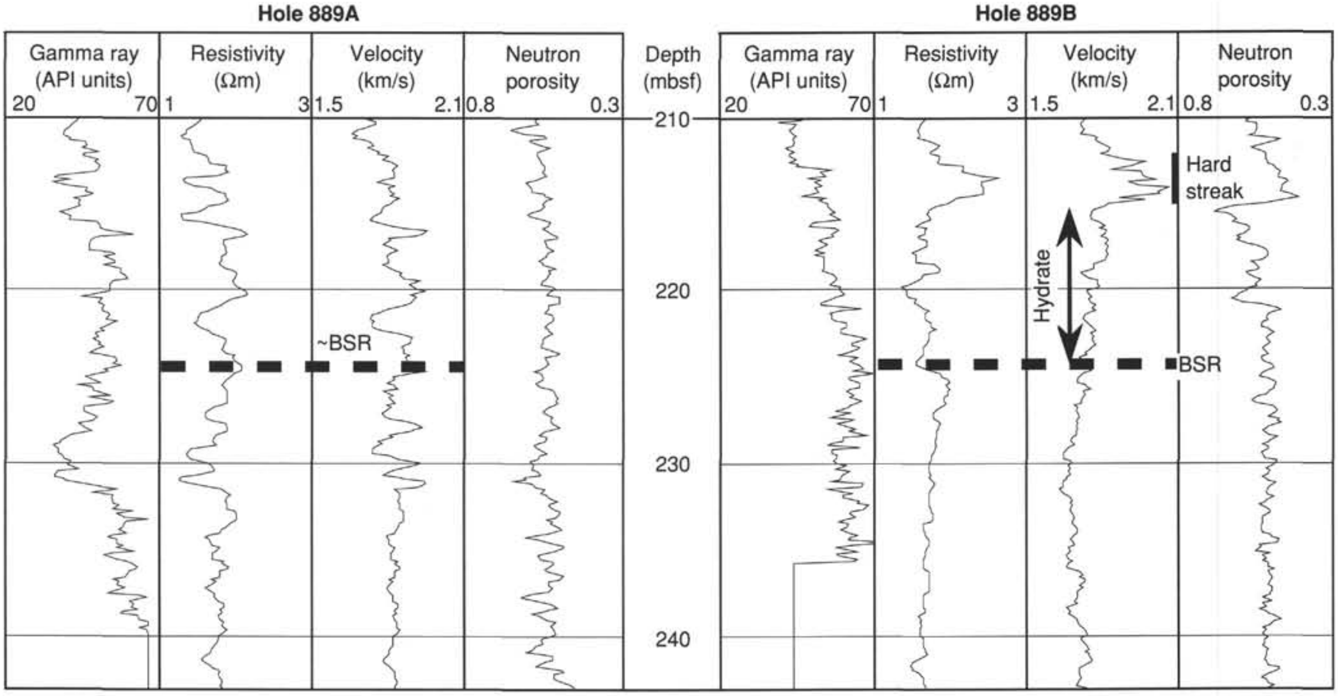

Figure 91. Log responses in the vicinity of the BSR and possible hydrates at Holes 889A and 889B. Note that the velocity log shows no evidence of a substantial velocity decrease at or near the BSR.

In contrast to the lateral homogeneity of Unit I, the discontinuous reflectors and pervasive faulting seen in the MCS data in Unit II indicate heterogeneity on a seismic scale. Because the VSP uses lower frequencies than the sonic log (10–40 Hz vs. 5–18 kHz, respectively) and has a much greater source-receiver separation, it effectively averages velocity over several tens of meters around the borehole, in contrast to sonic-log penetration of less than 0.5 m. Lateral heterogeneity on this scale will result in sonic-log velocities that may not be representative of velocities farther from the borehole.

The BSR occurs in the MCS data at 276 ms TWT below the seafloor. Based on the VSP time-depth relationship (Fig. 92), this traveltime corresponds to 224 mbsf (±5 m).

Interval Velocity and the Origin of the BSR

The BSR has generally been regarded as the pressure/temperature-dependent base of the gas hydrate stability field. All BSR models predict a sudden decrease in velocity (and therefore impedance) across the BSR in order to form a strong seismic reflection with negative polarity (opposite to that of the seafloor). This velocity decrease has been alternatively modelled as either high-velocity hydrate above the BSR or low-velocity free gas beneath. The VSP data show a sudden decrease in velocity across the BSR that is not readily apparent in the sonic logs. The velocity decrease is evident in Figure 92 as a decrease in slope through the three deepest VSP stations.

The VSP data are not consistent with a high-velocity hydrate above the BSR. Instead, we find that VSP-based interval velocities beneath the BSR (224–243 mbsf) are slower than water: 1.2–1.4 km/s, depending on the interval averaged. Such low velocities indicate free gas.

Sonic-log velocities for the interval below the BSR at Hole 889B are low (1.65–1.70 km/s), but higher than VSP-based velocities; sonic-log velocities beneath the BSR at Hole 889A exhibit no significant decrease (Fig. 86). The difference between the VSP and sonic-log velocities can be explained by the loss of gas in the vicinity of the borehole as a result of drilling disturbance (e.g., Serra, 1984). If free gas were present in situ, drilling may have affected its detection in either of two ways: (1) drilling circulation may have created an invaded zone adjacent to the borehole, thereby driving gas away from the near-borehole region measured by the sonic log, or (2) temperature decrease or pressure increase during drilling may have driven low concentrations of free gas across the gas/liquid threshold.

Vertical Seismic Profile and the BSR

The reflected arrival corresponding to the BSR (labeled "R_{bsr}" on Fig. 93) begins at 224 mbsf just beneath receiver station 5 and moves out uphole. Because the VSP is restricted to a short interval, the reflected arrival at R_{bsr} is largely confined to the region between the direct arrival of the primary pulse ("D_p") and the downgoing bubble pulse ("D_{b1}"). The downgoing energy is significantly greater and obscures the reflected arrival. Additional processing is necessary to separate upcoming (reflected) from downgoing events and to remove the effects of the bubble from the air-gun signature.

Synthetic Seismogram

To create synthetic seismograms, we digitized a wavelet from a representative section of seafloor in the seismic-reflection data. This produced a slightly asymmetrical wavelet with a negative peak (see "Site 888" chapter, this volume). We first calculated synthetic seismograms for Holes 889A and 889B from the sonic-log velocities assuming constant density (Fig. 94A); incorporating density values did not significantly change the resulting synthetic seismogram. The sonic-based synthetic seismogram for Hole 889A provides a poor match to the seismic data and fails to produce a reflector at the BSR (Fig. 94A). The sonic-based synthetic seismogram at Hole 889B is significantly better overall, but it still provides a poor match in the vicinity of the BSR.

We also used VSP-based velocities to create a synthetic seismogram for Hole 889B. In contrast to the sonic-based synthetic seismogram, the VSP-based synthetic seismogram is a good match to the seismic data and reproduces the character of the BSR (Fig. 94B). We conclude that the sonic-velocity log is not representative of the velocity-depth function at seismic frequencies because of lateral velocity

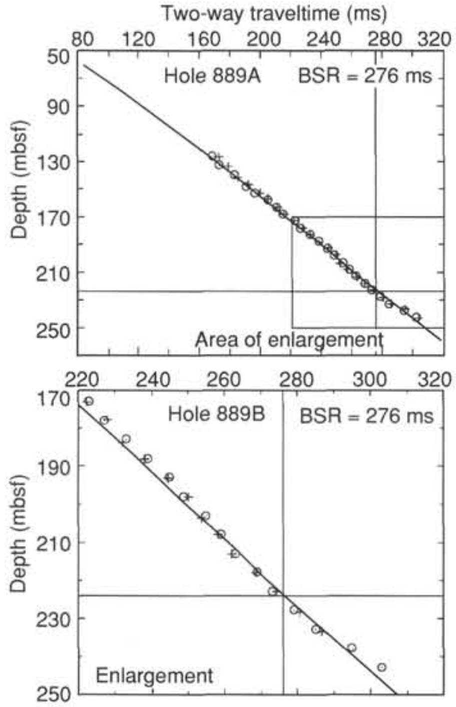

Figure 92. Time-depth relationship for Hole 889B. The integrated sonic log is shown by the solid diagonal line. The VSP time-depth points are shown by circles and pluses, for real-time and reprocessed data, respectively. Based on this time-depth relationship, the BSR, which occurs at 276 ms below the seafloor, is at 224 mbsf. Sub-bottom times shown were calculated from total traveltime using a value of 1773 ms TWT to the seafloor.

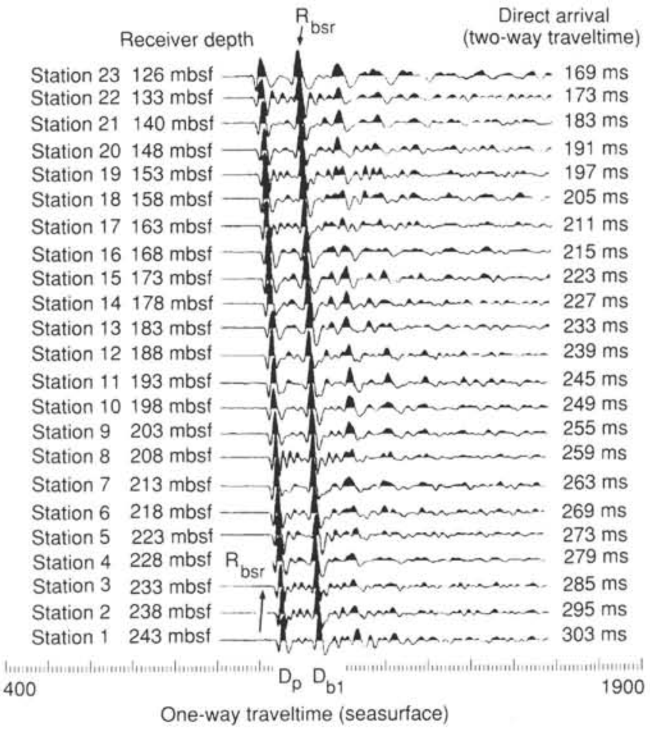

Figure 93. Stacked VSP data. Receiver depth and two-way traveltime for the direct arrival are shown. The reflected arrival corresponding to the BSR (R_{bsr}) begins just beneath receiver station 5 at 224 mbsf and moves out uphole between the direct arrival (D_p) and downgoing bubble pulse (D_{b1}).

heterogeneity. More importantly, free gas as indicated by low velocities beneath the BSR in the VSP data is subdued or absent in the sonic log and sonic-based synthetic seismogram, but creates a BSR-like reflector in the VSP-based synthetic seismogram.

Core, Log, and Seismic Integration

The high-accuracy curve of traveltime vs. depth (Fig. 92) allows the correlation of geologic phenomena to the seismic-reflection data. Reflectors caused by sedimentary layering can be traced between Holes 889B and 889A, consistent with the lithologic similarity of the cored intervals in the two holes. Overall, the seismic data show that the slope basin fill is less disturbed by faulting at Hole 889B than at Hole 889A (Fig. 95). Specifically, the seismic data around Hole 889A show a little-deformed layered sedimentary sequence overlying layered sediments cut by many small faults. The onset of faulting seen in the seismic section (about 97 mbsf) lies slightly above the boundary between structural Domains I and II (104 mbsf; see "Structural Geology" section, this chapter). The biostratigraphically defined hiatus occurs at 87 mbsf, about 10 m above the onset of faulting, whereas the reworked interval identified in the cores occurs just beneath (see "Biostratigraphy" and "Lithostratigraphy" sections, this chapter). Gravity deposits such as debris flows and missing sections are consistent with the observed faulting, because highs created by faulting induce transport of sediment, and scouring and nondeposition occur around topographic irregularities. The BSR is at 224 m sub-bottom depth.

Formation MicroScanner Data

The Formation MicroScanner (FMS) tool made two passes at speeds of about 550 m/hr in Holes 889A and 889B. The tool was run in Hole 889A from 64 to 252 mbsf; Hole 889B was logged from 91 to 250 mbsf. The images are degraded because of the large hole diameter, but some features can be interpreted by immediate examination. A detailed interpretation of the images will require correlation to other logs and core data.

The large hole size and lack of pronounced resistivity variations associated with bedding precluded determination of bedding inclinations with any confidence, although in Hole 889A the FMS images show steeply inclined, sharp contrasts between the conductive (dark) layers and the resistive (light) layers. As noted previously (see "Correlation of Logs to Lithostratigraphic Units," this section), small-scale variations in resistivity are positively correlated with variations in gamma-ray values, suggesting that resistive layers are more clay rich. The boundaries between layers are irregular and have a sinusoidal shape in places, indicating a dipping bedding surface (Fig. 96).

In Hole 889B the images are mottled or speckled throughout the interval from 110 to 228 mbsf, with conductive surfaces bounding sharply angular, resistive areas suggesting pervasive fracturing and elongated or wavy conductive features (possible mud clasts). Rounded and elongated resistive features, suggestive of nodular concretions or pebbles, begin to appear at 122 m sub-bottom depth (Fig. 97) and increase in abundance downhole.

The FMS correlates well with the structural information in the cores, showing high concentrations of planar conductivity fabrics in structural Domains II and III (see "Structural Geology" section, this chapter). Hole 889A appears to have more planar high- and low-conductivity features (bedding plane fractures) than Hole 889B. Throughout Hole 889A these planar features dip westward at angles ranging from 42° to 64°. If the features represent fractures, conductive fractures are probably water filled, whereas the resistive fractures must be filled with either mineral cement (calcite, dolomite) or hydrate. The images also contain patterns of planar features crossing at a high angle, perhaps representing conjugate fractures, and patterns resembling microfractures (Fig. 98). Within lithostratigraphic Sub-unit IB this resistivity fabric could represent debris flows or slumps (Fig. 99).

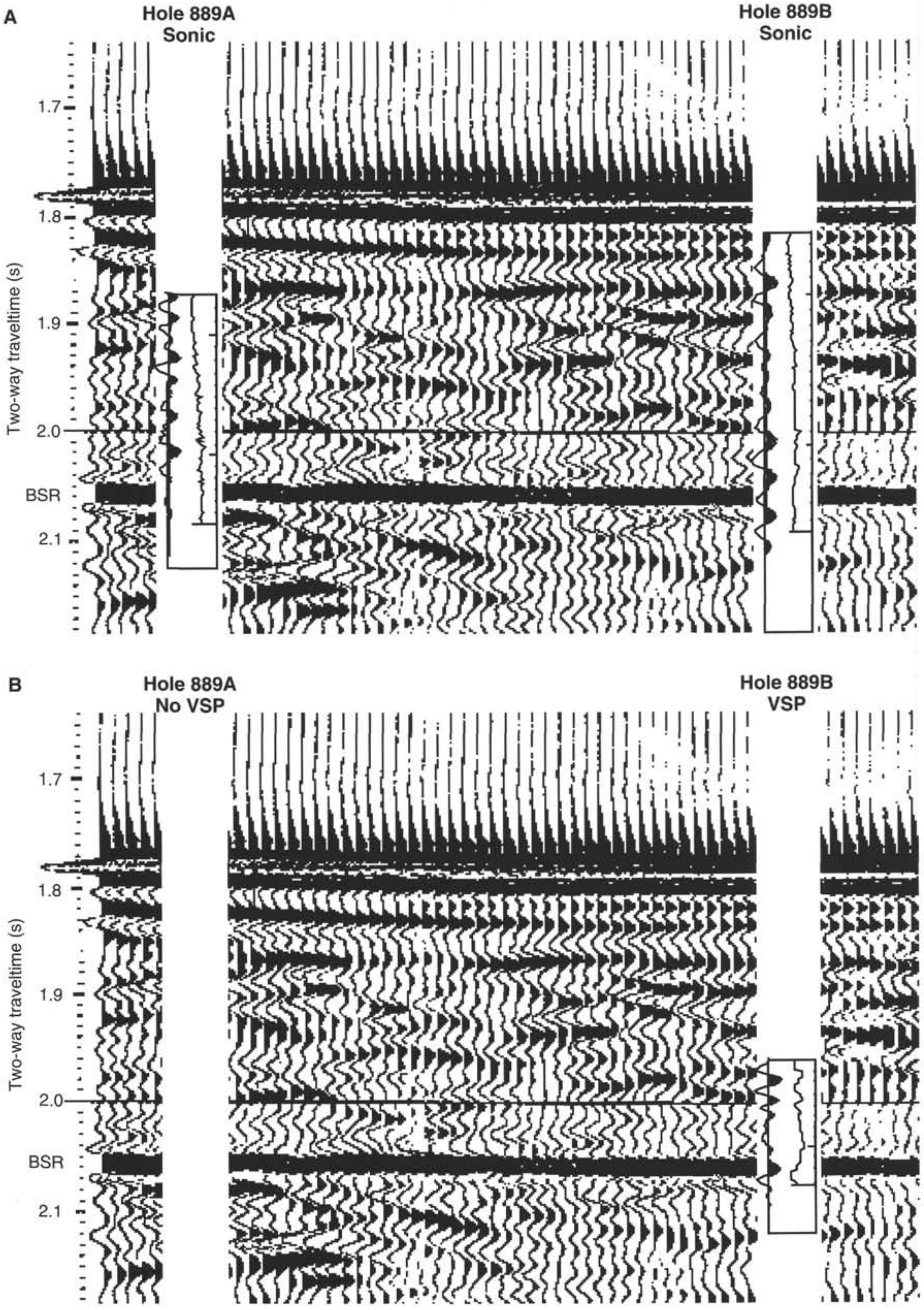

Figure 94. **A.** Synthetic seismograms based on sonic logs from Holes 889A and 889B, superimposed on the seismic section. Constant density is assumed. Velocity log is shown to the right of the synthetic seismogram. **B.** Similar display of a synthetic seismogram based on VSP interval velocities from Hole 889B, with log of interval velocities shown to right. Note that the sonic-based synthetic seismograms are a fair to poor match for the seismic data, whereas the VSP-based synthetic seismograms provide a good match, particularly at the BSR.

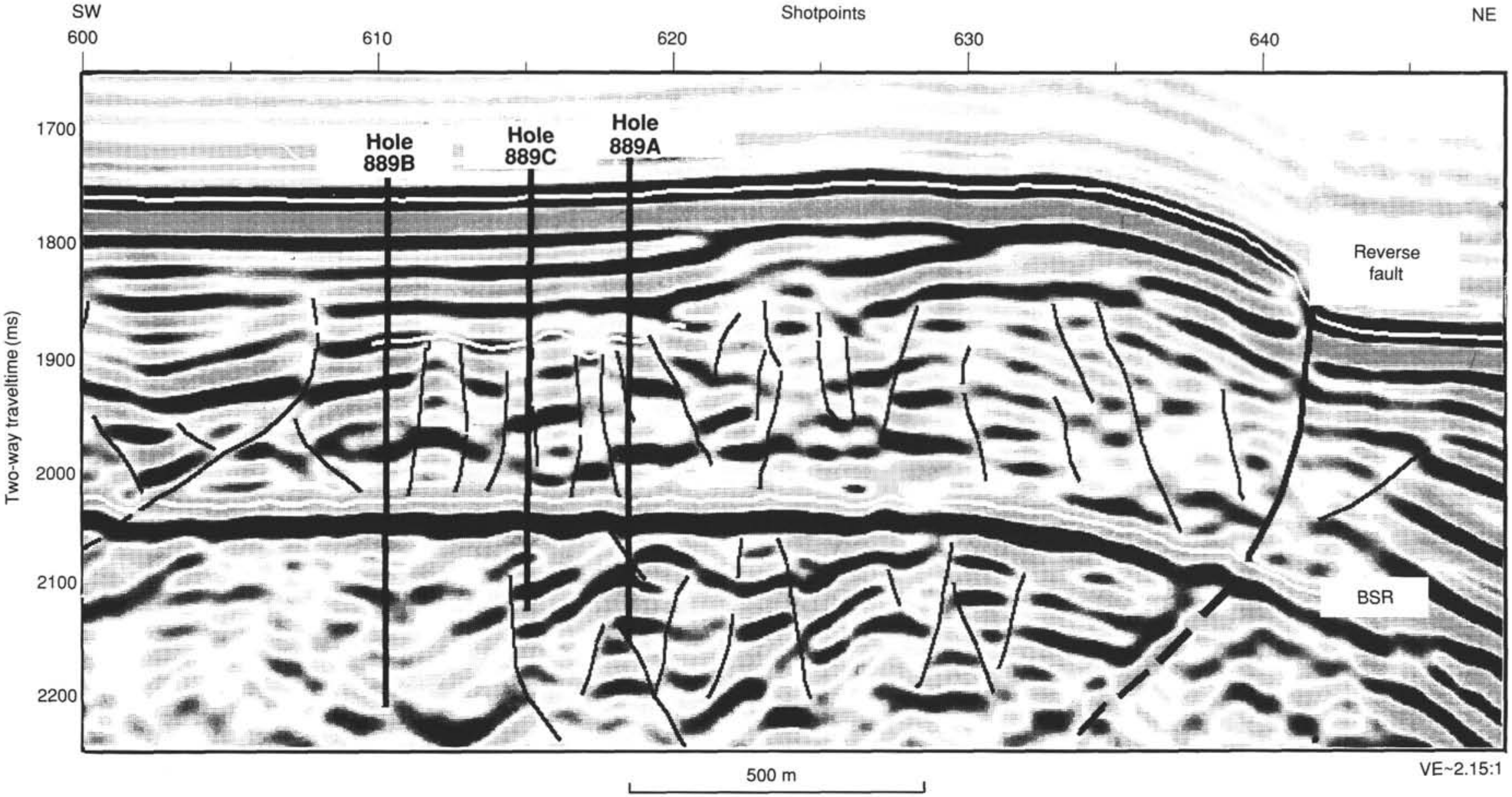

Figure 95. Detail of seismic line 89-08 showing hole locations and depth penetrations. Depth conversion scale is created from a traveltime-depth curve. The reverse fault on the right side of the section bounds a major slope basin. The widely distributed minor faulting beneath the drill holes was probably caused by movement of the hanging wall over irregularities in the footwall of the reverse fault. The reflector marked in white at about 1880 ms separates planar and faulted reflectors. The biostratigraphically defined hiatus occurs just above this reflector, whereas the reworked interval occurs just beneath (see "Biostratigraphy" and "Lithostratigraphy" sections, this chapter). Note that the reflectors and presumably the sedimentary layering can be traced from Holes 889B to 889A, although the section is more faulted at Hole 889A.

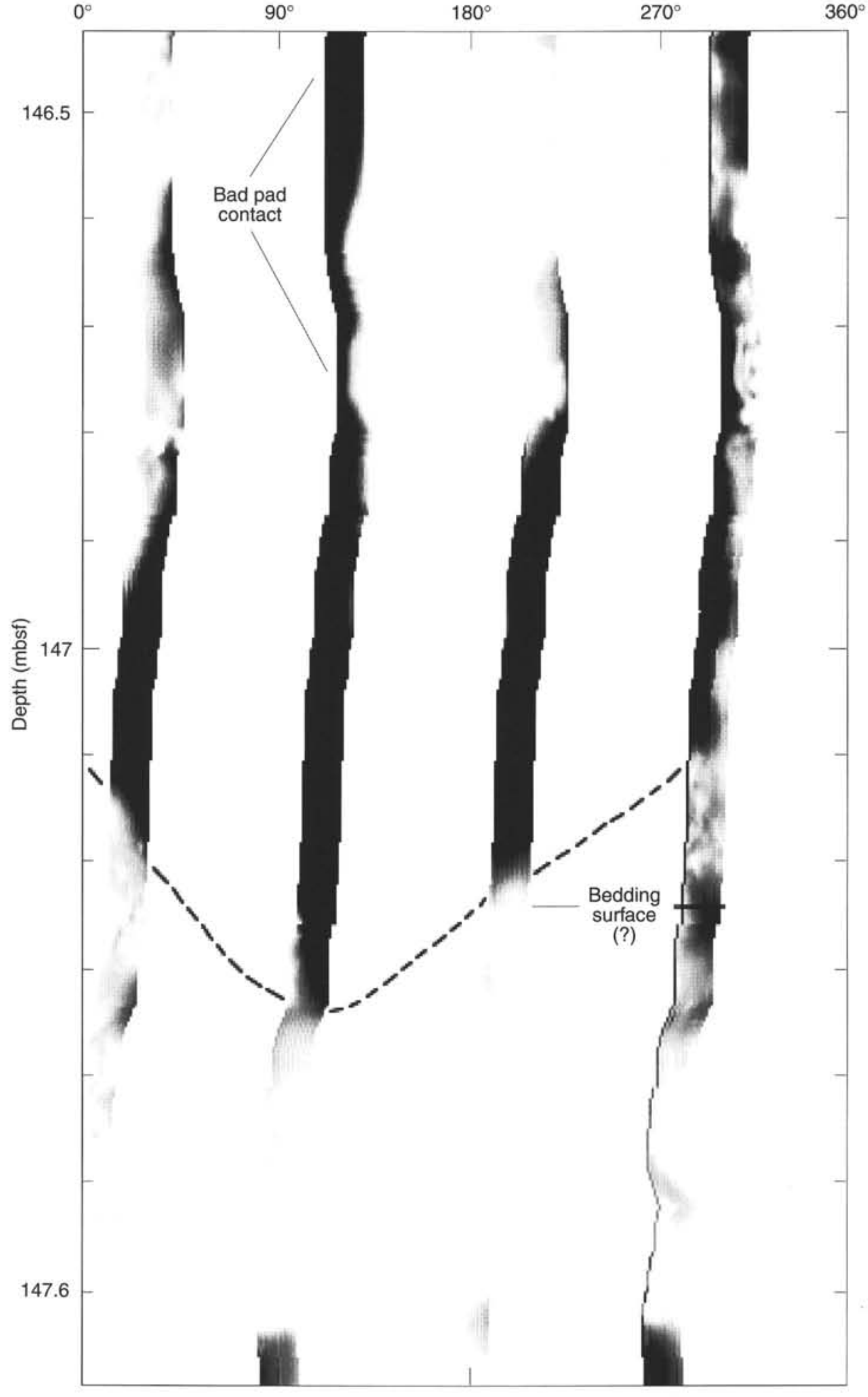

Figure 96. Formation MicroScanner (FMS) image demonstrating irregular, steeply inclined bedding surfaces and contrasts of resistive and conductive layers in Hole 889A. The base of the dark sinusoidal feature marks a bedding surface.

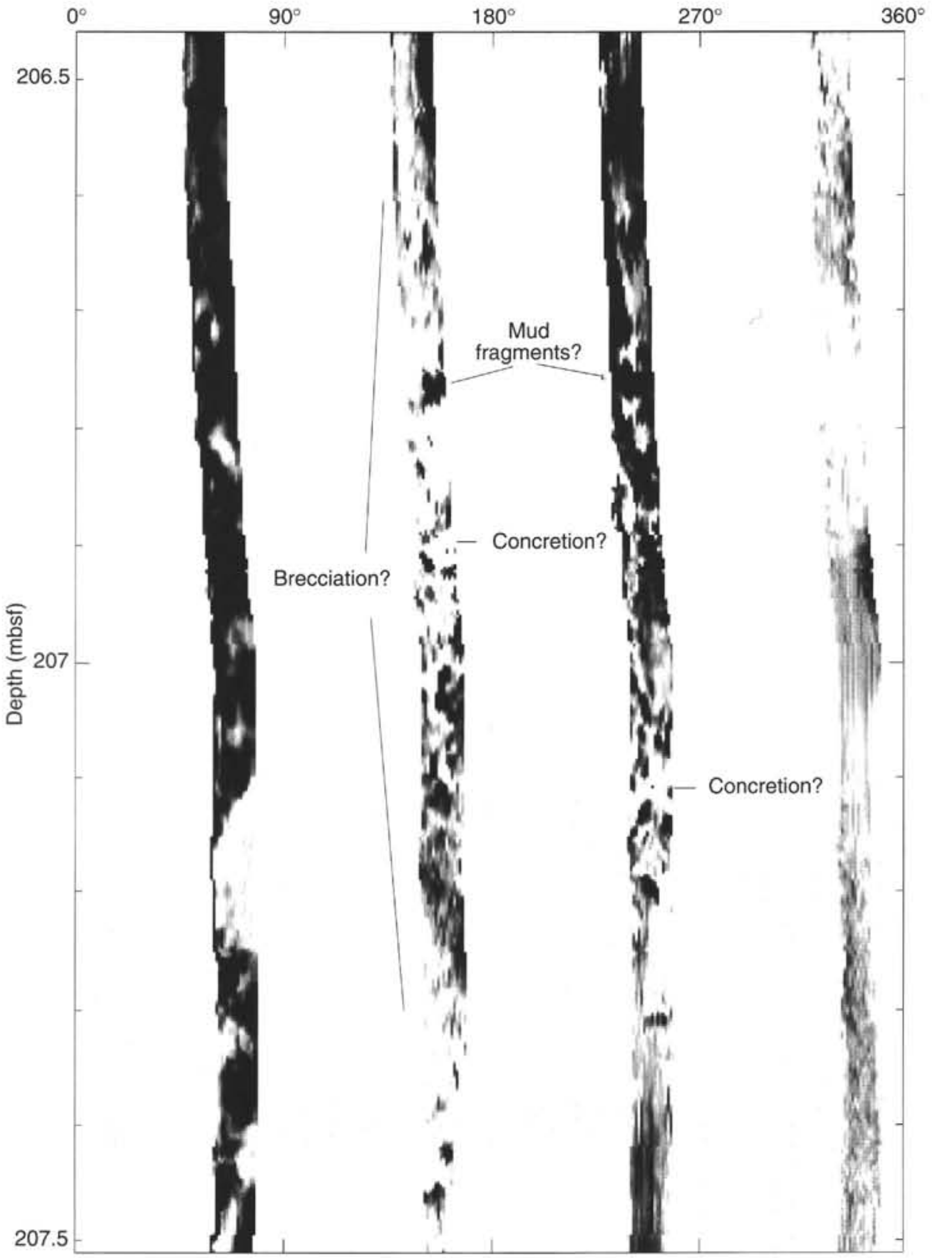

Figure 97. The mottled conductive/resistive FMS image in Hole 889B possibly indicates pervasive fracturing, mud clasts, and nodular concretions. The mud clasts are distributed within resistive sediments.

At 250 mbsf in Hole 889A and 242 mbsf in Hole 889B, the FMS image changes abruptly downhole from relatively resistive to relatively conductive. This transition is also observed on the resistivity log (Fig. 86). Fourteen meters higher at 236 and 228 mbsf in Holes 889A and 889B, respectively, the layers are mottled, changing from high-resistivity zones to mixed-resistivity zones from 236 to 240 mbsf in Hole 889A and from 228 to 232 mbsf in Hole 889B (Fig. 100). This mixed zone shows many resistive planar and nodular fabrics along with almost an equal amount of conductive polygonal and planar shapes. The region below 250 mbsf in Hole 889A and 242 mbsf in Hole 889B exhibits the highest conductivity observed throughout the entire site.

Temperature

The LDGO temperature tool was run at the bottom of the geophysical tool string in Holes 889A and 889B and on the VSP tool string in Hole 889B. The results are presented in Figure 101. Depths were calculated from pressures recorded by the temperature tool. Because the hole temperatures were reduced by circulation during coring and by hole conditioning immediately before logging, it is difficult to infer an equilibrium thermal profile from these logging runs. Our recorded maximum temperatures of 9° and 13°C at Holes 889A and 889B, respectively, are therefore minimum estimates of equilibrium temperature. The ADARA and WSTP measurements at this site indicate a thermal gradient of about 54°C/km and a bottom-water temperature of 2.7°C (see "WSTP and ADARA Temperature Measurements" section, this chapter). Temperature logging measurements of bottom-water temperature for both holes agree well with the ADARA measurements.

The temperature tool was run primarily to detect any fluid flow that may be present. The temperature patterns in the upcoming logs exhibit evidence of thermal lags resulting from a mud-clogged end-sub. The downgoing logs are probably minimally affected by mud clogging. The

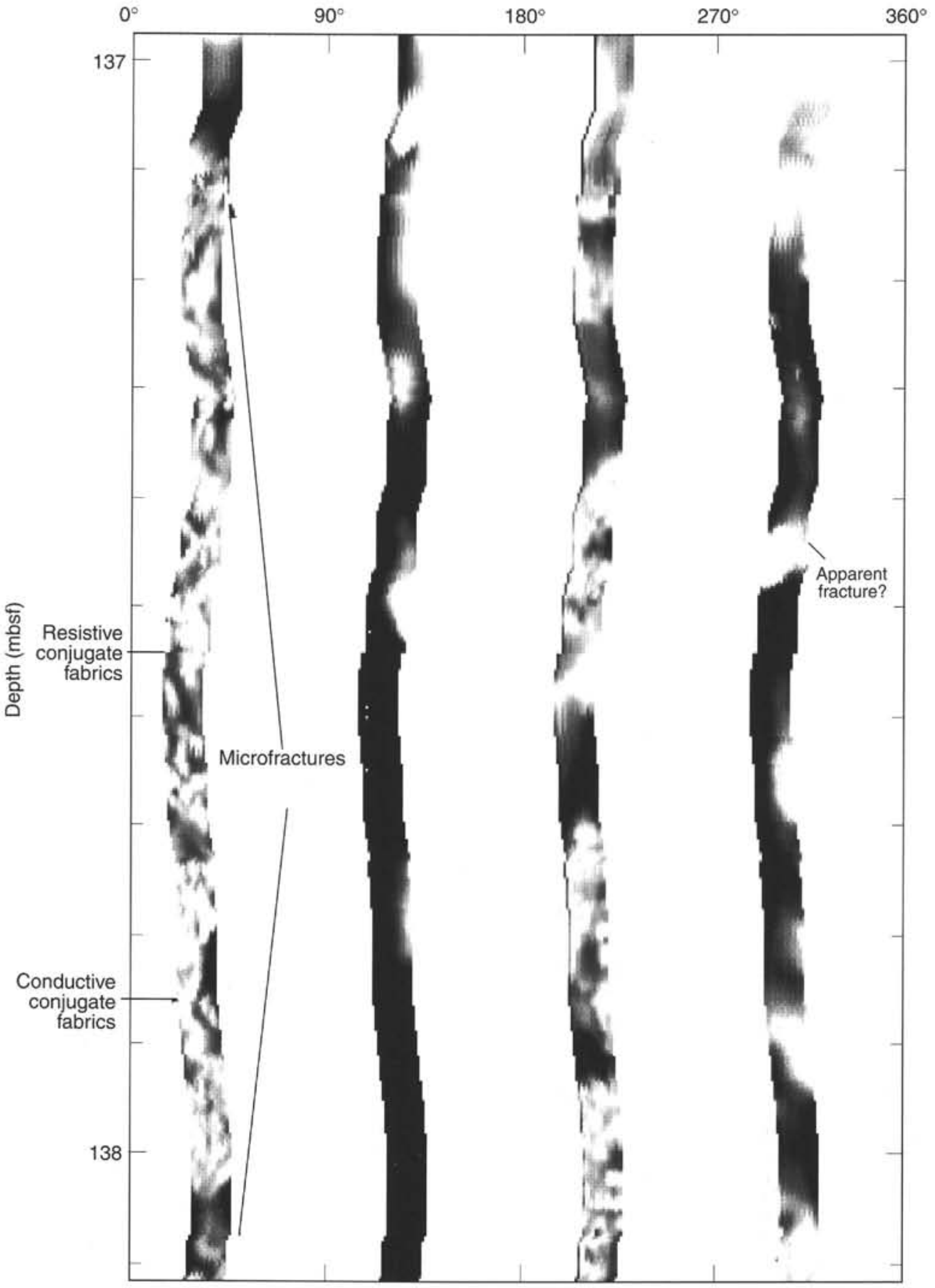

Figure 98. This FMS image from Hole 889A strongly exhibits fracture-like fabrics and conjugate linear fabrics of resistive and conductive materials. Also in evidence throughout the entire image are patterns of deformation that resemble microfolds and microfractures.

pattern in Hole 889A indicates that temperature increases approximately linearly between the base of pipe and the bottom of the hole with a break in slope at approximately 230 mbsf. In Hole 889B, a break in slope is observed at approximately 170 mbsf in the downgoing log and 140 mbsf in the upcoming log. A possible explanation for the change in slope in Hole 889B may be a flux of warmer fluids into the borehole.

SUMMARY AND CONCLUSIONS

Sites 889 and 890 (prospectus Site VI-5) are located on a 15- to 20-km-wide region of gently undulating seafloor on the continental slope off Vancouver Island, in water depths of 1315 and 1326 mbsl, respectively. Coring at both sites (Fig. 104) began in bedded, slope-basin sediment, and at Site 889 extended into the underlying, deformed sediments of the accretionary wedge. Site 890 was drilled only to 50 mbsf to sample the near-surface sediments. A major objective at Site 889 was the definition and characterization of a well-developed BSR at approximately 225 mbsf. Holes 889A, 889B, and 889C penetrated that reflector. An instrumented borehole seal (CORK) was emplaced in Hole 889C to provide long-term observation of the distribution of temperature through the gas hydrate zone inferred to overlie the BSR and to enable hydraulic testing and pore-water sam-

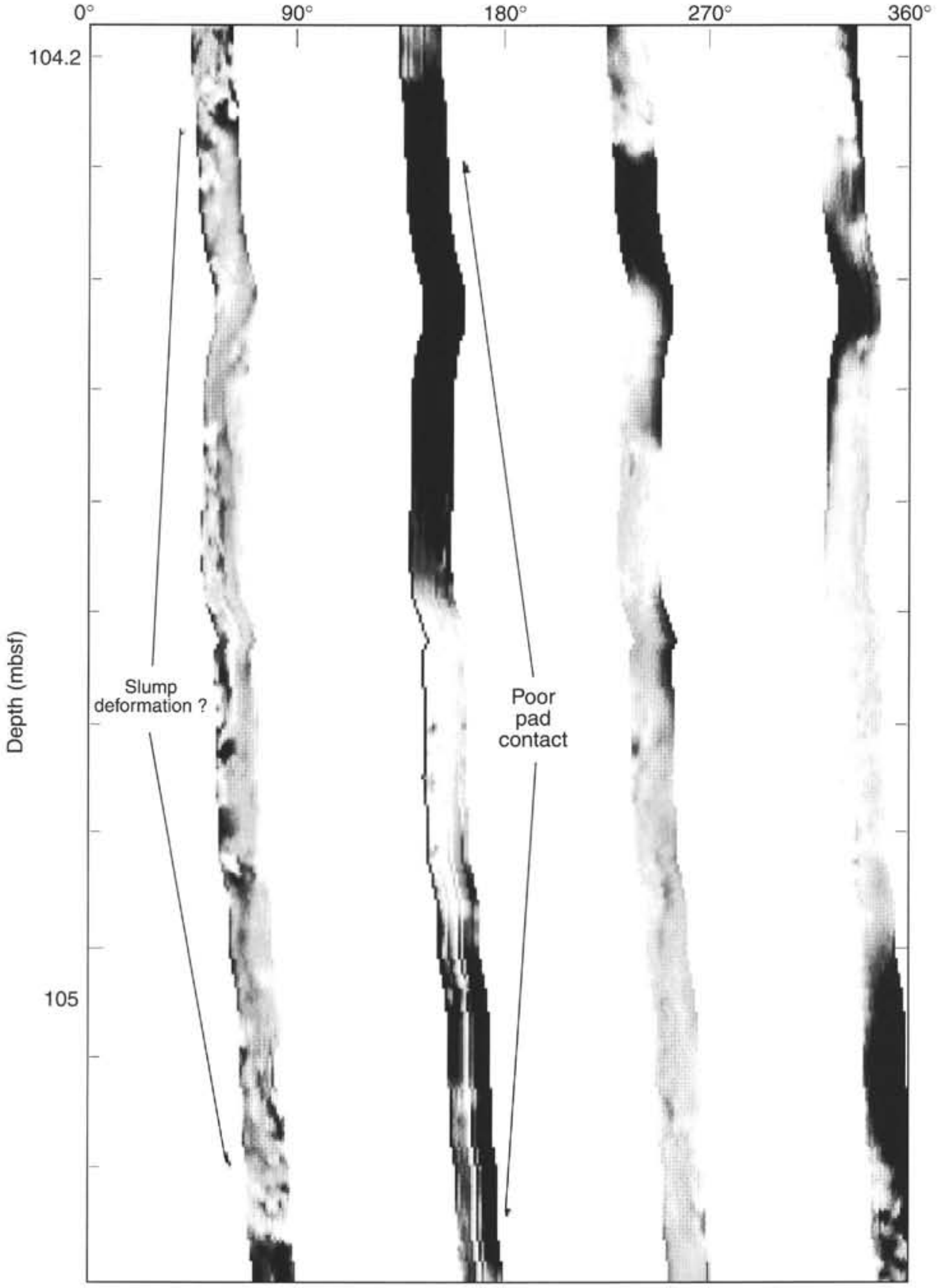

Figure 99. An FMS image from the top of the data set in Hole 889A that illustrates a pattern of deformation that could be caused by a slump, but only in the first and third pads out of the four. Bad pad contact in the enlarged borehole has degraded the record from the other two pads.

pling of the region beneath the BSR, from which it has been hypothesized that the gas hydrate is fed by ascending pore-water enriched in methane (Hyndman and Davis, 1992).

Preliminary biostratigraphic data indicate that sediments at Sites 889 and 890 range in age from late Quaternary to late Pliocene. There is a hiatus in the record at 87 mbsf, separating upper Quaternary from lower Pleistocene deposits. Most sediments at Sites 889 and 890 represent deposition in a middle bathyal environment; however between 92 and 113 mbsf, lower bathyal foraminifer species are common, suggesting uplift of this portion of the sequence or the deposition of allochthonous, reworked sediment.

Three lithostratigraphic units were recognized at Site 889. Unit I includes clayey silts, fine sands, and diagenetic carbonates and extends from the surface to a depth of 128.0 mbsf in Hole 889A. Unit II is compositionally similar to the lower portion of Unit I, but is noticeably more consolidated than the overlying unit and is highly fractured. Unit II extends to 301.5 mbsf. At greater depths, a greatly increased glaucony content is taken as the defining characteristic of Unit III.

Unit I is divided at Site 889 into Subunits IA and IB, largely on the basis of the proportion of turbiditic sand present. Subunit IA (0–91.5 mbsf, Hole 889A) is dominated by homogeneous or laminated clayey silt near the seafloor, but sands rich in volcanic glass and lithic fragments become increasingly common downsection. Most cores in this interval showed deformation associated with gas expansion. Subunit IB (91.5–128.0 mbsf, Hole 889A) exhibits a marked reduction in sand layers and consists largely of fine silt. Clasts of mud are common and are usually mixed with pebbles, concretions, and shell fragments, in what appear to be matrix-supported debris-flow

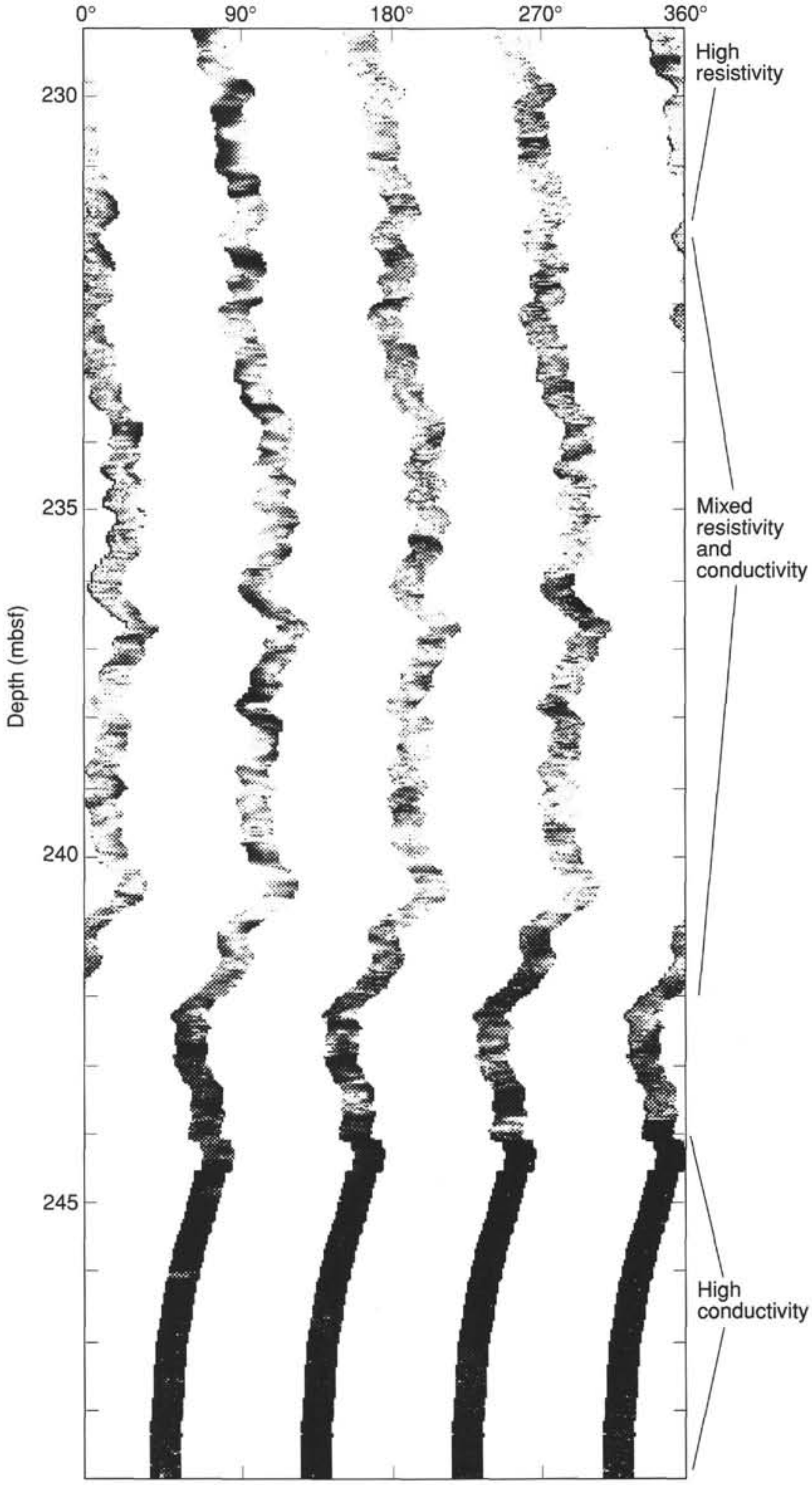

Figure 100. This compressed version of the FMS image from 229 to 249 mbsf in Hole 889B demonstrates the high-resistivity, the mixed resistivity/conductivity, and the high-conductivity intervals within this section. Because of the image compression, the linear and nodular resistive features are not as apparent here as they are in the standard 1:6 horizontal and vertical scale; this image is designed to show the overall changes in resistivity and conductivity only.

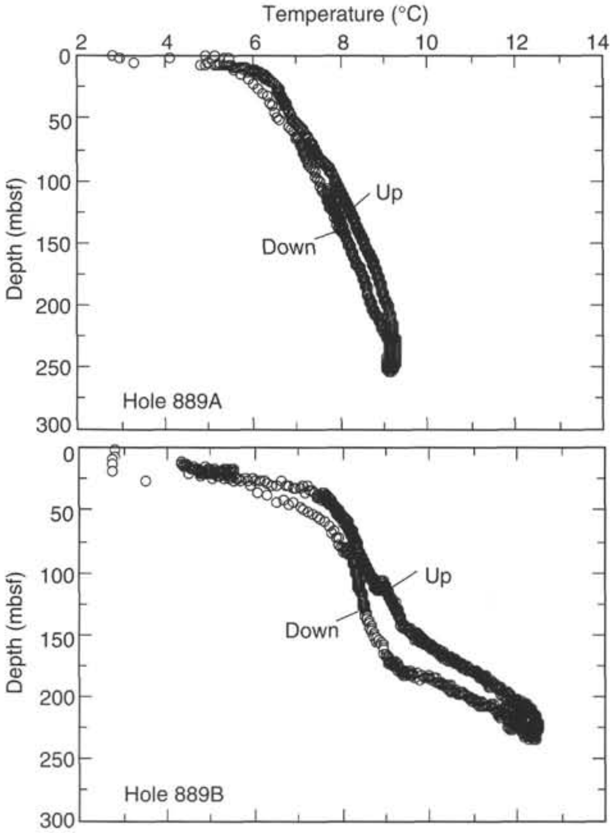

Figure 101. Temperature logs as a function of depth for Holes 889A and 889B.

deposits. Overall, Unit I consists of slope and slope basin sediments, comprising hemipelagites, turbidites, and mass-flow deposits.

Unit II (128–300 mbsf, Hole 889A; lower boundary at 307–312 mbsf, Hole 889B) is defined at its upper boundary by an unusually sharp increase in consolidation that is manifested by small-scale fracturing of the sediment. The closely spaced fractures observed in the cores may be induced by drilling, but the sediment fragments commonly interlock and the fractures appear to reflect the development of an in-situ shear fabric. Diagenetic carbonates occur throughout the section, although their original position is uncertain as they were commonly recovered either in the core catcher or at the top of the cores. Carbonate is more prevalent in Hole 889B, where a 30-cm-thick acumulation was penetrated and sampled at 258 mbsf. Some sections of Unit II were fluidized; their occurrence was concentrated between 128 and 260 mbsf. Unit II is thought to consist of abyssal plain silts and clays that were fractured postdepositionally, during accretion.

Unit III (>300 mbsf, Hole 889A; 307–312 mbsf, Hole 889B) contained up to 60% glaucony, which occurred as authigenic pellets, coatings, and clays and as rounded, allogenic grains. Carbonate concretions were also observed. Unit III deposits appear to be abyssal plain deposits like those in Unit II above, but the abundant authigenic glaucony suggests deposition under suboxic, low accumulation rate conditions.

Postdepositional structures were difficult to recognize in most cores, as drilling disturbance was considerable in all holes. However, three structural domains were delineated. Structural Domain I (0–104 mbsf, Hole 889A) is dominated by subhorizontal bedding, with little apparent deformation of the slope basin sediments. In structural Domain II (104–127 mbsf, Hole 889A) widely separated sand/silt beds dip 40°–70° to the west. From 127 to 150 mbsf (structural Domain III, Hole 889A), small-scale fractures become increasingly closely spaced. Below 150 mbsf, fractures are pervasive and produce well-developed angular fragments that commonly exhibit an interlocked geometry. Some of the fragment surfaces are polished and slickensided. The dominant fracture fabric dips 45°–60°. Healed fractures and deformation bands were observed only twice in cores from Site 889, but their orientation parallel to the open fracture pattern substantiates the conclusion that fractures in the cores, although opened in the drilling process, are natural features of the lower sediment column. Because fractures are ubiquitous in Domain III and no clear indicators of fault zones were recovered, we infer that tectonic stress in the accretionary wedge sediments sampled at this site is accommodated largely by distributed strain.

The downhole variation in degree of consolidation, reflected in the degree of fracturing of the cores, is clearly delineated by the distribution of bulk density and porosity at Site 889 (Fig. 68). Unit I is characterized by normally consolidated deposits in which porosity declines regularly with increasing depth. Regression analysis indicates that mean porosity decreases from about 59% at the seafloor to 57% at 128 mbsf. The considerable variation (±11%) in porosity reflects the lithologic heterogeneity of these slope basin sediments. Between 128 and 160 mbsf (upper Unit II) the average porosity declines by about 5%. Porosity within Unit II declines from about 52% at 160 mbsf to 48% at 301 mbsf, although there are distinct excursions (see particularly 215–255 mbsf) to the general pattern associated with variations in diagenetic carbonate cementation and organic geochemistry (organic carbon content, methane, N, and S concentrations; Figs. 55 and 57). The position of the BSR falls within one of these excursions, where bulk density decreases irregularly from a peak of 2.07 Mg/m^3 at 215 mbsf to a low of 1.72 Mg/m^3 at 240 mbsf, but there is nothing unique about the interval. Lithostratigraphic Unit III exhibits an apparently anomalous increase in porosity with increasing depth.

The inorganic chemistry of the pore waters defines two distinct zones, the first of which is coincident with lithostratigraphic Unit I. Within this zone, sulfate declines to 0 at 10 mbsf (Fig. 64), increasing the alkalinity to 30 mM (from about 2.5 mM in seawater; Fig. 64). The loss of sulfate removes inhibition to carbonate deposition, and as a result Ca^{2+} and Mg^{2+} decrease significantly to 50 mbsf, as Mg/Ca increases from 2 to about 20 over the same interval (Fig. 64). This change promotes the deposition of dolomite and high-Mg^{2+} calcite as diagenetic cements and concretions. Concentrations of Cl$^-$ (Fig. 64) decline from 550 mM at the sediment/water interface to 363 mM at the base of chemical Zone 1 (130.0 mbsf), a dilution of 33%. The change in chlorinity is characteristic of a diffusion gradient, which must have persisted for a minimum of 1.6×10^5 to 2.1×10^5 yr. The base of Zone 1 is defined by a distinct minimum in Cl$^-$ and Mg^{2+}, with corresponding concentration maxima in Ca^{2+}, alkalinity, and NH$_4^+$ that clearly reflect an aquifer hydrologically connected to a deeper fluid source.

Zone 2 (130.0–386.5 mbsf) shows a nearly constant Cl$^-$ concentration of 370 mM. The concentrations of Na$^+$, Mg^{2+}, and phosphate are also nearly constant, indicating that the low Cl$^-$ concentration is a dilution effect. This dilution of 35% relative to seawater over such a large depth range is unusual. Although low-Cl$^-$ fluids might be derived by lateral advection from land, by dehydration of hydrated mineral species at depths greater than 1–2 km within the accretionary wedge, or perhaps by clay membrane filtration, the most probable source is the dissociation of gas hydrate disseminated within this interval. Dissociation of the hydrate would certainly occur upon retrieval of the cores, but it may also have occurred in situ, following an increase in temperature that is sufficiently recent (a few thousand years) for the low chlorinity not to have been dispersed by diffusion or by fluid advection. The degree of dilution suggests that less than 40% of the pore volume is filled with hydrate, assuming an average porosity of 45%. Below 300 mbsf, increases in the gradients of concentration of calcium and silica, and a decrease in potassium, indicate diffusion or mixing with a deeper seated fluid.

Organic geochemistry in lithostratigraphic Unit I (0–128.0 mbsf) defines a region of elevated methane concentration (60×10^3 to 80×10^3 ppmv) below the sulfate-reduction zone. Methane declines with considerable variability to $<30 \times 10^3$ ppmv at the base of the unit (Fig. 57). Over this same interval, ethane and propane are essentially absent and the C_1/C_2 ratio is $>10^3$, indicating that the methane is biogenic. A small spike (33 ppmv) in ethane concentration at 129 mbsf (associated with the Cl^- minimum) confirms a deeper source for the fluids sampled at this level.

Gas compositions change markedly in the interval 130–247 mbsf. Headspace samples contained 30×10^3 to 77×10^3 ppmv methane, 5–35 ppmv ethane, and 0.5–3.4 ppmv propane. For methane and ethane, the upper boundary of this interval is defined by a rapid increase in concentration downhole, and the lower boundary by a concentration reduction (Fig. 57).

At greater depths (247–338 mbsf, Hole 889A; 310–378 mbsf, Hole 889B), the methane concentrations become highly variable (10×10^3 to 70×10^3 ppmv); ethane increases markedly below 300 mbsf, and propane increases abruptly below 360 mbsf (Fig. 57). Within this interval, the C_1/C_2 ratio declines from values of about 2000 to <100, indicating a mixture of thermogenic and bacterially derived gas.

The general pattern of methane abundance described here for HS samples is approximated by the distribution of organic carbon and total nitrogen (Fig. 55). Total sulfur (Fig. 55), EVG nitrogen (Fig. 57) and EVG carbon dioxide (Fig. 60) exhibit vertical distributions that do not vary in sympathy with methane.

Both Holes 889A and 889B were logged with the geophysical and FMS tool strings; a VSP was run in Hole 889B. These data clearly define lithostratigraphic Units I and II. Unit I has low sonic velocities and resistivities owing to its high porosity. As defined by logging, the base of Unit I (126 mbsf, Hole 889A; 129 mbsf, Hole 889B), which is also the base of the debris-flow deposits, is a zone of particularly high porosity. Associated with this zone are the geochemical anomalies (Cl^-, Ca^{2+}, Mg^{2+}, S, N, methane, ethane) noted above. Within Unit II, locally high velocity and resistivity values correlate with low neutron porosity and indicate the presence of carbonate cementation (see, e.g., data set at 150, 190, and 213 mbsf in Figs. 86, 88, and 91). A major change in the resistivity of the wall of the borehole is defined by the FMS data between 240 and 250 mbsf (Fig. 100). In this zone, highly conductive

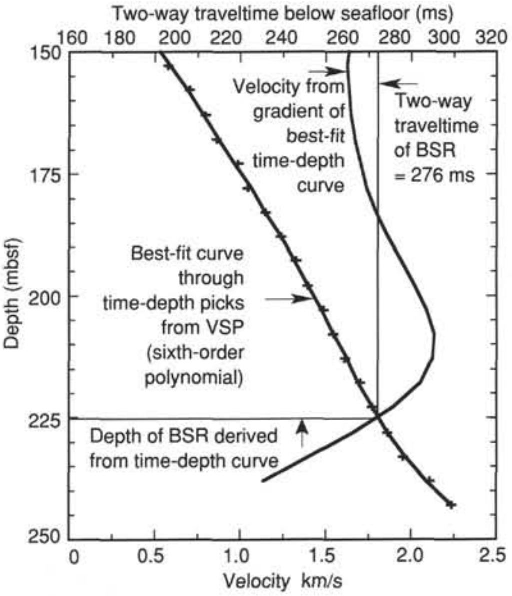

Figure 102. Plot of first arrival times of seismic waves (converted to two-way traveltime below seafloor) vs. depth of the downhole geophone in the vertical seismic profile experiment. From these data, the reflection time of the BSR below seafloor (276 ms TWT) is found to correspond to a depth of 225 mbsf. By a fitting a smooth curve through the time-depth points and differentiating it, the broad variation in velocity in the region of the BSR was derived. Velocity gently increases to a maximum at about 210 mbsf, beneath which it decreases with increasing steepness to a value of about 1.1 km/s at 238 mbsf. The velocities lower than 1.5 km/s could be caused by the presence of a small quantity of free gas (<5%) in the sediment. The increased velocity above the BSR could be produced by the presence of hydrate.

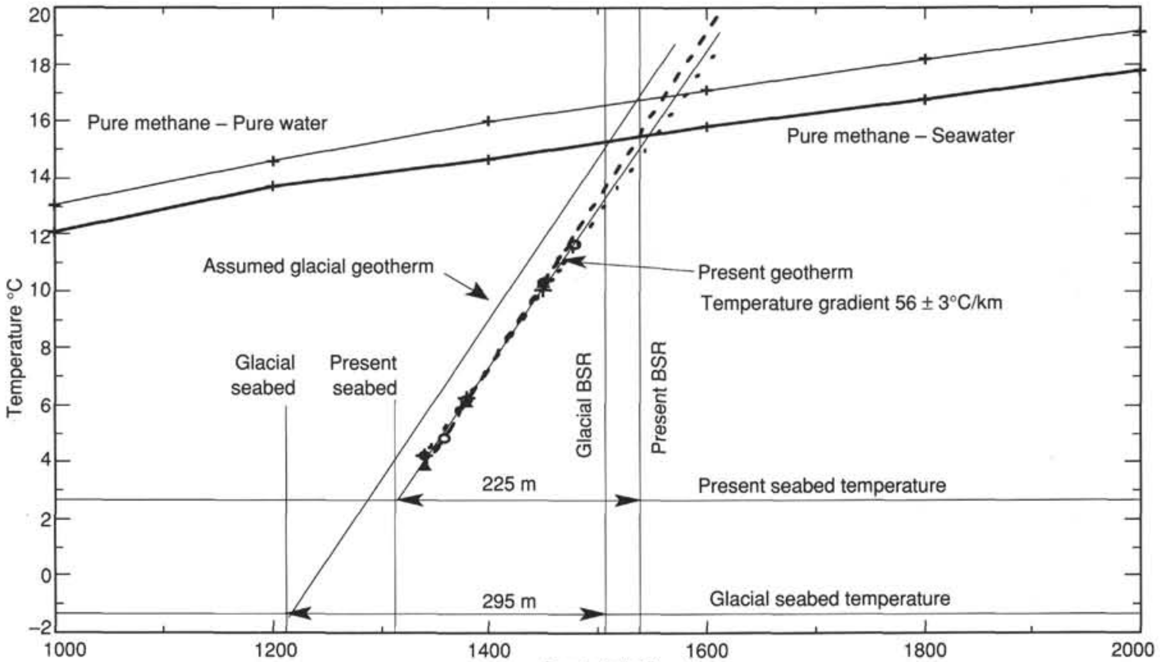

Figure 103. Plot of the temperature measurements made in Hole 889A, showing the best-fit linear gradient and limits of error (dashed lines). The boundaries of the stability fields of hydrate formed from pure methane and pure water and from pure methane and seawater are taken from Hyndman et al. (1992). Also illustrated is a speculative estimate of the thermal conditions during the last glacial period, with sea level lowered by 100 m and the seabed temperature at −1.3°C. Under the assumed glacial conditions, the BSR would have been at a depth of 295 mbsf, rather than the 225 mbsf of today.

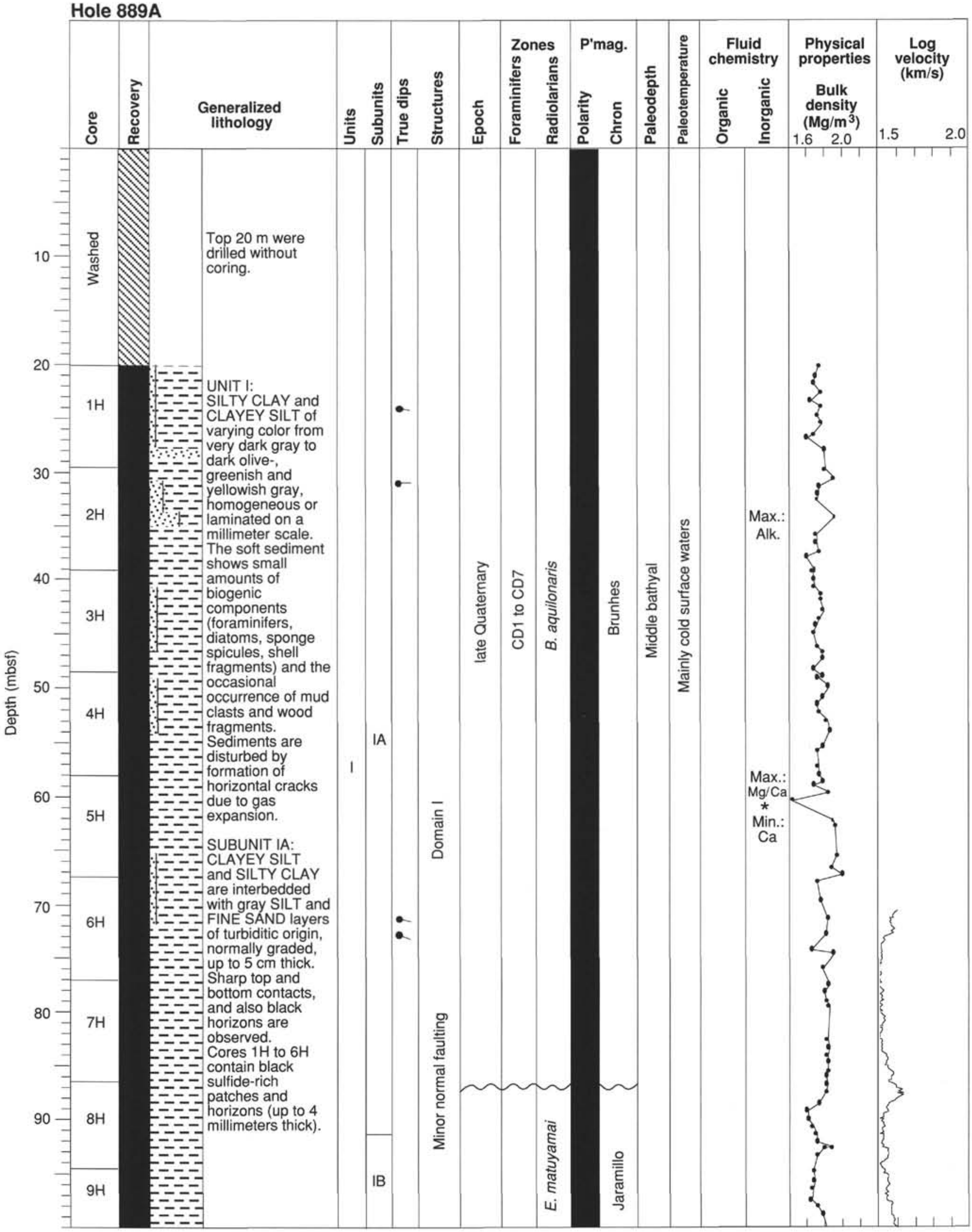

Top 20 m were drilled without coring.

UNIT I: SILTY CLAY and CLAYEY SILT of varying color from very dark gray to dark olive-, greenish and yellowish gray, homogeneous or laminated on a millimeter scale. The soft sediment shows small amounts of biogenic components (foraminifers, diatoms, sponge spicules, shell fragments) and the occasional occurrence of mud clasts and wood fragments. Sediments are disturbed by formation of horizontal cracks due to gas expansion.

SUBUNIT IA: CLAYEY SILT and SILTY CLAY are interbedded with gray SILT and FINE SAND layers of turbiditic origin, normally graded, up to 5 cm thick. Sharp top and bottom contacts, and also black horizons are observed. Cores 1H to 6H contain black sulfide-rich patches and horizons (up to 4 millimeters thick).

Figure 104. Master charts, Sites 889 and 890.

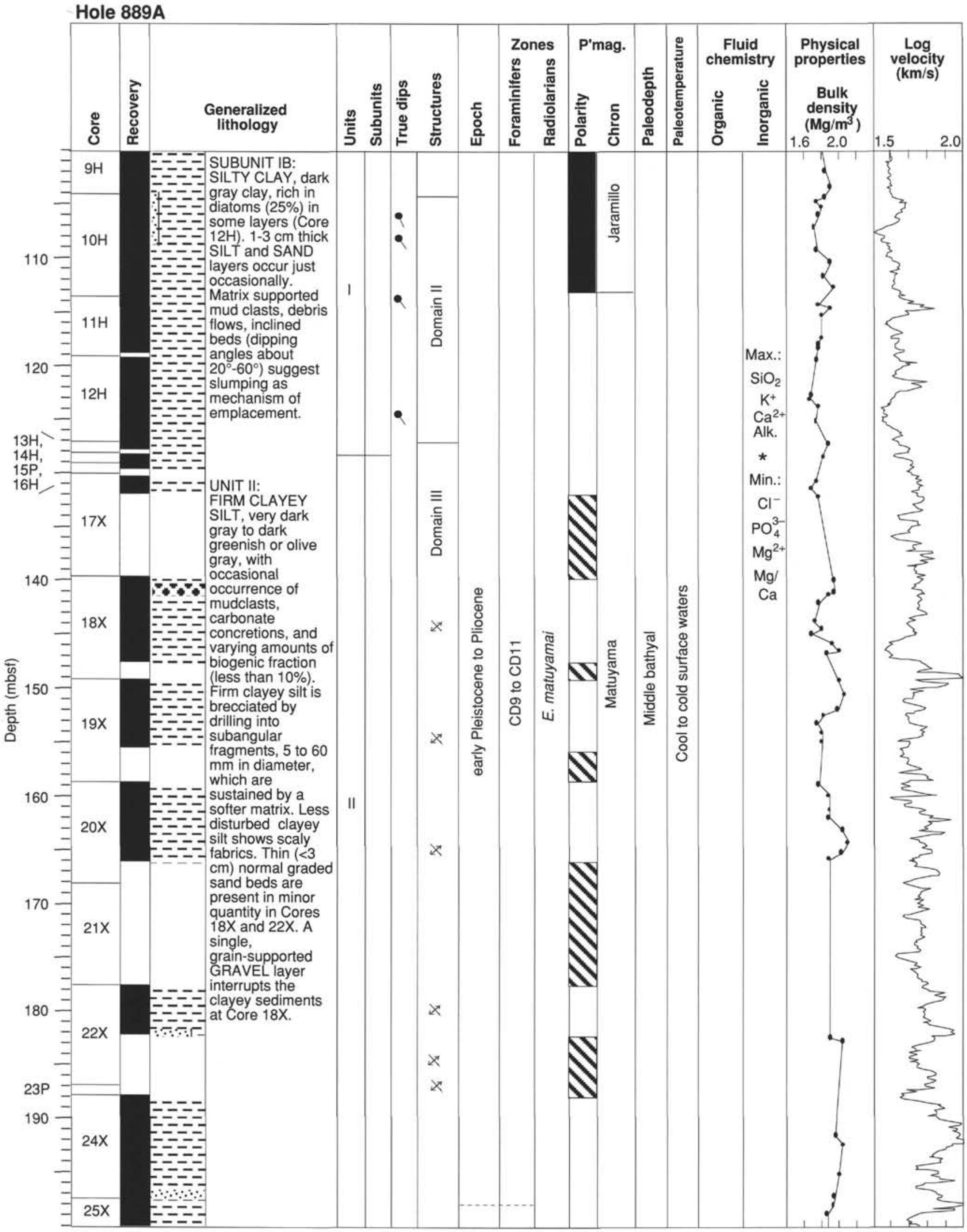

Figure 104 (continued).

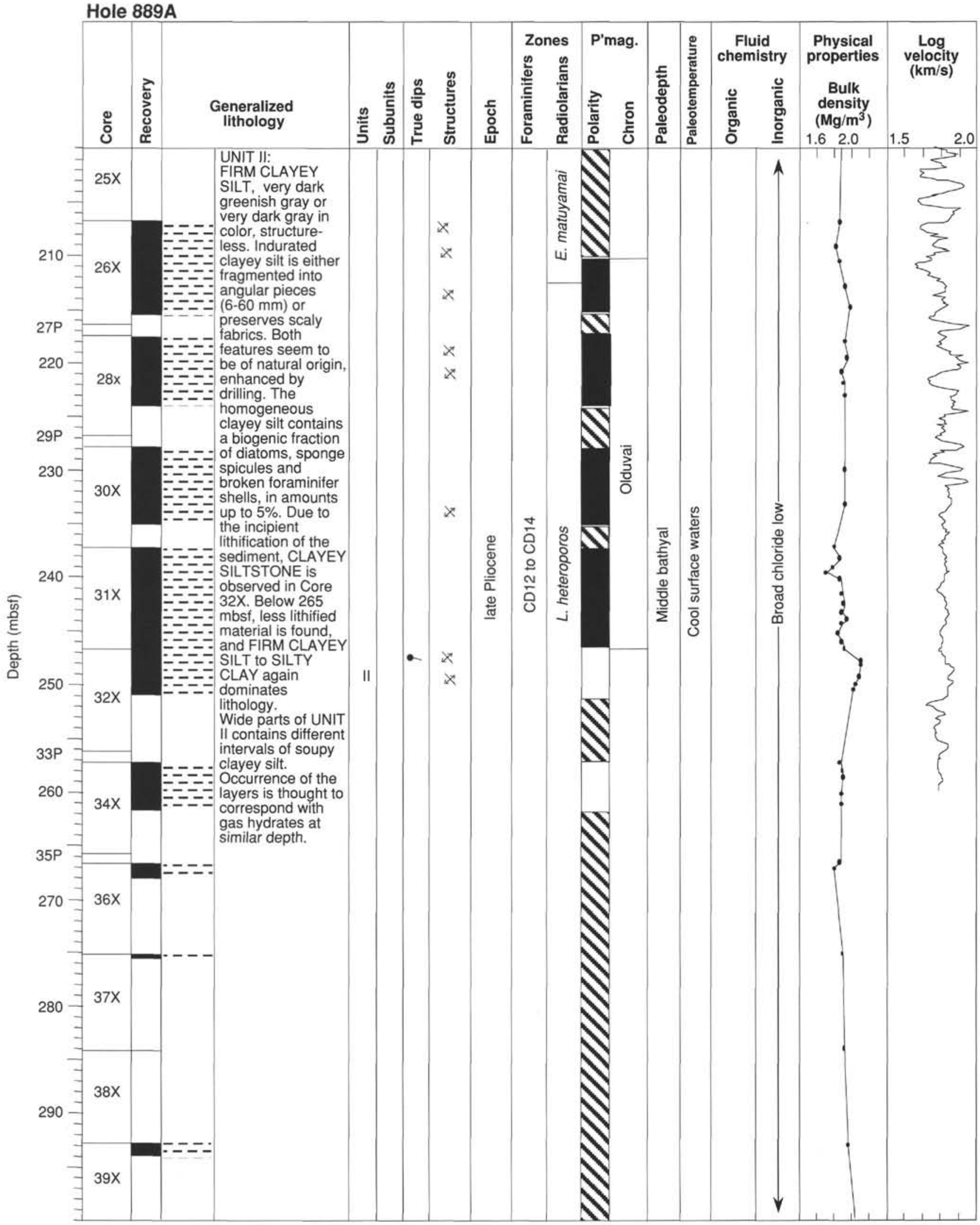

UNIT II:
FIRM CLAYEY SILT, very dark greenish gray or very dark gray in color, structureless. Indurated clayey silt is either fragmented into angular pieces (6-60 mm) or preserves scaly fabrics. Both features seem to be of natural origin, enhanced by drilling. The homogeneous clayey silt contains a biogenic fraction of diatoms, sponge spicules and broken foraminifer shells, in amounts up to 5%. Due to the incipient lithification of the sediment, CLAYEY SILTSTONE is observed in Core 32X. Below 265 mbsf, less lithified material is found, and FIRM CLAYEY SILT to SILTY CLAY again dominates lithology.
Wide parts of UNIT II contains different intervals of soupy clayey silt. Occurrence of the layers is thought to correspond with gas hydrates at similar depth.

Figure 104 (continued).

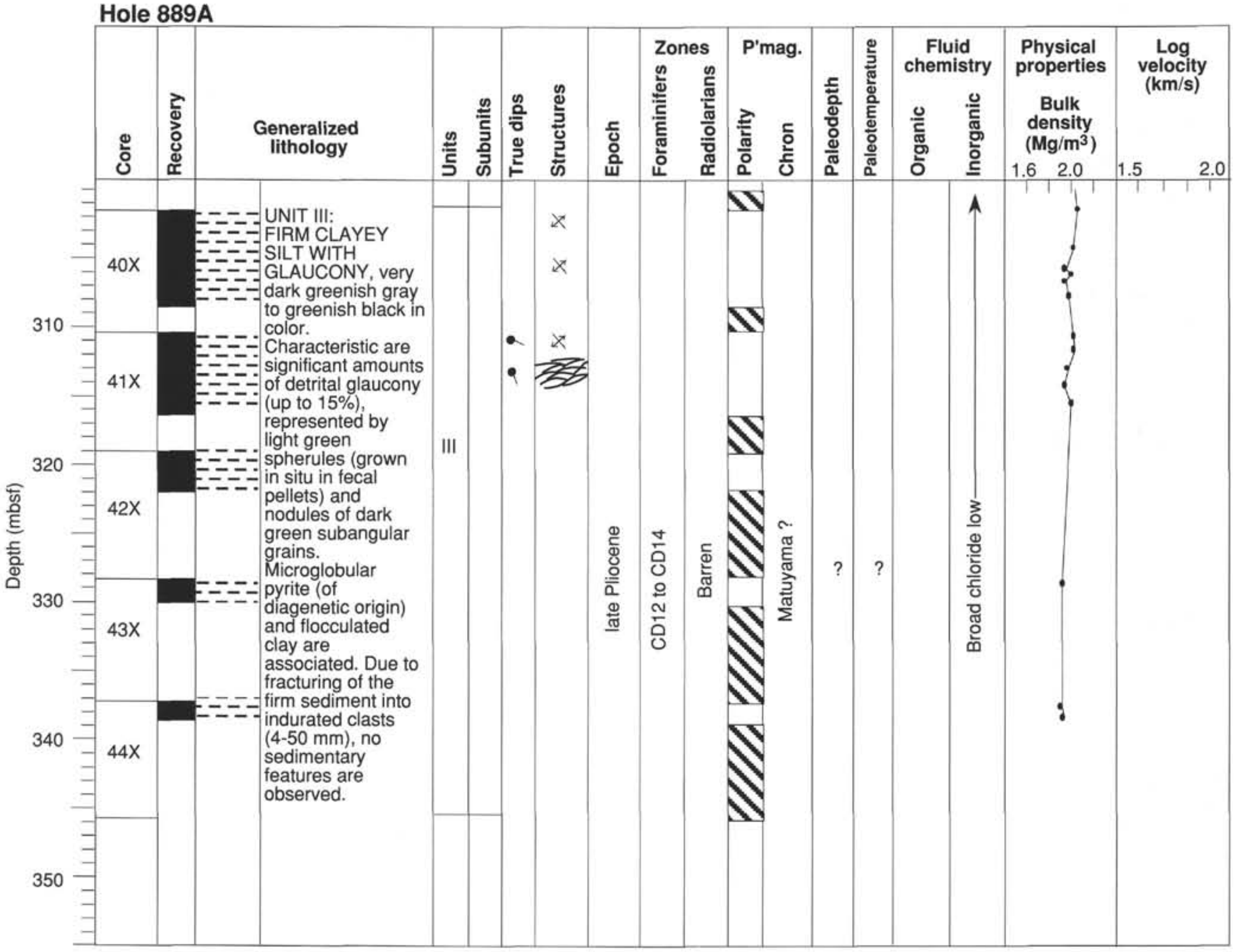

Figure 104 (continued).

deposits are overlain by mottled, resistive sediments. This change correlates with a marked downward decrease in methane concentration.

Six in-situ temperature determinations were made with the WSTP and ADARA tools (Fig. 80). Temperature increases linearly with depth, with a gradient of 54°C/km. Thermal conductivities measured on core samples are nearly constant at 1.15 W/(m · K), and yield an estimated heat flow of 62 ± 9 mW/m^2. This heat-flow value is significantly lower than surface heat-flow values of 84–110 mW/m^2 measured about 3 km to the south by Davis et al. (1990). The linearity of the temperature gradient implies conductive heat loss rather than advection. From the gradient, the base of the stability field for a hydrate formed from a mixture of pure methane and pure water (17°C at hydrostatic pressure) is predicted to be at 260 mbsf.

Temperature measurements made on the cores from Hole 889B showed that Core 146-889B-3R, taken from between 215.9 and 225.3 mbsf, had internal temperatures between –0.9° and –1.4°C, when measured shortly after its recovery on deck. Temperatures in subsequent cores were never less than 7°C. The low temperature of Core 146-889B-3R can be explained by the cooling effect of the dissociation of hydrate into methane and water. It was estimated from the latent heat of fusion of gas hydrate and the thermal capacity of the sediment that more than 8% of the pore space needed to have been occupied by hydrate to produce the measured temperature reduction (see "Gas Hydrate Studies" section, this chapter).

The BSR, commonly inferred to be the base of the gas hydrate stability field, at Sites 889 and 890 is shown at 276 ms TWT below the seafloor on the migrated seismic section. Time-depth curves derived from the sonic log and VSP place the BSR at 225 mbsf (Hole 889B). The sonic logs also indicate a tendency to shorter wavelength fluctuations above the BSR than below it, apparently as a result of fracturing in lithostratigraphic Unit II (Fig. 91). There is no evidence in the logs of massive hydrate accumulation. Instead, in the interval 10 m above the BSR (215–225 mbsf; Hole 889B), which is inferred to contain methane hydrate, sonic velocity is only slightly anomalous (high by 0.1 km/s), if the porosity derived from the sonic log is compared with porosity derived from the resistivity and neutron logs.

Although the sonic log does not exhibit a substantial decrease in velocity across the BSR, the VSP data define a distinct low-velocity zone beneath the BSR (Fig. 102). Velocities between 231 and 243 mbsf are lower than compressional-wave velocity in seawater (reaching 1100 m/s), and suggest the presence of small amounts (<5%) of free gas (Domenico, 1976). The disparity between the sonic log and VSP results may be attributed to flushing of the borehole wall by drill water, which could deplete the gas phase in the immediate vicinity of the borehole. In any case, the sonic log would not record velocities slower than that of the water filling the borehole. The difference in response between the sonic log and VSP is apparent in the synthetic seismograms produced from the sonic logs, which exhibit moderate (Hole 889A) to poor (Hole 889B) agreement with the seismic sections, and in both cases do not define a BSR (Fig. 94A). By contrast, the VSP-based synthetic seismogram reproduces both the general seismic section and the BSR well (Fig. 94B).

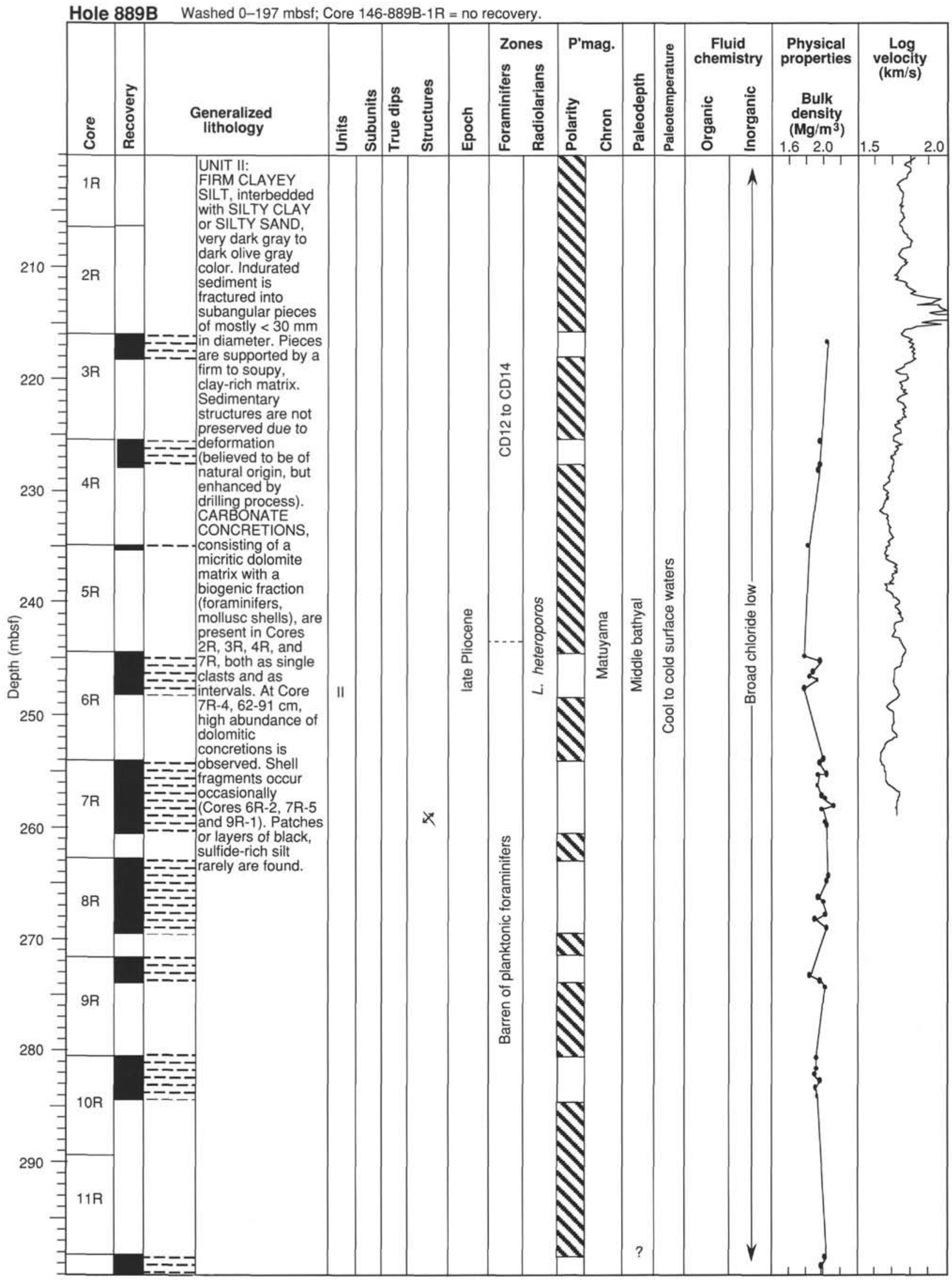

UNIT II: FIRM CLAYEY SILT, interbedded with SILTY CLAY or SILTY SAND, very dark gray to dark olive gray color. Indurated sediment is fractured into subangular pieces of mostly < 30 mm in diameter. Pieces are supported by a firm to soupy, clay-rich matrix. Sedimentary structures are not preserved due to deformation (believed to be of natural origin, but enhanced by drilling process). CARBONATE CONCRETIONS, consisting of a micritic dolomite matrix with a biogenic fraction (foraminifers, mollusc shells), are present in Cores 2R, 3R, 4R, and 7R, both as single clasts and as intervals. At Core 7R-4, 62-91 cm, high abundance of dolomitic concretions is observed. Shell fragments occur occasionally (Cores 6R-2, 7R-5 and 9R-1). Patches or layers of black, sulfide-rich silt rarely are found.

Figure 104 (continued).

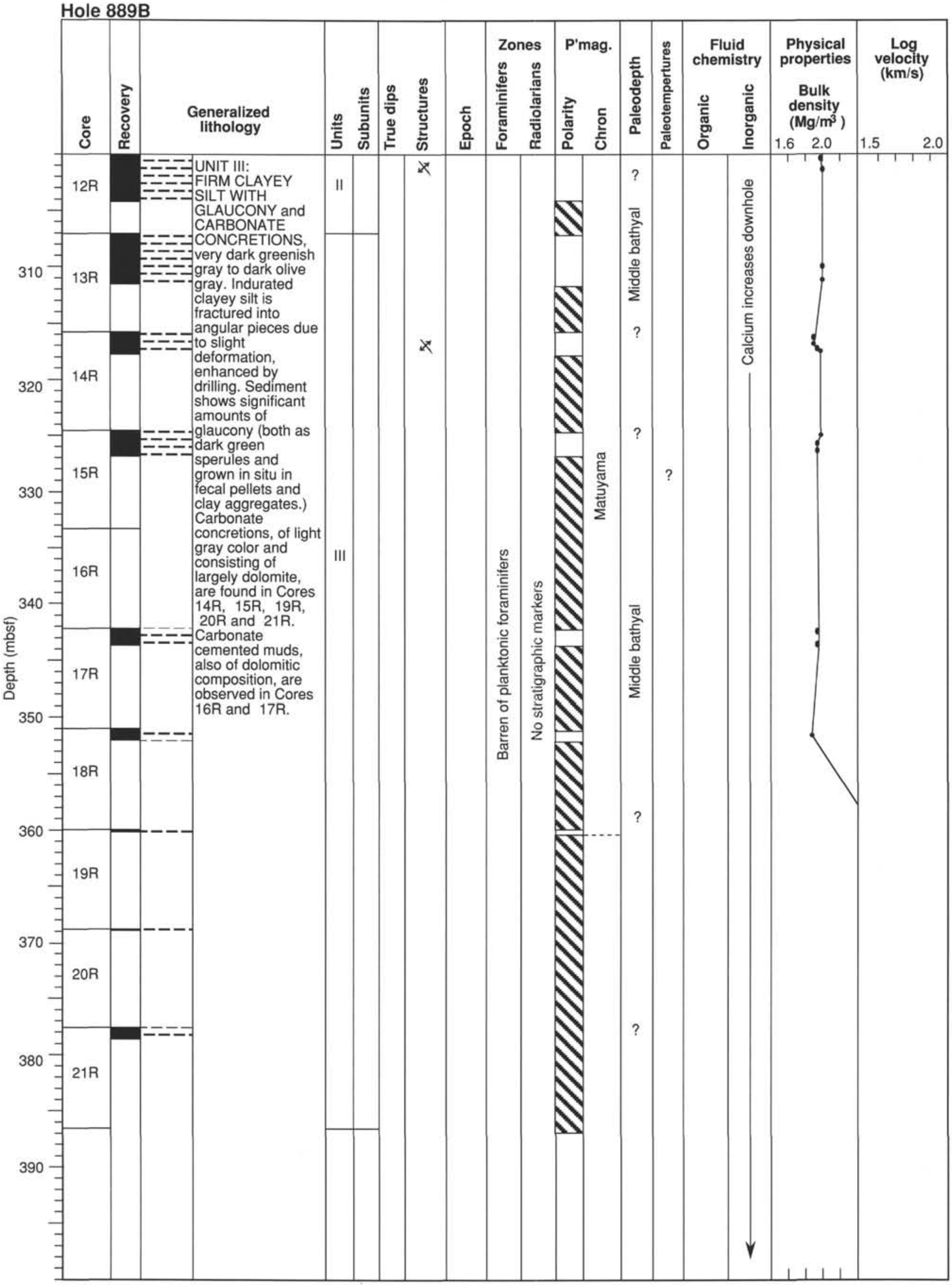

Figure 104 (continued).

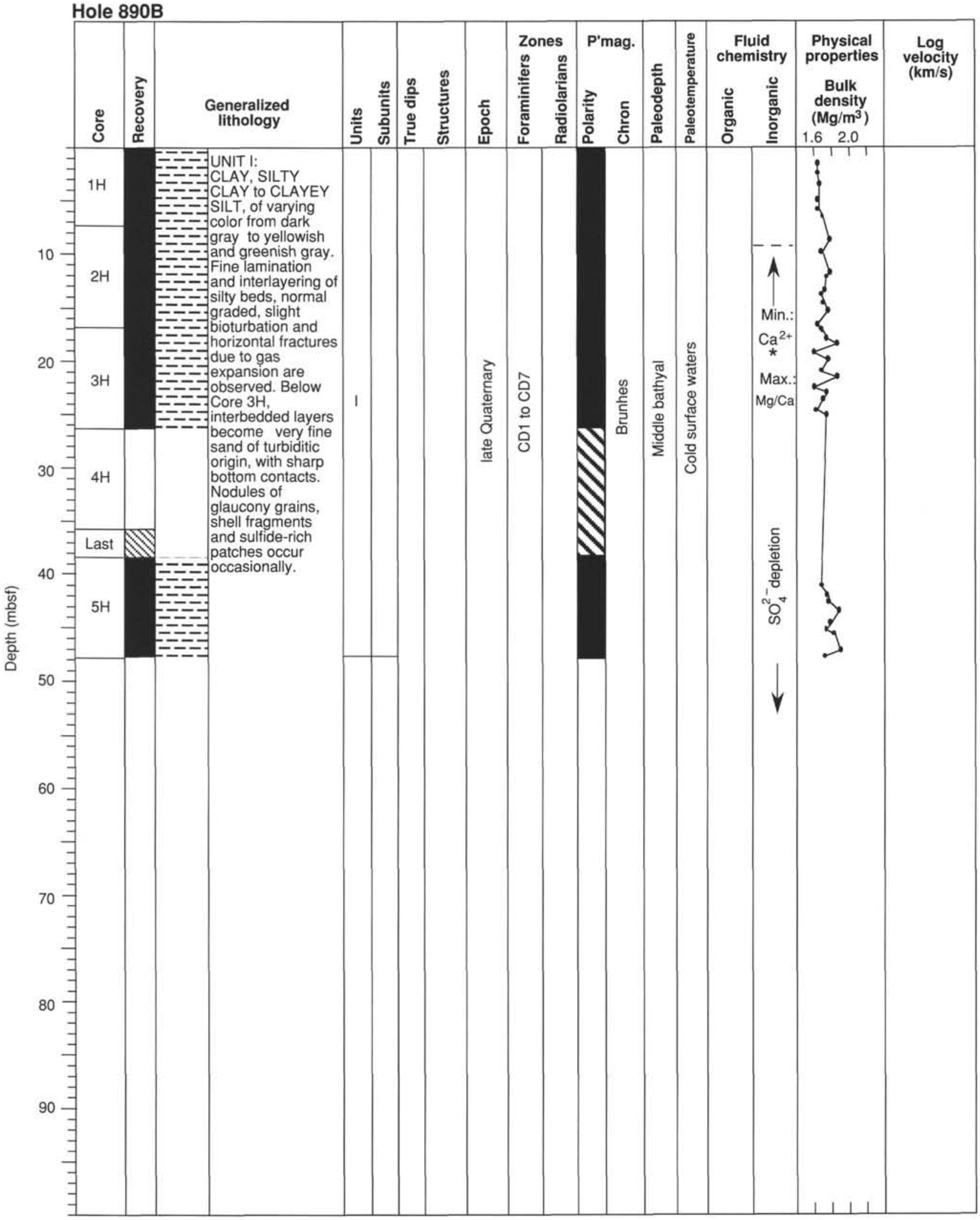

Figure 104 (continued).

The greatest surprise in the data collected at Site 889 was that the temperature measurements predict the base of the stability field for a hydrate formed from pure methane in pure water to occur at a depth of 260 mbsf, rather than the depth of the BSR at 225 mbsf. An analysis of the results of earlier ODP and DSDP drilling in three locations at or near to BSRs, by Hyndman et al. (1992), had suggested that the depths of BSRs are most compatible with the base of the stability field of hydrate formed from pure methane and pure water. In the case of Site 889, it appears that the estimated base of the stability field for pure methane and seawater is a better predictor of the depth of the BSR (Fig. 103). The important question to be answered is, does the base of the hydrate zone actually lie at the BSR or elsewhere? Temperature measurements made on cores indicate that hydrate is present in the region immediately above 225 mbsf, but not below it. No hydrate that could be recognized by eye was seen in any of the cores from the two holes that were cored at Site 889. Methane measured as HS gas locally achieves concentrations in excess of 60,000 ppmv throughout the interval 128–380 mbsf. In Hole 889A, methane concentration declines sharply below 250 mbsf, and although it increases again in places below 250 mbsf to about 40,000 ppmv, it never attains the levels meas- ured above 250 mbsf. In Hole 889B, however, concentrations in excess of 60,000 ppmv were measured in six cores at intervals beneath 250 mbsf. The distribution of methane, therefore, does not directly indicate the presence of hydrate in any part of the section. An as yet imperfectly understood correlation between the distribution of gases and the BSR is the strong peak in the concentration of carbon dioxide, of 33,000 ppmv in Hole 889A and 15,000 ppmv in Hole 889B, immediately beneath the BSR.

The variation in seismic velocity measured by the VSP through the interval 150–243 mbsf, a gentle increase in velocity from 1680 to 2150 m/s down to 215 mbsf, turning to a rapid decrease in velocity to 1100 m/s below 225 mbsf (Fig. 103), would be well explained by a boundary at 225 mbsf between sediment containing hydrate above it and sediment with a small percentage of gas present beneath it (Domenico, 1976).

The concentration of chloride in pore water has been used by several authors to estimate the proportion of hydrate present in pore spaces by its dilution effect upon pore water, assuming that the concentration of chloride in pore water is the same as that in seawater. Between 130 and 300 mbsf at Site 889, the concentration of chloride is about 35% below that of seawater, with a variation of about ±2%, and the uniformity of the Ca/Cl and Mg/Cl ratios indicates that this depression of the Cl^- concentration is caused primarily by dilution. No major change in the concentration of chloride is seen at either the BSR or the predicted base of the stability field of pure-methane/pure-water hydrate at 260 mbsf. Below 300 mbsf, chloride still has the anomalous average value of about 368 mM, but systematic changes in the Ca^{2+} and Mg^{2+} concentrations indicate that the low chlorinity is not simply a dilution effect, and could be an indication of fluid flow in the section or an effect of diagenesis in a different lithology. The low chlorinity of the section above 300 mbsf cannot be explained simply by the dilution effect of the dissociation of hydrate brought up in the cores, as part of that interval lies outside the stability field of even pure-methane/pure-water hydrate.

A possibility that should be explored is that the low chlorinity below 225 mbsf has been produced by the dissociation of hydrate that was present in that interval in the past and that the rates of flow of pore water through the interval have been too slow to flush out the diluted water. The base of the hydrate stability field has presumably migrated upward, relative to the sediments in the section, because the seafloor was elevated as the accretionary wedge grew and because of the deposition of the slope basin sediments. These two processes together have probably produced a relative upward migration of the base of the hydrate stability field of nearly 200 m, over several hundred thousand years. A much more rapid migration of about 70 m over a period of about 10,000 yr could be the result of recovery from cooling during the last glacial period. During the last glacial, the temperature of the seafloor may have been reduced by up to 4°C from its present-day value of 2.7°C to −1.3°C, if the present-day bottom-water temperatures in regions such as the Weddell Sea close to permanent ice caps (Carmack and Foster, 1975) are analogous, and it would have been for a sufficiently long time for a steady-state geotherm to be established in the uppermost 400 m of the section. If so, the base of the hydrate stability field would have been about 70 m deeper (Fig. 104). As the seabed warmed and the geotherm transformed into its current profile, the base of the stability field would have migrated upward, causing the dissociation of the hydrate in the interval that it had traversed and consequent dilution of the pore water. Darcian flow rates of pore fluid through this part of the Vancouver accretionary wedge have been estimated by Hyndman and Davis (1992) to be about 1 mm/yr from the rates of compaction of the sediments forming the accretionary wedge and by Wang et al. (1993) to be only 0.5 mm/yr. If porosity is about 50%, then the average linear velocity of the pore fluid is between 1 and 2 mm/yr. Over 10,000 yr, the path length of the flushing fluid is only 10–20 m, much less than the distance migrated by the base of the stability field. If the distance of migration of the base of the stability field has been about 70 m, we might expect to find a 55-m-thick zone beneath the BSR in which the pore water is diluted. The upward migration of the base of the hydrate stability field will have had the potential to increase the concentration of hydrate in the region above it by releasing methane to migrate upward.

This hypothesis satisfies the geophysical and some of the geochemical data, but does not, by itself, explain the persistence of the low chloride deeper than about 300 mbsf in the section, unless we can invoke longer time scales, with other glacial periods, uplift, and sedimentation contributing, and slower fluid movement. Several issues remain to be resolved, such as the significance of the peak in concentration of carbon dioxide immediately beneath the BSR, the in-situ levels of gas saturation, the stability field for the formation of hydrate in seawater (rather than simply sodium chloride solution and extrapolation to conditions of high pressure and temperature), and the actual seafloor temperatures at the site during the last glacial period.

The pattern of variation in the organic and inorganic geochemistry of the pore fluids and in the physical properties does not show some of the large discontinuities that are seen at Sites 891 and 892 in association with major faults. With the exception of a narrow interval at about 130 mbsf, there is little evidence of significant fluid flow that is confined to conduits or fluid pathways provided by permeable beds or faults. Lithostratigraphic Units II and III are pervasively fractured, and it seems probable that flow through the section will be quite dispersed through this fractured rock. An in-situ measurement of pore-fluid pressure made with the LAST-II at a depth of 140 mbsf in Hole 889D yielded a value close to hydrostatic, indicating only small excess pressure gradients (further processing is required to remove the effect of heave from the data). No direct evidence for large-scale fluid flow through the section was discovered at Site 889, and the linearity of the increase of temperature with depth implies that any flow that is occurring must be at velocities of less than a few millimeters per year.

The CORK borehole seal deployed at Hole 889C is designed to provide data on temperature and pressure, after the effects of drilling have equilibrated. These data should enable the physical conditions of the hydrate stability zone to be defined more precisely, and post-cruise hydrogeologic tests at the seal should define rates of fluid advection below the BSR. These results and the post-cruise analyses of the shipboard data and recovered samples are expected to establish more clearly the relationship between the acoustically defined BSR and the hydrate stability field.

REFERENCES[*]

Archie, G.E., 1942. The electrical resistivity log as an aid in determining some reservoir characteristics. *Trans. Am. Inst. Min. Metall. Pet. Eng.*, 146:54–62.

---

[*] Abbreviations for names of organizations and publication titles in ODP reference lists follow the style given in *Chemical Abstracts Service Source Index* (published by American Chemical Society).

Arthur, M.A., Carson, B., and von Huene, R., 1980. Initial tectonic deformation of hemipelagic sediment at the leading edge of the Japan convergent margin. *In* Langseth, M., Okada, H., et al., *Init. Repts. DSDP,* 56, 57 (Pt. 1): Washington (U.S. Govt. Printing Office), 569–613.

Athy, L.F., 1930. Density, porosity and compaction of sedimentary rocks. *AAPG Bull.,* 14:1–24.

Baker, P.A., and Kastner, M., 1981. Constraints on the formation of sedimentary dolomite. *Science,* 213:215–216.

Behrmann, J.H., Lewis, S.D., Musgrave, R.J., et al., 1992. *Proc. ODP, Init. Repts.,* 141: College Station, TX (Ocean Drilling Program).

Brigaud, F., and Vasseur, G., 1989. Mineralogy, porosity and fluid control on thermal conductivity of sedimentary rocks. *Geophys. J.,* 98:525–542.

Brindley, G.W., and Brown, G. (Eds.), 1980. *Crystal Structures of Clay Minerals and Their X-ray Identification.* Mineral. Soc. London Monogr., 5.

Brückmann, W., 1989. Typische Kompakationsmuster mariner Sedimente und ihre Modifikation in einem rezenten Akkretionskeil (Barbados Ridge). *Beitr. Geol. Inst. Univ. Tübingen, Rh. A,* 5:1–135.

Cande, S.C., and Kent, D.V., 1992. A new geomagnetic polarity time scale for the Late Cretaceous and Cenozoic. *J. Geophys. Res.,* 97:13917–13951.

Carlson, P.R., and Nelson, C.H., 1987. Marine geology and resource potential of Cascadia Basin. *In* Scholl, D.W., Grantz, A., and Vedder, I.Y. (Eds.), *Geology and Resource Potential of the Continental Margin of Western North America and Adjacent Ocean Basin—Beaufort Sea to Baja California.* Circum-Pac. Counc. Energy Miner. Res., Earth Sci. Ser., 523–535.

Carmack, E.C., and Foster, T.D., 1975. On the flow of water out of the Weddell Sea. *Deep-Sea Res. Part A,* 22:711–724.

Carslaw, H.S., and Jaeger, J.C., 1959. *Conduction of Heat in Solids* (2nd ed.): Oxford (Clarendon Press).

Claypool, G.E., and Kaplan, I.R., 1974. The origin and distribution of methane in marine sediments. *In* Kaplan, I.R. (Ed.), *Natural Gases in Marine Sediments:* New York (Plenum), 99–140.

Cowan, D.S., 1985. The origin of some common types of melange in the western Cordillera of North America. *In* Nasu, N., et al. (Eds.), *Formation of Active Ocean Margins:* Tokyo (Terra Publ.), 257–272.

Davis, E.E., and Hyndman, R.D., 1989. Accretion and recent deformation of sediments along the northern Cascadia subduction zone. *Geol. Soc. Am. Bull.,* 101:1465–1480.

Davis, E.E., Hyndman, R.D., and Villinger, H., 1990. Rates of fluid expulsion across the northern Cascadia accretionary prism: constraints from new heat flow and multichannel seismic reflection data. *J. Geophys. Res.,* 95:8869–8889.

Dekkers, M., 1988. Some rock-magnetic properties of fine-grained hematite, goethite, and pyrrhotite [Ph.D. dissert.]. Univ. of Utrecht.

Domenico, S.N., 1976. Effect of brine-gas mixture on velocity in an unconsolidated sand reservoir. *Geophysics,* 41:882–894.

Englezos, P., and Bishnoi, P.R., 1988. Prediction of gas hydrate formation conditions in aqueous solutions. *Am. Inst. Chem. Eng.,* 34:1718–1721.

Ferguson, I.J., 1991. Numerical modelling of heat flow and fluid flow in subduction-accretion complexes [Ph.D. thesis]. Univ. of Birmingham.

Froget, C., Desprairies, A., Latouche, C., and Maillet, N., 1989. Paleoenvironmental significance of Cenozoic clay deposits from the Norwegian Sea: ODP Leg 104. *In* Eldholm, O., Thiede, J., Taylor, E., et al., *Proc. ODP, Sci. Results,* 104: College Station, TX (Ocean Drilling Program), 41–60.

Gassmann, F., 1951. Elastic waves through a packing of spheres. *Geophysics,* 26:673–685.

Hamilton, E.L., 1976. Variations of density and porosity with depth in deep-sea sediments. *J. Sediment. Petrol.,* 46:280–300.

Hesse, R., Lebel, J., and Gieskes, J.M., 1985. Interstitial water chemistry of gas-hydrate-bearing sections on the Middle America Trench slope, Deep Sea Drilling Project Leg 84. *In* von Huene, R., Aubouin, J., et al., *Init. Repts. DSDP,* 84: Washington (U.S. Govt. Printing Office), 727–737.

Hitchon, B., 1974. Occurrence of natural gas hydrates in sedimentary basins. *In* Kaplan, I.R. (Ed.), *Natural Gases in Marine Sediments:* New York (Plenum), 195–226.

Hyndman, R.D., and Davis, E.E., 1992. A mechanism for the formation of methane hydrate and seafloor bottom simulating reflectors by vertical fluid expulsion. *J. Geophys. Res.,* 97:7025–7041.

Hyndman, R.D., Foucher, J.P., Yamano, M., Fisher, A., and Scientific Team of Ocean Drilling Program Leg 131, 1992. Deep sea bottom-simulation-reflectors: calibration of the base of the hydrate stability field as used for heat flow estimates. *Earth Planet. Sci. Lett.,* 109:289–302.

Hyndman, R.D., and Spence, G.D., 1992. A seismic study of methane hydrate marine bottom simulating reflectors. *J. Geophys. Res.,* 97:6683–6698.

Karig, D.E., and Lundberg, N., 1990. Deformation bands from the toe of the Nankai accretionary prism. *J. Geophys. Res.,* 95:9099–9109.

Katz, D.L., Cornell, D., Kobayashi, R., Poettmann, F.H., Vary, J.A., Elenbaas, J.R., and Weinaug, C.F., 1959. Water-hydrocarbon systems. *In* Katz, D.L., Cornell, D., Kobayashi, R., Poettmann, F.H., Vary, J.A., Elenblas, J.R., and Weingug, C.F. (Eds.), *Handbook of Natural Gas Engineering:* New York (McGraw-Hill), 189–221.

Keller, G., 1980. Planktonic foraminiferal biostratigraphy and paleoceanography of the Japan Trench, Leg 57, Deep Sea Drilling Project. *In* von Huene, R., Nasu, N., et al., *Init. Repts. DSDP,* 56, 57 (Pt. 2): Washington (U.S. Govt. Printing Office), 809–833.

Krs, M., Krsová, M., Pruner, P., Zeman, A., Novák, F., and Jansa, J., 1990. A petromagnetic study of Miocene rocks bearing micro-organic material and the magnetic mineral greigite (Sokolov and Cheb basins, Czechoslovakia). *Phys. Earth Planet. Inter.,* 63:98–112.

Kulm, L.D., von Huene, R., et al., 1973. *Init. Repts. DSDP,* 18: Washington (U.S. Govt. Printing Office).

Kvenvolden, K.A., and Barnard, L.A., 1983. Hydrates of natural gas in continental margins. *In* Watkins, J.S., and Drake, C.L. (Eds.), *Studies in Continental Margin Geology.* AAPG, 631–640.

Kvenvolden, K.A., and McMenamin, M.A., 1980. Hydrates of natural gas: a review of their geologic occurrence. *Geol. Surv. Circ. (U.S.),* 825:1–9.

Le Pichon, X., Foucher, J.-P., Boulegue, J., Henry, P., Lallemant, S., Benedetti, M., Avedik, F., and Mariotti, A., 1990. Mud volcano field seaward of the Barbados accretionary complex: a submersible survey. *J. Geophys. Res.,* 95:8931–8943.

Lowrie, W., 1990. Identification of ferromagnetic minerals in a rock by coercivity and unblocking temperature properties. *Geophys. Res. Lett.,* 17:159–162.

Lundberg, N., and Moore, J.C., 1986. Macroscopic structural features in Deep Sea Drilling Project cores from forearc regions. *In* Moore, J.C. (Ed.), *Structural Fabrics Preserved in Deep Sea Drilling Project Cores from Forearcs.* Mem.—Geol. Soc. Am., 166:13–44.

Makogon, Y.F., 1981. *Hydrates of Natural Gas:* Tulsa (PennWell).

Maltman, A.J., Byrne, T., Karig, D.E., Lallemant, S., Knipe, R., and Prior, D., 1993. Deformation structures at Site 808, Nankai accretionary prism, Japan. *In* Hill, I.A., Taira, A., Firth, J.V., et al., *Proc. ODP, Sci. Results,* 131: College Station, TX (Ocean Drilling Program), 123–133.

Mathews, M.A., and von Huene, R., 1985. Site 570 methane hydrate zone. *In* von Huene, R., Aubouin, J., et al., *Init. Repts. DSDP,* 84: Washington (U.S. Govt. Printing Office), 773–790.

McManus, D.A., 1991. Suggestions for authors whose manuscripts include quantitative clay mineral analysis by X-ray diffraction. *Mar. Geol.,* 98:1–5.

Miller, J.J., Lee, M.W., and von Huene, R., 1991. A quantitative analysis of gas hydrate phase boundary reflection (BSR), offshore Peru. *AAPG Bull.,* 75:910–924.

Minshull, T., and White, R., 1989. Sediment compaction and fluid migration in the Makran accretionary prism. *J. Geophys. Res.,* 94:7387–7402.

Musgrave, R.J., Delaney, M.L., Stax, R., and Tarduno, J.A., 1993. Magnetic diagenesis, organic input, interstitial water chemistry, and paleomagnetic record of the carbonate sequence on the Ontong Java Plateau. *In* Berger, W.H., Kroenke, L.W., Mayer, L.A., et al., *Proc. ODP, Sci. Results,* 130: College Station, TX (Ocean Drilling Program), 527–546.

Mutti, E., and Ricci Lucchi, F., 1972. Le torbiditi dell'Appennino settentrionale: introduzione all'analisi di facies. *Mem. Soc. Geol. Ital.,* 11:161–199.

Nigrini, C.A., and Caulet, J.P., 1992. Late Neogene radiolarian assemblages characteristic of Indo-Pacific areas of upwelling. *Micropaleontology,* 38:139–164.

Odin, G.S., 1985. Significance of green particles (glaucony, berthierine, chlorite) in arenites. *In* Zuffa, G.G. (Ed.), *Provenance of Arenites:* Berlin (Reidel), 279–307.

Odin, G.S., and Matter, A., 1981. Die glauconarium origine. *Sedimentology,* 28:611–643.

Odin, G.S., and Stephan, J.F., 1981. The occurrence of deep water glaucony from the eastern Pacific: the result of *in situ* genesis or subsidence? *In* Watkins, J.S., Moore, J.C., et al., *Init. Repts. DSDP,* 66: Washington (U.S. Govt. Printing Office), 419–428.

Perry, E.A., and Hower, J., 1972. Late-stage dehydration in deeply buried pelitic sediments. *AAPG Bull.,* 56:2013–2021.

Revelle, R., 1983. Methane hydrates in continental slope sediments and increasing atmospheric carbone dioxide. *Changing Climate:* Washington (National Academy Press), 252–261.

Richter, C., van der Pluijm, B.A., and Housen, B.A., 1993. The quantification of crystallographic preferred orientation using magnetic anisotropy. *J. Struct. Geol.,* 15:113–116.

Serra, O., 1984. *Fundamentals of Well Log Interpretation* (Vol. 1): *The Acquisition of Logging Data:* Amsterdam (Elsevier).

Sloan, E.D., 1990. *Clathrate Hydrates of Natural Gasses:* New York (Marcel Dekker).

Spence, G.D., Hyndman, R.D., et al., 1991. Seismic structure of the northern Cascadia accretionary prism: evidence from new multichannel seismic reflection data. *In* Meissner, R., Brown, L., Birbaiet, W., et al. (Eds.), *Continental Lithosphere, Deep Seismic Reflection.* Am. Geophys. Union, Geodyn. Ser., 22:257–263.

Spence, G.D., Hyndman, R.D., Davis, E.E., and Yorath, C.J., 1991. Marine multichannel seismic reflection data across the continental margin of Vancouver Island. *Geol. Surv. Can., Open File,* 2391.

Taira, A., Hill, I., Firth, J.V., et al., 1991. *Proc. ODP, Init. Repts.,* 131: College Station, TX (Ocean Drilling Program).

Toksöz, M.N., Cheng, C.H., and Timur, A., 1976. Velocities of seismic waves in porous rocks. *Geophysics,* 41:621–645.

Wang, K., Hyndman, R.D., and Davis, E.E., 1993. Thermal effects of sediment thickening and fluid expulsion in accretionary prisms: mode and parameter analysis. *J. Geophys. Res.,* 98:9975–9984.

Wang, M.C., Nacci, V.A., and Markert, C.D., 1976. Electrical resistivity method for marine sediment consolidation study. *Proc. 8th Ann. Offshore Technol. Conf.,* Houston, TX, Pap. 2623.

Whalley, E., 1980. Speed of longitudinal sound in clathrate hydrates. *J. Geophys. Res.,* 85:2539–2542.

Whiticar, M.J., Faber, E., and Schoell, M., 1986. Biogenic methane formation in marine and freshwater environments: CO_2 reduction vs. acetate fermentation—isotope evidence. *Geochim. Cosmochim. Acta,* 50:693–709.

Wood, A.B., 1941. *A Textbook of Sound* (2nd ed.): New York (MacMillan).

Ms 146IR-008

NOTE: For all sites drilled, core-description forms ("barrel sheets") and core photographs can be found in Section 6, beginning on page 429. Forms containing smear-slide data can be found in Section 7, beginning on page 591.

Hole 889A: Resistivity-Velocity-Natural Gamma Ray Log Summary

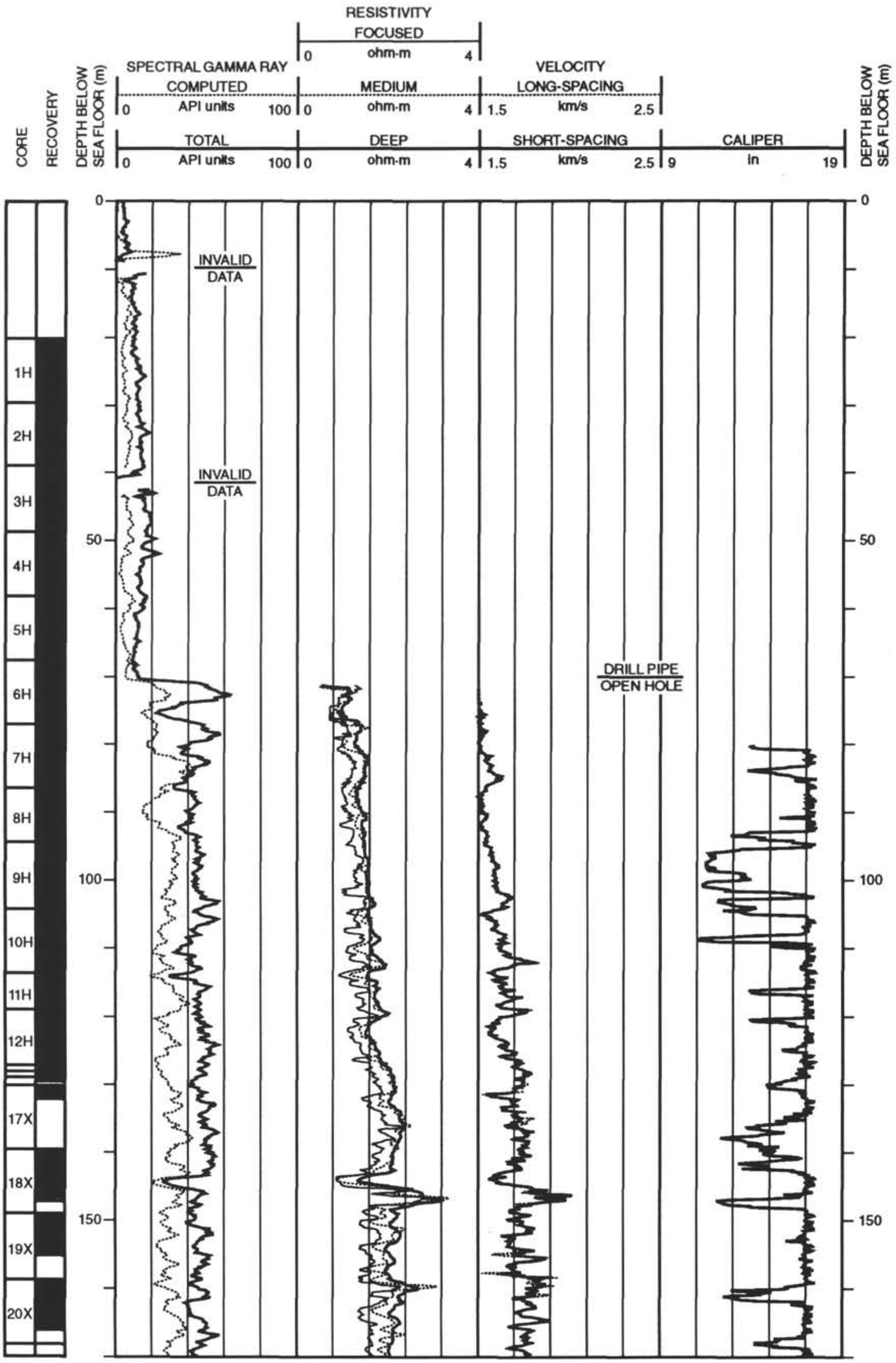

Hole 889A: Resistivity-Velocity-Natural Gamma Ray Log Summary (continued)

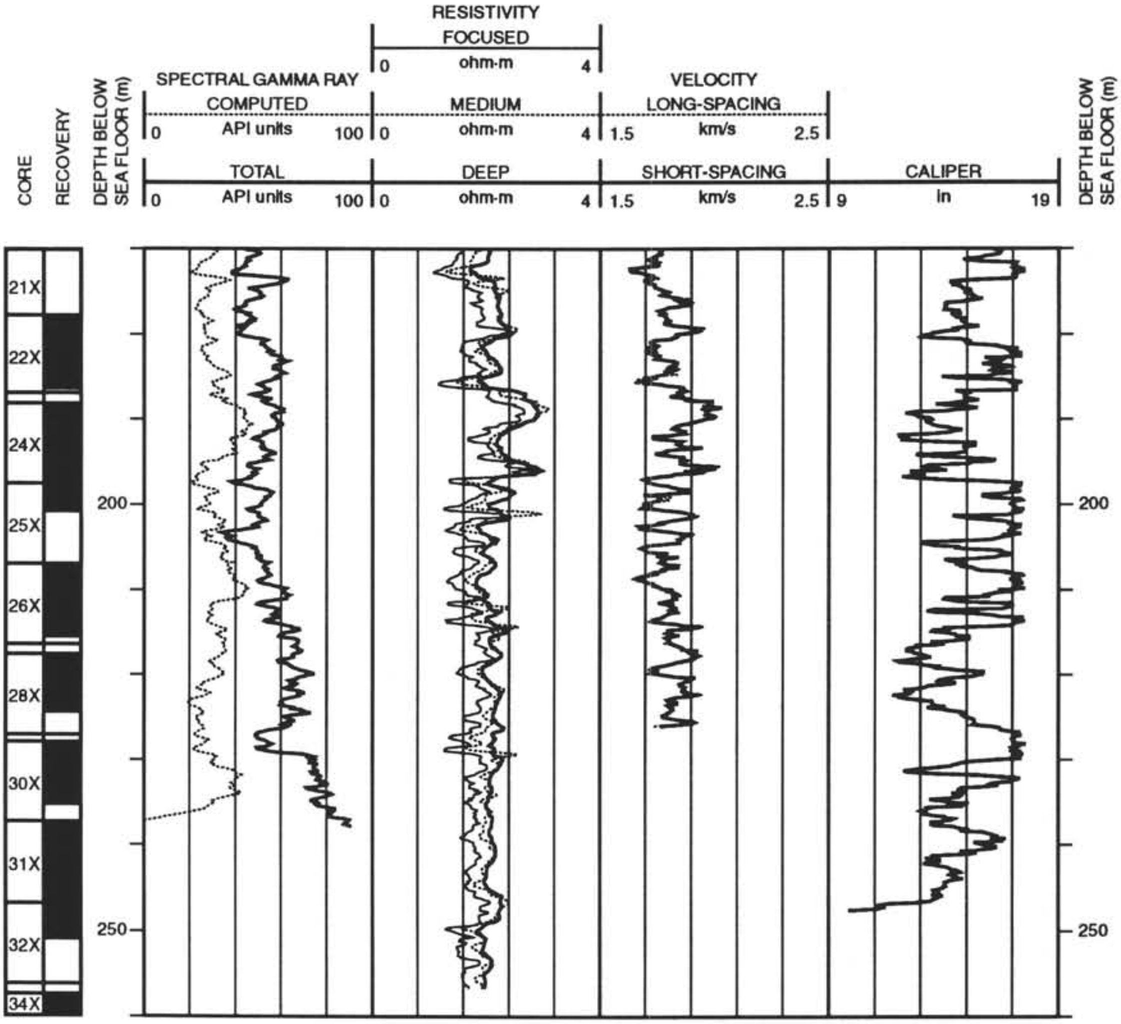

Hole 889A: Porosity-Natural Gamma Ray Log Summary

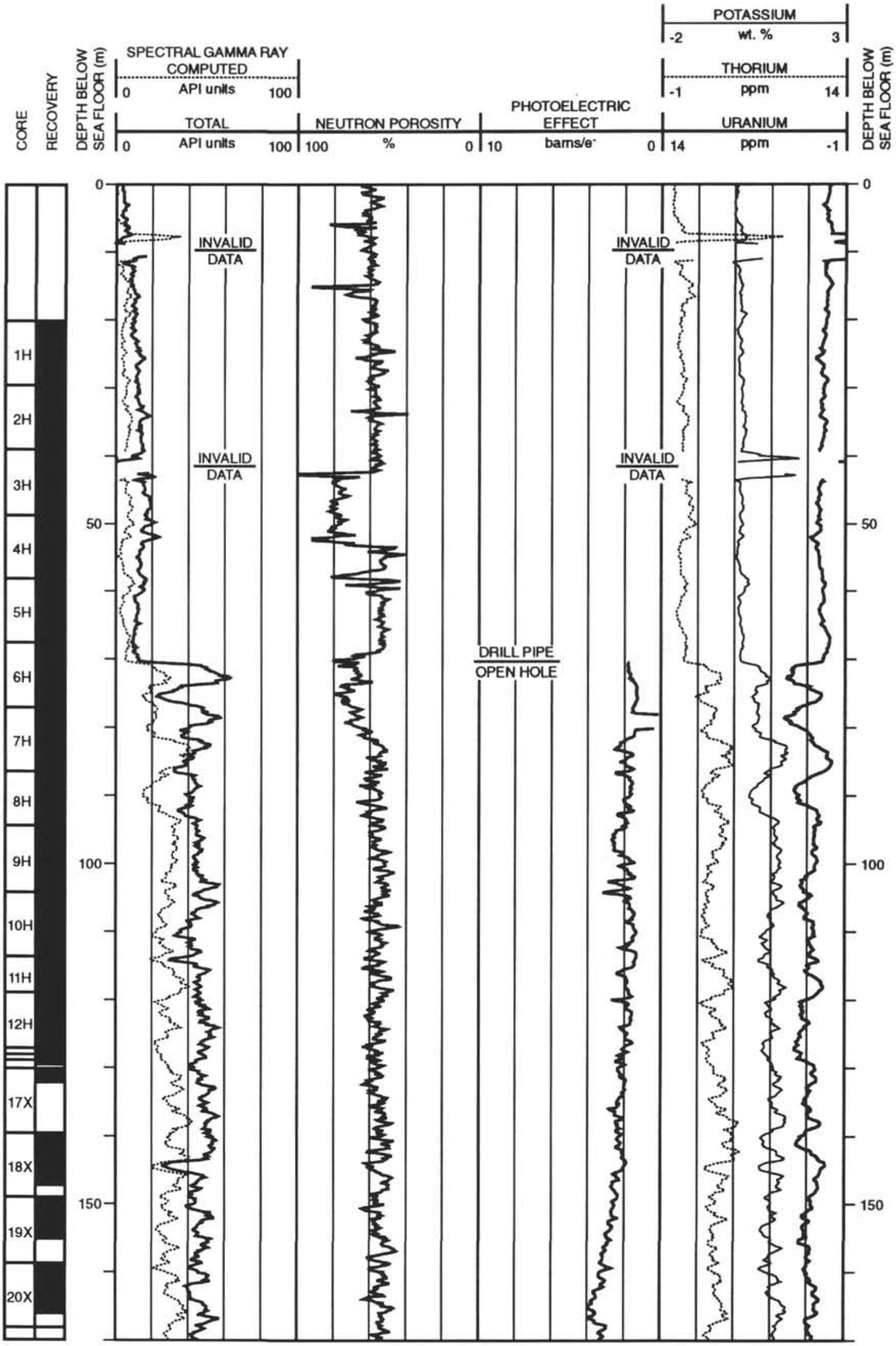

Hole 889A: Porosity-Natural Gamma Ray Log Summary (continued)

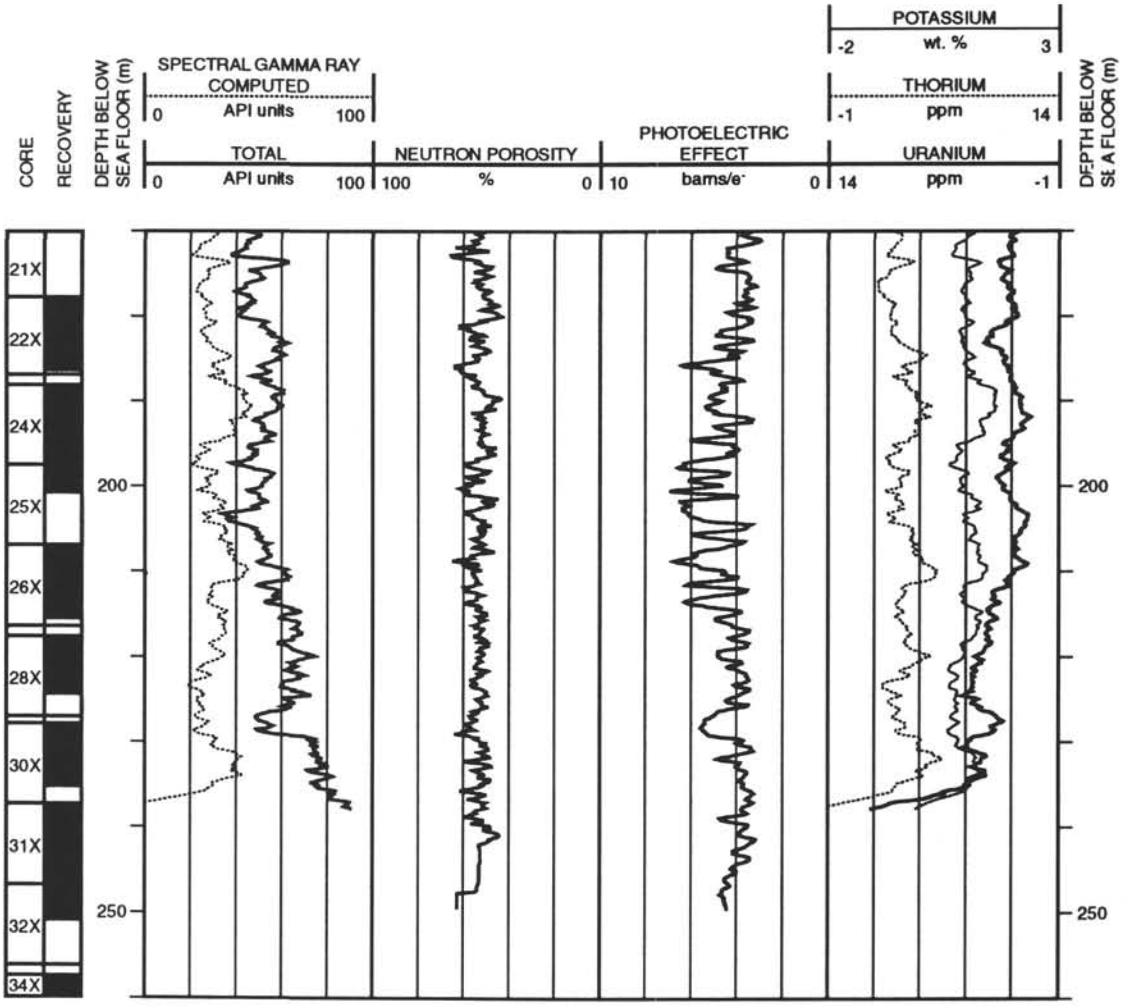

Hole 889B: Resistivity-Velocity-Natural Gamma Ray Log Summary

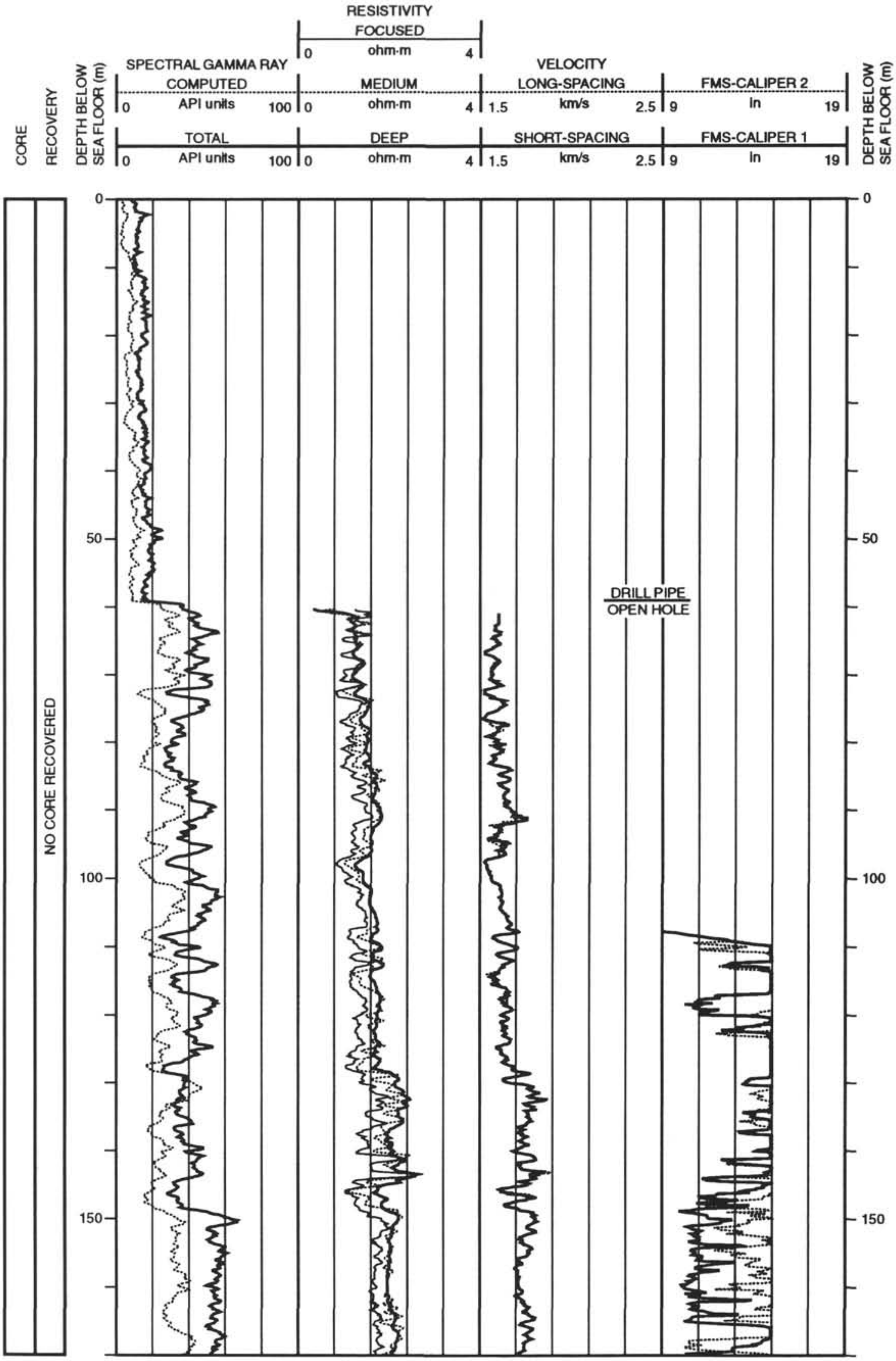

Hole 889B: Resistivity-Velocity-Natural Gamma Ray Log Summary (continued)

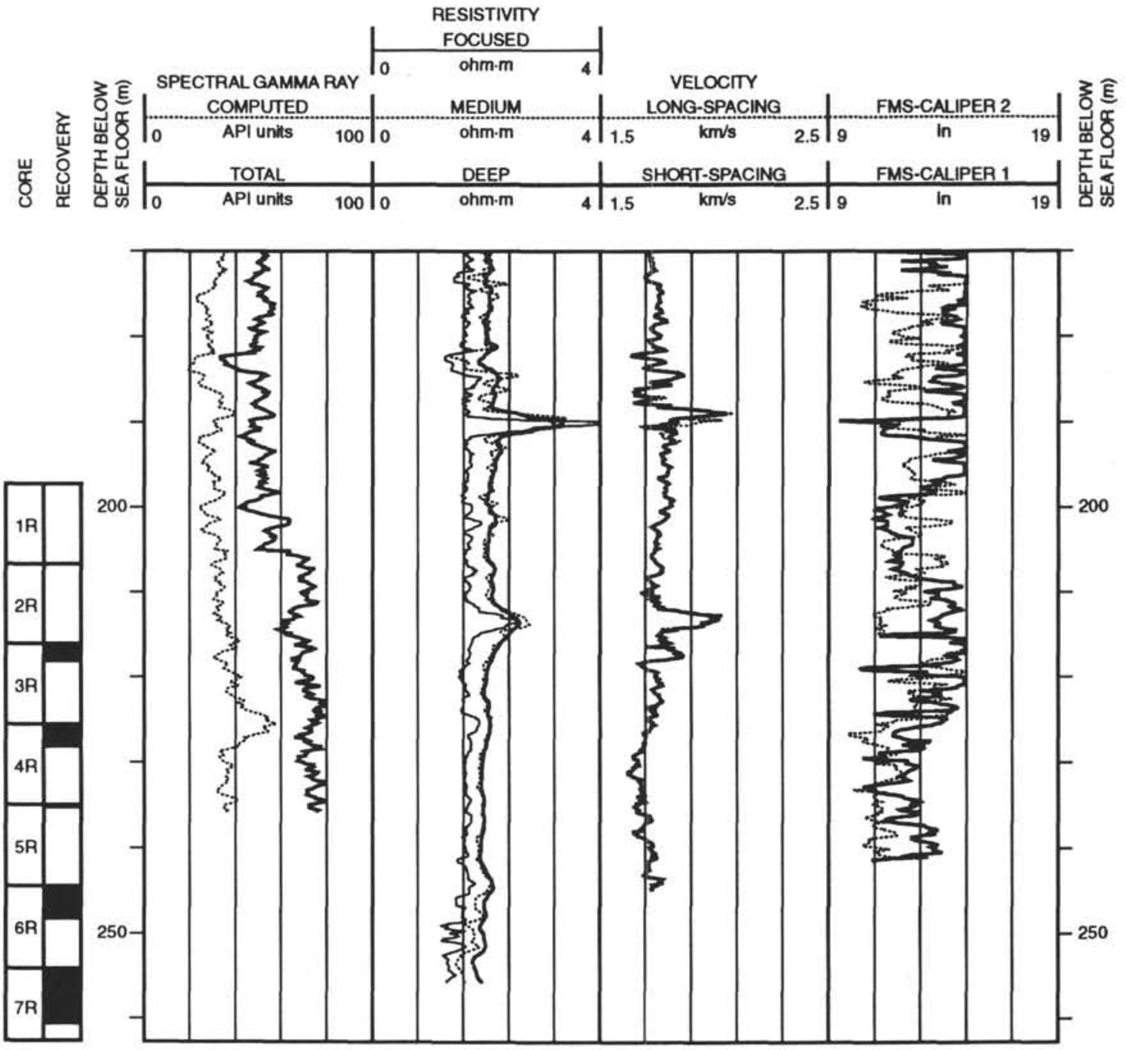

Hole 889B: Porosity-Natural Gamma Ray Log Summary

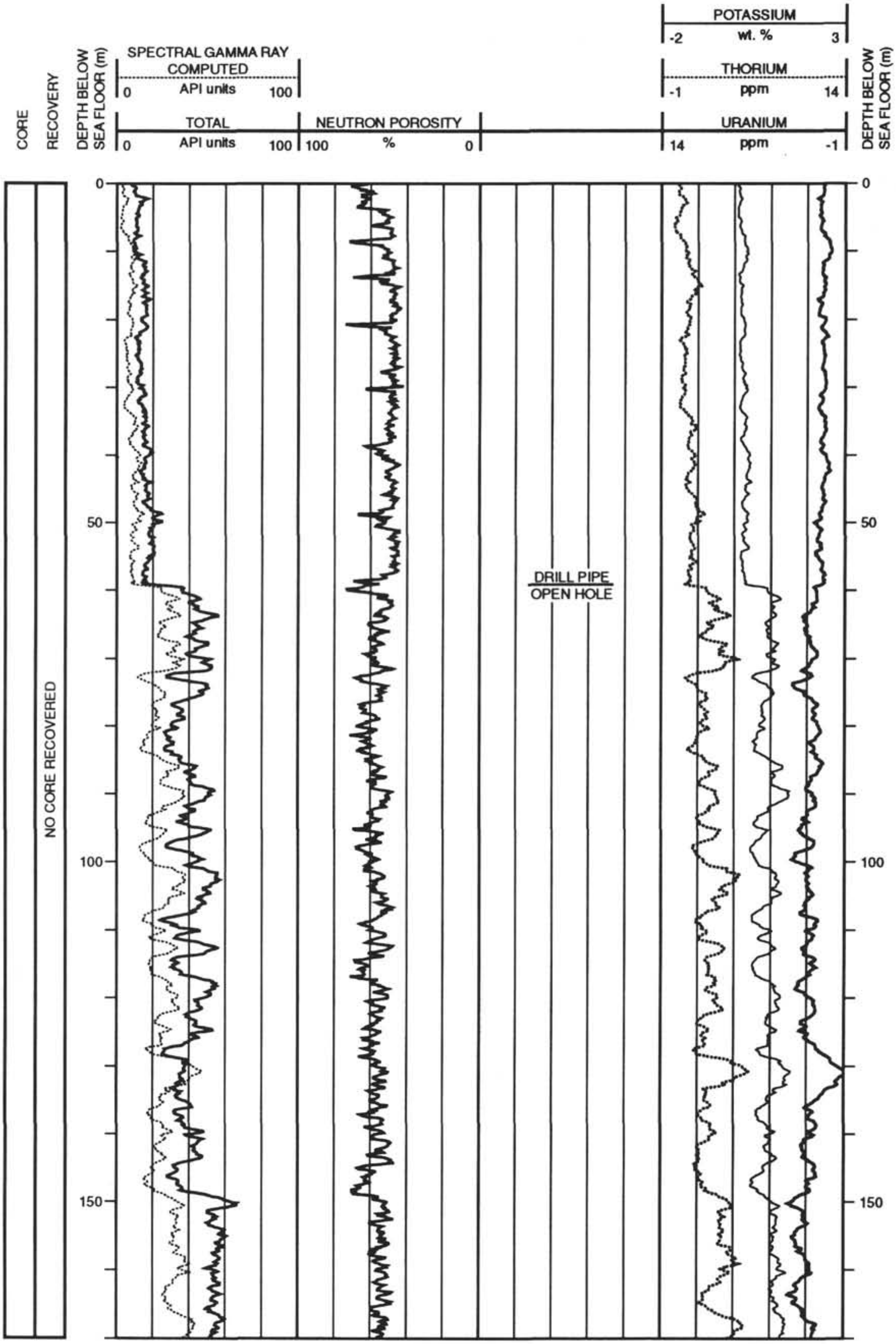

Hole 889B: Porosity-Natural Gamma Ray Log Summary (continued)